Advanced fibre gratings in near- and mid-infrared region and their applications for structure monitoring and biosensing

Namita Sahoo

Doctor of Philosophy

Aston University

November 2021

Aston University

Advanced fibre gratings in near- and mid-infrared region and their applications for structure monitoring and biosensing

Namita Sahoo

Doctor of Philosophy

November 2021

This thesis emphasises an elaborate research finding on the fabrication, analysis of resonance spectral response and sensing applications in various fields using different type of optical fibre grating devices over an entire wavelength range from near- to mid-infrared (IR).

Firstly, the major contribution described in the thesis is a thorough investigation of sensor structures, detailed in respect to writing techniques for optical fibre gratings irradiated by a frequency-doubled Argon ion laser. Thereafter spectral modulation for these UV-inscribed fibre Bragg gratings (FBGs), long period gratings (LPGs) and tilted fibre gratings (TFGs) of small and large angled structures are analysed. Special LPG devices with both dual peaks and 1st&2nd orders, and excessively tilted TFGs (Ex-TFGs) are also achieved with the resonances in the mid-IR range for enhanced sensitivity. Investigations of different sensing measurements, such as temperature, strain, bending and surrounding refractive index (SRI) for these fibre grating devices are performed.

Another important contribution is the study on experimental investigation for the fabrication of FBGs into multicore fibre such as four core fibre (4CF) with two different core spacings and seven core fibre (7CF) are explained. A selective inscription method is utilised for inscribing FBGs into different cores of multicore fibre (MCF). The measurement performance with vector bend/twist sensing results in an enhanced sensitivity for FBGs in the distributed cores around the circumference of 4CF and 7CF is analysed in detail, showing the effective detection of both amplitude and direction. Whereas, in 7CF the central core FBG acts as the temperature reference having low bending sensitivity of -8.83 pm/m^{-1}, presenting extra function for eliminating temperature cross-talk effect. The application for these grating devices is largely associated to structural monitoring in astronomy, biomedical sciences, and robotics.

Finally, I have investigated different enzyme functionalised and nano-deposited LPG devices for bio and environmental sensing applications. The experimental findings for these sensors are discussed in glucose sensing measurements by observing resonance wavelength shift. Whereas LPGs fabricated with mono or multi-layered deposition of 2D nanomaterials, such as graphene oxide (GO) solution and single walled carbon nanotubes (SWCNT) are demonstrated with SRI measurement. Here, the fabricated devices show a significant intensity change into the transmission spectrum. The resonance response is observed in the near- to mid-IR ranges. This enhanced sensitivity is utilised for haemoglobin sensing in the detection of anaemia in human body and relative humidity sensing for monitoring environmental condition respectively. All demonstrated optical fibre grating based sensors have potential for a wide range of future applications in industry, medical and environmental sectors.

Keywords: Optical fibre gratings, Vector sensors, Enzyme functionalisation, Glucose sensing, Haemoglobin sensing, Relative humidity.

To my beloved husband Jyotirmoy Koley,

my lovely parents, my sister Amita, family, and friends

Acknowledgements

Firstly, I want to sincerely thank my respected supervisor Prof. Lin Zhang for offering me the great opportunity to pursue research work in the field of optical fibre grating sensors and providing me the guidance throughout my time in Aston University. I always appreciate her advice for showing me the right path in establishing a good research plan and continually motivating me towards academic progress along with my teaching activities. I will remain grateful to her forever.

My sincere thanks to Dr. Kaiming Zhou for his suggestion in following the laser health and safety procedures. I also want to mention his advice regarding biosensing experiments and preparation of presentation for conferences. I would also like to thank Dr. Xianfeng Chen for his valuable guidance in the biosensing experiments. I am thankful to Dr. Yidong Tan, Dr. Binbin Luo and Dr. Biqiang Jiang for their suggestions and discussions.

I acknowledge the advice from Prof. David Webb in following the general health and safety guidelines to continue my research work successfully. My sincere gratitude always for his support in actively providing research facilities during Covid-19 situation. The seminars, conferences and trainings organised by Prof. David Webb, Prof. Sergei Turitsyn and PGR committee provided me immense learning opportunities.

My sincere thanks to Dr. Tom Suen and Dr. Shen Liu for their immense support during the fabrication and measurements of fibre grating sensor devices. I also want to thank Dr. Changle Wang and Dr. Weijia Bao for their support on grating fabrications into multicore fibre.

Specifically, I am grateful to the lab technicians, Dr. Kirill Tokmakov and Ms. Swaroopa Mucheli-Sudhakar for their support during any troubleshooting for our UV laser system and other needs specially associated with laboratory equipment. I am thankful to the postgraduate research team, particularly, Research Student Administrator Mrs. Sandra Mosley for her guidance in preparing the research method for IS4001 and qualifying report during my study time and Academic Support Administrator, Mrs. Helen Yard for assisting me with office logistics.

My cordial thanks to the library in assisting me with online and physical access of required research materials during my entire study. Thanks must go to the IT service department for their continuous help to resolve any issues related to setting up the required software to pursue research work.

I also want to acknowledge the support and guidance from all collaborators, my friends, and colleagues for their continuous support in my study life.

Finally, and most importantly, I would always express my heartiest gratitude to my parents and all of my family members for their continuous encouragement and infusing enthusiasm in my post graduate education in India and pursuing research in the UK. Their invaluable support and togetherness made my journey easier towards successfully completing my research work.

Contents

ACRONYMS

APTES	3-Aminopropyl triethoxysilane
BBS	Broadband source
B-Ge	Boron- Germanium
CMT	Coupled mode theory
CNT	Carbon nanotube
CW	Continuous wave
DI	Deionised
DID	Drawing induced defects
dLPG	Dual peak long period grating
EDFA	Erbium-doped fibre amplifier
EMI	Electromagnetic interference
Ex-TFG	Excessively tilted fibre grating
FBG	Fibre Bragg grating
FSR	Free spectral range
FWHM	Full width at half maximum
Ge	Germanium
GODC	Germanium oxygen - deficient centre
HE	Hybrid mode-waves
IR	Infrared ray
LPG	Long period grating
LP	Linear polarisation
LPMM	Line per millimetre
MCF	Multicore fibre
MCVD	Modified chemical vapor deposition
NaOH	Sodium hydroxide
NIR	Near infrared

OH	Hydroxyl
OSA	Optical spectrum analyser
PBS	Polarisation beam splitter
PC	Polarisation controller
PDL	Polarisation dependent loss
PER	Polarisation extinction ratio
PMC	Phase matching condition
RI	Refractive index
RIU	Refractive index unit
SDM	Space division multiplexing
SA	Sodium acetate
SMF	Single mode fibre
SRI	Surrounding refractive index
WDM	Wavelength division multiplexing

List of figures

Chapter 2

Chapter 3

Chapter 4

Chapter 5

Chapter 6

List of tables

Chapter 3

Chapter 5

Chapter 1

Introduction and Thesis structure

1.1 Introduction

Fibre optics is one of the technological advancements over the last few decades and currently its vast application in different areas of research is highly advantageous. The propagation of light through a fibre core is not only utilised for near-infrared wavelength telecommunication but it can also be used for sensing purposes in biomedical science, civil engineering etc. So as a result, the fibre optics has two main applications: telecommunication and sensing. Communication implies a transfer of information such as speech, images, data etc over a distance, i.e., from one point to another. In this case the modulated wave acts as a carrier and reaches the receiving end. In another application the fibre itself is modulated with difference in refractive index within it, typical examples are optical fibre gratings. In-fibre gratings were first demonstrated by Hill et al. in 1978 [1]. This utilises the application in sensing fields depending on different temperature, strain, and other environmental conditions. Our research focus is optical fibre grating based sensing for various real time applications.

Photosensitivity has significant role in optical fibres and waveguides. It is utilised from telecommunication industry to sensing technology through fibre grating inscriptions. Photosensitivity was first discovered into germanium doped silica fibres [2]. It depends on different mechanisms, namely photochemical, photomechanical, thermochemical etc. It is also dependent on the intensity and wavelength of incident light. There are different models that can explain photosensitivity mechanism. These are mainly colour centre model and compaction densification model. The other alternative models are electric dipole model and electron charge migration model.

The non-photosensitive or weak-photosensitive effect of the fibre also could directly affect the refractive index modulation within fibre in the presence of strong laser illumination. This method is based on compaction-densification model. Fiori and Devine explored their work based on this model and they used a KrF excimer laser to irradiate thin-film amorphous silica samples grown on silica wafer. As the laser illuminates the film thickness is reduced continuously and corresponding refractive index is formed. They retrieved the original refractive index and thickness after annealing at 950 °C for an hour when the compaction disappears [3]. Later, photosensitivity enhancement technique with much followed hydrogen loading method was reported by Lemaire et al. [4], and all these techniques have been utilised to inscribe grating structures in optical fibres.

More dominated applications in using optical fibre gratings are in fibre optic sensing area. A grating is formed by periodic perturbations of refractive index within the fibre core or cladding. The refractive index modulated structures can be created by exposing the Ge and B/Ge doped fibre to

ultraviolet (UV) radiation with a wavelength range of 244-248 nm [4]. Depending on the refractive index modulation period length, the gratings are of two major types: Fibre Bragg Grating (FBG) and Long Period Grating (LPG). In an FBG, it is required to couple a forward propagating core mode to the backward mode and the period length lies in the order of few micrometres. Whereas, in an LPG the coupling occurs between co-propagating core and cladding modes, and it has a period length of several hundred micrometres.

For the past 15 years or more, the optical fibre gratings with tilted structures became more attractive due to their excellent optical properties. Meltz et al. first reported the light coupling phenomena from the core mode to cladding and radiation modes through tilted fibre gratings (TFGs) [5]. Erdogan & Sipe elaborated a complete theoretical analysis of TFG structure with gratings inscribed at 45° tilted angle, enables the light coupling through s-polarised light from guided core-mode to the radiation mode and propagation of p-polarised light through the fibre [6].

In recent years, optical fibre gratings are largely implemented in structural health monitoring purposes, bio and environmental sensing applications. The optical fibre gratings fabricated into special fibres such as thin-cladding single mode - single core fibre and single mode - multicore fibres (SM-MCF) are useful in-fibre components operating through near-IR to mid-IR. The UV-inscribed FBGs into SM-MCF in the near IR enable these for the applications in vector bending and load sensing in structural health monitoring and medical devices [7, 8]. Ultrasensitive-sensors fabricated into normal SMF and thin cladding fibres in the mid-IR range have potential applications in health and environment [9, 10].

1.2 Structure of thesis

The thesis consists of six chapters and the content summary for each chapter are listed as below:

Chapter 1 contains a brief introduction and elaborates the structure of thesis.

Chapter 2 represents a brief historical perspective for the development of fibre gratings. The photosensitivity effect with different models such as, colour centre, stress relaxation and compaction/densification are briefly discussed. Then, different photosensitivity enhancement methods are reviewed in detail. A complete theoretical analysis for different types of grating formation in the phase matched condition and light coupling mechanisms are schematically explained. Finally, different fabrication methods for UV-inscription of FBG, LPG and TFGs are explained.

Chapter 3 is discussed in two parts. Part A emphasises about the fabrication and characterisation of different types of grating in the near IR range. The chapter starts with the fabrication of normal FBGs with the chosen centre wavelengths in the range of 1530 – 1568 nm and followed by the thermal and strain sensing measurements. Then the fabrication and characterisation for UV-inscribed LPGs are discussed. These LPGs with the sensitivity measurements not just for temperature but also surrounding refractive index (SRI) are presented. Following this, a section for the inscription of small angle titled gratings (STFGs) and their thermal sensing analysis are discussed. The Part B is focused onto the fabrication and characterisations of optical fibre gratings in the mid-IR range. The spectral response of LPGs and TFGs are explained with temperature and SRI sensing results.

Chapter 4 investigates the FBG inscription into multicore fibre (MCF) such as 4-core fibre (4CF) and 7-core fibre (7CF) and the details for the vector sensing measurements using MCFs are presented. This chapter starts with the discussion on core positioning into MCF with various core spacings for selective inscription. Then the inscription methods and characterisation for the UV-inscribed FBGs into different cores for both 4CF and 7CF are presented in detail. Finally, vector sensing measurements using FBGs in 4CF and 7CF are demonstrated, and the sensitivity analysis shows clearly these sensors are not just capable of measuring the amplitude but also recognising the direction of the physical structure changes under bending condition.

Chapter 5 describes the fabrication and characterisation of biomaterials coated fibre grating sensors based on LPG and dual peak LPG (dLPG) operating in the near IR to mid-IR region. Initially, the chapter starts with theoretical analysis for fibre sensor with respect to light-matter interaction and investigated for glucose sensing. Then the fabrication and characterisation of enzyme functionalised LPG/dLPG based biosensors are discussed for glucose sensing. In the later section, the GO-based LPG device is demonstrated for fabrication methods and detailed characterisation with respect to thermal and SRI sensing measurements. Thereafter, GO-LPG/ dLPG are presented for haemoglobin

sensing and RH sensing measurements for bio and environmental applications. Finally, nanodeposition with SWCNT for LPG device is investigated for SRI sensing.

Chapter 6 is the thesis conclusion with the discussions of important research findings and suggesting possible future works that might be explored.

Chapter 2

Review: History, photosensitivity, theoretical background of fibre grating and inscription methods

2.1 Brief history of optical fibre grating

The successful experimentation for fibre Bragg gratings (FBGs) formation into germanosilicate fibre was first achieved by Hill et al. in 1978 at the Canadian Communication Research Centre (CRC) [2]. The photosensitivity is the periodic modulation of refractive index along the fibre length. The experiment was performed by the irradiation through an Argon ion laser with the emission wavelength in the visible range of 488 nm or 514.5 nm. These are known as 'Hill' gratings. It was noted from their experiment that the reflectivity continuously increases when a light is launched into the fibre core. As a result, refractive index grating is written in the form of intensity distribution from the 4% back reflected light at the end of fibre core and the forward propagating light. The refractive index modulation increases with an increase in reflectivity. During this process a permanent, narrowband Bragg reflection filters achieved with 100% reflection. The only requirement for this method is a longer exposure time of few minutes. This renowned phenomenon remained unexplored further for almost ten years due to difficulties in the experimental setup. The experimental observation was thought to be limited to one "magic" fibre at CRC in Canada. At that time an increased interest has been shown for developing new methods for grating inscription with different types of fibre such as non-germanosilicate varieties. It is found that the photosensitivity is achievable in several different type of optical fibres that do not have germanium content or very minor fraction of it. This effect is induced by a two-photon process [11] . Germania doped fibre shows maximum photosensitivity than other fibres doped with cerium [12] and erbium [13].

Later there was a continuation of experimental research on second- harmonic generation in a germanium doped optical fibre. A Germania-doped silica fibre has a zero second-order nonlinear co-efficient and is responsible for second-harmonic generation. Another phenomenon called sum-frequency generation was reported by Ohmori and Sasaki [14]. The efficiency of second harmonic generation is found to be increased by a long exposure and it was first shown by Ulf Osterberg and Walter Margulis [15].

The famous grating writing technique using two beam holographic method was first reported by Gerry Meltz et al. [16]. They showed the formation of gratings using single photon absorption in the UV range at 244 nm. A further demonstration depicts that the reflection gratings using two interfering beams were formed at the visible range of spectrum, i.e., 571 - 600 nm. The angle between the interfering beams plays a major role in grating formation. It induces the shift of Bragg condition to higher wavelengths, and it was achievable to fabricate reflection grating at around 1530 nm. This spectrum is very useful for telecommunication purposes and also utilised for demonstrating fibre laser operation [17]. Later a lot of improvements have been done to achieve fibre gratings with longer period length. Lemaire and co-workers showed that a greater refractive index change can be obtained using hydrogen loaded photosensitive fibre [4].

Further technological advancement enhanced the application of FBG in different areas. The optical fibre dispersion was compensated using FBGs reported by Hill et al. [18]. The other type of gratings namely sampled gratings [19], apodised gratings [20], Moiré gratings [21], phase shifted gratings [22] etc. were designed depending on the area of application. Vengsarkar et al. [23] first investigated a special type of grating, that is different from the normal Bragg grating. The main purpose of these gratings is their usage as band rejection filters to get low loss fibres. The difference in period length varies in the range of few hundred microns, named as long period grating (LPG). In this case fundamental guided mode is coupled to the forward propagating cladding modes. Transmission spectrum is measured due to absorption and scattering loss of these propagating modes. The absolute periodicity of LPG depends on phase matching condition during the coupling from one mode to another [24].

A new sensing area was explored with the availability of microstructured fibre to polarisation maintaining fibre [25]. The radiation mode coupling can be increased with an introduction of tilt in the grating fringes. The fabrication of tilted fibre grating (TFG) requires a fibre to be tilted out of the plane. Grating inscription takes place along the direction of propagation of the mode through a fibre. P.S. Westbrook demonstrated the first 45° tilted fibre grating (TFG) in 2000; and later in 2005, Zhou et al., shown the function of 45°-TFG as an in-fibre polariser [26, 27]. Again, the large angled TFGs were developed in 2006 by Zhou et al. at Aston university, UK, which has excellent performance for their high refractive index sensitivity and optimised thermal sensitivity [28].

Effectively, there is a wide exploration of optical fibre grating technology in the modern age. Photosensitivity enhancement and its utilisation with the fabrication of various types of optical fibre gratings are most discussed topic in a number of books, journals, proceedings of conferences etc. Different fabrication methods require high power pulsed laser for writing strong gratings. However, inscription of optical fibre gratings most uses femtosecond laser [29] and UV laser, which produce high-power output to make strong refractive index perturbation onto the fibre.

2.2 Optical fibre photosensitivity

The photosensitivity effect is associated with the formation of optical fibre gratings in silica fibre after the fibre section is exposed to laser radiation at suitable wavelength. The change in refractive index is influenced by UV power and wavelength. It also depends on other parameters such as the fibre type and laser consisting of an absorption band near to 244 nm. In this process a standing wave interference pattern is generated by the counterpropagating light emissions. The photosensitivity enhancement for standard silica fibre depends on several factors, most importantly, fibre core material and type, the radiation wavelength and intensity of light, and the treatment method of fibre such as hydrogen loading. The photosensitivity into germanosilicate fibre induces the perturbed refractive index after a suitable exposure to incident radiation. The photosensitivity phenomenon

enables fibre grating formation, and the grating devices have been widely used in applications as fibre sensors [30], lasers [31] and narrowband filters [32].

2.2.1 Photosensitivity mechanisms

The manufacturing and fabrication of different materials introduce minor defects within it. These can create enormous risks if applied in some applications such as high-speed rotating turbines. Whereas in some fields, this has advantages by utilising the energy band structure for semiconductor materials such as in germanium doped silica fibres.

Optical fibre glass material has significant defects in it. It happens during the fabrication process such as modified chemical vapor deposition (MCVD) method developed by Bell labs in 1978, where the germanium-doped preform is prepared. In this process the doping concentration can be adjusted by the proportion of gases, such as nitrogen and oxygen with silicon/germanium tetrachloride. However, this complex system of chemical reactions introduces the formation of suboxides and defects into the host matrix with silica.

The suboxides formation also occurs at the time of fibre drawing process. Different absorption bands associated with the defects are affected by the incident radiation. A new type of defect known as the drawing induced defect (DID) can be formed due to a partial chemical reaction into the silica matrix and as a result many sub - oxides and defects are formed [33, 34]. These are primarily known as wrong bonds which are 2- coordinated Ge or Ge-Si or Ge-Ge and situated into the core of an optical fibre. These are highly thermally unstable at the time of fabrication process [35].

In a germanium-doped optical fibre an absorption band at 240 nm is associated with GeO defect (oxygen-deficient Ge defect). After the exposure to UV irradiation, the Ge-Si band breaks, forming the GeE′ centre and emitting free electrons into the glass matrix until it finds another defect site. As a result, some wavelength matches with the incident light and some other creates an absorption band that leads to a refractive index change following the Kramers-Kronig relationship. Evidence showed that a number of experiments support this GeE′ model and original Hill gratings were developed by this process. The fundamental phenomena involved in this process is two photon absorption into the 240 nm band. Theoretical implementation of Kramers-Kronig model for the calculation of refractive index strongly agrees with the measurement of photoinduced grating.
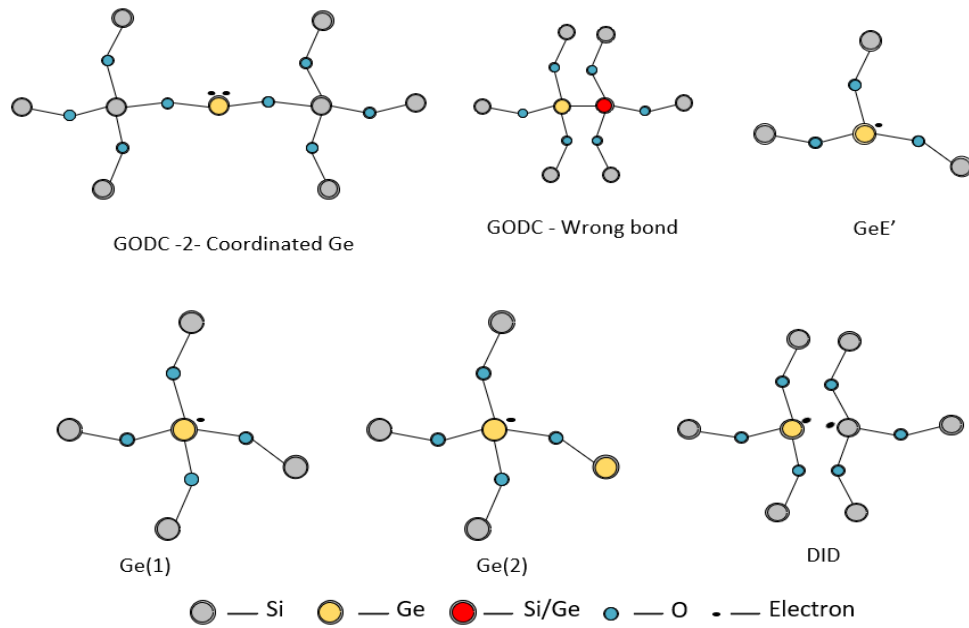
Figure 2. 1 Point defects of Germanium doped silica glass for enhanced photosensitivity [35].

Germanium oxygen deficiency centres (GODC) are formed as the concentration of germanium becomes large. The absorption related to GODC is eliminated by the incident UV radiation and creates new defects with associated new absorption bands. Figure 2.1 shows the details of GODC structures and its modification with UV radiation.

An extra defect with Ge (1) is created and bonded in the silica matrix whenever an emission of GeE′ is there, resulting in a release of an electron [36]. The photo- induced refractive index modulation occurs due to transformation of the diamagnetic (with paired electron spins) GODC defects to paramagnetic defects (with unpaired electrons). Another technique enhanced by the thermal effect, known as the stress modified or compaction of silica that results in an improved level of index change. This happens with UV exposed germane-silicate fibre creating a modification of stress and refractive index.

2.2.2 Photosensitisation techniques

Photosensitivity depends on different mechanisms, namely photochemical, photomechanical, thermochemical etc. It is also dependent on the intensity and wavelength of incident light. There are different models that can explain photosensitivity mechanism. These are mainly colour centre model [37] and compaction densification model [38]. The other alternative models are stress relief/relaxation model [39], electron charge migration model [40] etc.

a. Colour centre model

Firstly, Hand and Russell used Kramers - Kronig model [41] to show defect centres into an optical fibre material and mentioned the popular colour centre model. A quasi-periodic structure comprises of four silicon atomic bonds with four adjacent oxygen atoms to form a tetrahedral structure of pure amorphous silica. Deformation of normal tetrahedral lattice occurs in this process. Germanium also has similar atomic structure like silicon and four valency creates a silica matrix. GeO and GeO_2 are the two stable oxidation states (+2 and +4 respectively). Chemical vapour deposition (CVD) method is used to prepare a germanium doped preform and the doping concentration is modified using the ratio of silicon/ germanium tetrachloride and oxygen.
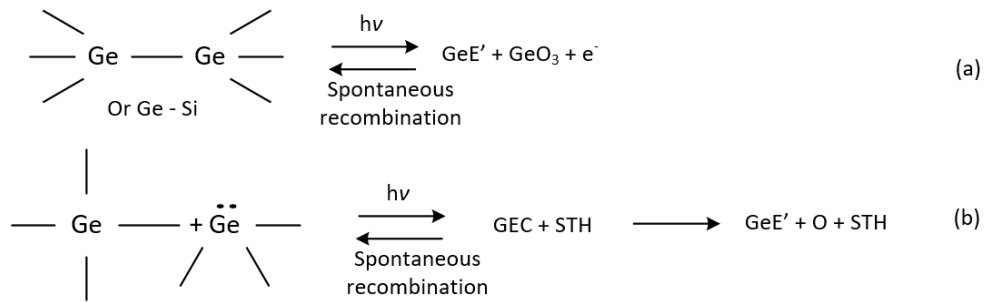
Figure 2. 2 Two photochemical reactions (a) single photon process and (b) two-photon process [41].

With reference to above explanation, the GODC comprises of two possible compositions with Ge^{2+} ions organised with two oxygen atoms and having two electrons lone pair as depicted in Fig. 2.2 [36, 41]. The Ge-Ge or Si-Ge wrong bonds are famously linked with two different possibilities for photochemical reaction. These are single-photon process and two-photon process respectively. A photon absorption occurs through a wrong bond based GODC and converts it into GeE′, GeO_3^+ and an electron [41, 42]. Whereas, in the latter case the two photon absorption takes place for the wrong bond GODC and Ge electron centre (GeC) with self-trapped hole centre (STH) is created in the process. After this there is GeE′ as shown in Fig. 2.2(b).

In colour centre model there is refractive index modulation with the absorption of UV radiation. The index change could be expressed by Kramers - Kronig relation [37] as shown below:

$$\Delta n_{eff}(\lambda) = \frac{1}{2\pi^2} p \int_0^\infty \frac{\Delta \propto_{eff}(\lambda)}{1-(\lambda/\lambda')^2} d\lambda \qquad (2.1)$$

Here, p is the principal part of the integral, λ' is the wavelength for refractive index modulation and the change in effective absorption coefficient for the defects is expressed as $\propto_{eff}(\lambda)$.

The effective refractive index is the function of both real and imaginary parts of the complex equation. In this colour centre model, the imaginary part is associated with the UV absorbed

refractive index change in the infrared and visible range. So, the calculation dealt into their model by considering the real term of imaginary part. This efficient equation was applied in various experimental measurements [41, 43-45].

b. Stress relaxation model

The stress-optic effect causes the refractive index perturbation within silica fibre at the presence of UV exposure of certain intensity. There is inherent thermo-elastic stress relaxation within the fibre core which induces the refractive index change [41]. The strength of stress within the fibre depends on property of fibre material and the manufacturing process through which fibre is produced. The difference in stress in the fibre cladding and core region makes various thermal expansion coefficients. After the fibre is drawn and cools down, thereby restoring the additional stress. The refractive index is reduced by the modified tension of the fibre.

Theoretically the core of the fibre has higher thermal expansion coefficient compared to the cladding ($\alpha_{core} > \alpha_{clad}$). The reason is because the core cools down to lower temperature due to thermal contraction or due to the condition that the core has lower thermal expansion with respect to the cladding. Mathematically if the integration of stress for the fibre is zero, the additional stress at different points of the fibre will be dependent on the value of the ratio of their area. While drawing the fibre, the applied tensile force solidifies that region and other part of the silica glass would solidify with lower temperature as it gradually decreases. With this effect a complete stress in that part of the fibre is obtained with comparatively lower transition temperature [42]. An approximate refractive index modulation of the order of $\Delta n \sim 10^{-3}$ can be achieved from this stress relation in largely stressed fibre [46].

c. Densification compaction model

The densification/compaction happens due to UV irradiation and thereby perturbation of refractive index. An amorphous silica film is structurally deformed through the compaction effect and it was first shown by Fiori and Devine [3, 47]. Different silica glasses have different softening temperature proportional to the UV induced densification while processing through lithography applications [48]. An atomic force microscope (AFM), tunnelling electron microscope (TEM) [49] and variations in Raman spectra [50] were used to observe UV induced densification for a germanium-doped silica fibre. An increase in refractive index causes a compaction within the core and therefore an increased tensile stress.

In the process of FBG fabrication, there is a strong change in tension within the fibre core. It is different from the stress relief model [51]. The compaction or increasing refractive index and the tensile stress or decreasing refractive index are combined to observe the mentioned effect while FBG inscription is taking place. Some analysis showed that UV induced refractive index modulation is

reduced by 30%-35%. This is because of photo-elastic effect whereas it is increased by the compaction induced RI change.

2.2.3 Photosensitivity enhancement techniques

The photosensitivity of normal telecommunication fibre (SMF-28) needs to be increased for refractive index modulation. A standard silica fibre has low germanium dopant (approximately 3%) resulting in low photosensitivity and the photoinduced refractive index perturbation is less, about 3×10^{-5} [30]. There are several materials except germanium which can be used as dopant with silica matrix to increase the refractive index. Germanium has the advantage with respect to the overall fibre designing and flexibility in the fabrication process. But to avoid an excessive germanium doping, another co-dopant like Boron can be used to enhance the photosensitivity [3].

a. Hydrogen loading technique

The hydrogen loading technique is applied to enhance the photosensitivity of normal silica fibre while the physical properties are unaffected. This is a substitution of any other complex method such as increasing dopant concentration in germane-silicate glass. The hydrogenation for standard silica (SMF-28) fibre was firstly reported by Lemaire et al., where a 100 times higher index change was achieved compared to non-hydrogenated fibre. Here hydrogen is diffused within silica matrix while a high pressure (ranging from ~20 atm to 750 atm) is maintained at a suitable temperature range from 20 °C to 75 °C [4]. The fibres are soaked into a loader for few days depending on the set pressure and temperature and it is seen that a higher index change of the order of 3.43×10^{-3} is obtained in the optical fibre as it is exposed to UV irradiation.

There is temperature induced effect between hydrogen and existing defect sites at the time photoreaction takes place [52, 53]. Later Awazu studied that the absorption band within the optical fibre can be influenced by the hydrogenation process at 242 nm, 325 nm and 2.75 μm [54]. The first two absorption bands at 242 nm and 325 nm are linked with GODCs. Fig. 2.3 represents the proposed model for the chemical reaction that takes place within the hydrogen diffused fibre [54].
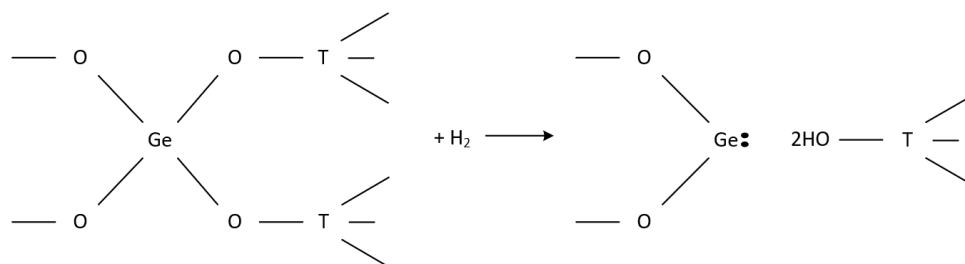
Figure 2. 3 The proposed model for chemical reaction within the fibre into a hydrogen loading system [54].

The important feature of hydrogenation process is that the hydrogen gets diffused as the sample is taken out from high pressure environment. Silica contains hydroxyl ('-OH') group which has an absorption band at 1400 nm and is extendable to 1550 nm in the telecommunication region (C- band). '-OH' groups can be formed within the silica matrix during hydrogen loading and UV irradiation process, but this structure gives increased transmission loss. The additional hydrogen causes a major loss around the communication windows [52, 53]. One alternative method is by using deuterium with similar properties to hydrogen, and the higher wavelength loss can be removed from the telecommunication window [55].

b. Co-doping technique

At the beginning photosensitivity was dependent on a single dopant, i.e., germanium concentration within the core of an optical fibre. Later other different materials were used for doping or co-doping with germanium to increase the photosensitivity. Highly photosensitive fibres are obtained when silica fibres are co-doped with B_2O_3 or GeO_2. When a GeO_2 doped silica fibre is co-doped with B_2O_3 and if the doping concentration is less than 10 mol%, the absorption band remains unchanged for 240 nm UV radiation. Therefore, an increased B_2O_3 concentration reduces the 240 nm absorption band. The UV absorption starts at 190 nm and it diminishes at 240 nm for a $B_2O_3 - SiO_2$ glass [38]. This co-doping method is influenced by the increased densification when there is a stress effect [39].

The photosensitivity enhancement for a germano-silicate fibre can be done by using other materials as the co-dopants, except boron. These are tin (Sn) co-doped fibre and nitrogen (N_2) co-doped fibre. There are some limitations with respect to the fabrication with these materials. Tin (Sn) as a co-dopant has the advantage over boron as it has very low loss at the telecommunication window [40, 56].

Another co-doping material such as nitrogen (N_2) doped with germanosilicate fibre enhances large photosensitive effect, where the high index change of the order of 2×10^{-3} can be achieved for normal non-hydrogenated fibre, and an index change of 1×10^{-2} for hydrogenated fibre [57]. An increased absorption band at 240 nm can be obtained for N_2-doped fibre as the concentration of GODC defect centres becomes high.

c. Flame brushing technique

The principle involved in flame brushing method is similar to the hydrogen loading technique. Here the photosensitising method depends on locally heating the fibre and waveguide using hydrogen flame which creates an increase in the UV absorption wavelength. A hydrogen fuelled flame and oxygen at high temperature (nearly 1700 °C) are used to treat the fibre for around 20 mins resulting in the creation of GODC defect centres within the core of germanosilicate fibres after the diffusion

of hydrogen and hydroxyl molecules in it. Therefore, the UV absorption band of 240 nm becomes wider and it increases the UV induced refractive index perturbation [33].

One of the disadvantages of this method is mechanical degradation when the fibre is processed for a long time. However, low loss achievement at the telecommunication window is relatively short time for fibre treatment and creating the photosensitivity locally are the main advantages of this technique.

2.3 Coupled mode theory

An optical fibre is a cylindrical waveguide with the energy distribution between two orthogonal modes is linear while considering an ideal structure in an unperturbed condition. The energy transfer takes place when there is a refractive index modulation within an optical fibre. Various propagating modes coupled with each other, and power exchange occurs. Hence, the diffraction efficiency and spectral characteristics of optical fibre gratings was analysed using couple-mode theory (CMT). It is an accurate model with largely accepted approximate solutions to explain the optical properties of an in-fibre gratings. Yariv [58], Kogelnik [59] and Erdogan [60, 61] have derived this theory in a rigorous way. The following will provide a description of the CMT as discussed in Erdogan's model.

The transverse component of an electric field is considered as a superposition of the ideal modes for an ideal waveguide without any refractive index modulation,

$$\vec{A}^T(x,y,z) = \sum_m (A_m(z)\exp(i\beta_m z) + B_m(z)\exp(-i\beta_m z))\vec{e}_m^T(x,y)\exp(-i\omega t) \qquad (2.2)$$

The two coefficients $A_m(z)$ and $B_m(z)$ are the amplitude variations for the mth mode where the mode propagation is along +z and -z directions respectively.

$\vec{e}_m^T(x,y)$ is the transverse mode field that depends on the function of time exp(-iωt) represented as a bound-core, cladding or radiation LP modes and β is the propagation constant.

It can be expressed as,

$$\beta = \frac{2\pi}{\lambda} n_{eff} \qquad (2.3)$$

n_{eff} denotes the effective refractive index of mth order mode and λ is the propagation wavelength.

As the mth mode propagates along the $\pm z$ directions with amplitudes $A_m(z)$ and $B_m(z)$, mode coupling occurs with the presence of dielectric perturbation and the change in amplitudes can be expressed as:

$$\frac{dA_m}{dz} = i\sum_q A_q\left(C_{qm}^T + C_{qm}^L\right)\exp\left[i(\beta_q - \beta_m)z\right] + i\sum_q B_q\left(C_{qm}^T - C_{qm}^L\right)\exp\left[-i(\beta_q + \beta_m)z\right] \tag{2.4}$$

$$\frac{dB_m}{dz} = -i\sum_q A_q\left(C_{qm}^T - C_{qm}^L\right)\exp\left[i(\beta_q + \beta_m)z\right] - i\sum_q B_q\left(C_{qm}^T + C_{qm}^L\right)\exp\left[-i(\beta_q - \beta_m)z\right] \tag{2.5}$$

Here the transverse and longitudinal coupling coefficients between two modes (q and m) are expressed as C_{qm}^T and C_{qm}^L. Usually the longitudinal coupling is extremely less than the transverse coefficient, i.e., $C_{qm}^T \gg C_{qm}^L$. C_{qm}^T can be written as follows:

$$C_{qm}^T(z) = \frac{\omega}{4}\iint \Delta\varepsilon\,(x,y,z).\vec{e}_q^T(x,y)dxdy \tag{2.6}$$

$$\Delta\varepsilon(x,y,z) = 2n_{eff}\delta n_{eff}(x,y,z) \tag{2.7}$$

Here, $\Delta\varepsilon(x,y,z)$ is the change in permittivity and it is approximately equal to $2n\delta n$. δn is the effective refractive index modulation which is lower than the local index n in an ideal fibre.

An ideal optical waveguide gives zero coupling coefficient, i.e., $C_{qm}^T(z) = 0$, when there is no perturbation ($\Delta\varepsilon = 0$). In this case the transverse mode becomes orthogonal with no energy transformation. If a spatially varying UV radiation is exposed on a photosensitive fibre, a refractive index change, $\delta n_{eff}(z)$ occurs along the propagation direction

$$\delta n_{eff}(z) = \bar{\delta n}_{eff}(z)\left[1 + v\cos\left(\frac{2\pi}{\Lambda}z + \phi(z)\right)\right] \tag{2.8}$$

In the above equation $\bar{\delta n}_{eff}(z)$ is the 'dc' index variation spatially averaged over a grating period and it results in a slowly varying envelope of the grating. Λ is the grating period, $\phi(z)$ gives the grating chirp and the fringe visibility of the modulated refractive index is obtained from v. The term $\delta n_{eff}(x,y,z)$, i.e., UV exposed refractive index change is uniform across the core of a fibre grating

and it is very low at the outside of the core. So, the equation can be replaced in terms of $\delta n_{co}(z)$ and rewritten as below:

$$C_{qm}^T(z) = \psi_{qm}(z) + 2k_{qm}(z)\cos\left(\frac{2\pi}{\Lambda}z + \phi(z)\right) \tag{2.9}$$

Here, $\psi_{qm}(z)$ and $k_{qm}(z)$ are the *dc* and *ac* coupling coefficients respectively and are given by,

$$\psi_{qm}(z) = \frac{\omega n_{eff}}{2}\bar{\delta}n_{eff}(z)\iint_{core}\bar{e}_q^T(x,y)dxdy \tag{2.10}$$

$$k_{qm}(z) = \frac{v}{2}\psi_{qm}(z) \tag{2.11}$$

2.3.1 Backward mode coupling

An FBG structure in an optical fibre enables the light interaction occurring between the counter-propagating modes, i.e., the light from the forward-propagating core mode couples to the backward-propagating core mode. Under this condition the equations (2.4) and (2.5) can be modified to the following equations [59].

$$\frac{dR}{dz} = i\hat{\psi}R(z) + ikS(z) \tag{2.12}$$

$$\frac{dS}{dz} = -i\hat{\psi}S(z) - ik^*R(z) \tag{2.13}$$

Where R and S are the amplitudes, $\hat{\psi}$ is the general "dc" self-coupling co-efficient, k is "ac" coupling coefficient.

$$R(z) = A(z)\exp\left(i\delta z - \frac{\phi(z)}{2}\right) \tag{2.14}$$

$$S(z) = B(z)\exp\left(-i\delta z + \frac{\phi(z)}{2}\right) \tag{2.15}$$

$$\hat{\psi} = \delta + \psi - \frac{1}{2}\frac{d\phi(z)}{dz} \tag{2.16}$$

δ is a detuning factor and is independent of z. It is expressed as:

$$\delta = \beta - \frac{\pi}{\Lambda} = \beta - \beta_d = 2\pi n_{eff}\left[\frac{1}{\lambda} - \frac{1}{\lambda_d}\right] \tag{2.17}$$

A very weak grating $\left(\delta n_{eff} \to 0\right)$ represents the Bragg scattering with a "design wavelength" of $\lambda_d = 2n_{eff}\Lambda$. The following simplified equations show the relations for a single mode Bragg grating:

$$\psi = \frac{2\pi}{\lambda}\overline{\delta n_{eff}} \tag{2.18}$$

$$k = k^* = \frac{\pi}{\lambda}v\overline{\delta n_{eff}} \tag{2.19}$$

$\overline{\delta n_{eff}}$ along z axis remains unchanged and $\frac{d\phi}{dz} = 0$ for a uniform grating without any grating chirp. Thus, the first order ordinary equations can be obtained using equation (2.12) and (2.13) with constant co-efficients $k, \psi, \hat{\psi}$. The reflectivity of a uniform fibre grating structure with a length L can be evaluated as below:

$$R = \frac{sinh^2\sqrt{(kL)^2 - (\psi L)^2}}{-\left(\frac{\psi}{k}\right) + cosh^2\sqrt{(kL)^2 - (\psi L)^2}} \tag{2.20}$$

The maximum reflectivity (R_{max}) is obtained at $\psi = 0$ and it is expressed as:

$$R_{max} = tanh^2(kL) \tag{2.21}$$

The wavelength difference between the first order minima on either side of central maximum reflectivity is depicted as the bandwidth for a uniform FBG. This is given by:

$$\frac{\Delta\lambda}{\lambda} = \frac{v\overline{\delta n_{eff}}}{n_{eff}}\sqrt{1 + \left(\frac{\lambda_d}{Lv\overline{\delta n_{eff}}}\right)^2} \tag{2.22}$$

$v\overline{\delta n_{eff}}$ becomes very small for a weak grating and then the above equation modifies to,

$$\frac{\Delta\lambda}{\lambda} \cong \frac{\lambda_d}{n_{eff}L} \tag{2.23}$$

Therefore, the grating length L is related with the bandwidth. For a strong grating the term $\overline{v\delta n_{eff}}$ becomes large and in this case the expression for bandwidth is given as:

$$\frac{\Delta\lambda}{\lambda} = \frac{\overline{v\delta n_{eff}}}{n_{eff}} \tag{2.24}$$

It is evident that a strong grating condition is not dependent on the grating length. That means, the incident beam completes the Bragg diffraction before the mode propagates through the whole grating length.

2.3.2 Forward mode coupling

In the case of an LPG, the light from the forward propagating core mode is coupled to the co-propagating cladding modes. The two equations (2.4) and (2.5) for an LPG can be rewritten in the term that constitutes these two modes and synchronous approximations need to be considered.

$$\frac{dR}{dz} = i\hat{\psi}R(z) + ikS(z) \tag{2.25}$$

$$\frac{dS}{dz} = -i\hat{\psi}S(z) + ik^*R(z) \tag{2.26}$$

The amplitudes R and S can be expressed as:

$$R(z) = A_1(z)exp\left(i(\psi_{11} + \psi_{22})\frac{z}{2}\right)exp\left(i\delta z - \frac{\phi}{2}\right) \tag{2.27}$$

$$S(z) = A_2(z)exp\left(-i(\psi_{11} + \psi_{22})\frac{z}{2}\right)exp\left(-i\delta z + \frac{\phi}{2}\right) \tag{2.28}$$

As previously mentioned, ψ_{11} and ψ_{22} are the "dc" coupling co-efficient and k is the "ac" coupling co-efficient. $\hat{\psi}$ is the "dc" coupling co-efficient and is defined as:

$$\hat{\psi} = \delta + \left(\frac{\psi_{11} + \psi_{12}}{2}\right) - \frac{1}{2}\frac{dQ}{dz} \tag{2.29}$$

For a constant detuning factor along the z axis, the expression of it is as below:

$$\delta = \frac{1}{2}(\beta_1 - \beta_2) - \frac{\pi}{\Lambda} = \pi \Delta n_{eff} \left[\frac{1}{\lambda} - \frac{1}{\lambda_d}\right] \quad (2.30)$$

The term $\lambda_d = \Delta n_{eff} \Lambda$ is known as the "design wavelength" for any grating with zero index modulation. The conditions for a Bragg grating are given as:

$$\delta = 0 \text{ or } \lambda = \lambda_d = \Delta n_{eff}\Lambda \quad (2.31)$$

A uniform forward coupled grating is constant and needs to be solved numerically. The first order coupled differential equations with constant co-efficient and necessary boundary conditions can be solved to obtain forward coupled grating equations [61].

2.4 Phase matching condition

With the presence of perturbation in an optical fibre there is a coupling probability of the bounded waves with the co-propagating or counter-propagating waves. Different type of fibre gratings is classified depending on the coupling of a particular mode with the bounded wave. When light couples in the opposite direction, that is to the counter propagating mode, it is known as backward-coupled grating. The examples of these type of gratings are uniform Fibre Bragg grating (FBG), chirped structures, tilted fibre grating (TFG) with small tilt angle. But when light coupling occurs in the same direction or co-propagating modes, it is known as the forward-coupled grating. The example of this type is long period grating (LPG) and large angle tilted grating, also known as excessively tilted fibre grating (Ex-TFG).

The phase mismatch factor for any coupled modes is known as the detuning factor and it is defined as:

$$\Delta\beta = \beta_i \pm \beta_d - \frac{2\pi}{\Lambda_g} N cos\theta \quad (2.32)$$

Here, β_i is the propagation constant for incident mode and β_d is the propagation constant for the diffracted mode respectively, Λ_g is the grating period, θ is the tilting angle of the grating, N is any

integer number. The "±" sign indicates the propagation direction which is either +z axis or -z axis. To transfer a certain amount of energy, the phase is expressed as:

$$\beta_i \pm \beta_d = \frac{2\pi}{\Lambda_g} N cos\theta \tag{2.33}$$

The phase matching for a particular mode has been decided by the signs of these two parameters β_i and β_d. N is assumed to be unity as the first order diffraction mode is the dominant mode. The following expression explains resonant wavelength:

$$\lambda = \left(n_i^{eff} \pm n_d^{eff}\right)\frac{\Lambda_g}{cos\theta} \tag{2.34}$$

Another way to explain phase-matching condition (PMC) can be expressed in terms of energy conversion. The wave vector equation for mode coupling in a fibre grating known as PMC and can be expressed in terms of vector K.

$$\vec{K_X} = \vec{K}_{core} + \vec{K}_G \tag{2.35}$$

Here, $\vec{K}_X$ is the wave vector for core or cladding or radiation mode which depends on the applied subscript. $\vec{K}_{core}$ and $\vec{K}_G$ are the wave vectors for core mode and grating, respectively.

The wave vector and the grating vector for the incident light into the fibre core can be written as:

$$\vec{K}_{core} = n_{core}\frac{2\pi}{\lambda} \tag{2.36}$$

$$\vec{K}_G = \frac{2\pi}{\Lambda_G} \tag{2.37}$$

In an FBG structure the light coupling between forward propagating core mode to backward propagating core mode is shown in Fig. 2.4 (a) and given by the expression as:

$$\vec{K}_{core}^+ = \vec{K}_{core}^- = n_{core}\frac{2\pi}{\lambda} \tag{2.38}$$

For the light coupling in an LPG, the grating couples the incident light with forward propagating cladding modes as depicted in Fig. 2.4 (b). The corresponding equation is represented as:

$$\vec{K}_G = n_{clad}\frac{2\pi}{\lambda} \tag{2.39}$$

For TFGs as shown in Fig. 2.4 (c,d,e), the grating has the tilted angle of θ with respect to the fibre axis. The grating vector is given by,

$$\vec{K}_G = n_{core} \frac{2\pi}{\lambda} cos\theta \tag{2.40}$$

Different types of optical fibre grating with propagating directions are shown in Fig. 2.4, showing phase matched vectors. A more complex analysis of phase matching condition can be seen in tilted gratings where the angle varies in the range of 23.1° and 66.9° (Fig. 2.4 (c-e)).

TFGs are mainly of three types: TFG with $\theta < 23.1°$, couples forward-propagating core mode to backward-propagating lower order cladding modes; if the tilt angle lies between 23.1° and 66.9° coupling occurs between the fundamental core-mode and the radiation mode; for $\theta > 66.9°$, coupling occurs between core-mode to forward propagating higher order cladding modes [27, 33].
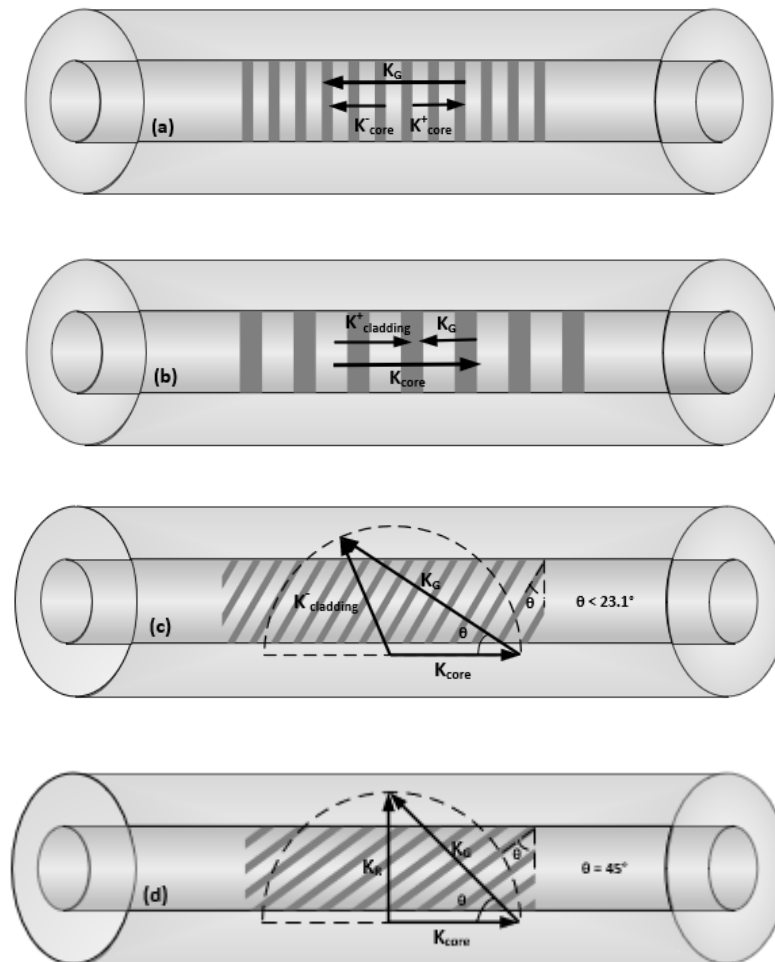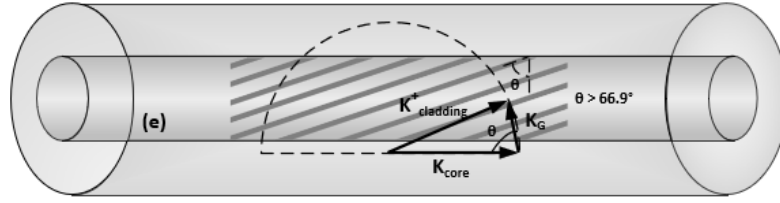
Figure 2. 4 Different type of optical fibre gratings and their phase matching conditions. (a) FBG; (b) LPG; (c) TFG for θ< 23.1°; (d) TFG for θ = 45°; (e) TFG for θ> 66.9°.

2.4.1 Fibre Bragg gratings (FBGs)

An FBG light coupling process involves the reaction of transferring energy between the forward and backward propagating core modes. It has a periodic refractive index variation in a symmetric pattern along the fibre axis, as shown in Fig. 2.5. The period length is normally less than a micron and generally ranges in between few microns. The Bragg wavelength (λ) for a backward coupling FBG (θ = 0°) under phase matching condition is given by,

$$\lambda = 2n_{eff}\Lambda \tag{2.41}$$

Where n_{eff} is the effective refractive index of the core.
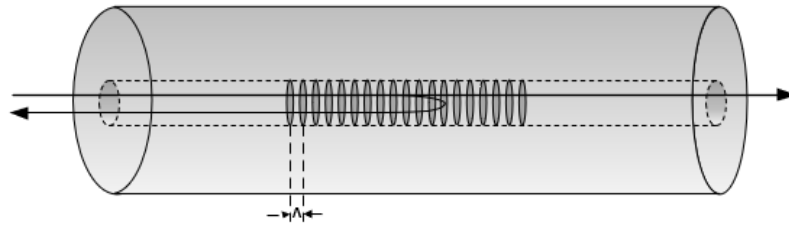
Figure 2. 5 Schematic of mode-coupling of fibre Bragg grating (FBG).

2.4.2 Long period gratings (LPGs)

For an LPG, the coupling occurs between a core mode and a co-propagating cladding mode (θ = 0°) as depicted in Fig. 2.6. In this case the resonant wavelength under phase matching condition is defined as:

$$\lambda_{res} = \left(n_{co}^{eff} - n_{cl,m}^{eff}\right).\Lambda \tag{2.42}$$

n_{co}^{eff} and $n_{cl,m}^{eff}$ are the effective refractive indices of the core mode and the mth cladding modes respectively. As the factor $\left(n_{co}^{eff} - n_{cl,m}^{eff}\right) \ll 1$, the length of grating period of a forward coupled grating is larger than the backward coupled grating at a particular wavelength. The length of the period normally lies in the range of few hundred microns.
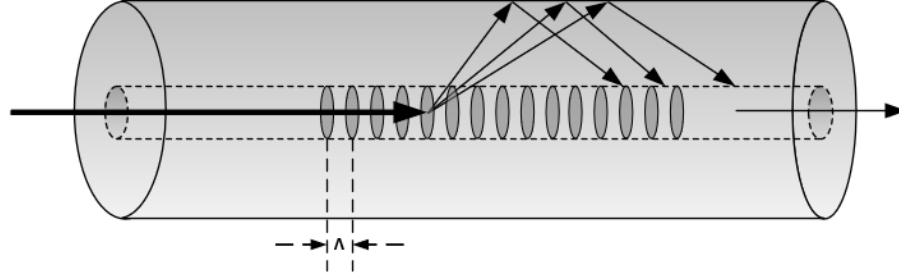
Figure 2. 6 Schematic of mode-coupling of long Period grating (LPG).

The expression for the minimum transmission of the attenuation bands is given by [62, 63].

$$T_i = 1 - sin^2(k_i L) \tag{2.43}$$

where the LPG length is given as L and the coupling coefficient for the i-th cladding mode is mentioned as k_i. This is calculated by knowing the overlap integral of the core and cladding mode and determining the amplitude for periodic modulation of the mode propagation constants.

2.4.3 Tilted fibre gratings (TFGs)

TFG has a more complex mode coupling mechanism than FBG and LPG. Figure 2.7 shows the structure of the tilted grating within fibre core. At the phase matching condition, for a TFG the expression for the resonant wavelength [6, 64, 65] for a particular tilt angle is given by,

$$\lambda_{co-cl} = \left(n_{co}^{eff} \pm n_{cl,m}^{eff}\right).\frac{\Lambda_g}{cos\theta} \tag{2.44}$$

and the effective grating period is expressed in equation (2.37).

$$\Lambda = \frac{\Lambda_g}{cos\theta} \tag{2.45}$$

Where, n_{co}^{eff} is the effective refractive index of the core and $n_{cl,m}^{eff}$ is the effective refractive index of the mth cladding mode. Λ_g is the inscription grating period and θ is the inner tilt angle of the fringes. This will determine the resonant wavelength, which is a function of tilt angle and inscribed period.
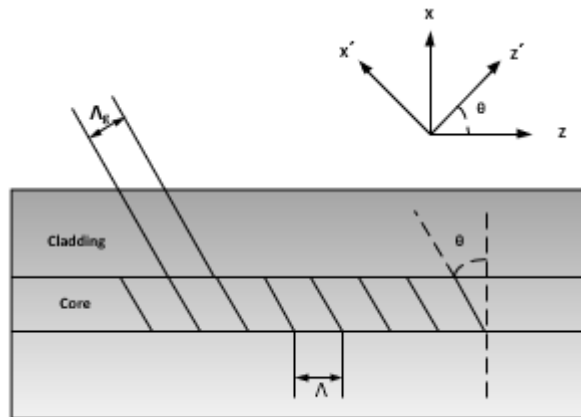
Figure 2. 7 Schematic diagram of tilted fibre grating within core.

2.5 Fabrication method

There are different fabrication techniques to make various type of gratings. Grating inscription using different methods has some limitations, advantages and some specifications required for the process. The first technique was the standing wave inscription process and later this fundamental technique was improvised to develop other methods for inscribing grating.

Nowadays the frequently implemented fibre grating inscription techniques are classified into three types: Two-beam holographic technique, point-by-point writing technique and phase mask scanning technique. The following four subsections give brief description of these four grating fabrication methods.

2.5.1 Standing wave inscription technique

In 1978 Hill et al. first showed the experimental setup using the mentioned standing wave inscription technique [2].
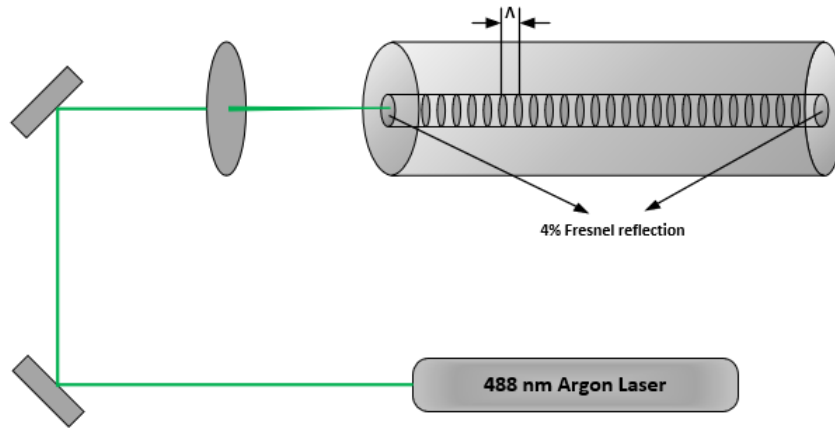
Figure 2. 8 Schematic of Hill's experimental setup for FBG inscription by standing wave inscription technique.

Figure 2.8 shows the details of the experimental arrangement where the standing wave was generated when a frequency doubled Argon ion laser was exposed onto an optical fibre core and 4% Fresnel reflection occurs at both ends of the fibre [2]. The period of the grating is determined by the wavelength of incident laser and the effective refractive index of the fibre. In their experiment they used a germanium doped fibre which has a limited UV absorption band resulting in a weak FBG at 488 nm.

The expression for the grating period is given as,

$$\Lambda = \frac{\lambda_{uv}}{2n_{eff}}$$ (2.46)

This type of grating is not suitable for telecommunication system, so a further improved technique was developed.

2.5.2 Two-beam holographic inscription technique

Two beam holographic inscription method was first invented by Meltz et. al, [16]. This is an external fabrication technique where an incident UV-laser splits into two beams with equal intensity. Fig. 2.9 shows the beam splitting and interaction of the two-beam holographic inscription set up. A 50:50 beam splitter is used to split the incoming light into equal amplitudes and reflected by two highly reflecting mirrors before interference takes place. Then both the reflected beams superimpose with each other to produce interference fringes. The optical fibre with stripped section is placed in the interference area and the refractive index modulation takes place in that region to make the gratings. Two additional cylindrical lenses are used in the setup to increase the intensity for interfering beams at the focus of the fibre core. The grating period can be modified by adjusting the distance between the mirrors and the splitter, thus changing the angle between the two beams. This method is very

efficient for getting uniform gratings with different wavelength response. However, one of the disadvantages of this method is that the grating length is limited by the size of two interfering beams.

The relationship between the grating period, Λ_g, and the Bragg reflection wavelength, λ_B, and the inscription laser wavelength, λ_{uv}, in a two-beam holographic grating inscription system is expressed as below:

$$\Lambda_g = \frac{\lambda_{uv}}{2\sin\left(\frac{\theta}{2}\right)} \tag{2.47}$$

$$\lambda = 2n_{eff}\Lambda_g \tag{2.48}$$

$$\lambda = \frac{n_{eff}\lambda_{uv}}{\sin\left(\frac{\theta}{2}\right)} \tag{2.49}$$

In this method a fixed distance is maintained between the beam splitter and the fibre holder, whereas by changing the mirror positions the angle between the beams can be adjusted and the change is given by the following equation,

$$\frac{\theta}{2} = a\,tan\left(\frac{L_1}{\sqrt{2}L_0 - L_1}\right) \tag{2.50}$$

Where as shown in Fig. 2.9, in the setup two cylindrical lenses F_1 and F_2 are placed in front of the fibre, the position of the mirrors M_1 and M_2 are adjusted to maintain a distance with the 50:50 beam splitter, L_1 and L_2 are the two arm lengths with L_0 fixed. Substituting the expression for angle from equation (2.50) into equation (2.51), the Bragg wavelength can be defined as:

$$\lambda = \frac{n_{eff}\lambda_{uv}}{\sin\left(a\,tan\left(\frac{L_1}{\sqrt{2}L_0 - L_1}\right)\right)} \tag{2.51}$$
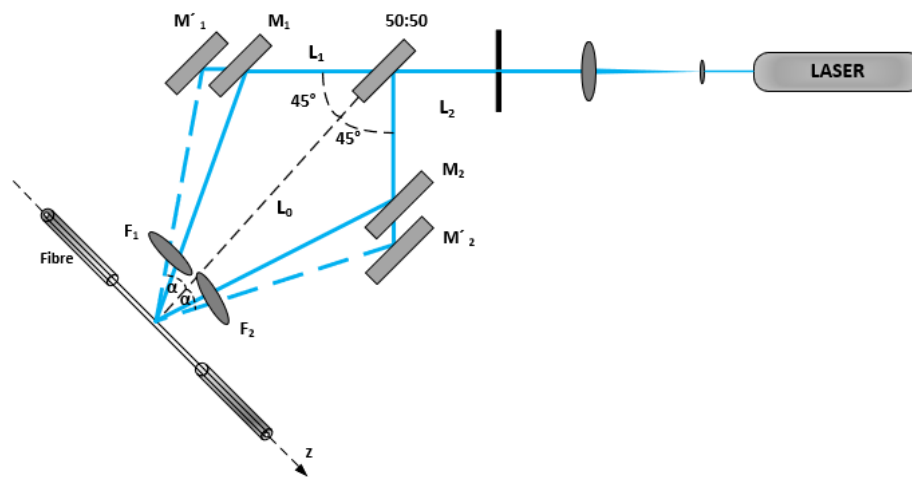
Figure 2. 9 Two-beam holographic inscription method showing how to change the interference angle between the two split beams.

This method allows the FBGs inscribed at arbitrary wavelengths, meeting the application required reflection, which is the most significant development stage for the optical fibre grating technology.

2.5.3 Point-by-point inscription technique

Another popular grating inscription method is point-by-point writing technique, as shown in Fig. 2.10. Here the grating is written a point at a time. The focused UV laser beam is directly modulating the refractive index within the fibre core. Due to the limitation of focus spot size, it is difficult to set up the translation stage accurately for writing FBG structure. Hence it is most suitable for fabricating LPGs of periods ranging from 10 μm to 600 μm. A third order FBG was written by Malo et al. and they used point-by-point writing technique where the slit's image is imprinted within the fibre core as grating [66].
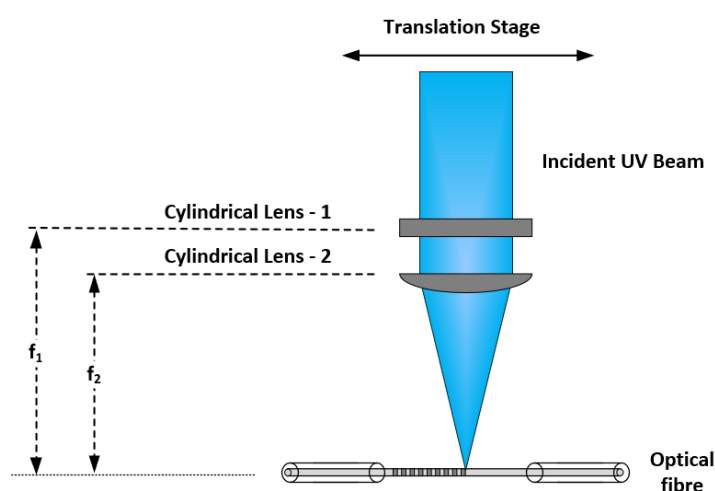
Figure 2. 10 Schematic diagram for point-by-point writing for a long period grating (LPG).

In this method for LPG inscription, two orthogonally placed cylindrical lenses are used to focus the light onto the fibre core. For the grating inscription the shutter speed is controlled with 50:50 duty

cycle and with the shutter switching on and off the linear displacement of the translation stage is managed. The same principle applies with the femtosecond laser for fabrications of fibre gratings and micro-structures.

2.5.4 Phase mask scanning technique

Phase mask scanning method is one of the greatest developments of the grating inscription technique. Anderson and Hill first showed this technique [67, 68] and after that it has been the most effective method for grating fabrication. In comparison with the two-beam holographic method, this technique requires a simple fabrication setup with lesser number of optical components.

The phase mask is a UV transparent diffractive optical element made with silica on which an one-dimensional surface relief grating is etched. Different manufacturers are applying various methods such as holography or electron beam lithography to produce phase mask. In the setup the optical fibre is closely placed after the phase mask for achieving effective grating pattern on it. The setup is shown below.

The light beam is diffracted into different orders while passing through the phase mask. The ±1 diffraction order constitute 80% of incident UV intensity and these interfere to inscribe grating onto the fibre core. Our phase mask gives maximum diffracted light of ±1 order. So, an optimised diffraction for zero order can be achieved by designing the mask with the amount of light less than 5% and approximately 40% transmission is achieved for ±1 diffracted order. Then the two first order diffraction beams interfere to inscribe a grating pattern in the optical fibre core.
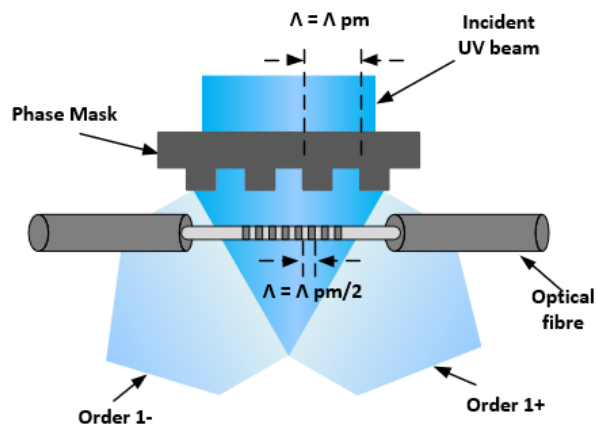
Figure 2. 11 Schematic of phase mask scanning technique experimented firstly by Hill/Anderson et al.

The phase mask inscription principle is shown in Fig. 2.11. The depth of corrugation for zeroth-order diffraction is given by,

$$d = \frac{\lambda_{uv}}{2(n_s(\lambda_{uv})-1)} \tag{2.52}$$

$$\Lambda_g = \frac{\Lambda_{PM}}{2} \tag{2.53}$$

Here λ_{uv} is the wavelength of the UV light, $n_s(\lambda_{uv})$ is the refractive index of the fibre at λ_{uv}. In equation (2.53) the grating period is given by half of the period of phase mask, and it is independent of incident UV intensity.

$$\Lambda_g = \frac{\Lambda_{PM}}{2}$$

2.6 Chapter conclusion

This chapter reveals a brief review of historical development of fibre grating and the UV photosensitive effect of optical fibre, with different models namely, colour centre, stress relaxation and compaction/densification. The methods for photosensitivity enhancement have also been discussed with hydrogen loading, co-doping and flame-brushing technique. A comprehensive theoretical analysis through couple mode theory and phase matching condition has been described and discussed for different structured fibre gratings including FBG, LPG and TFG. Finally, several inscription methods for fibre gratings are detailed including four methods as the standing wave, two-beam holographic, point-by-point and phase mask scanning technique.

Chapter 3

Advanced optical fibre gratings: fabrication, spectral characteristics, and sensing measurements

3.1 Introduction

This chapter discusses the inscription and spectral and sensing characteristics of different types of fibre gratings, including fibre Bragg grating (FBG), long period grating (LPG), small angle tilted fibre grating (STFG) and excessively tilted fibre grating (Ex-TFG). The chapter is presented in two parts. The first part A covers the inscription of FBGs, LPGs and STFGs in the near infrared (NIR) range, and the second part B describes dual-peak LPG, second-order LPGs and Ex-TFGs in the mid infra-red (MIR) range. The fabricated gratings of different structure are analysed for their typical spectral response and also investigated for sensing function including temperature, strain, refractive index measurements.

Part A

Grating inscription, characterisation, and sensing measurements in the near infrared (NIR) range

3.2 FBG inscription and sensing measurements

An outline of different fabrication methods is described in Chapter 2. For the FBGs presented in this thesis are inscribed using the UV laser and scanning with phase mask method. The following sections will give some examples of FBGs fabricated with Bragg resonances distributed in 1550 nm range and their typical temperature and strain response characterised.

3.2.1 Using phase mask (PM) scanning method

As discussed in Chapter 2, FBG inscription using phase mask scanning technique was first demonstrated by Hill and Anderson et al., in 1993 [67, 68]. Though this method is suitable for a fixed wavelength, but in the later stage it shows high effectiveness due to its reproducibility. The PM fabrication method involves the movement of UV focused beam along with the one-dimensional translation stage by controlling a software programme designed using LabVIEW. The fibre is placed near to the phase mask and uniform Bragg grating is written with a focused UV-beam. The scanning PM set-up working design is shown in Fig. 3.1.
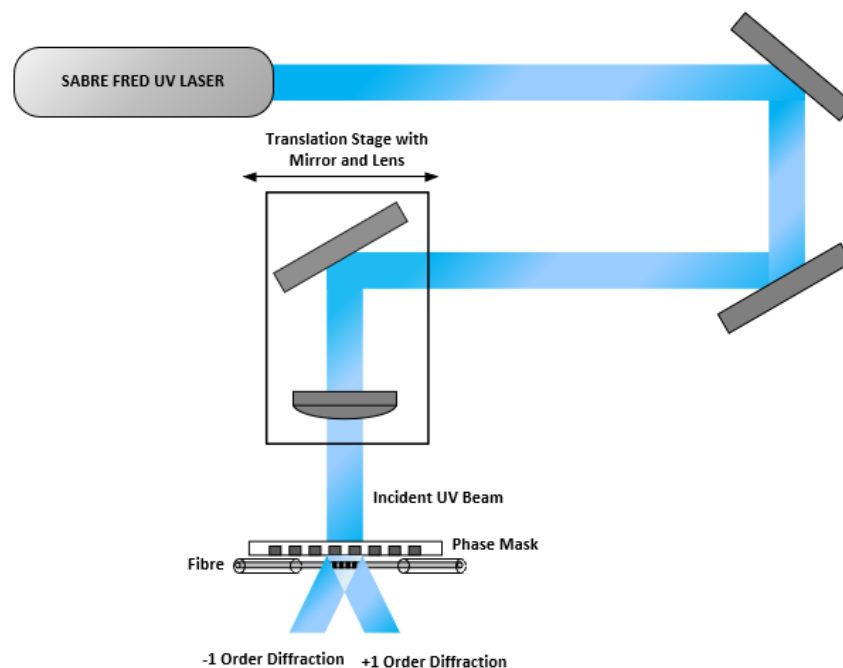
Figure 3. 1 Schematic of the experimental arrangements for inscribing FBG using UV-beam scanning through a phase mask.

In the inscription experiment, a multiwavelength PM with corrugated surface-relief grating etched onto a fused silica plate was used. For the normal incidence, the UV beam gets diffracted into orders, $m = \pm1, \pm2,\ldots$ with the central zeroth order. The manufacturing capability enables the mask to do the light suppression in 0 order and maximum diffraction efficiency for the first ±1 order of ~40% per

beam is obtained. Figure 3.2 clearly shows an interference pattern for ±1 order diffracted beams when the UV beam goes through the mask.

The FBGs reported in this thesis are fabricated mainly using a 50-mm long multi wavelength phase mask, and the phase mask structure with period sizes and grating wavelengths are shown in Fig. 3.3. The utilisation of this phase mask allows to inscribe FBGs at five different wavelengths of 1535.9 nm, 1543.7 nm, 1551.7 nm, 1559.6 nm, and 1567.6 nm respectively with the grating periods at 1060.85 nm, 1066.39 nm, 1071.92 nm, 1077.45 nm, and 1082.98 nm. The UV laser for grating inscription is the Sabre FreD from Coherent and it is a frequency doubled Ar+ laser with an UV power of around 100 mW at 244 nm. The fibre used for FBG inscription is the standard single mode telecom fibre (SMF-28) with core diameter 8.2 μm and cladding diameter 125±0.7 μm, and the refractive indices of core and cladding of the SMF-28 are 1.461 and 1.456 respectively.

The SMF-28 fibre has very limited UV photosensitivity, thus before the FBG inscription, the SMF-28 fibre samples were hydrogen loaded to enhance the photosensitivity. The hydrogen loading procedure involves storing the virgin fibre samples into a hydrogen chamber set at a temperature of ~75 °C and a pressure of 150 atm for at least 48 hours. The hydrogen loaded fibre was then stripped for the outer jacket, cleaned with Isopropyl Alcohol (IPA) solution and placed behind the phase mask onto the two translation stages in the inscription system as shown in Fig. 3.2. The fibre was then aligned in parallel to the phase mask pattern, indicated by the fibre diffraction fringes on the screen placed behind the fibre, as shown in Fig. 3.2. Then the FBG is written with a scanning speed of 0.05 mm/s over a 20 mm length of the fibre core.

Figure 3. 2 Diffraction pattern when the SMF-28 fibre is placed in front of the phase mask for grating inscription.

Namita Sahoo, PhD Thesis, Aston University 2021   56
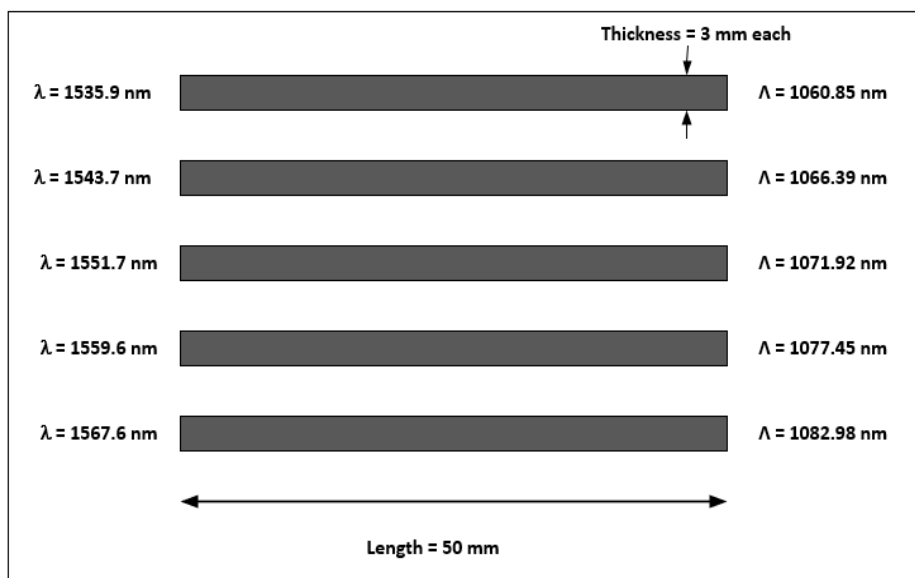
Figure 3. 3 Schematic of the five-period phase mask used for the fabrication of FBGs with five different wavelengths.

All fabricated FBGs were measured for the spectral response using the experimental setup shown in Fig. 3.4 where a broadband source (BBS- AFC Technologies Limited) with a wavelength range from 1500 nm to 1600 nm and an optical spectrum analyser (OSA) of the model YOKOGAWA AQ6375 were used for spectral characterisation.
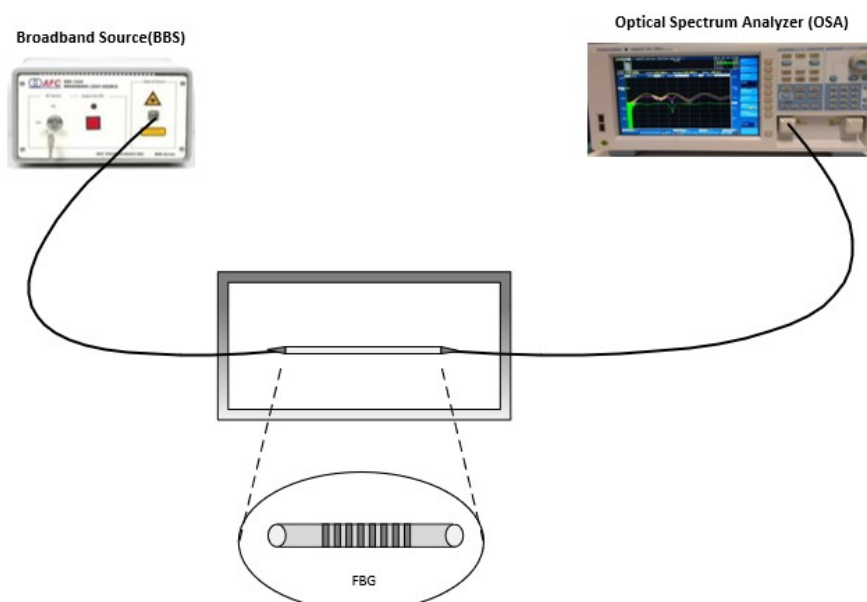
Figure 3. 4 Experimental setup of the spectrum measurement of an FBG.

Figure 3.5 shows the transmission spectra for FBGs inscribed using the multi wavelength phase mask showing five Bragg resonances at 1535 nm, 1543 nm, 1551 nm, 1559 nm and 1567 nm respectively.

For a fibre grating the perturbed index change is saturated with UV exposure and the reduction of effective length occurs as the transmitted signal is depleted by reflection [69]. The grating transmittance is generally utilised with FBG reflectivity by the equation as,

$$T = 10\log_{10}\left(\frac{I}{I_0}\right) \text{ dB} \tag{3.1}$$

$$T = 100\% - R \tag{3.2}$$

Here, T and R are the transmittance and reflectance respectively, the power intensities are given by the achieved power I in dB and the reference power I_0.

From the plot it can be seen all five FBGs achieved high transmission about 50 dB, except FBG at 1551.7 nm having a transmission of 30 dB. The spectral profiles clearly indicate the UV laser inscription system in our laboratory at the Aston Institute of Photonic Technologies (AiPT) is highly efficient and versatile for fabricating FBGs with designed wavelength and transmission for applications.
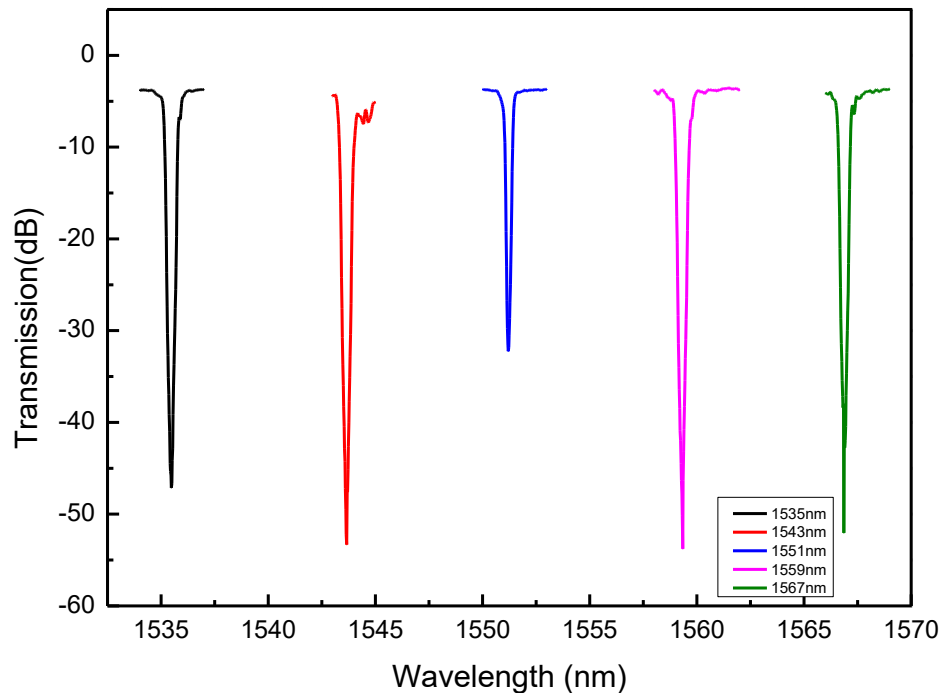
Figure 3. 5 FBG transmission spectra with five different centre wavelengths (1535.9 nm – 1567.6 nm) fabricated by a multiwavelength phase mask with five different periods.

After the UV inscription process, the residual hydrogen in the hydrogen loaded fibre will diffuse out, which will shift the Bragg resonance peak. In order to stabilise the grating property, after the grating inscription, all FBGs inscribed in the hydrogen loaded fibre were thermally annealed in an oven at a

temperature of 80 °C for 48 hours. Figure 3.6 shows the spectra for two FBGs with the initial centre wavelengths at 1535.9 nm and 1543.7 nm written into the hydrogen loaded SMF-28 telecom fibre before and after annealing. From the figure, we can clearly see there is a ~0.5 nm resonance shift towards smaller wavelength in comparison to before annealing.
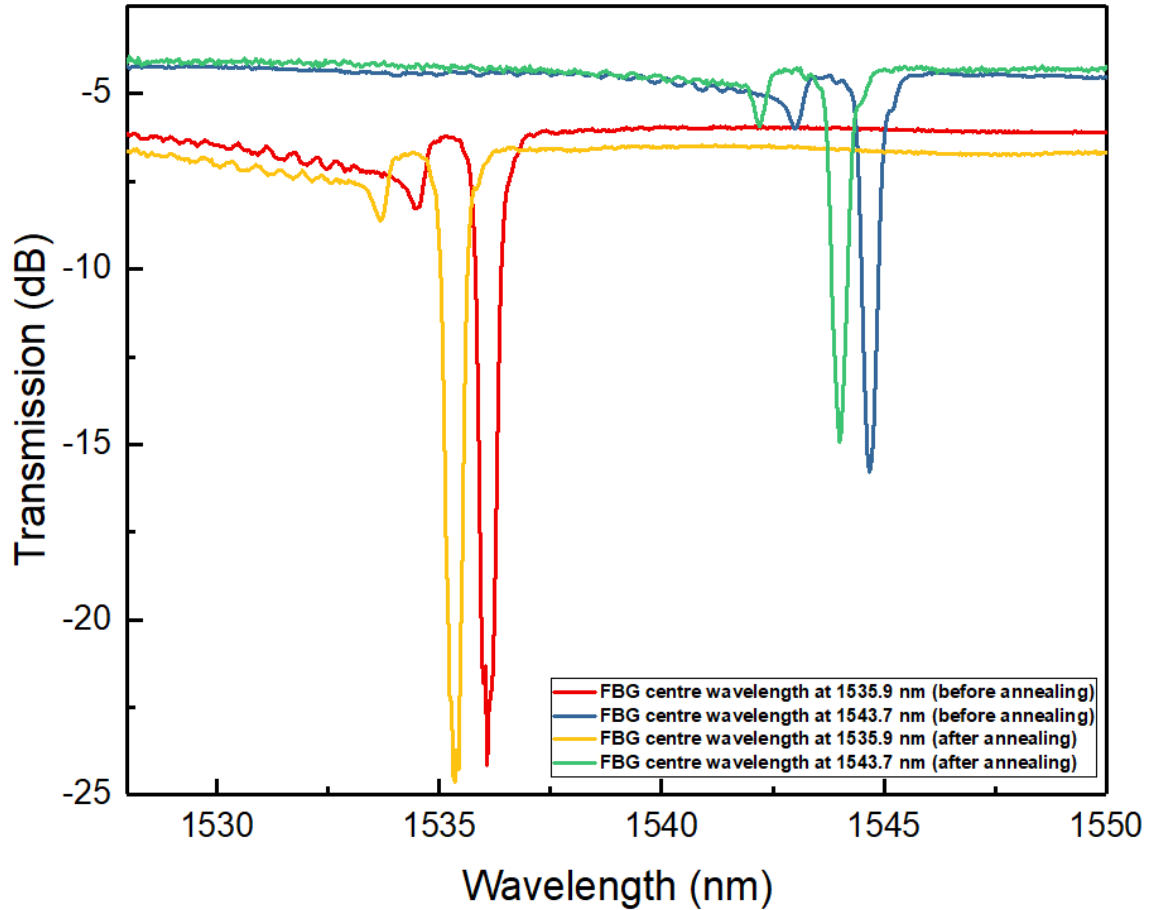
Figure 3. 6 FBG spectra for UV inscribed into hydrogenated SMF-28 before and after annealing.

3.2.2 FBG sensing characteristics

Due to the presence of external parameters, such as temperature and strain there is Bragg wavelength shift. This unique sensitivity property has made FBGs as one of the most thought after in-fibre sensors and have been applied in many sensing applications. The temperature and strain responses of the FBG depend on the changes of the effective refractive index and grating period, and the sensing function expression is as below [70]:

$$\Delta\lambda_B = 2\left\{\Lambda\frac{\partial n_{eff}}{\partial T} + n_{eff}\frac{\partial \Lambda}{\partial T}\right\}\Delta T + 2\left\{\Lambda\frac{\partial n_{eff}}{\partial l} + n_{eff}\frac{\partial \Lambda}{\partial l}\right\}\Delta l \tag{3.3}$$

The first term in equation (3.3) is the grating space change and thermo-optical effect on the refractive index. Therefore, the Bragg wavelength shift can be expressed in terms of thermal expansion co-efficient as,

$$\Delta\lambda_B = \lambda_B(\alpha_\Lambda + \alpha_n)\Delta T \tag{3.4}$$

Here the fibre thermal expansion co-efficient is given by:

$$\alpha_n = \left(\frac{1}{\Lambda}\right)\left(\frac{\partial\Lambda}{\partial T}\right) \tag{3.5}$$

and the thermo-optical coefficient is given as:

$$\alpha_\Lambda = \left(\frac{1}{n_{eff}}\right)\left(\frac{\partial n_{eff}}{\partial T}\right) \tag{3.6}$$

The UV inscribed FBGs were firstly investigated experimentally for their temperature sensing properties. Figure 3.7 represents the experimental arrangement for FBG temperature sensing. In this experiment, the FBG was fixed onto the Peltier unit, which controls the temperature. The temperature changes applied to the FBG were from 0 °C to 80 °C with 5 °C step and the spectral response for each temperature was measured and recorded using the OSA.
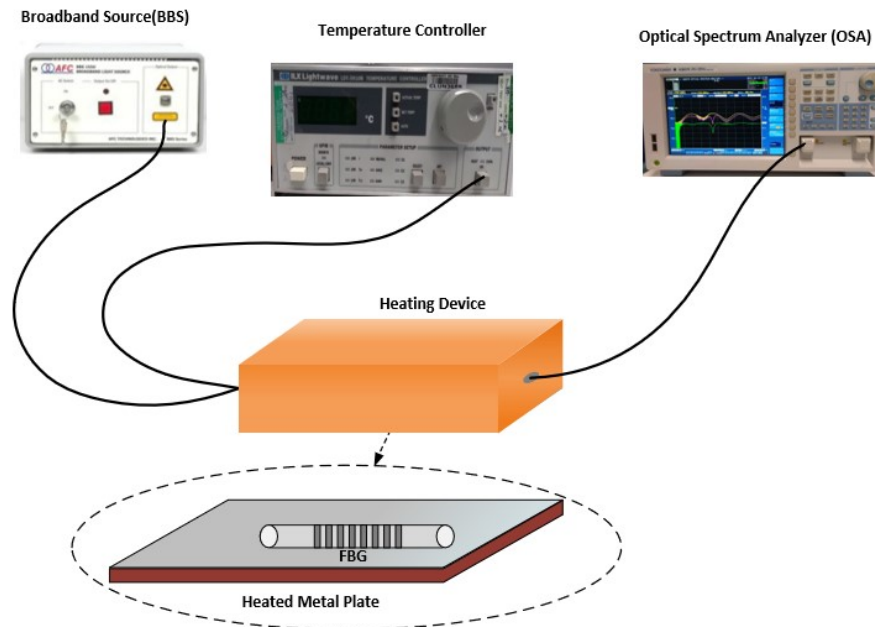
Figure 3. 7 Experimental setup for thermal sensing of FBG.

The thermal sensitivity for three UV inscribed FBGs with wavelengths at 1551.7 nm, 1543.7 nm and 1559.6 nm were investigated for both increasing and decreasing temperature cycle and the Bragg wavelength responses to the temperature for the three FBGs are plotted in Fig. 3.8. From Fig. 3.8 (a, b), it can be seen clearly that the temperature sensitivity for FBG with centre wavelength 1551.7 nm is 11.3 pm/°C for both temperature increment and decrement respectively. Whereas, for FBG with centre wavelength 1543.7 nm, the temperature sensitivity becomes 11.6 pm/°C and 11.5 pm/°C respectively for both temperature increment and decrement as shown in Fig. 3.8 (c, d). Following Fig. 3.8 (e, f) it is seen that there is 0.3 pm/°C difference between temperature increment and decrement for FBG with centre wavelength at 1559.6 nm. The table 3.1 summarises the temperature sensitivity for the three FBGs at different centre wavelengths. The experimental results indicate the FBGs made in standard SMF-28 fibre give a typical thermal response of about 11 pm/°C, which agrees well with previously reported work [71].
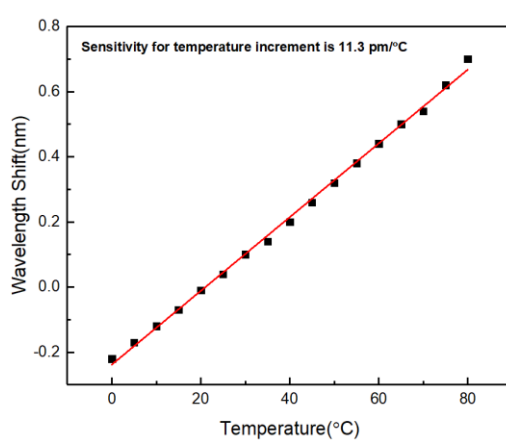
(a)
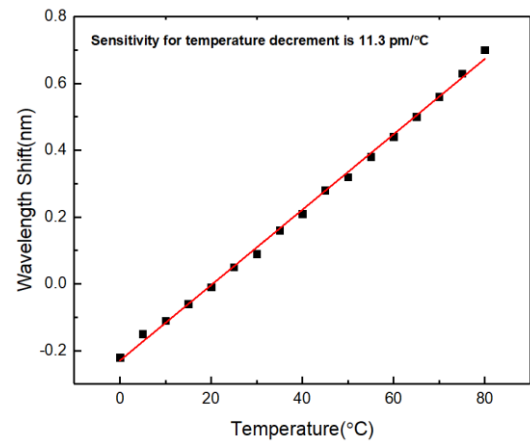
(b)
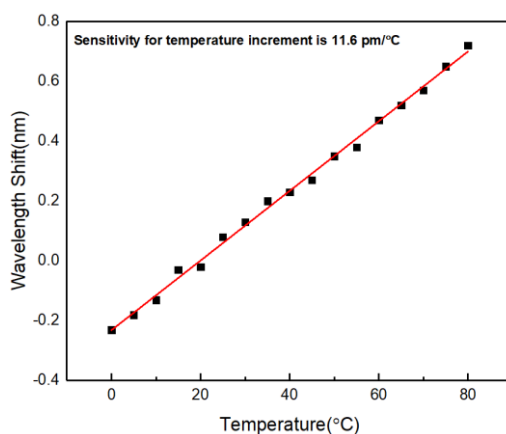
(c)
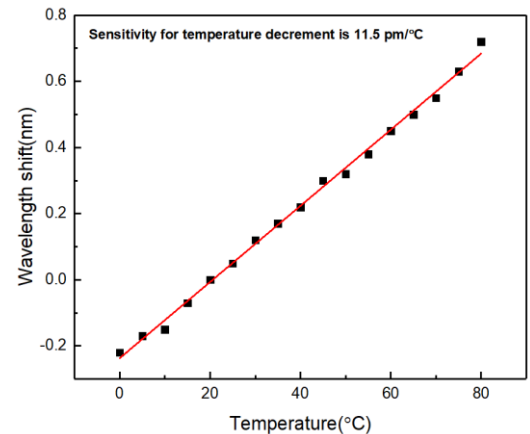
(d)
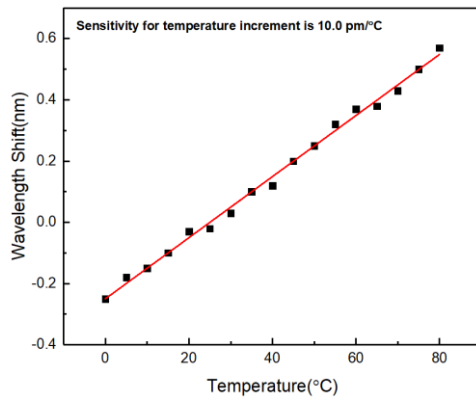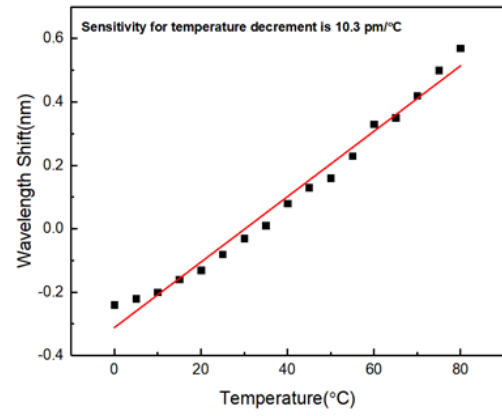
(e)   (f)

Figure 3. 8 Thermal sensing responses of FBGs (centre wavelength of 1551.7 nm, 1543.7 nm, 1559.6 nm) when temperature (a), (c), (e) increasing and (b), (d), (f) decreasing.

Table 3. 1 Thermal sensing of FBG at three different centre wavelengths.

Centre Wavelength of FBG	Temperature Sensitivity	
	Increment	Decrement
1551.7 nm	11.3 pm/°C	11.3 pm/°C
1543.7 nm	11.6 pm/°C	11.5 pm/°C
1559.6 nm	10 pm/°C	10.3 pm/°C

The UV inscribed FBGs were also investigated for their strain sensing response. The strain induced wavelength shift due to strain effect is expressed through the second term of equation (3.3). The Bragg wavelength shift can be expressed in terms of strain expansion that modifies the grating spacing and the effective refractive index.

$$\Delta\lambda_B = \lambda_B(1 - p_e)\varepsilon_z \tag{3.7}$$

p_e is known as the strain-optic constant and it is expressed as,

$$p_e = \frac{n_{eff}^2}{2}\left(p_{12} - v(p_{11} + p_{12})\right) \tag{3.8}$$

Here, v is the Poisson's ratio, p_{11} and p_{12} are the components for strain-optic tensor.

The strain sensing measurement has been done by fixing the grating onto two rotational stages as shown in Fig. 3.9. The strain sensing was conducted with the FBG fibre fixed onto two translation stages and the strain was applied by moving one end of the fibre grating. The distance between the

two fixed stages kept 25.5 cm apart. The right-hand stage is moved from 0 mm to 0.05 cm with a step of 0.0254 mm that provides the strain range up to 2490 µε. The spectrum for each strain applied was recorded using the OSA.
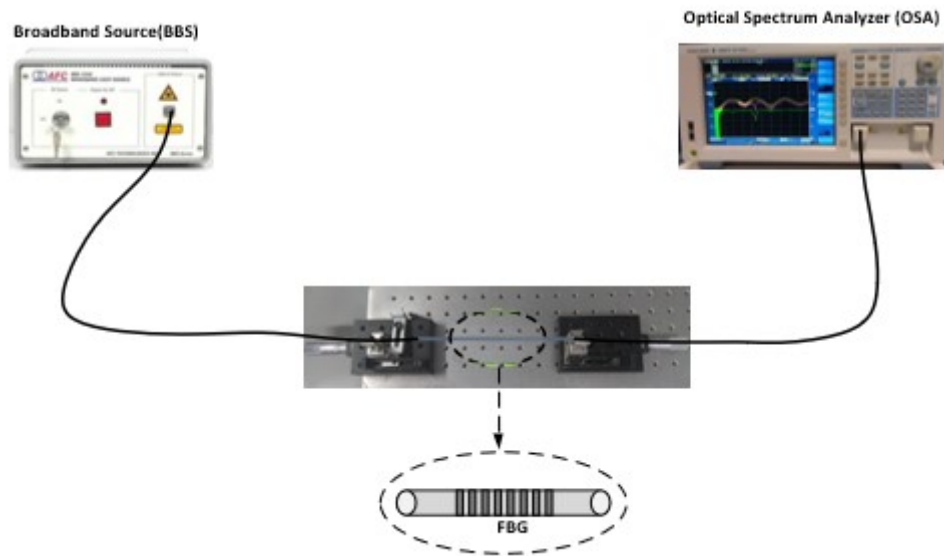
Figure 3. 9 Experimental setup for FBG strain sensing.

Figure 3.10 (a & b) shows the strain response of an FBG with centre wavelength of 1543.7 nm. It is clearly seen in Fig. 3.10 (a), as the strain is increased the wavelength is red shifted with the value observed as ~0.11 nm over the total strain of 0.8 pm/µε applied. A 100 µε was applied in each step and it provides a strain sensitivity of 0.8 pm/µε for the range as depicted in Fig. 3.10 (b).
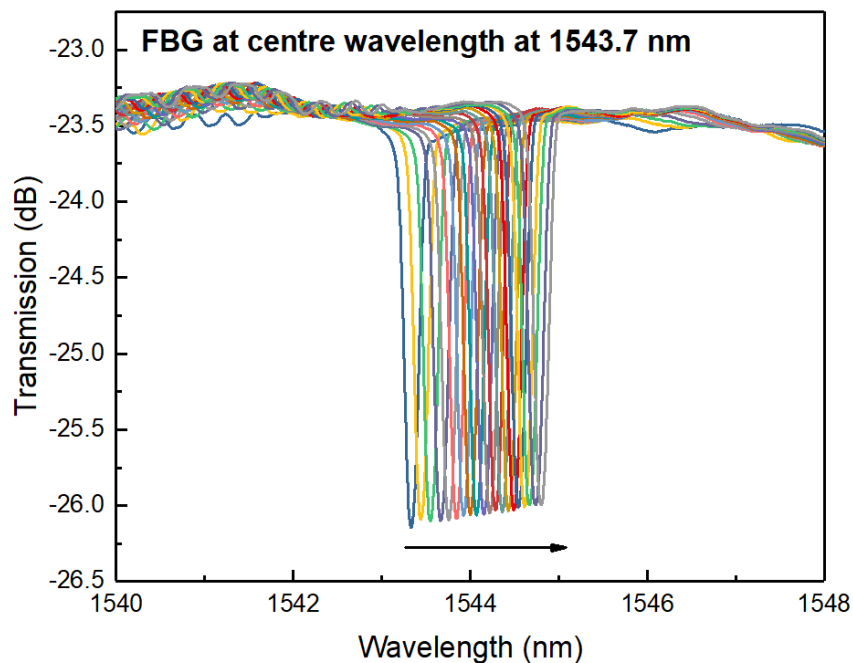
(a)
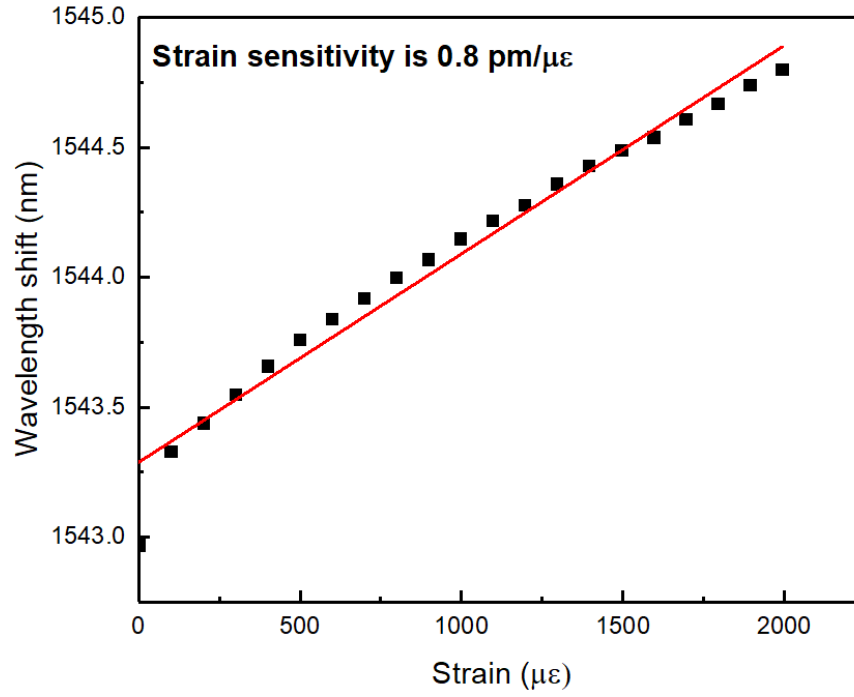
(b)

Figure 3. 10 (a & b) Strain sensing results for FBG with centre wavelength at 1551.7 nm.

3.3 LPG fabrication and sensing characteristics

This section elaborates the fabrication and sensing property characterisation of long period gratings (LPGs). The prime objective of this experiment is the grating inscription using point-by-point writing technique and sensitivity measurements for temperature and the refractive index of the surrounding medium.

In an LPG, the fundamental mode in the core is coupled with forward propagating cladding modes. The grating period ranges from few hundred microns to few millimetres. While coupling through the fibre core and the high diffraction order (m) cladding modes, there is scattering loss due to radiation in the phase matched condition. A set of resonant bands are centred at different wavelengths in the transmission spectrum and the LPG resonance peak wavelength can be expressed as:

$$\lambda_m = \left[n_{co}^{eff} - n_{cl,m}^{eff}\right]\Lambda = \partial n_{eff}\Lambda \tag{3.9}$$

The wavelength of m-th mode (λ_m) depends on the effective refractive index (n_{eff}) which is equal to the difference between the effective refractive index of core and the effective refractive index of m-th cladding mode respectively; Λ is the grating period. The cladding mode is a function of cladding refractive index and the surrounding medium (n_s) . The spectral distribution of each cladding mode depends on the fibre structure and can be observed through their attenuation bands as the intensity decays. A wavelength shift in the transmission spectrum can be obtained with the change in refractive

index of surrounding medium as because $n_{cl,m}^{eff}$ is affected. This unique property of LPG makes this suitable for the applications in bending, loading etc as because these are very sensitive to the variations in temperature, strain, deformations, and a wavelength shift for the loss peak is available here.

3.3.1 UV-inscribed LPGs

Earlier in Chapter 2 it is mentioned, the LPGs have grating periods in the range of ~10 μm to ~600 μm and they enable the light coupling between fundamental core mode and co-propagating cladding modes. The LPGs fabricated and reported in this thesis used point-by-point writing method with various periods. A 244 nm frequency doubled Argon ion UV laser was used for the refractive index modulation into fibre core (Section 2.5.3 in Chapter 2). A LabVIEW programme setup was utilised for different grating periods and the laser scanning speed of 0.2 mm/s was set for LPG inscription within the fibre core. The LPGs with periods of 300 μm, 340 μm, 350 μm and 400 μm were UV-inscribed into B-Ge photosensitive fibre. The spectra were recorded with light launched from a broadband source to one end of LPG device and other end connected to an OSA (YOKOGAWA) at a resolution of 0.20 nm. Figure 3.11 shows the transmission spectra of LPGs with four different periods. According to the phase matched curve, it is clearly seen that the shorter period LPG such as 300 μm has fewer number of attenuation peaks (LP05 and LP06) in the wavelength range from 1200 nm to 1600 nm compared to the longer period length LPG like 400 μm, which shows 4 resonant peaks (LP03, LP04, LP05 and LP06) [72]. Both the LPG with periods of 340 μm and 350 μm has three attenuation peaks and their longest resonances occurred at 1559 nm and 1700 nm respectively as plotted in Fig. 3.11 (b&c). However, the transmission peaks are shifted towards the red wavelength range as period length is increasing. The strength of the resonance peak is varying depending on the period, and the mode order excitation and coupling coefficient during fabrication process. For example, a maximum intensity is nearly 25 dB for LP06 mode for LPG with 300 μm period, whereas the maximum reaches approximately 30 dB for LP06 mode for 400 μm LPG.

(a)   (b)
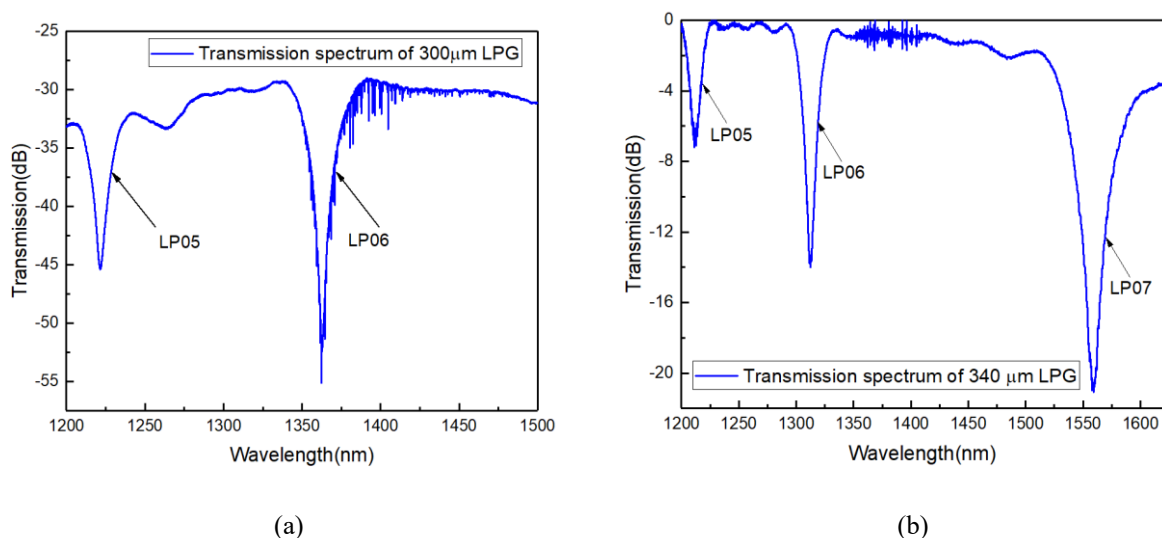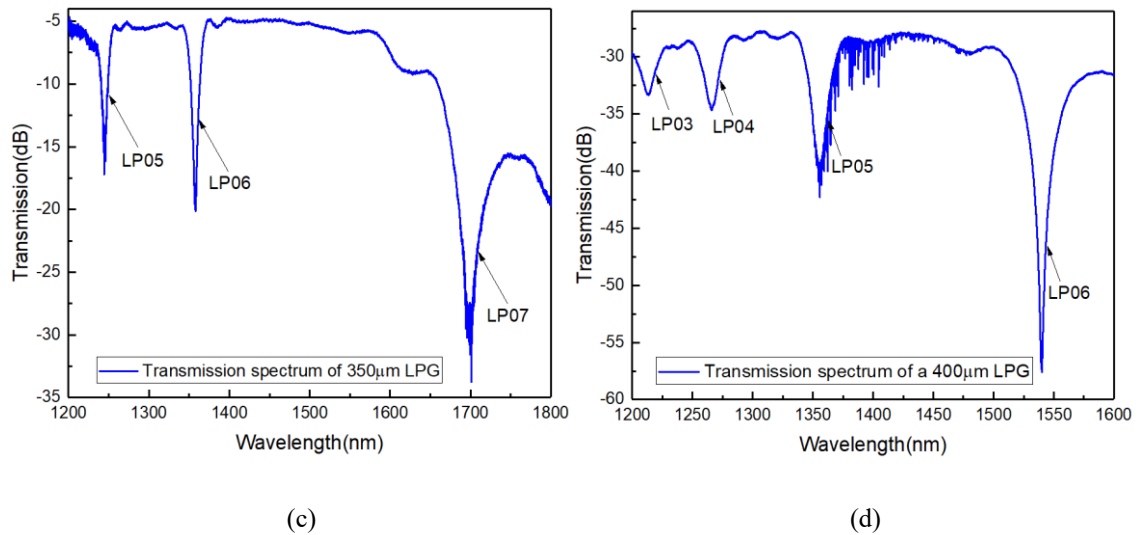
Figure 3. 11 Transmission spectra for LPGs with different periods: (a) 300 μm, (b) 340 μm, (c) 350 μm and (d) 400 μm.

As the standard single-mode telecom fibre (SMF-28) is at much lower price in comparison with the B/Ge photosensitive fibre, LPG fabrication was also investigated for SMF-28 fibre for potential low-cost devices. The hydrogen loading technique as discussed in section 2.2.3 was applied to SMF-28 to increase its UV photosensitivity. An LPG with grating period of 400 μm was fabricated into a hydrogen loaded SMF-28. A stable spectra is achieved after annealing the LPG placed into an oven for 48 hours at 80 °C. The spectral characterisation was recorded using a broadband light source (1200-1700 nm) and an optical spectrum analyser (YOKOGAWA AQ6375). Figure 3.12 shows the LPG spectra and it can be seen that, in comparison with the LPGs UV inscribed in B/Ge fibre, the strength of the LPG resonances in SMF-28 fibre is relatively weaker as the marked three peaks show only about 5-10 dB transmission loss. Also, for the LPG made in hydrogenated SMF-28 fibre, there are multiple ripples occur in the spectrum, this may be due to non-uniform UV exposure to the fibre.
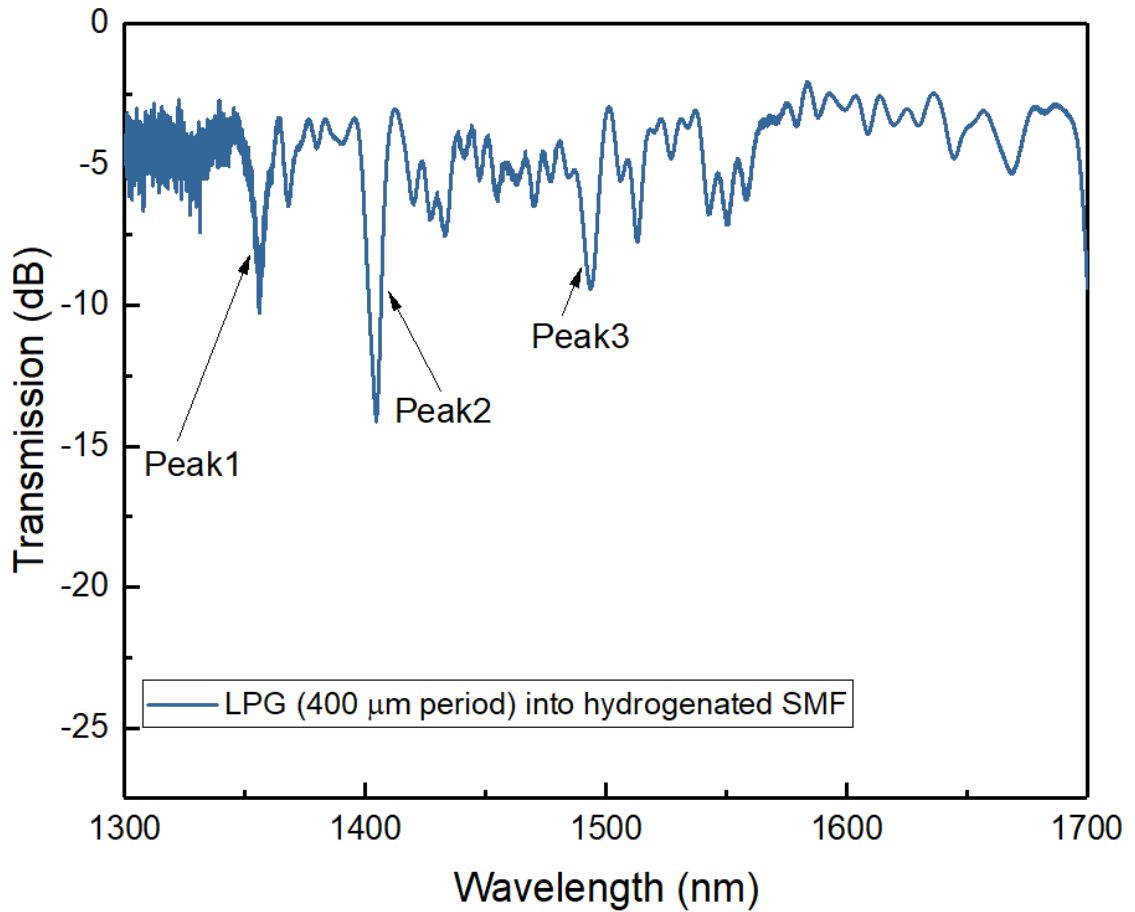
Figure 3. 12 Transmission spectrum for a 400 µm LPG UV inscribed into a hydrogenated SMF-28 fibre.

In order to fabricate LPGs with resonances at designed wavelengths, the tunability of wavelength shift for LPG attenuation bands was investigated by slightly varying the grating period. This was performed by adjusting the writing parameters for scanning length and speed into the LabVIEW programme during point-by-point fabrication method. Four LPGs were written into normal B-Ge photosensitive fibre with periods of 400 µm, 410 µm, 415 µm and 450 µm respectively. The transmission spectra were measured with a supercontinuum source (1200-1800 nm) and an OSA (YOKOGAWA) are shown in Fig. 3.13 (a-d). Following the phase- matched curve and as mentioned in the equation (3.9) the increase in grating period modulates the effective refractive index between core and higher order cladding modes, hence the resonance is red shifted [72]. It is seen that with the increase in period the LPG resonance red-shifts. An LPG with period of 400 µm has the resonance peaks at ~1207 nm (peak 1), ~ 1259 nm (peak 2), ~1347 nm (peak 3) and ~ 1528 nm (peak 4) respectively. The observed resonance shift for peaks 1 to 4 were obtained as 14 nm, 16 nm, 22 nm and 34 nm as the period is changed from 400 to 410 µm. Similarly, with the change in LPG period from 410 µm to 415 µm all transmission peaks from 1 to 4 are red shifted as 6 nm, 7 nm, 11 nm and 31 nm respectively. However, a maximum resonance shift of 40 nm, 49 nm, 71 nm and 207 nm were achieved for all the peaks (1 to 4) as the LPG period is increased from 415 µm to 450 µm. Whereas

the intensities are approximately same for all the attenuation bands as seen in the recorded spectra in Fig. 3.13 (a,b&c). However, a maximum resonace shift of more than 200 nm could be obtained as the LPG period is increased to 450 μm as depicted in Fig. 3.13 (d). Thus by tuning the period length the peak shift can be controlled for an LPG.

(a)

(b)

(c)

(d)
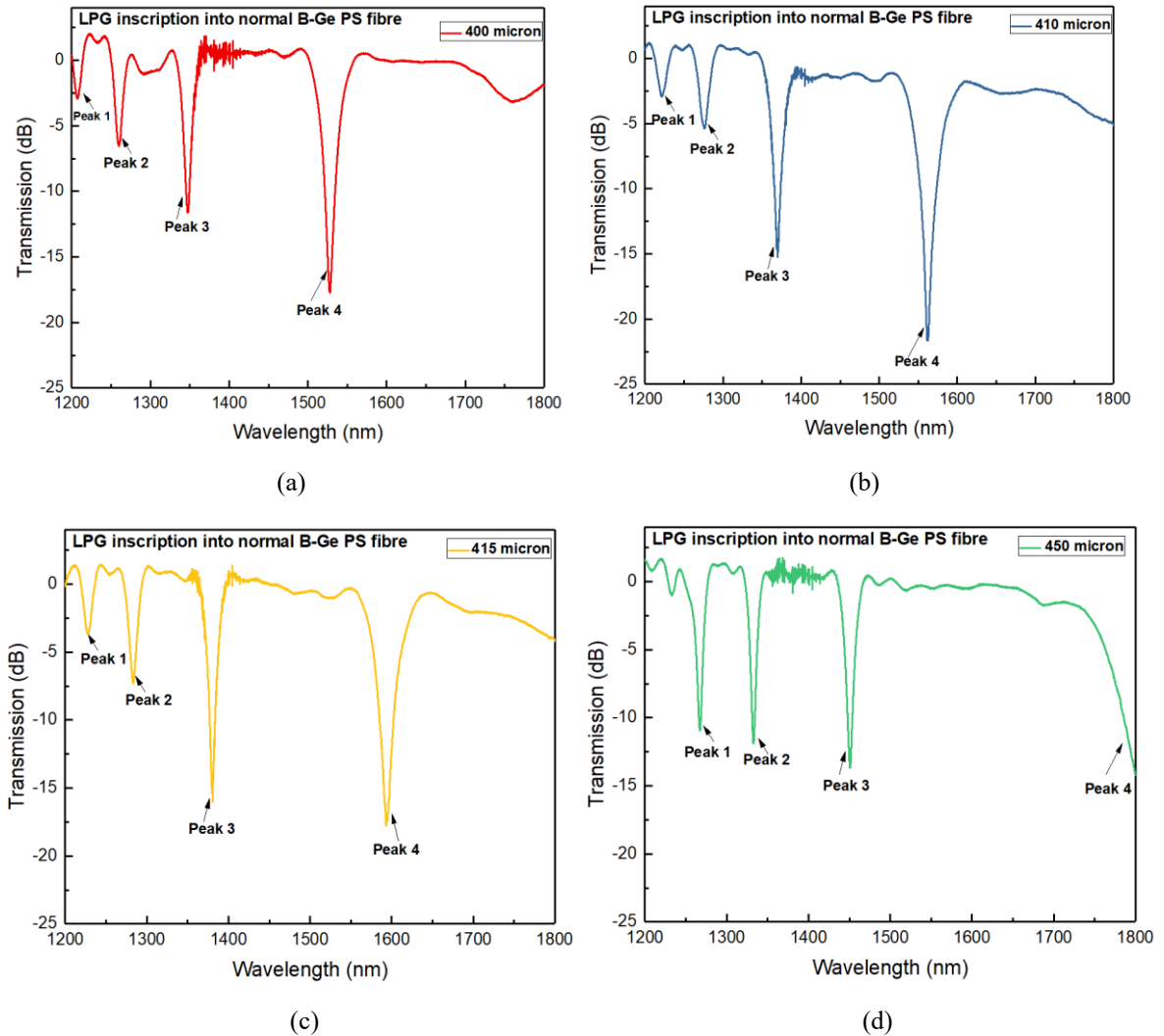
Figure 3. 13 Transmission spectra for LPGs into B-Ge photosensitive fibre at periods of (a) 400 μm, (b) 410 μm, (c) 415 μm and (d) 450 μm.

So this novel method can be utilised for fabricating the LPG device at the required wavelength for application needs.

3.3.2 LPG sensing characteristics

The advantages of LPG devices are associated with the easy fabrication, low insertion loss, small back reflection and compactness. Highly sensitive fibre sensors are for various applications such as monitoring environmental conditions. The LPGs are unique sensing device as it has higher temperature sensitivity than normal FBG and has excellent surrounding refractive index (SRI)

sensitivity. This is due to special mode coupling mechanism between the core mode to the cladding modes. The unique SRI sensitivity of LPG makes it as a suitable candidate for potential biochemical, biomedical and environmental sensing applications. This section will present some measurements of temperature and RI index sensing property using the UV inscribed LPGs. We demonstrated both thermal and SRI sensing properties for an UV-inscribed LPG.

3.3.2.1 Thermal sensing measurement for LPGs

For the temperature sensitivity, the direction of resonant wavelength shift of an LPG is dependent on fibre dispersion factor γ and the temperature dependence of the waveguide dispersion Γ_{temp}. A positive dispersion factor is obtained when the cladding mode order is less than or equal to 7 (m ≤ 7). Thereby, the direction of peak shift is only dependent on the factor Γ_{temp} and is defined by [72],

$$\Gamma_{temp} = \frac{\xi_{co} n_{co}^{eff} - \xi_{cl} n_{cl,m}^{eff}}{n_{co}^{eff} - n_{cl,m}^{eff}} \tag{3.10}$$

ξ_{co} and ξ_{cl} are the thermo-optic coefficients of the fibre core and cladding materials respectively. For a fibre, the effective refractive index of the core is higher than the refractive index of the cladding, thereby the term $(n_{co}^{eff} - n_{cl,m}^{eff})$ is positive and the resonant wavelength peaks will have red shift after annealing.

Rewriting the equation for transmission spectra of LPG for the attenuated band are given by,

$$T_i = 1 - sin^2(k_i L) \tag{3.11}$$

From the above equation it is seen that the length (L) of the LPG and the coupling co-efficient of the *i-th* cladding mode (k_i) are the important parameters for achieving the intensity of resonant wavelength. The temperature sensitivity equation can be expressed by differentiating the phase matching expression (2.27) and is given by,

$$\frac{d\lambda_{res}}{dT} = \lambda_{res} \cdot \gamma \cdot (\alpha + \Gamma_{temp}) \tag{3.12}$$

Where α is the thermal expansion coefficient; γ is the waveguide dispersion and is defined as,

$$\gamma = \frac{\frac{d\lambda_{res}}{d\Lambda}}{n_{co}^{eff} - n_{cl,m}^{eff}} \tag{3.13}$$

The LPG temperature sensing setup is shown in Fig. 3.14 and the characterisation was performed for two LPGs with periods of 300 μm and 400 μm respectively. The individual LPG was placed onto

the plate mounted on a Peltier device which is connected with the temperature controller. A high thermal resistant tape was used to fix the grating. The temperature was varied from 0 °C to 80 °C with 10 °C step while the surrounding medium is considered to be air with refractive index 1.
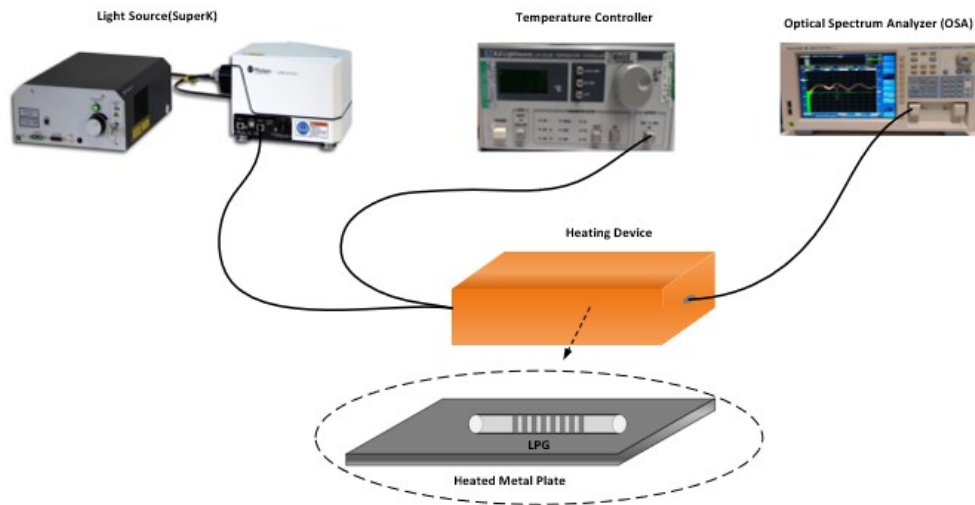
Figure 3. 14 Experimental setup for temperature sensing of an LPG.

Figure 3.15 (a) and (b) show the temperature sensitivities of the LPGs with grating period 300 μm and 400 μm, respectively. The figure 3.15 (a) is plotted for the two modes of the short period LPG and figure 3.15 (b) plotted for the four modes of the long period one. It can be clearly seen, the temperature sensitivity increases with coupled mode order. The peak thermal sensitivity of -462.4 pm/°C is obtained for LP06 mode of the 300 μm LPG and it is further increased to -521.4 pm/°C for LP06 in 400 μm LPG. However, the thermal sensitivity of 300 μm period LPG with lower order mode LP05 is obtained as -305.7 pm/°C. Even enhanced temperature sensitivity was achieved for the lower order resonances for 400 μm LPG with LP03, LP04 and LP05 modes as -279.6 pm/°C, -320.3 pm/°C and -346.4 pm/°C respectively. These results clearly show the thermal sensitivity of LPG is significantly higher than normal FBG, quantitatively, the former is about 50 times higher than the latter, which is typically about 10 pm/°C. All results are summarised in Table 3.2.
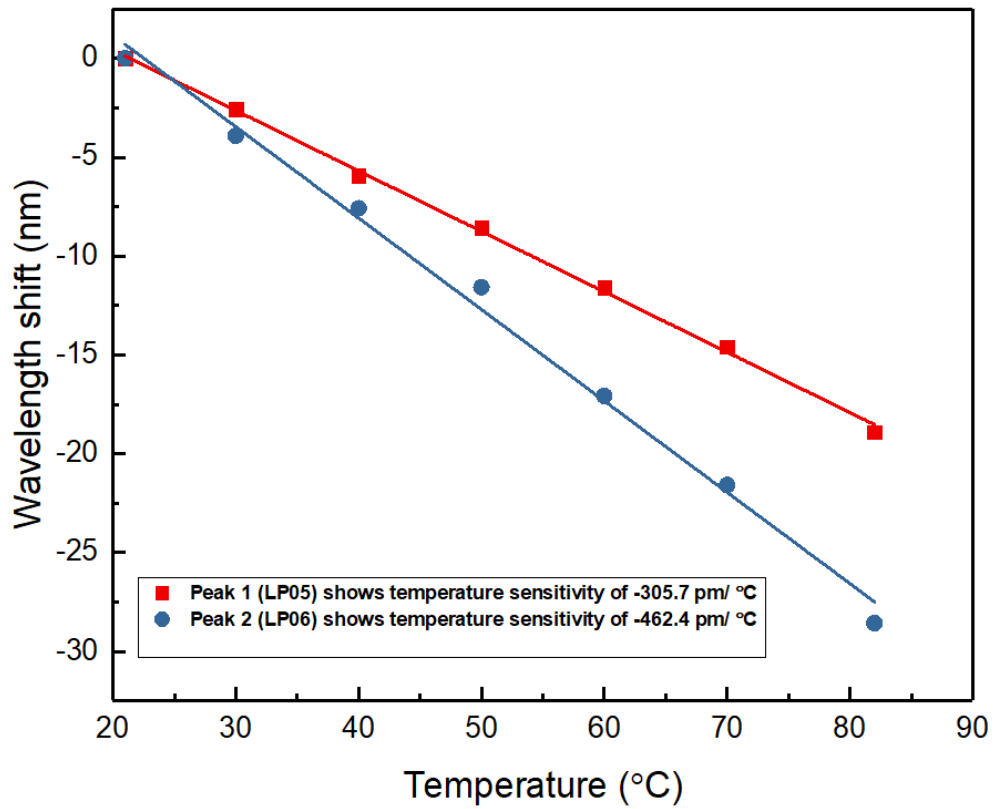
(a)
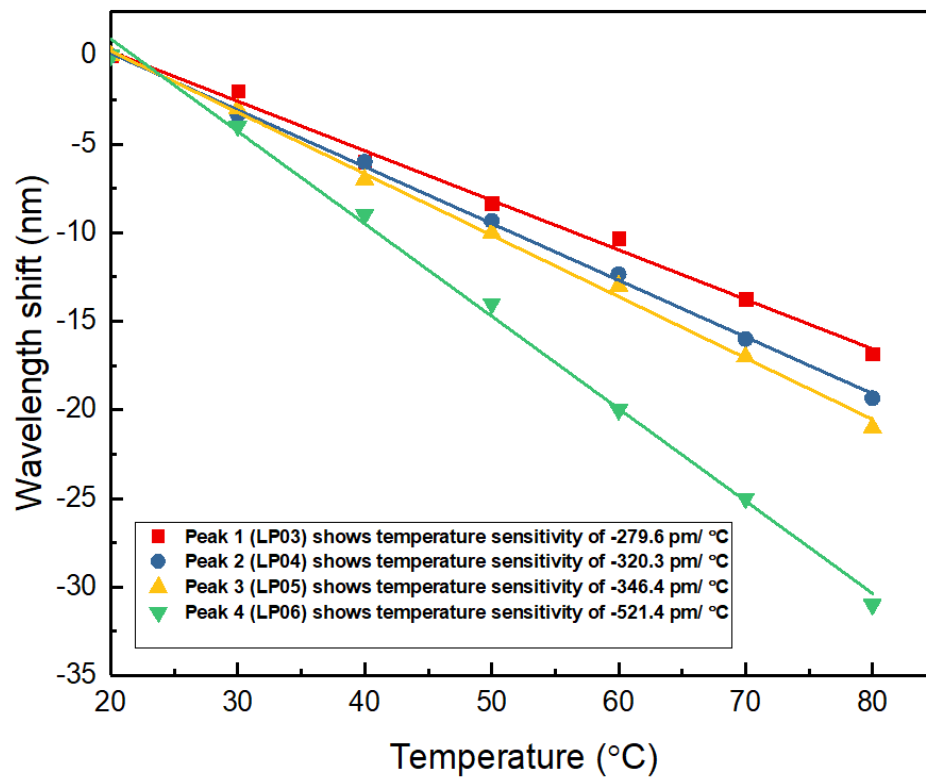
(b)

Figure 3. 15 LPG temperature sensitivity plots for different coupled cladding modes for (a) LPG (300 μm) and (b) LPG (400 μm).

Table 3. 2 Thermal sensing of LPG at different periods.

Period of grating	Cladding modes	Sensitivity
300 μm	LP05	-305.7 pm/°C
	LP06	-462.4 pm/°C
400 μm	LP03	-279.6 pm/°C
	LP04	-320.3 pm/°C
	LP05	-346.4 pm/°C
	LP06	-521.4 pm/°C

3.3.2.2 SRI sensor based on LPGs

The attenuation bands for LPGs are influenced with the change in surrounding refractive index. Due to light-matter interaction the effective refractive index gets modulated at the core-cladding interface. The SRI sensitivity of LPG depends on the overall refractive index variation to get the resonance wavelength shift and intensity change.

We can derive the analytical equation for SRI sensitivity and is expressed as $d\lambda_{res}/dn_{sur}$ in equation (3.14).

$$\frac{d\lambda_{res}}{dn_{sur}} = \lambda_{res}.\gamma.\Gamma_{sur} \tag{3.14}$$

where γ is the waveguide dispersion and is given by,

$$\gamma = \frac{d\lambda_{res}/d\Lambda}{n_{co}^{eff} - n_{cl,m}^{eff}} \tag{3.15}$$

The term Γ_{sur} is the surrounding refractive index dependent factor and is defined as,

$$\Gamma_{sur} = -\frac{u_m^2 \lambda_{res}^3 n_{sur}}{8\pi r_{cl}^3 n_{cl}(n_{co}^{eff} - n_{cl,m}^{eff})(n_{cl}^2 - n_{sur}^2)^{3/2}} \tag{3.16}$$

Here, u_m is the m-th root of the zeroth order Bessel function of the first kind, r_{cl} is the radius of fibre cladding, n_{cl} and n_{sur} are the refractive indices for the fibre cladding and surrounding medium

respectively. Therefore, the SRI sensitivity of LPG based sensor devices are determined from the γ and Γ factors. These are dependent on the grating design parameters and fibre materials.

The SRI sensitivity characteristics was investigated for the UV inscribed LPGs. Fig. 3.16 shows the experimental setup for SRI sensing. The two ends of the LPG fibre are fixed onto two translation stages and the care was taken as it should not be affected by strain and bending effect. A set of refractive index gels (bought from Cargille) with index values ranging from 1.32 to 1.44 was applied to the LPG sample and in the experiment, the grating was completely immersed in the index gel. The resonance wavelength shift was noticed from the transmission spectrum when the index applied to the LPG and the spectrum was recorded on the OSA for each index applied.
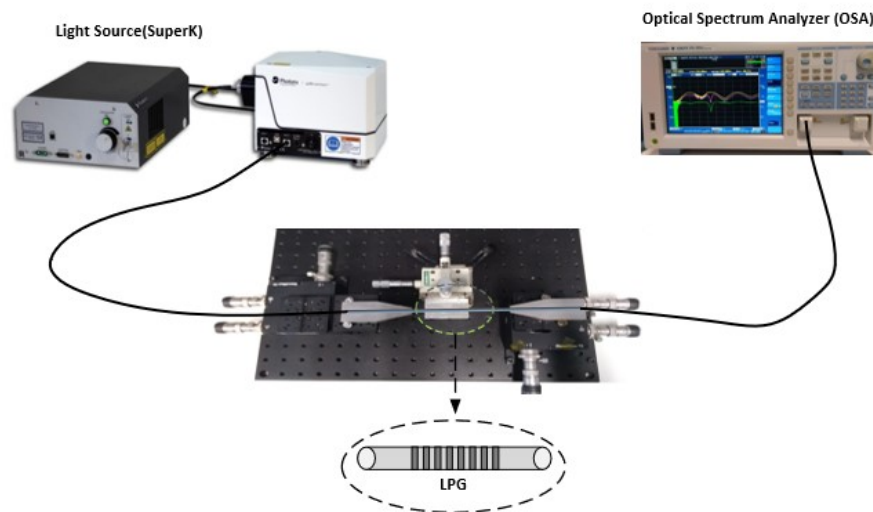
Figure 3. 16 Experimental setup for refractive index sensing of an LPG.

LPGs are very sensitive to surrounding refractive index (SRI) change. The LPG of 400 μm period was subjected to refractive index sensing and the results are presented in Fig. 3.17. It is clear from the plots that, the two modes show very different SRI sensitivities. The maximum refractive index sensitivity of -56 and - 315 nm/RIU are obtained for LP06 for a 400 μm LPG while only -7 and - 47 nm/RIU for the LP05 mode in the two index ranges of (1.32 – 1.38) and (1.404 – 1.44) respectively, the former is nearly 7 times higher than the latter. A summarised SRI sensitivity for these modes is briefed in the table 3.3. The "-"sign indicates the LPG resonance blue-shifts against the SRI increase. It can also be clearly noted from the SRI sensitivity plots in Fig. 3.17 (a&b) that the sensitivity is nonlinearly increase with the SRI, and most sensitive when the SRI approaching to the cladding index of the fibre. This is due to the higher order cladding modes closed to the evanescent field enhance the light matter interaction, and hence experience a greater sensitivity than lower order cladding modes.
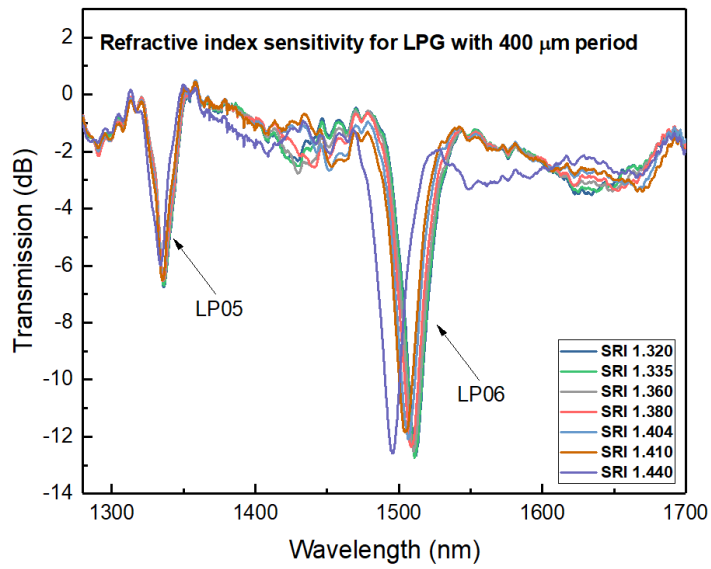
(a)
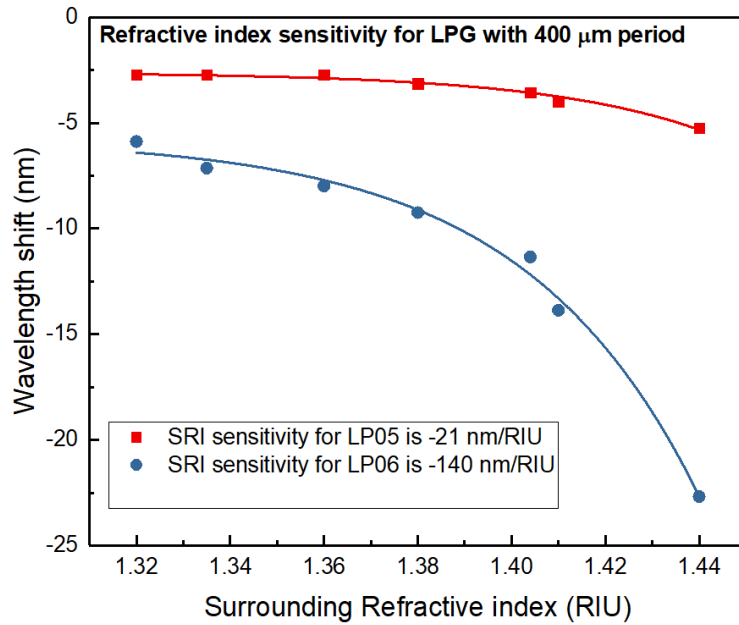
(b)

Figure 3. 17 SRI sensing for 400 μm LPG: (a) the wavelength is blue shifted with the change in refractive index of 1.32-1.44; (b) SRI sensitivity for different cladding modes.

Table 3. 3 SRI sensing of LPG for different cladding modes.

Resonance wavelength	Cladding modes	SRI range	SRI Sensitivity (~ nm/RIU)
1340 nm	LP05	1.32 – 1.38	- 7
		1.404 – 1.44	- 47
1518 nm	LP06	1.32 – 1.38	- 56
		1.404 – 1.44	- 315

3.4 Small angle tilted fibre grating inscription and sensing measurements

The small angle (1°-23°) tilted fibre gratings (STFGs) were reported for dual-parameter (temperature and strain) sensing and especially unique and advantageous for biosensing [73-75]. This PhD project has also aimed to investigate UV inscribed STFGs.

An optical fibre is a cylindrical structure with the incident light propagating in a perpendicular direction with respect to the central axis. When there is a tilt angle between the interference fringe and the fibre axis analysis becomes more complex. There will be distortion of the interference fringes within the fibre core and therefore the differentiation will occur between the grating tilt angle both inside (θ_{int}) and outside (θ_{ext}) of the optical fibre as represented in the schematics of Fig. 3.18.
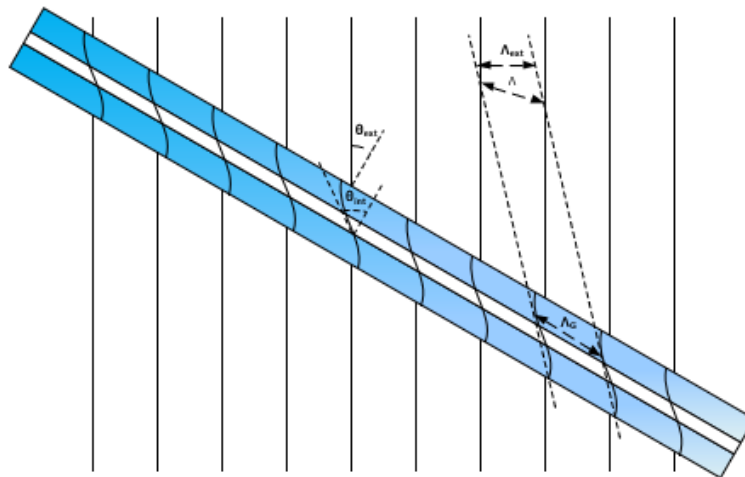
Figure 3. 18 The structure of TFG with an external angle θ$_{ext}$ and an internal angle θ$_{int}$.

The internal angle (θ_{int}) is related with the external angle (θ_{ext}) as below [76]:

$$\theta_{int} = \frac{\pi}{2} - tan^{-1} \left[\frac{1}{n_{uv} \tan(\theta_{ext})} \right] \qquad (3.17)$$

Here n_{uv} is the refractive index of the fibre at the presence of UV exposure.

For a grating with tilted angle of 45°, the external angle is calculated through above equation, and it becomes 33.7°. The angle is always measured with respect to the fibre axis.

The relationship between the grating period of internal interference fringe and that of the external interference fringe is given below:

$$\Lambda = \frac{\Lambda_{ext}}{cos\theta_{ext}} = \frac{\Lambda_G}{cos\theta_{int}} \qquad (3.18)$$

3.4.1 Fabrication and spectral response of STFG

The small angle TFGs (STFGs) were successfully inscribed into the fibre core of hydrogen loaded SMF-28 for tilt angles 2°, 4° and 6° using phase mask of pitch 1083 nm. The fabrication technique for inscribing STFGs is similar to that for FBGs, except that the phase mask is mounted on goniometer, thus can be rotated for the designed tilted angles. The transmission spectra of the three STFGs with tilt angles of 2°, 4° and 6° are presented in Fig. 3.19 (a,b&c). As the STFG couples the forward propagating mode to backward core and cladding modes, we see the single Bragg resonance and a series of cladding mode resonances in the spectrum. It is also clear that when the angle increases, the Bragg reflection becomes weaker while the cladding resonances grow strong. As Fig. 3.19 shows, for the 2°- STFG, the Bragg reflection is strongest at around 15 dB while for the 6°- STFG, the Bragg reflection reduced to 0.2 dB. From the figures we also can see apart from the cladding resonances grow strong with increased tilted angle, the envelope of the cladding resonance becomes broader, and the centre of the resonances moves to the shorter wavelength side. The centre of the cladding resonances of the 2°-STFG is at 1560 nm whereas that moves to 1535 nm for the 6°- STFG. These are the important design parameters one needs to consider in the fabrication for particular applications such as in the low-cost in-fibre wavelength division multiplexing (WDM) devices and in erbium-doped fibre amplifiers (EDFA) for gain flattening [77-79].
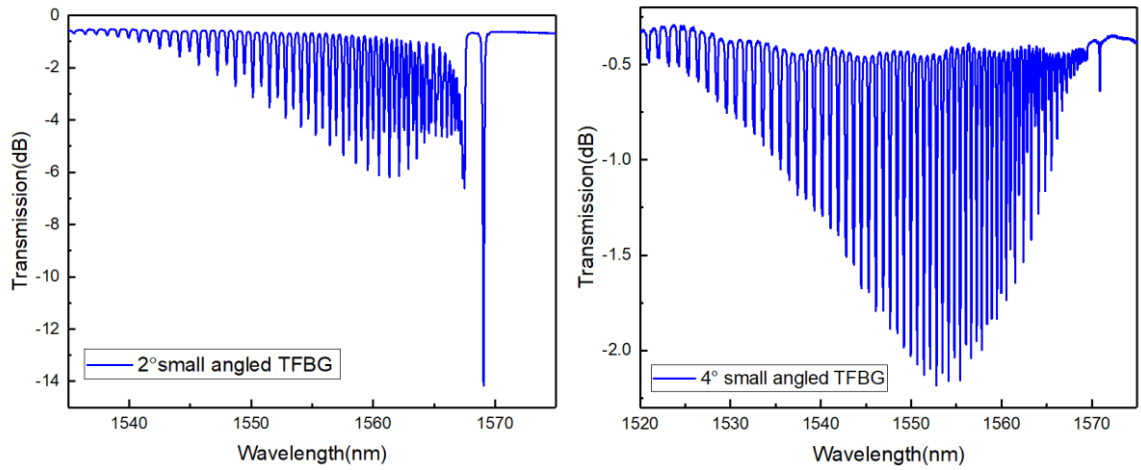
(a)

(b)
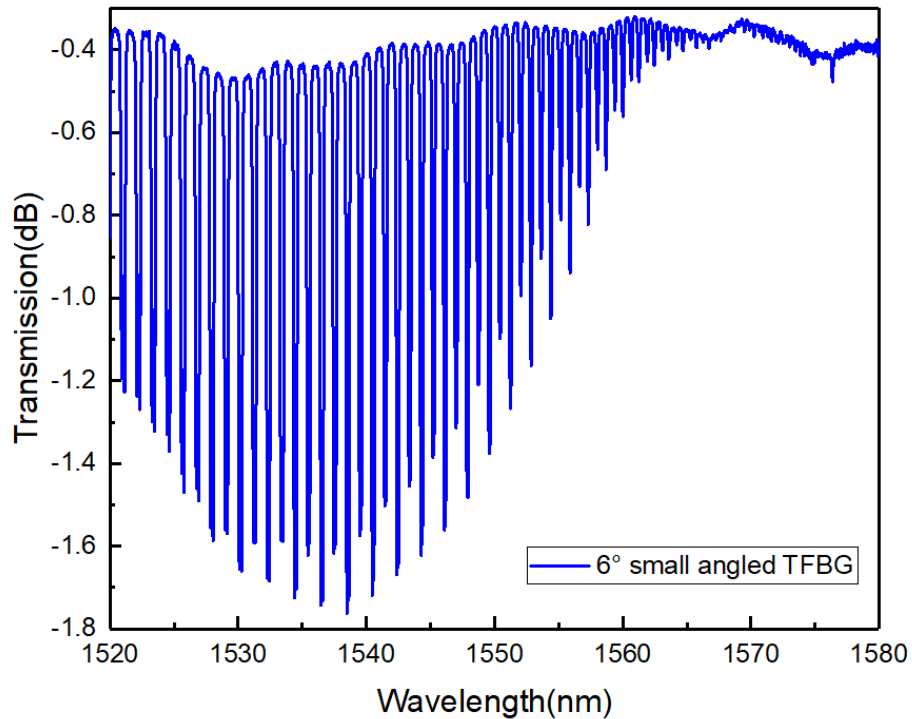
(c)

Figure 3. 19 Transmission spectra of STFGs with tilted angle of (a) 2°, (b) 4°, and (c) 6°.

3.4.2 STFG temperature sensing characteristics

The temperature sensing measurement of the STFG was performed using the experimental setup as in Fig. 3.7. An STFG with 2° tilt angle was subjected to this experiment with the temperature variation from 10 °C - 70 °C. Four cladding mode peaks at 1558.8 nm, 1559.3 nm, 1559.7 nm and 1560.1 nm were evaluated and the results are plotted in Fig. 3.20. From the figure, it can be evaluated that the first three cladding modes are giving a similar sensitivity of 10 pm/°C whereas the one

resonance closed to longer wavelength gives a slightly higher sensitivity of 11.8 pm/°C. These results show that the temperature sensitivity of STFG is similar to the Bragg gratings, which agrees with previous reported work.
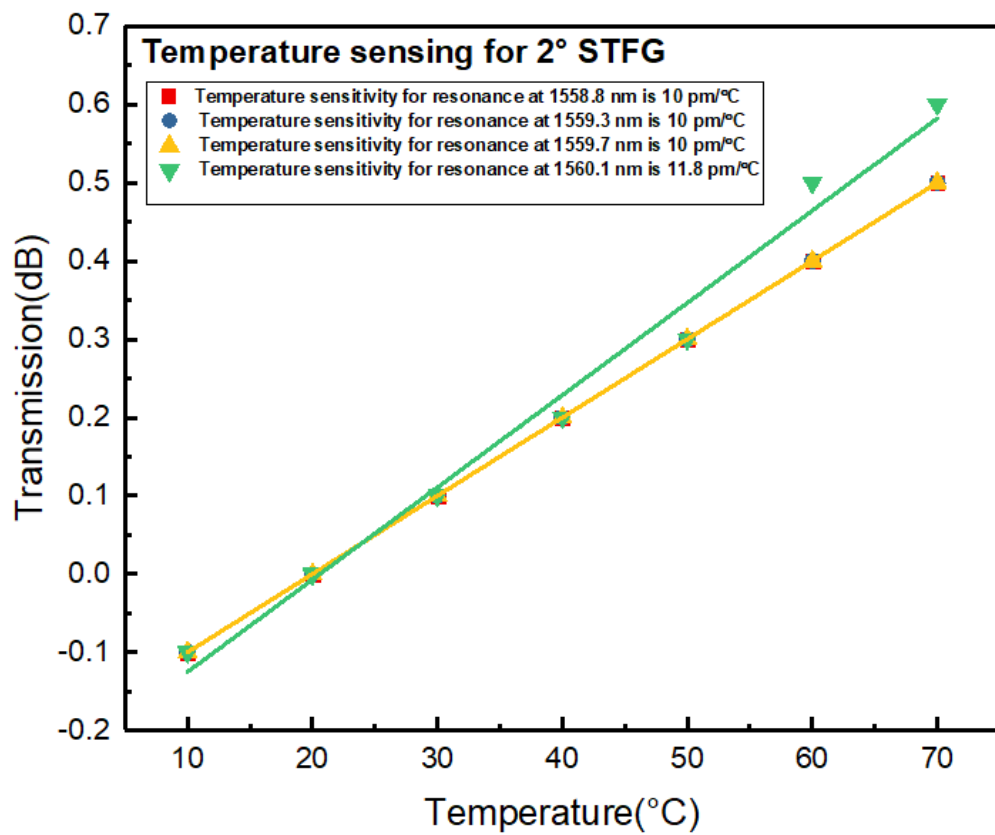
Figure 3. 20 The transmission wavelength shifts plotted against the temperature for the four selected cladding modes of the STFG with tilt angle of 2°.

Part B

Grating inscription, characterisation, and sensing measurements in the mid infrared (MIR) range

3.5 Introduction

The optical fibre sensing devices operating at mid infrared (mid-IR) range have shown interesting applications in defence [80], health [81, 82] and environmental sensing [83]. The thermal and surrounding refractive index (SRI) sensitivities of these sensing devices fabricated in the mid-IR range are high due to unique cladding mode coupling capabilities. On other hand, an in-fibre grating sensor is useful operating at eye-safe location as laser source in 2 μm region. The special attention is focused on operating in the atmospheric transmission window of 2.05 - 2.3 μm. As most of the fibre lasers are comprising with bulk mirrors in the cavity, hence a compact device with low insertion loss is required such as in-fibre laser in the mid-IR range [84]. UV-inscribed long period gratings (LPGs) with both ultrasensitive dual peak (dLPG) and 1st & 2nd order resonances and excessively tilted fibre gratings (Ex-TFG) are investigated in the 2 μm range. The fabrication was performed using point-by-point writing and amplitude mask technique. The temperature and SRI sensitivity were evaluated for these sensors.

3.5.1 Fabrication and characterisation of dual-peak LPGs

The conventional LPG devices has a period range between 300-500 μm. In the phase matched condition, the resonances are distributed over a wavelength span of 1200-1700 nm. Shu et al., experimentally demonstrated that there is a dispersion-turning points in the LPG structures with the periods around 160 μm [72, 85]. For LPGs with dispersion-turning point, a pair of conjugate cladding mode pairs are observed with an increased wavelength range from 900 nm- 2400 nm. Since the dual peak resonances are in a closed proximity to the dispersion-turning point, those two cladding modes are extremely sensitive for both surrounding temperature and refractive index change. Because one of the paired peak occurs in the wavelength range closed to the mid-infrared 2 μm, it was the aim to design and fabricate dual-peak LPGs with resonance around 2 μm to be explored for environmental and biomedical sensing applications. Experimentally dual-peak LPGs (dLPGs) were fabricated into a special small cladding B-Ge photosensitive fibre with core and cladding diameters of 4.2 μm and 80 μm respectively. The thin cladding fibre SM1500 (4.2/80) was bought from Nortel (Bell Northern Research). The dLPGs with 150 μm period were UV-inscribed for a grating length of 10-15 mm. The typical transmission spectra of dLPGs are shown in Fig. 3.21 (a&b). In order to examine the spectral resonance from 900 nm to 2400 nm, two OSAs (HP and YOKOGAWA) were used to record the spectra for all the peaks covering a wavelength range of 950-2400 nm.
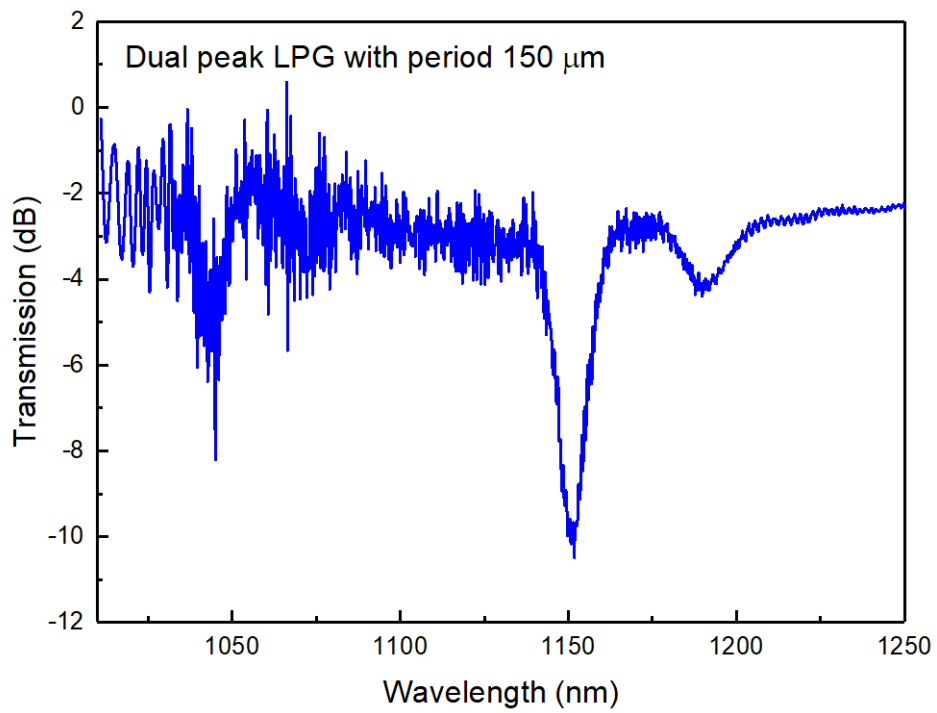
(a)
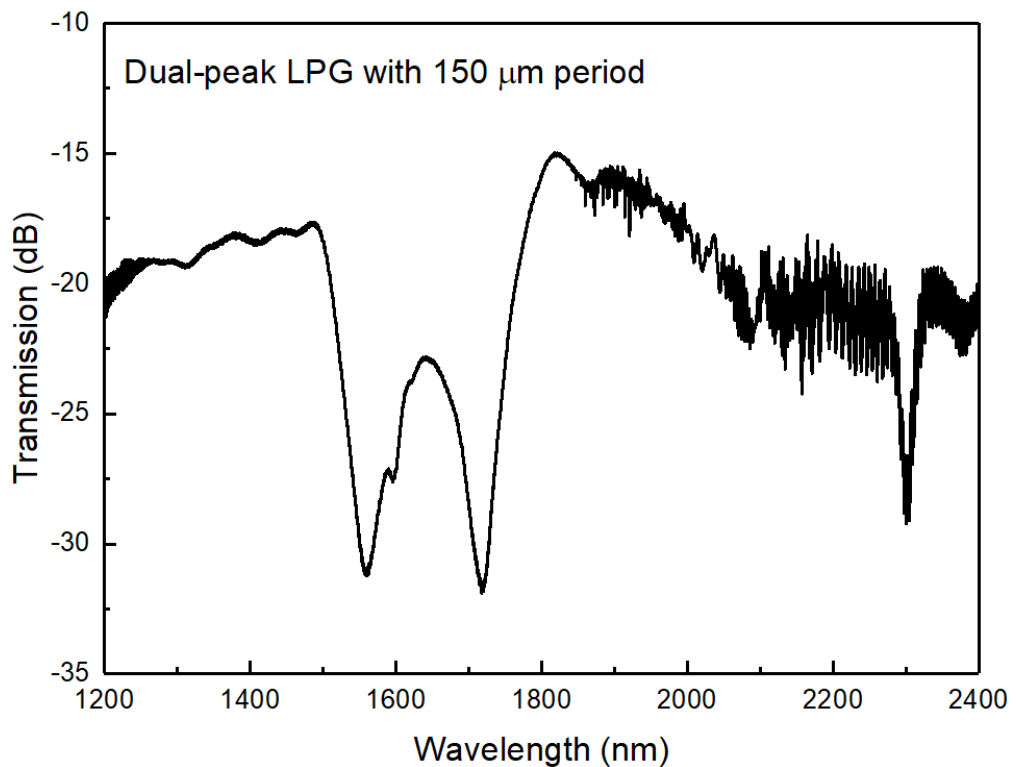
(b)

Figure 3. 21 Transmission spectra for a dLPG with 150 μm period UV-inscribed in SM1500 (4.2/80) fibre: (a) spectrum from 950 nm to 1250 nm showing three individual peaks; (b) spectrum from 1200 nm to 2400 nm showing dual peak feature around 1650 nm area and another single peak at ~2300 nm.

The measurement for four major attenuation peaks, including the dual peaks, show their resonances are at wavelengths of 1151 nm, 1589.76 nm, 1793.52 nm and 2304 nm respectively with maximum 12 dB intensity. Theoretically each cladding mode has a turning point for a sufficiently large wavelength range. The dual-peak LPGs are designed as it has enhanced sensitivity. This unique property of the dLPGs was evaluated for the temperature and refractive index sensing experiment.

The fabricated dLPG was subjected to the temperature elevation experiment in the range of 10 °C – 50 °C with 10 °C step increment. Figure 3.22 (a,b&c) shows the thermal response measurement for all four peaks at 1151 nm, 1589.76 nm, 1793.52 nm and 2304 nm respectively. It can be clearly seen from the figures that the dual peaks are moving into the opposite direction with the rising temperature with much larger sensitivity, which is expected [85]. Table 3.4 summarises the dLPG temperature sensitivity for the measurement of four peaks. The dual-peak resonances are showing the temperature sensitivities as -760 pm/°C for peak 2 at 1589.76 nm and 640 pm/°C for peak 3 at 1793.52 nm, respectively. In contrast, the two normal single peaks are showing much lower temperature sensitivities as only -77.5 pm/°C for peak1 at 1151 nm and -120 pm/°C for peak 4 at 2304 nm, which are almost one order of magnitude lower than that of the dual-peak resonances. It is clearly evident that the dLPG is very sensitive at the dispersion turning point with wavelength shift for the conjugated peaks, while the sensitivity response for the attenuations obtained for first and higher order harmonics are showing the resonance shift similar as the normal LPG. Here, as depicted in Fig. 3.15 with the resonance is blue shifted. This is because the term Γ_{temp} as in equation (3.10) is decreasing with higher order cladding modes and also depends on the variation of thermooptic co-efficients of core and cladding depending on fibre type.
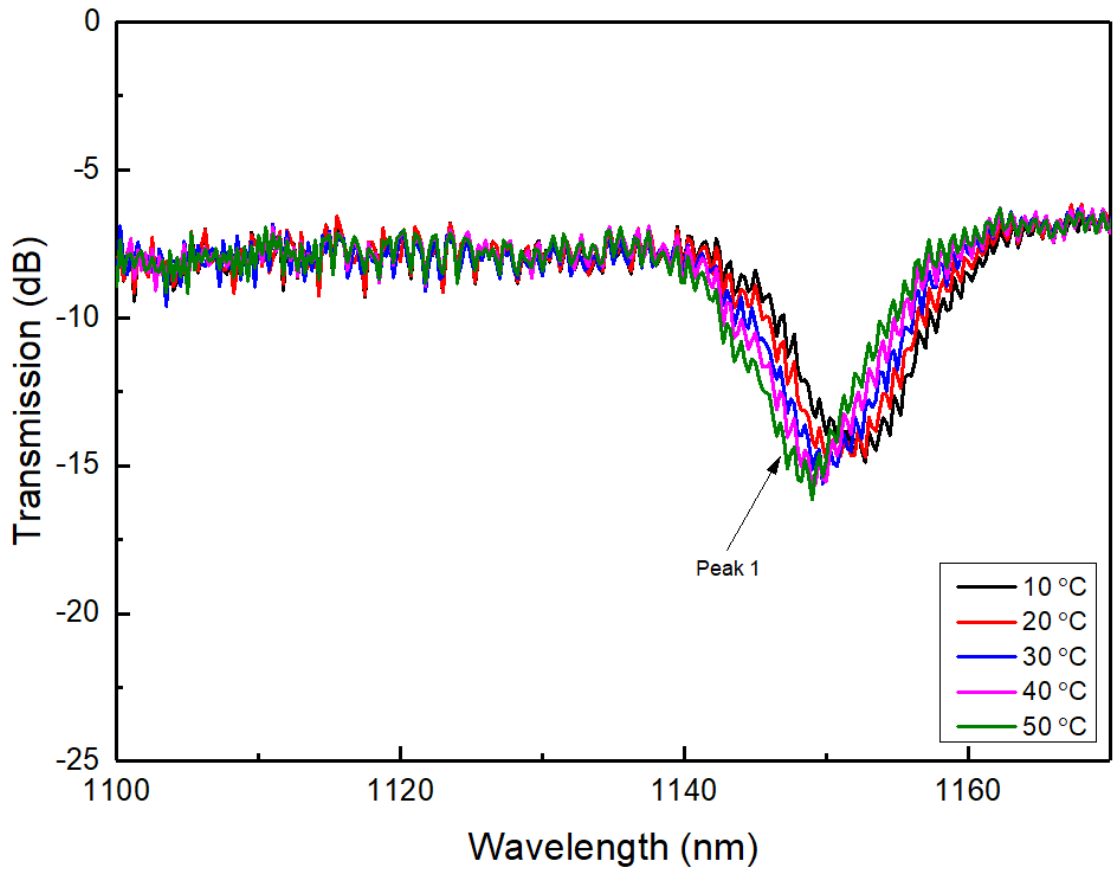
(a)
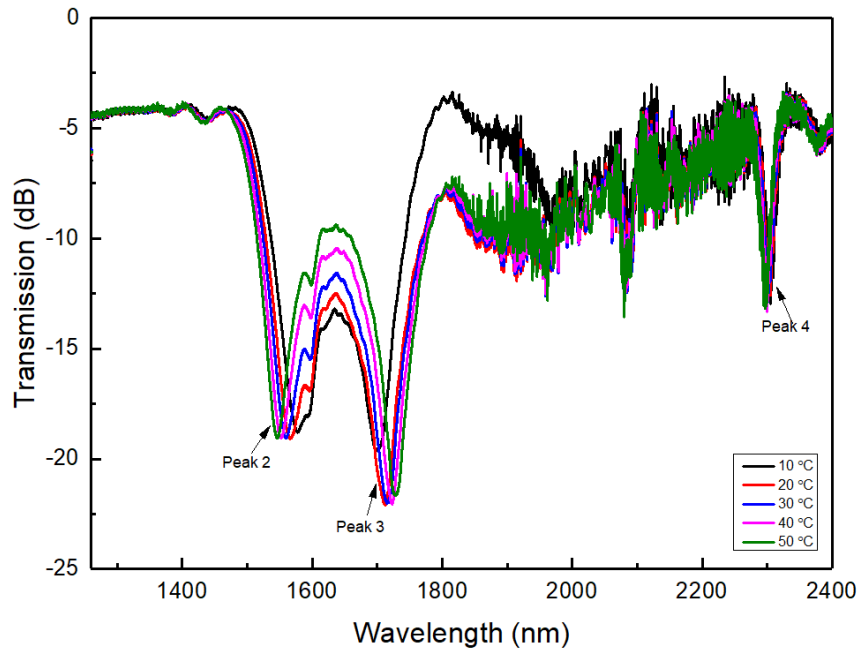
(b)
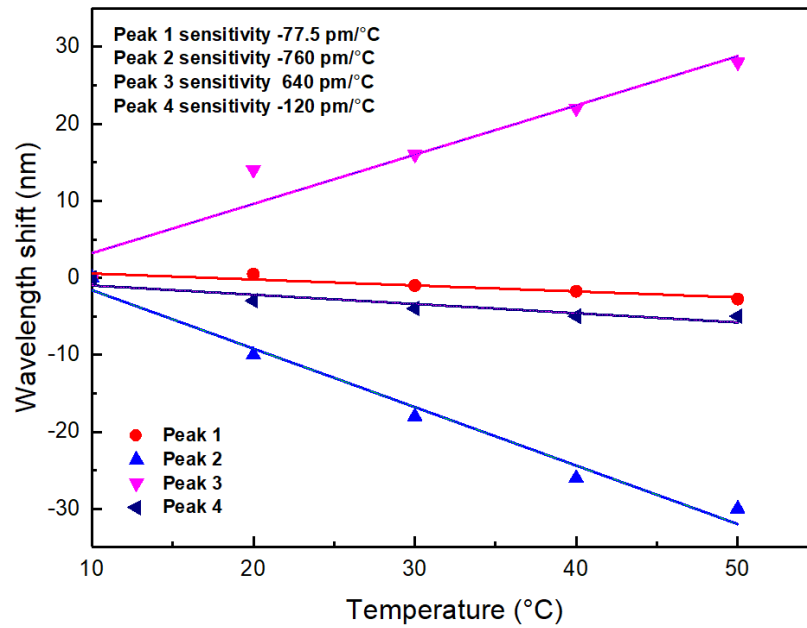
(c)

Figure 3. 22 Temperature response in the range of 10℃ - 50℃ for a dual-peak LPG UV-inscribed in thin cladding SM1500 (4.2/80) fibre with 150 μm period: (a) spectral evaluation for normal peak 1 with blue shifted wavelength; (b) spectral evaluation for dual peaks 2&3 with opposite wavelength shift and normal peak 4 with wavelength blue shifted; (c) The thermal sensitivity results for all the resonances with increased temperature.

Table 3. 4 Summary of the temperature sensitivities for the four resonances of the dual peak LPG.

Dual peak LPG resonance wavelengths	Temperature Sensitivity for an increment of 10 °C in the range of 10 °C -50 °C
1151 nm	-77.5 pm/°C
1589.76 nm	-760 pm/°C
1793.52 nm	640 pm/°C
2304 nm	-120 pm/°C

Further investigation for surrounding refractive index (SRI) sensing of dual-peak LPG was carried out by subjecting the dLPG into the SRI change. The grating was placed onto a glass plate to evaluate the SRI response. Both the ends were fixed onto two three dimensional stages to neutralise the strain and bending effects. A series of commercial immersion gels with RI ranging from 1.3 to 1.44 (purchased from Cargille) were used for this experiment. A supercontinuum source with broad wavelength range (950 – 2400 nm) was used to launch the light through the dLPG. Two OSAs with spectral measurement range of (950-1200) nm and (1200 – 2400) nm were connected in turn to the other end of dLPG for recording SRI response of peaks 1,2,3 & 4 respectively. The dLPG is immersed with each immersion gel and spectra were recorded with a resolution of 0.20 nm. It is seen

that as SRI value increases there is the blue wavelength shift for all the peaks except resonance peak 3, which has red shifted wavelength.
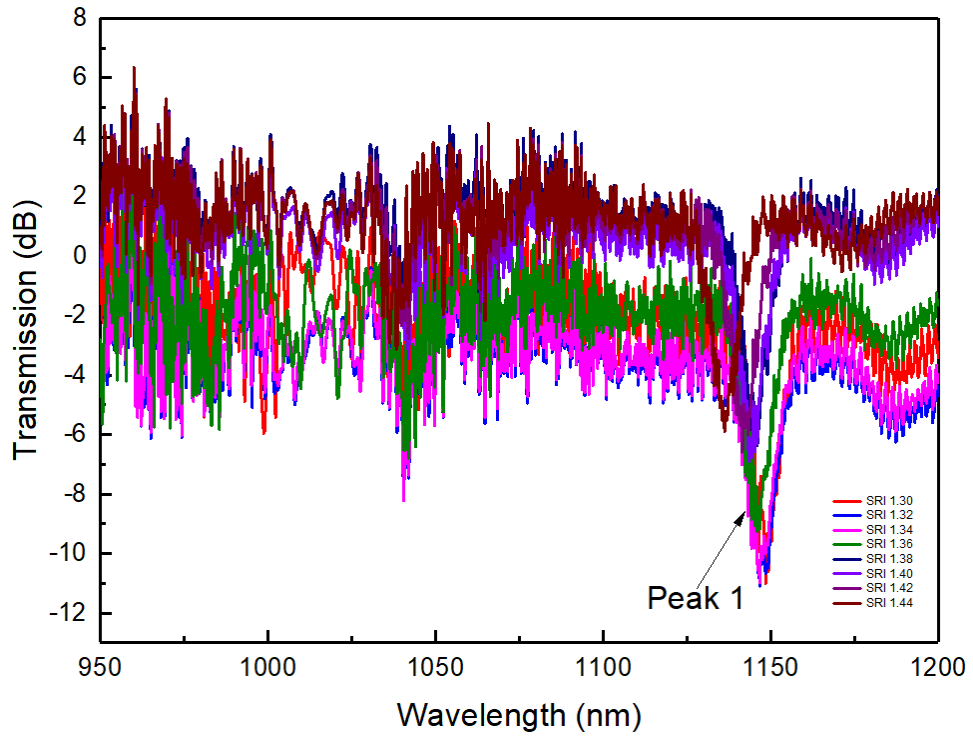
(a)
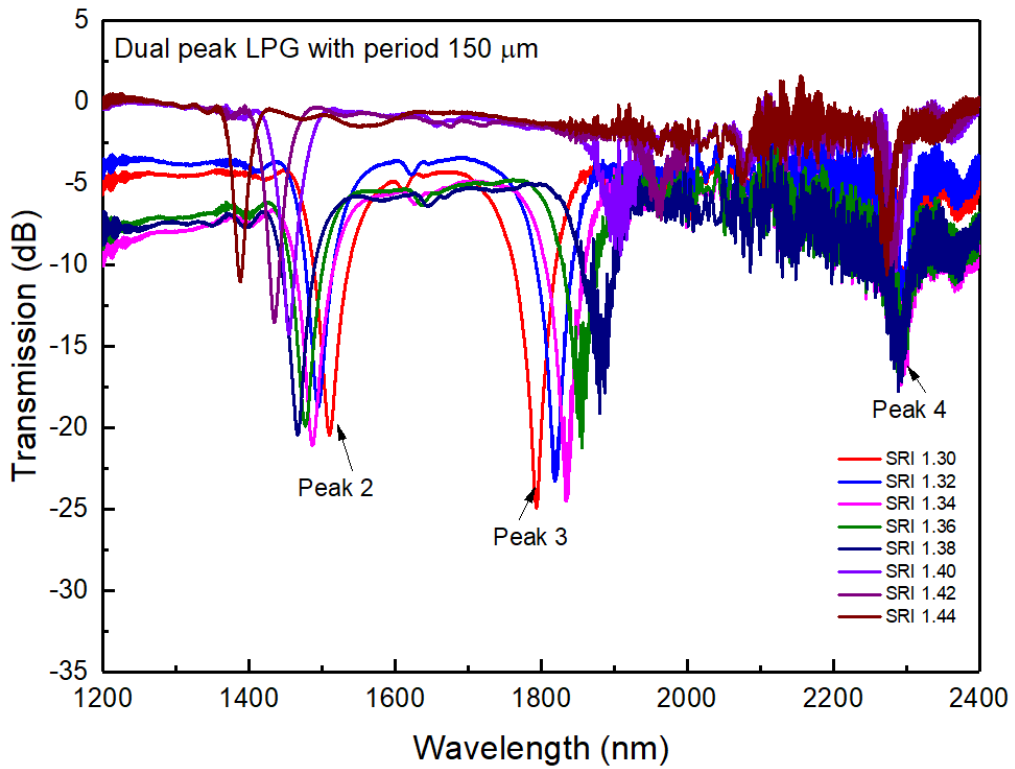
(b)
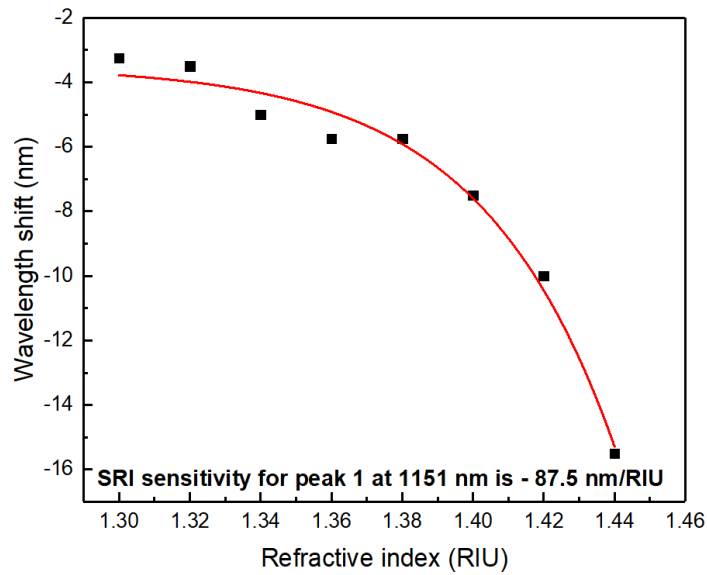
(c)
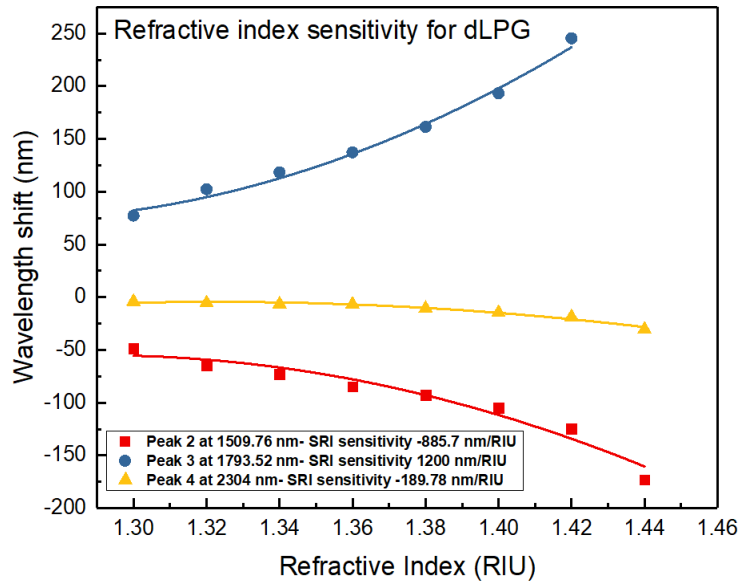
(d)

Figure 3. 23 SRI response in the range of 1.30 to 1.44 for a dual-peak LPG UV-inscribed in thin cladding SM1500 (4.2/80) fibre with 150 μm period: (a) spectral evaluation for normal peak 1 with blue shifted wavelength; (b) spectral evaluation for dual peaks 2&3 with opposite wavelength shift and normal peak 4 with wavelength blue shifted; (c) The SRI sensitivity result for the peak 1 resonance with increased RI values (d) The SRI sensitivity results for the peaks 2-4 resonances with increased RI values.

The spectral evolution of the dLPG when subjected to various SRI gels is shown in Fig. 3.23 (a) and (b). From the figures we can see that the dual-peak resonances are showing opposite movement with increasing SRI – the first dual peak (peak 2) blue shifts while the second (peak 3) red shifts - similar to the temperature response behaviour. The two individual peaks at shortest and longest wavelengths

are blue shifting with the SRI increasing but with smaller speed. Figure 3.23 (c) and (d) plot the SRI sensitivities for the four peaks and the average SRI sensitivities for the four peaks are summarised in Table 3.5. Considering the range of SRI from 1.30 to 1.44, for the first dual peaks (peak 2) is blue shifted and the conjugate peak 3 is red shifted. The overall wavelength shift for all the resonance peaks is as: -15.5 nm for peak 1, -121.44 nm for peak 2, 763.84 nm for peak 3 and -32.36 nm for peak 4 respectively. The SRI sensitivity results show that the dual peaks have much higher SRI sensitivity, as reached -885.7 nm/ RIU for peak 2 and 1200 nm/ RIU for peak 3, respectively for the entire SRI range of 1.30-1.44. A comparatively less sensitivity of -189.78 nm/ RIU is obtained for peak 4. However, a very low sensitivity of -87.5 nm/RIU is obtained for peak 1. Whereas it is noted in the SRI range of 1.30-1.38, there are maximum SRI sensitivity achieved with -550 nm/RIU for peak 2 and almost double of 1050 nm/RIU for conjugated peak 3.

Table 3. 5 Summary of the average SRI sensitivities of the four resonances of UV-inscribed dual peak LPG.

Dual peak LPG resonance wavelengths	Average SRI sensitivity in the range of 1.30-1.44
1151 nm	-87.5 nm/RIU
1589.76 nm	-885.7 nm/RIU
1793.52 nm	1200 nm/RIU
2304 nm	-189.78 nm/RIU

From above results we may draw some important points: (1) the dLPG have resonances closed to or in the mid-infrared wavelength range, as the second resonance (peak 3) of the dual-peak is at 1793.52 nm and the peak 4 is at 2304 nm; (2) due to they are so closed to the dispersion turning point, the dual-peaks are much more sensitive than the normal LPG single peaks, as the temperature and the SRI sensing results show their sensitivities are almost one order of magnitude higher than that of single peaks. Therefore, dLPGs could offer unique sensing function for bio, medical and environmental sensing applications in mid-infrared range.

3.6 Inscription and characterisation of first and second order LPGs

In phase matched condition the co-propagating core and cladding modes generate high diffraction orders into an LPG. Thus, coupling between forward co-propagating core modes with the higher 2nd order cladding modes generate the resonance response near to longer wavelength range closed to mid infrared range that we are investigating in this section. The resonance wavelength (λ_{res}) in phase-matching condition for a higher order diffraction grating can be expressed as,

$$\lambda_{res} = \left(n_{co}^{eff} - n_{cl,m}^{eff}\right) \Lambda/N \qquad\qquad (3.19)$$

Where, Λ is the grating period, N = 1, 2, 3….. is the diffraction order, and n_{co}^{eff} and $n_{cl,m}^{eff}$ are the effective indices of fundamental core mode and the m-th cladding mode respectively [86].

We have demonstrated the fabrication and characterisation of first and second order diffraction resonance peaks in the range from near infrared to mid-infrared. Thereafter, the thermal sensing measurement of this LPG sensing device was investigated.

The 2nd order LPGs were fabricated following the same point-by-point writing technique described in section 2.5.3, and the gratings were UV-inscribed in SMF-28 fibre photosensitised by hydrogen loading treatment. In order to create 2nd order resonances closed to 2 μm region, the period size of 300 μm was chosen.

The transmission spectrum of the UV-inscribed LPG with 300 μm period was examined for the spectral range from 950 nm to 2400 nm using two OSAs, and Fig. 3.24 (a) and (b) show the 1st order resonance of 6 peaks, which across the two figures with the first peak (named as peak 1) on the figure (a) occurring at around 1079 nm and the last peak (peak 6) on the figure (b) at around 1450 nm. From the figure (b) we can clearly see there are three 2nd order resonance peaks, named as peaks 7, 8 and 9, occurring around 2155 nm, 2244 nm and 2332 nm, all in the mid-infrared region. There should also be the 2nd order resonance for peaks 4, 5 and 6 but they are beyond the second OSA measurement range of 2400 nm. In order to stabilise the LPG property, this 300 μm period LPG was annealed at 80 °C for 48 hours, and its spectrum was measured after the annealing and also plotted on the figure (a) and (b). After annealing, the 1st order resonance peaks of 1,2 and 3 red-shifted by 9,12 and 14 nm respectively. Whereas there is comparatively larger wavelength shift for the corresponding 2nd order peaks of 7, 8 and 9 as they red-shifted by approximately 21, 27.7 and 33 nm respectively. The central wavelengths for the 1st and 2nd order peaks before and after the annealing are summarised in Table 3.6 (a) and (b).
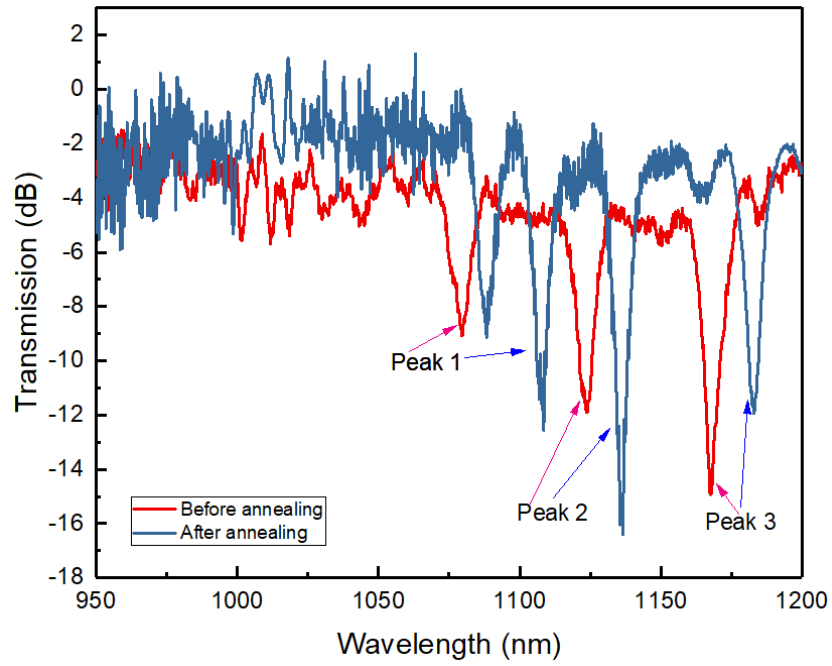
(a)
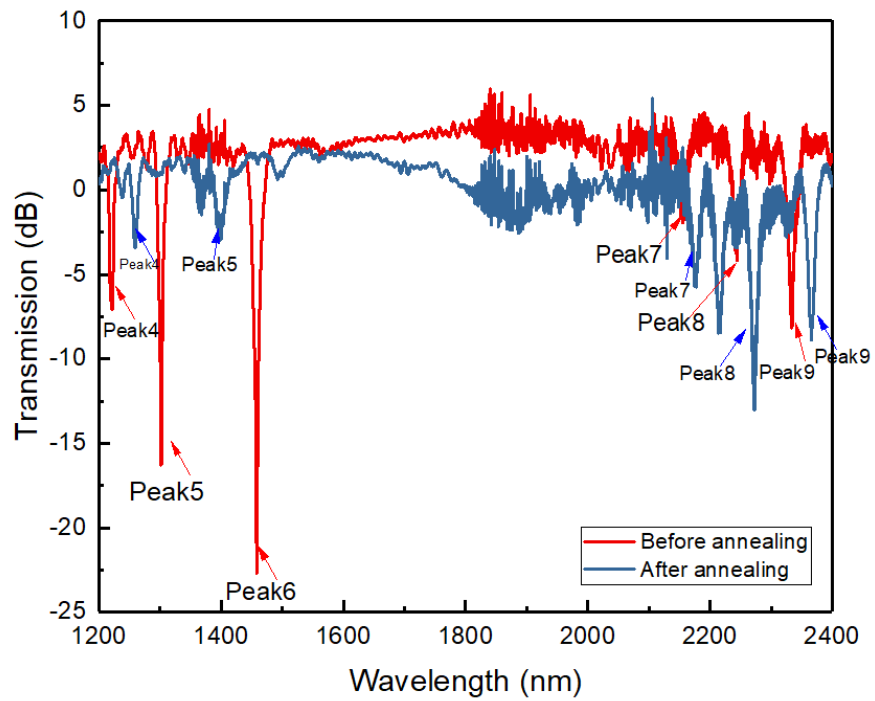
(b)

*Figure 3. 24 The transmission spectra of LPG with a period of 300 μm fabricated into hydrogenated SMF-28; (a) 1st order resonance peaks measured in the range of 950 - 1200 nm; (b) 2nd order resonance peaks measured in the range of 1200 - 2400 nm before and after anne*aling.

Table 3. 6 (a&b) The resonance wavelength for all the attenuation peaks of 1st and 2nd order LPG before and after annealing.

1st and 2nd order LPG with 300 μm period (before annealing)			
1st order resonance peaks		Corresponding 2nd order resonance peaks	
Peak 1	1079.0 nm	Peak 7	2155.7 nm
Peak 2	1124.0 nm	Peak 8	2244.3 nm
Peak 3	1167.7 nm	Peak 9	2332.8 nm

(a)

1st and 2nd order LPG with 300 μm period (after annealing)			
1st order resonance peaks		Corresponding 2nd order resonance peaks	
Peak 1	1087.7 nm	Peak 7	2176.9 nm
Peak 2	1136.7 nm	Peak 8	2272.0 nm
Peak 3	1182.5 nm	Peak 9	2365.4 nm

(b)

3.6.1 Thermal sensing measurements

The multiple resonant peaks generated due to light coupling between fundamental core mode and the cladding modes are intrinsically sensitive to the change in temperature of surrounding environment. Therefore, we demonstrated the thermal responses for three different 1st and 2nd order resonance peaks for the LPG with period of 300 μm. The thermal sensitivity measurement is achieved by placing the LPG device on to a Peltier setup similar to the one shown in Fig. 3.7. A temperature variation was performed from 20 °C – 70 °C with an increment step of 10 °C. The input light to the LPG sensing device was launched by a broadband source (Fianium superK) and the spectra were measured through OSAs at two different wavelength ranges to achieve entire response for both 1st & 2nd order series resonances. Following equation (3.12) the resonance response for higher order cladding modes near the mid-IR range shows larger sensitivity with enhanced core-cladding interaction for larger portion of evanescent wave penetrating into the surrounding. The experimental results for spectral evaluation and wavelength shift are plotted in Fig. 3.25 and are summarised in Table 3.7.

This may be advantages for some applications where high thermal sensitivity is desirable. However, for some sensing applications, thermal cross-talk may be an issue, which needs to be considered to be eliminated.
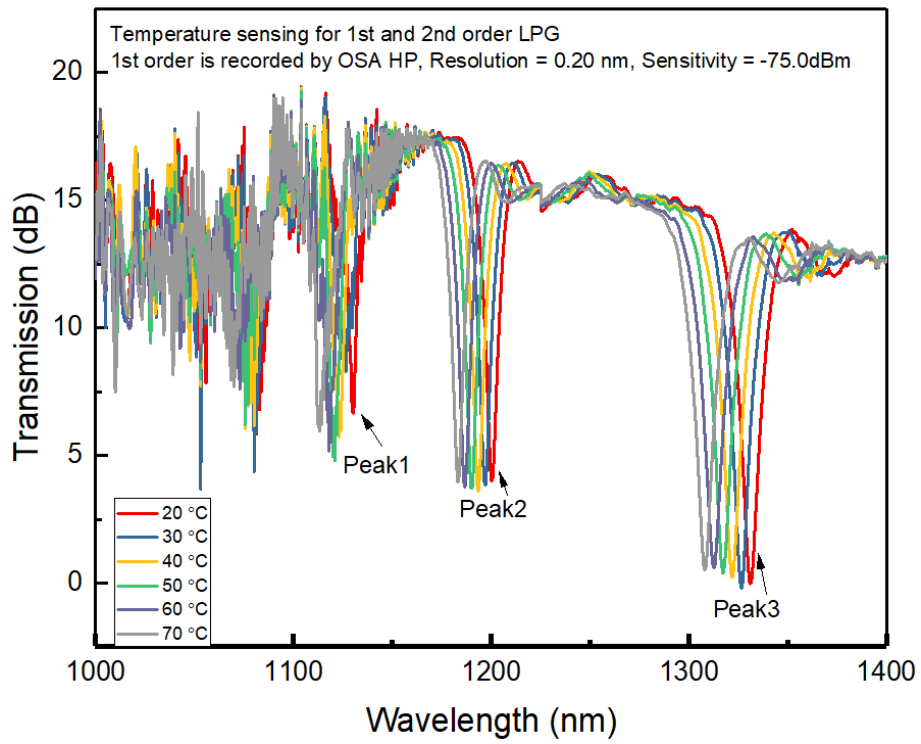
(a)
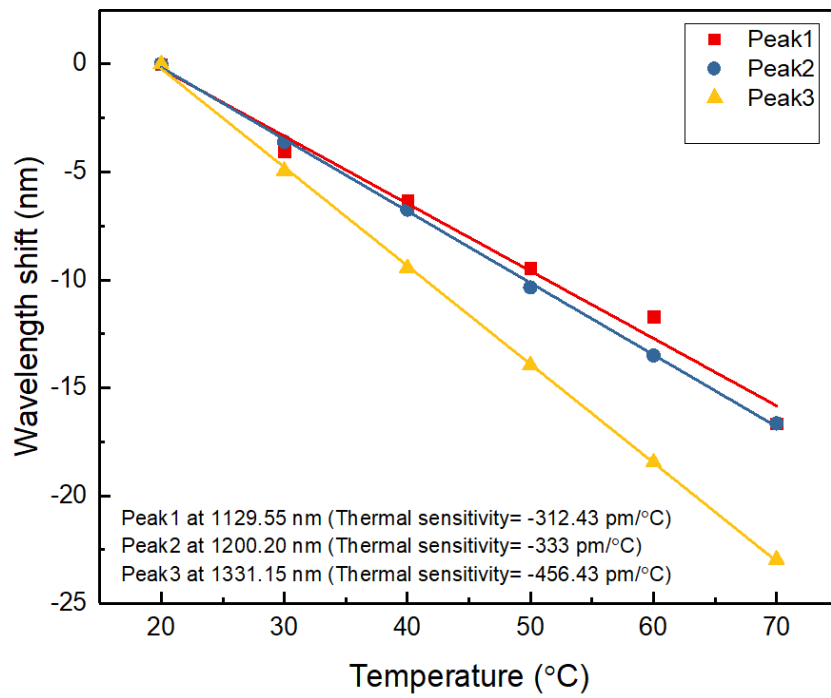
(b)
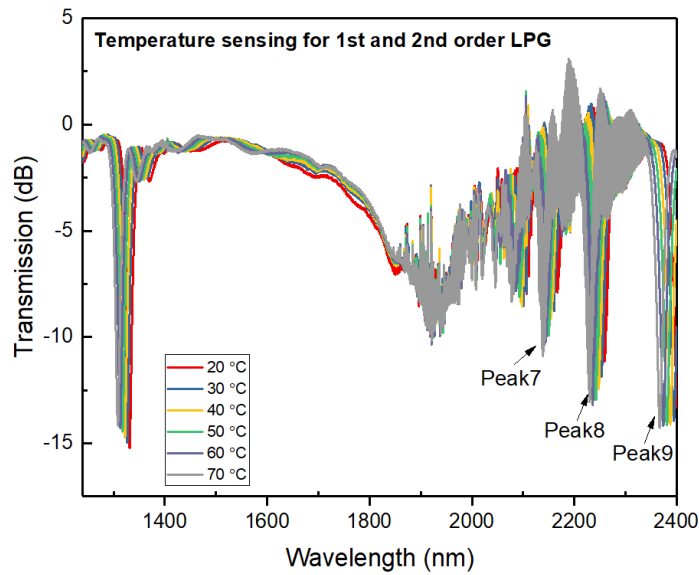
(c)
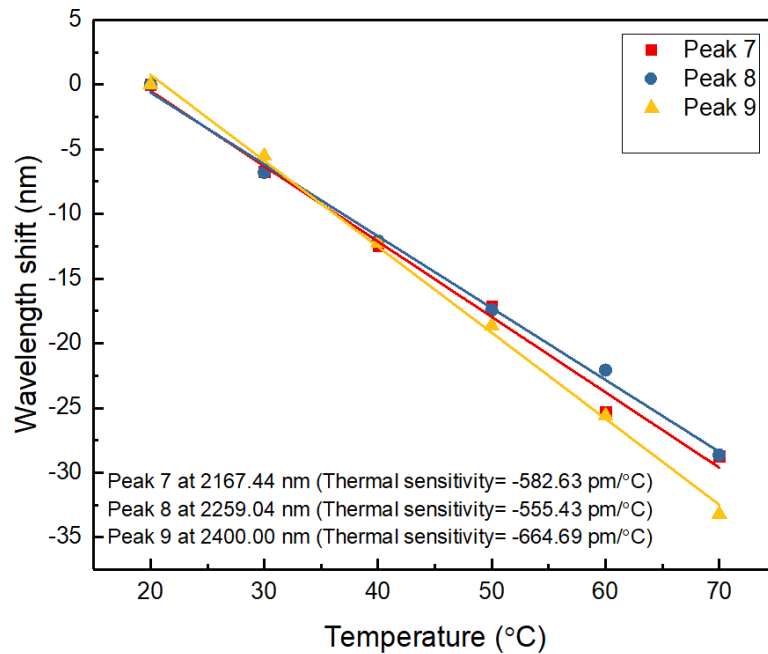
(d)

Figure 3. 25 Temperature response of the 1st and 2nd order resonances for an UV-inscribed LPG into hydrogenated SMF-28 with a period of 300 μm. (a) spectral evaluation of resonance peaks 1,2&3 in the 1st order series in the wavelength range of 1000- 1400 nm; (b) the thermal sensitivity results for 1st order resonance peaks with wavelength blue shifted; (c) spectral evaluation of resonance peaks 7,8&9 in the 2nd order series in the wavelength range of 1200- 2400 nm; (d) the thermal sensitivity results for 2nd order resonance peaks with wavelength blue shifted.

Table 3. 7 (a&b) Thermal sensitivity values for 1st and 2nd order series of LPG with period of 300 μm.

1st order LPG with 300 μm period		
1st order resonance peaks		Temperature sensitivity (pm/°C)
Peak 1	1087.7 nm	-312.43
Peak 2	1136.7 nm	-333.00
Peak 3	1182.5 nm	-456.43

(a)

2nd order LPG with 300 μm period		
2nd order resonance peaks		Temperature sensitivity (pm/°C)
Peak 7	2176.9 nm	-582.63
Peak 8	2272.0 nm	-555.43
Peak 9	2365.4 nm	-664.69

(b)

3.7 Ex-TFG inscription and sensing characteristics

3.7.1 Principle of Ex-TFGs

The fabrication process for large angled tilted grating is explained in this section. The transmission spectrum with polarisation controller setup is shown and a detailed experimental analysis is done with sensing measurement results.

For an optical fibre grating the fundamental core mode is coupled with the forward propagating cladding mode. The sensitivity becomes much higher compared to the coupling with the backward propagating cladding modes [87]. The LPGs and Ex-TFGs are following this principle and hence with very high sensitivity. The LPGs are used as an attenuation filter and environmental detectors [23, 24, 88-91]. Zhou et al., reported that the large angled tilted grating is highly sensitive for surrounding refractive index change whereas for the thermal sensing it has low sensitivity [28, 64]. An Ex-TFG is consisting of asymmetric structures within the fibre core. In phase matched condition the light is coupled with the higher order forward-propagating cladding modes. The dual peak resonance is achieved as the light splits into two sets of polarisation dependent cladding modes.

The phase matching condition of an Ex-TFG is given by the expression:

$$\lambda = \left(n_{co}^{eff}(\lambda) - n_{cl,m}^{i,eff}(\lambda) \right) \frac{\Lambda_G}{\cos\theta} \qquad \qquad i = TE \ or \ TM \qquad \qquad (3.20)$$

The strongest coupling occurs between the core and co-propagating cladding modes.

In equation (3.20) the resonant wavelength λ can be expressed in terms of effective refractive index of the core n_{co}^{eff} and mth order TE/TM cladding mode i.e., $n_{cl,m}^{i,eff}$ at the resonant wavelength. The grating period is given by Λ_G and θ is the tilt angle.

For the axial period the equation can be written as,

$$\lambda = \left(n_{co}^{eff}(\lambda) - n_{cl,m}^{i,eff}(\lambda)\right)\Lambda \qquad\qquad i = TE \ or \ TM \qquad\qquad (3.21)$$

3.7.2 Inscription and characterisation of Ex-TFGs

3.7.2.1 Inscription of Ex-TFGs

As previously discussed, in a TFG with tilted angle greater than 67° (for an air/glass interface) are regarded as excessively tilted TFG, thus named as Ex-TFG. An Ex-TFG exhibits similar properties as a conventional LPG, except the period is much small (~only tens micrometer), and it couples the light to the forward propagating higher order cladding modes. The fabrication technique for Ex-TFGs requires a different arrangement with an amplitude mask (AM). A custom designed AM with a period of 6.6 µm purchased from Edmund Optics was used for the inscription. Both SMF-28 and B-Ge photosensitive fibre were used, and they were hydrogenated to make them highly photosensitive. Figure 3.26 shows the schematic of UV inscription of Ex-TFG using the zeroth order diffraction of UV beam which is generated by the amplitude mask.
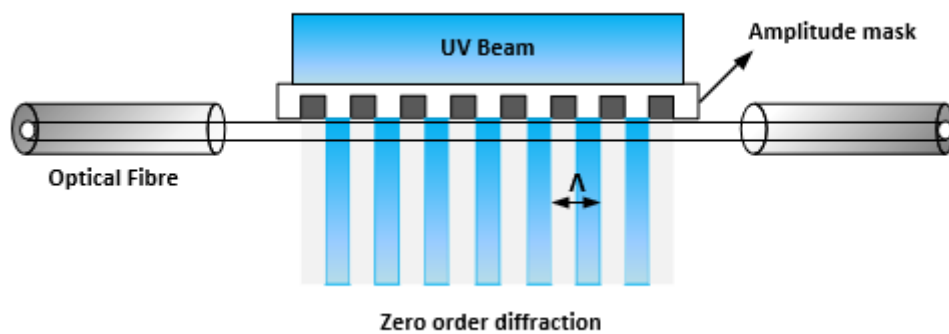
Figure 3. 26 Schematic of the amplitude mask and fibre with zero order UV diffraction beam into fibre core.

An optical fibre with the cylindrical structure has a lens effect. Therefore, the internal angle in the fibre core is different from the external tilt angle of amplitude mask. To achieve an Ex-TFG with a tilt angle of 81°, the external tilt angle needs to be set at 76°. The UV exposure directly passes through

the amplitude mask and with the zero order diffraction the Ex-TFG will be written into fibre core. Post fabrication results achieved with 28.3 μm axial grating period inside the fibre for a normal grating period set as 4.41 μm [64, 92].

The spectral property of UV-inscribed 81°-TFG was examined using the measurement setup shown in Fig. 3.27. The light from a super-continuum source (950-2400 nm) was launched into one end of Ex-TFG and the attenuation resonances were measured with an OSA (YOKOGAWA). Because the Ex-TFG has broken the total symmetric profile of the refractive index distribution in the fibre core, some birefringence effect has been introduced in the mode coupling generating two sets of modes with orthogonal polarisation status. Therefore, in the measurement setup, a combination of a linear polariser and a polarisation controller were set in between the broadband source and Ex-TFG to see the split modes. The transmission spectra are represented in Fig. 3.28.

Figure 3. 27 Experimental setup for measuring transmission spectra of Ex-TFG.

The spectral characteristics of the 81°-TFG was evaluated, and it was noted that some birefringence effect was introduced due to the asymmetric structure of Ex-TFG, and the coupled cladding modes are created into two sets of orthogonal polarisation states as shown in Fig. 3.28 (a) and (b). Particularly, when the probe light is at random polarisation, the coupled light is almost equally distributed into the two sets of different polarisation states, as we see the amplitude of the two sets of resonances shown in Fig. 3.28 (a) is about 3 dB. However, when the probe light is fully polarised, individual polarised set of modes will be excited to the maximum amplitude. This can be seen in zoomed spectral profile for one pair of polarised modes showing in Fig. 3.28 (b), where the corresponding peak resonance for transverse magnetic (TM) mode and transverse electric (TE) modes are labelled as P1 and P2 respectively in Fig. 3.28 (b): it shows the amplitude can reach 6 dB for TM polarised mode and 8 dB for TE polarised mode respectively.

Ex-TFG with a tilt angle of 81°
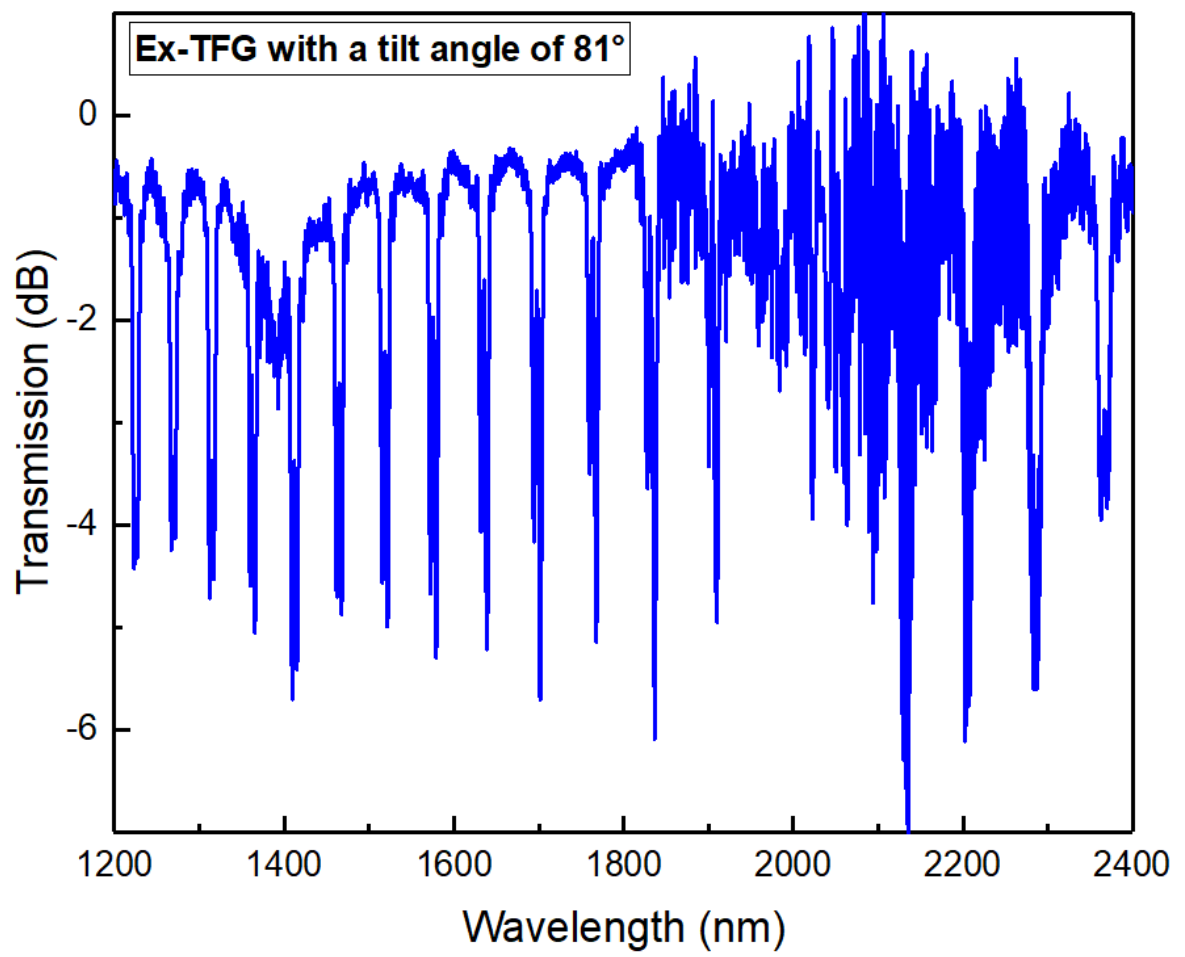
(a)
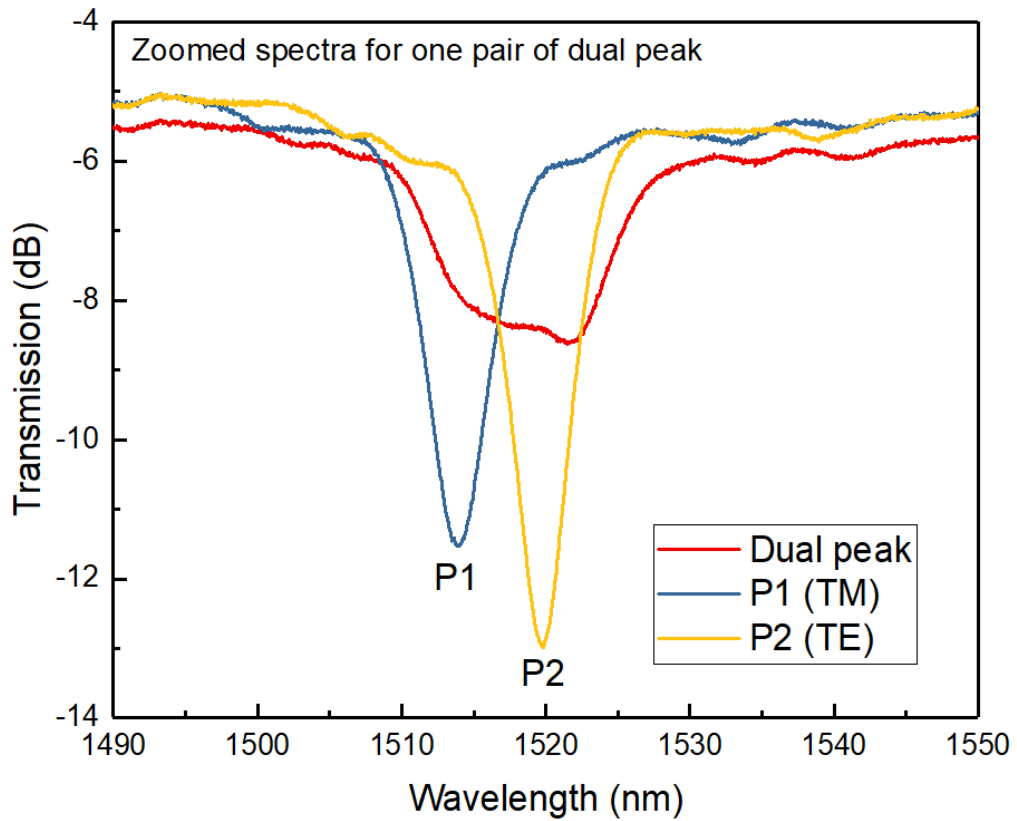
(b)

Figure 3. 28 The transmission spectra for 81°-TFG: (a) with a series of ~3 dB paired resonances from 1200 - 2400 nm when launched with random polarised light; (b) zoomed transmission spectra for one pair of dual peaks measured using light with two orthogonal polarisations.

3.7.2.2 Temperature sensitivity characteristics of Ex-TFGs

The thermal response of the 81°-TFG was investigated using the setup shown in Fig. 3.29. In the measurement, the grating was placed on the heat transfer plate and the temperature was varying in the range of 20 °C - 70 °C with 10 °C increment. The polariser and the polarisation controller were adjusted to ensure exciting either TM or TE modes under the investigation.
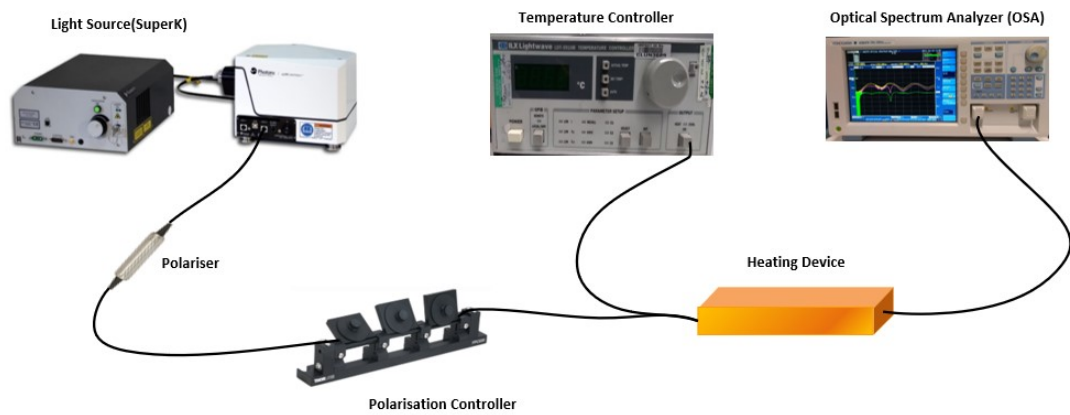
Figure 3. 29 Experimental setup for thermal sensing measurement performed for 81°-TFG.

In this experiment we consider three pairs of peaks for the 81°-TFG spread in three different wavelength ranges to examine if the temperature sensitivity is not just polarisation but also wavelength dependent. The measured results are shown in Fig. 3.30 and summarised in Table 3.8. From the results of the thermal response evaluation, we can see the temperature sensitivities of the Ex-TFG are much lower than that of LPGs, and even lower than that of FBGs. Typically, the temperature sensitivity of an FBG in a similar wavelength range is about 10 pm-12 pm/°C, here for the 81°-TFG, all three TM modes show the temperature sensitivities of -0.4, 7.77 and 8.57 pm/°C, and the TE mode at 1329.4 nm shows a sensitivity of 2.17 pm/°C; all lower than 10 pm/°C. From the results we can see the temperature sensitivity of an Ex-TFG is polarisation dependent as TE modes have higher value than TM modes. It is also wavelength dependent, as increasing with the wavelength. The reason for achieving low temperature sensitivity achieved can be explained following the theoretical proof as discussed by Zhijun Yan et al. [92]. Their simulated results showed that, there is the decreased thermal sensitivity for higher order cladding modes at 31st and more for relative resonance wavelength for TE and TM modes before the switchover point reached for an 81° Ex-TFG. This provides Ex-TFGs with some advantage for eliminating temperature cross-sensitivity in special applications.
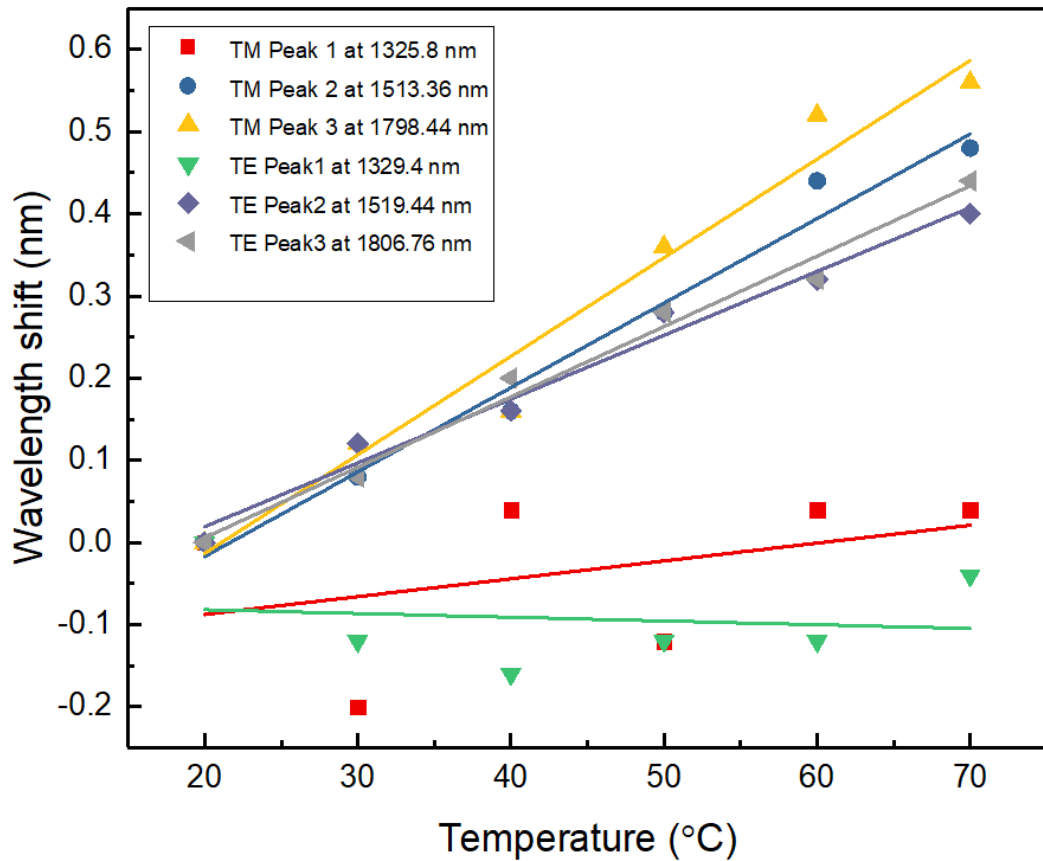
Figure 3. 30 The wavelength shifts of 81°-TFG at different temperatures for three pairs of TM and TE modes at different wavelength ranges.

Table 3. 8 Summary of thermal sensitivity of 81°-TFG for TM and TE modes.

Ex-TFG (81°)	TM peaks at	Temperature sensitivity (pm/ °C)	TE peaks at	Temperature sensitivity (pm/ °C)
	1325.8 nm	2.17	1329.4 nm	-0.4
	1513.36 nm	10.29	1519.44 nm	7.77
	1798.44 nm	12	1806.76 nm	8.57

3.7.2.3 Surrounding medium refractive index sensing of Ex-TFGs

Ex-TFGs may be explored as in-fibre sensors for biochemical, biomedical and environment sensing applications, it is important to evaluate the SRI response of the Ex-TFG. For this purpose, the UV inscribed 81°-TFG was subjected for SRI sensing characterisation.

The SRI sensing capability of Ex-TFG was evaluated using the experimental setup shown in Fig. 3.31. The 81°-TFG fibre sensing device was placed onto a glass slide and firmly clamped between two translational stages placed at same heights to avoid wavelength shift by bending and strain. A

series of refractive index gels (from Cargille) ranging from 1.305 to 1.385 were applied to the grating in turn. As Ex-TFG couples light to higher order cladding modes that have lower effective mode index value, when applying index gel > 1.39, all resonances disappear as they evolve to radiation modes. After the grating submerged into the immersion gel, the spectra were recorded onto the OSA. After each SRI measurement the glass slide was constantly replaced by a new one and the grating surface was rinsed with methanol and deionised water to restore it to previous position.
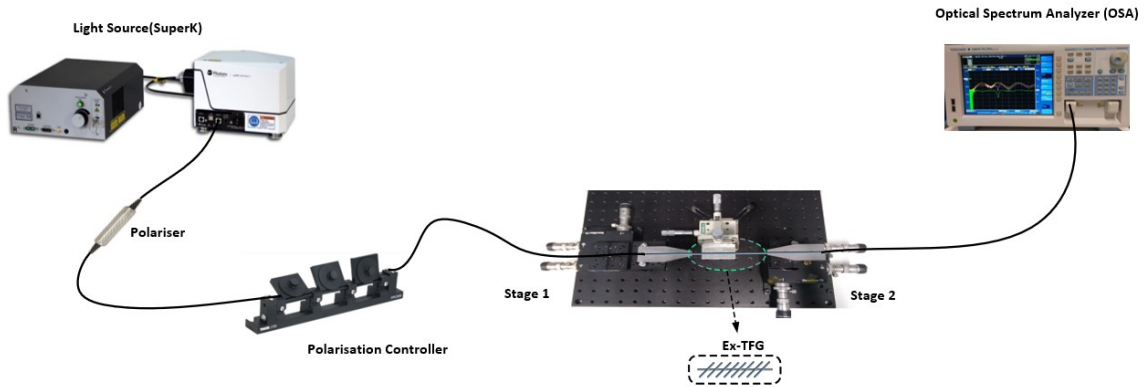
Figure 3. 31 Experimental setup for refractive index sensing for Ex-TFGs.

Three pairs of peaks with TE and TM modes in three different wavelength ranges were considered for SRI sensing measurement. The experiment was performed to compare the sensitivities in three different wavelength ranges starting from near IR and continuing towards to mid-IR. The measured results are plotted in Fig. 3.32 (a,b,c) and summarised in Table 3.9. The refractive index sensitivity response of the 81°-TFG is comparatively higher than normal LPG. The SRI response for three consecutive TM modes is evaluated as 142, 245 and 210 nm/RIU and for corresponding three TE modes are as 113.5, 222 and 215 nm/RIU in the RI range of 1.305 to 1.385. It is clearly visible that polarisation sensitive TM modes have slightly higher SRI response than for the TE modes, and the SRI sensitivity increases with wavelength, although small drop for the modes at 1789 nm. It is more important to know the SRI sensitivity of the Ex-TFG is much higher than that of the normal LPG in 1.305-1.383 SRI range. From previous Fig. 3.17 (b) we see the average SRI sensitivity for LPG with period of 400 μm is about 21 nm/RIU for resonance for LP05 mode at 1340 nm and 140 nm/RIU for LP06 mode at 1518 nm respectively. Both the modes show SRI sensitivity with blue shifted wavelength in the SRI range of 1.32 - 1.44, but here Ex-TFG has achieved SRI sensitivity of around 220 nm/RIU, which is two times higher than LPG. Thus, the Ex-TFGs could be better devices for

biomedical or biochemical sensing applications where the solutions have base index value around 1.305 - 1.385 range.

(a)

(b)

(c)
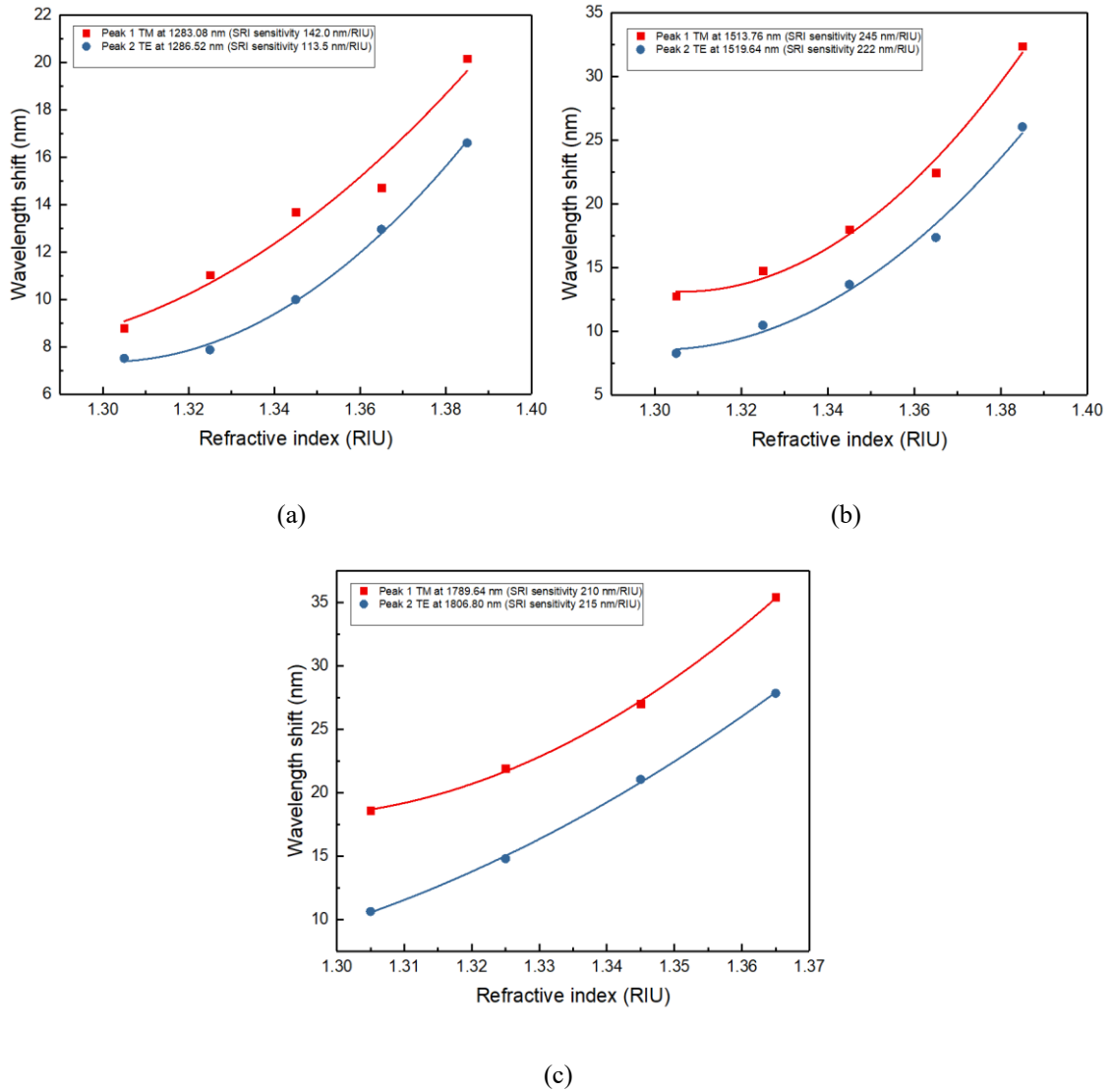
Figure 3. 32 The refractive index sensing for 81°Ex-TFGs with a series of TE and TM modes for the resonance peaks around 1283.08 nm (a), 1513.76 nm (b) and 1789.64 nm (c).

Table 3. 9 SRI sensitivity results for 81° Ex-TFG with three pairs of TM and TE modes.

Ex-TFG (81°)	TM peaks at	Refractive index sensitivity (nm/RIU)	TE peaks at	Refractive index sensitivity (nm/ RIU)
	1283.08 nm	142	1286.52 nm	113.5
	1513.76 nm	245	1519.64 nm	222
	1789.64 nm	210	1806.8 nm	215

3.8 Chapter conclusion

At the beginning of this chapter, we explained optical fibre fabrication techniques that have been used for grating inscription from near-IR to mid-IR range. The FBGs have been inscribed using phase mask scanning technique. This method facilitates a simple optical system through which a stable FBG writing is possible. LPGs with period length of 10 μm to 600 μm were fabricated by point-by-point writing technique. The tilted gratings were fabricated by optimising the designed tilt angles with the rotation adjustment of phase and amplitude mask mounted on goniometer setup. The FBGs, LPGs and TFGs are showing excellent sensing applications as temperature sensor, strain sensor and SRI sensor. All fibre gratings in the near IR range are fabricated into normal SMF-28. The thermal sensing measurement for both FBG and STFG shows similar response with average sensitivity of 10 pm/°C in the temperature range of ~ (10 - 70 °C). A strain sensing performance for FBG has obtained with sensitivity as 0.8 pm/με. Then, different types of LPGs, such as normal and 1st & 2nd orders were fabricated into standard and hydrogenated SMF-28. The dual-peak LPGs with periods of 150 μm have been fabricated into 80 μm thin cladding fibre. The temperature and SRI response for normal LPGs and dLPGs show very high sensitivity from near-IR to mid-IR range. A highest SRI sensitivity for dual LPG with conjugate resonance peaks is achieved as ~-885.7 nm/ RIU and ~1200 nm/ RIU respectively. However, 1st and 2nd order LPGs with higher thermal sensitivity for more than ~500 pm/°C is achieved for the 2nd order resonances in the mid-infrared range. Finally, a comparatively lower thermal sensitivity is obtained for UV-inscribed Ex-TFGs into hydrogenated B-Ge photosensitive fibre and much higher SRI sensitivity for orthogonally polarised cladding modes provides a sensitivity value more than 200 nm/RIU.

Chapter 4

Fibre Bragg gratings (FBGs) inscription into multicore fibre and sensing measurements

4.1 Introduction:

Fibre Bragg gratings (FBGs) fabricated into single mode-single core fibres have been used for sensing of different parameters such as temperature, strain, bending and twist. The superior flexibility of these devices makes them applicable as sensors that can be utilised in structural health monitoring and for medical devices [93-96]. These FBG based optical sensors are advantageous due to their high thermal stability, chemical inertness and immune to electromagnetic interference. The only limitation of the single mode-single core based FBG sensor is in single parameter sensing at a time. However, this limitation could be overcome with the sensor fabrication into single mode and multimode – multicore fibre (SM&MM-MCF) suitable for multi parameter sensing measurements.

The reported development of multicore fibre (MCF) is a recent advancement of fibre optical technology driven by huge demand for transmission capacity of a single fibre and long-haul communication with dense space-division multiplexing (DSDM) [97-100]. It has large data transmission capability compared to a single mode fibre-based system that is limited by data transmission of 100 Tb/s bit rates [101]. In addition, key applications utilising MCF such as fibre laser [102, 103] and fibre optical sensors [7, 8], were immediately followed. For these applications, existing device such as fibre gratings and optical couplers may be useable but require multiple splitting and combining between single core and either multiple single core fibres or a complex coupling between multiple fibres. New version of these devices in MCFs will make the system more elegant. Furthermore, FBGs fabricated into the MCFs can broaden their capabilities in regard to multi-parameter sensing of twist, bending, loading and temperature.

The sensing device with FBGs inscribed into the MCF has shown some applications into astronomical imaging system for developing a photonic lantern [104]. The present research is focused mainly on fabrication and application of sensor devices with the SM- MCF. The previous studies are reported on applying such sensor devices with four cores fibre (4CF) for bending and transverse load sensing [105] and seven cores fibre (7CF) as temperature, strain and fibre twist sensor [106] respectively.

There are different FBG writing techniques into MCF. These are namely (a) phase mask (PM) scanning method, (b) point-by-point writing method by femtosecond laser and (c) small spot direct ultraviolet writing (SSDUW).

Flockchart et al., reported that FBGs can be written into three cores of a hydrogenated 4CF using PM scanning method. Here, they faced the challenge for adjustment of different core locations to obtain uniform grating spectra [95]. Whereas a femtosecond point-by-point writing technique is more suitable for writing into selective cores of an MCF. In this case it is possible for writing into non-hydrogenated MCF by focusing individual cores at different FBG centre wavelength [107]. Recently

Senta L. Jantzen et al., have experimentally demonstrated a cost effective SSDUW technique, by focusing the UV irradiation through a small PM. The spot size is comparable with the core dimension, and it became cost-effective [108].

We have developed a novel research technique and measurement method to inscribe FBGs into MCF at AiPT research labs. It enables not only FBG inscription into all the cores simultaneously but also selective core inscription at different centre wavelength using phase mask scanning technique. The measurement method also shows uniqueness and preciseness without the requirement of expensive equipment. We also investigated the vector sensing applications using the MCF-FBGs. Such unique MCF-FBG sensors have potential to be used for structural health monitoring, biomedical sciences, and robotic technologies.

4.2 Core marking method and selective inscription for MCF

The MCFs with four cores for two different core spacings of 50 μm and 36 μm and seven cores (SM-7C1500) of spacing 35 μm were bought from Fibercore. These are Germanium and Boron co-doped photosensitive fibres. The cores are equally spaced apart and the core and cladding diameters of 6.1 μm and 125 μm respectively. The images of the optical fibre cross section are taken with an optical microscope (ZEISS Axioscope), as shown in Fig. 4.2 (a, b, c). In order to modulate the core refractive index to generate FBG structure, UV photosensitivity of the MCF was enhanced by hydrogen loading technique, with which the fibres were kept in a hydrogen loader under a constant pressure of 150 bar and at a temperature of 80 °C for 48 hours.

Prior to the FBG writing into MCF, the core position needs to be marked for selective inscription. The cores are distributed into a square lattice in the 4CF and into a hexagonal lattice structure with a central core for a 7CF as shown in Fig. 4.2 (a, b, c). The main challenge is controlling the core position for laser focus adjustment for FBG writing into selected cores. As reviewed, the previously reported results for FBG sensors into MCF with PM method were performed by exposing all cores with UV radiation [106]. This is first time in Aston research lab, following a novel method the cores are firstly marked at different positions and FBG inscription is performed selectively. It should be noted, there are other considerations such as the cores of MCF are not always axially parallel and there might be twist and helical distribution at a certain length, introduction of FBG inhomogeneity with random positions of fibre cores affect the FBG spectra and sensor performance.

The experimental setup in Fig. 4.1 (d) shows the core marking method in order to achieve an organised distribution of multiple cores within the fibre.
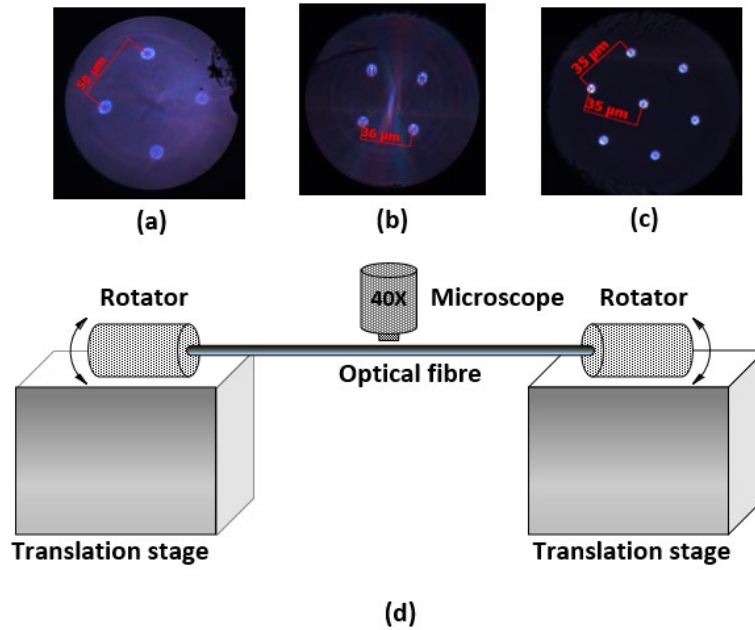
Figure 4. 1 The cross-section image of the 4CF with core to core spacing of 50 μm (a) and 36 μm (b) respectively, and 7CF with core to core spacing of 35 μm (c). The MCF is taken under a 40x microscope objective to set-up for marking the core positions (d).

Here, the MCF is clamped with two fibre rotators, positioned between two 3D stages with a 20 cm separation between them. A microscope objective with a magnification of 40x is used for observation of the core position with a sideview as depicted in Fig. 4.2 (a, b).
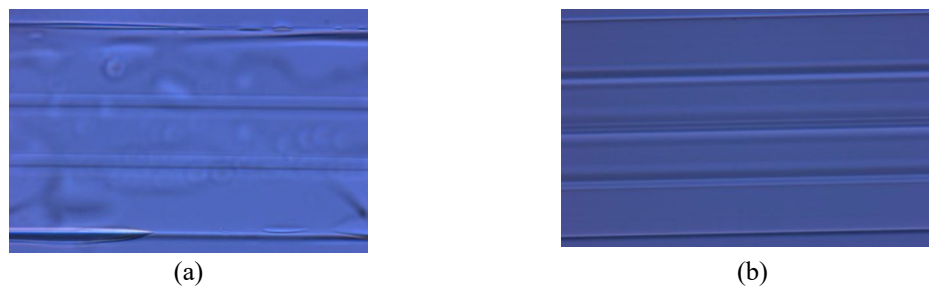
Figure 4. 2 Side view for the MCF with 4-cores (a) and 7-cores (b).

The rotators can be adjusted according to the requirement of the core alignment within the fibre. Once the position and orientation of the core are aligned, the fibre is fixed to a firm position for the inscription with UV irradiation.

The fibre grating is written using phase mask scanning technique where a commercial phase mask consisting of several periods as shown in Fig. 4.3 (a) is placed in front of the aligned MCF. The

exposure of the focused UV laser can be adjusted by the power of the laser and the scanning speed, which can be controlled by a software programme together with the scanning length. The fabrication technique used for writing FBG into MCF comprises phase mask method by focusing an Argon ion laser beam (Coherent Innova 300) into the fibre core using a cylindrical lens system as indicated in Fig. 4.3 (b).

The irradiation through UV laser is focused by the cylindrical lens and PM. The adjustment for both the laser beam size and focused position of the fibre can be done by changing the relative height of the fibre and defocusing distance. The conventional FBG inscription system comprises of focused laser beam size of 22 μm measured with a beam profiler (Thorlabs Beam 4.0) when the fibre is set at 87 mm distance from lens as seen in the 2D & 3D images in 4.4 (a & b). However, the focused spot size could be modified with further adjustment of distance between lens and fibre to 94 mm. In this case, the beam size becomes 96 μm with broader spot size as shown in both 2D & 3D images of 4.4 (c & d). It is possible to inscribe all the cores with this defocusing condition for lens and MCF. The defocusing distance (Δf) between the cylindrical lens and the phase mask is adjusted depending on the requirement of which cores need to be written. In the fabrication system the focal length (D + Δf) = 94 mm is maintained for writing into all the cores simultaneously. The MCF with selected cores are UV-inscribed for writing FBG at different centre wavelengths. The FBG inscription into MCF was performed with a laser power output of 100 mW and a scanning velocity of 0.05 mm/s for a length of 15 mm.

(a)

(b)
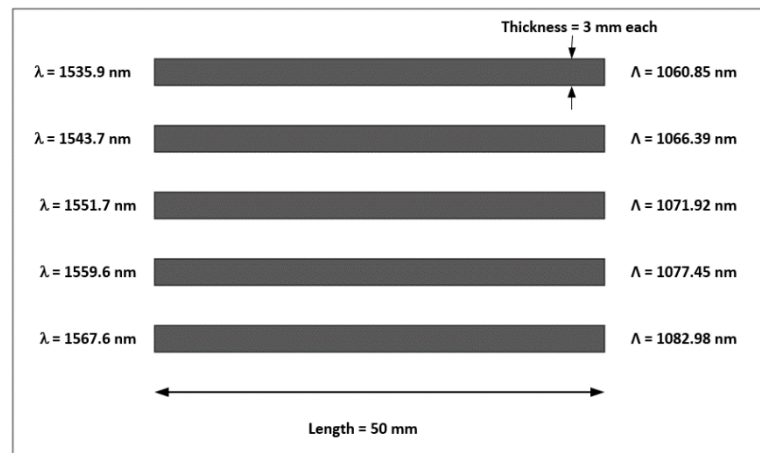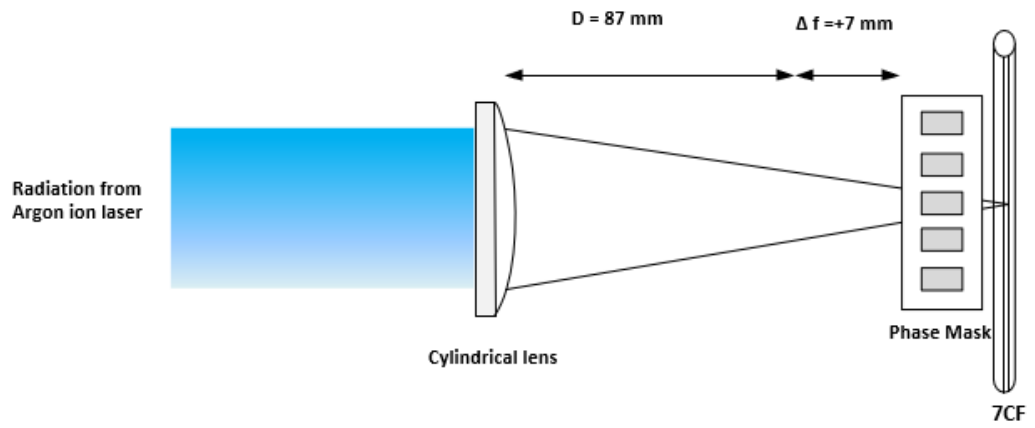
Figure 4. 3 (a) The schematic of the multiwavelength PM used for FBG inscription in MCF; (b) UV inscription scheme for FBG fabrication in MCF.

(a)

(b)

(c)

(d)
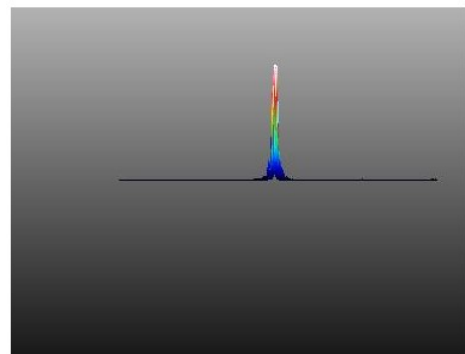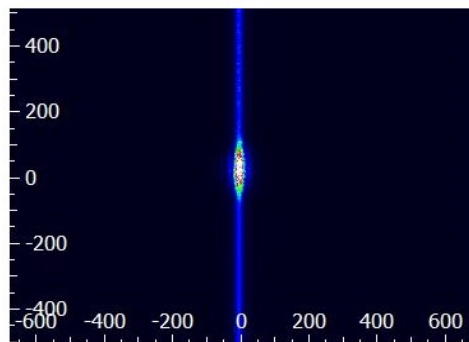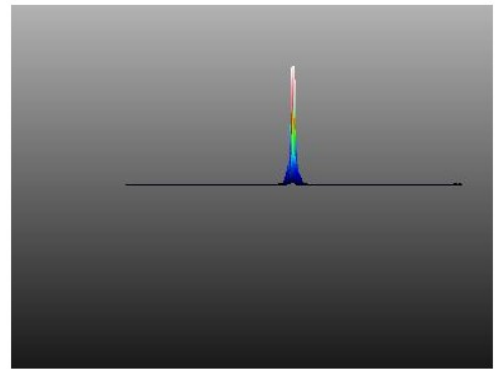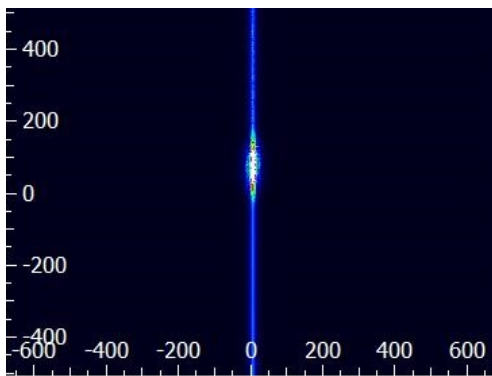
Figure 4. 4 The 2D and 3D images taken at different defocusing length between lens and the fibre with laser beam size of (a & b) 22 μm at 87 mm distance and (c & d) 96 μm at 94 mm distance.

4.3 Spectral characterisation and the experimental setup

As depicted in Fig 4.5, the spectrum of individual FBG in MCF was measured by butt coupling light from a single mode fibre to each individual core facilitated by X-Y adjustments of a splicer. The coupling ratio can be monitored with light from a low power He-Ne laser source (OZ Optics Limited). The opposite end of MCF is focused by a digital microscope (AMCap 10x-100x) to see the fibre cross section on a PC. Light coupling to a particular core can be monitored with its corresponding illumination seen on the PC screen. Figure 4.6 shows the four X-Y adjustments for light coupling through each core of a 4CF.
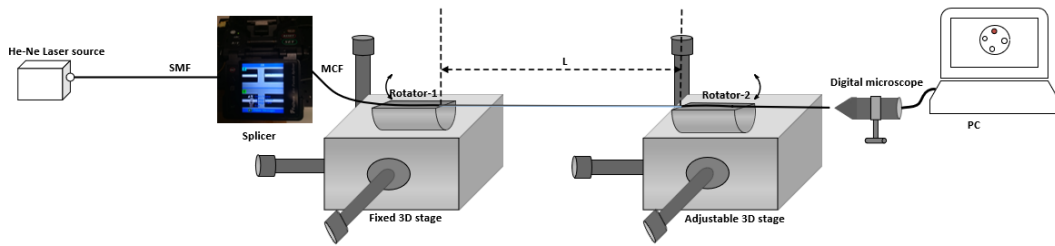
Figure 4. 5 Schematic of the experimental setup for core position adjustment for light coupling.
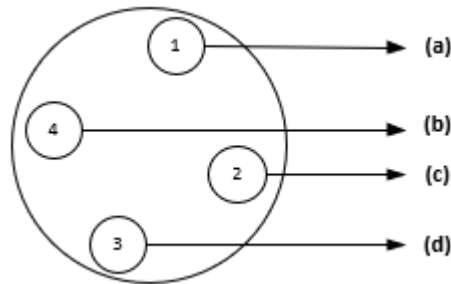
(i)
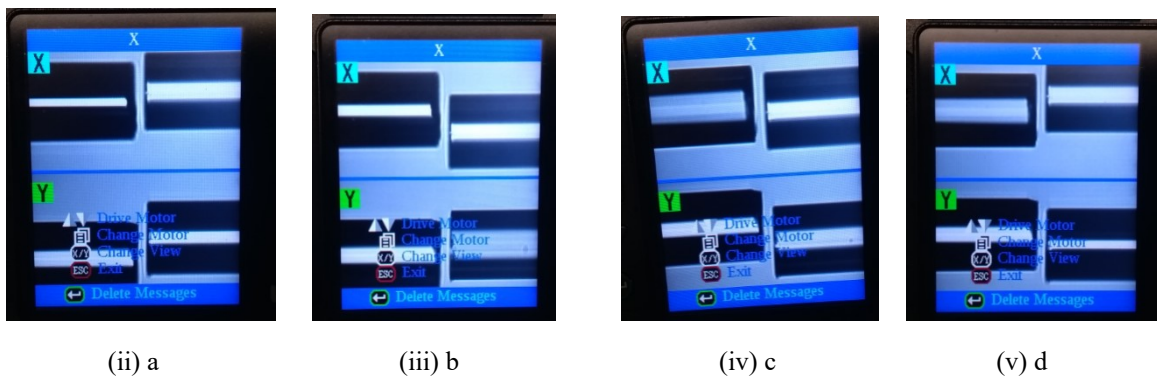
(ii) a	(iii) b	(iv) c	(v) d

Figure 4. 6 (i) Core position labelling for 4CF using optical microscope setup; (ii-v) Light coupling from SMF to MCF through a fusion splicer for each core positions of 1, 4, 2 & 3 at a, b, c & d respectively.

Once the coupling ratio for the selected core of the MCF is satisfactory which means a maximum of 100% light illumination can be seen on the PC screen with the input light launched from a He-Ne laser. The spectrum for the FBG inscribed into this particular core can be measured following the setup shown in Fig. 4.7; it replaces the He-Ne laser and microscope in Fig. 4.5 with a BBS and an OSA (YOKOGAWA AQ6375) with a resolution of 0.05 nm, respectively. The reflection or transmission spectrum was recorded following the light coupling into selected core.
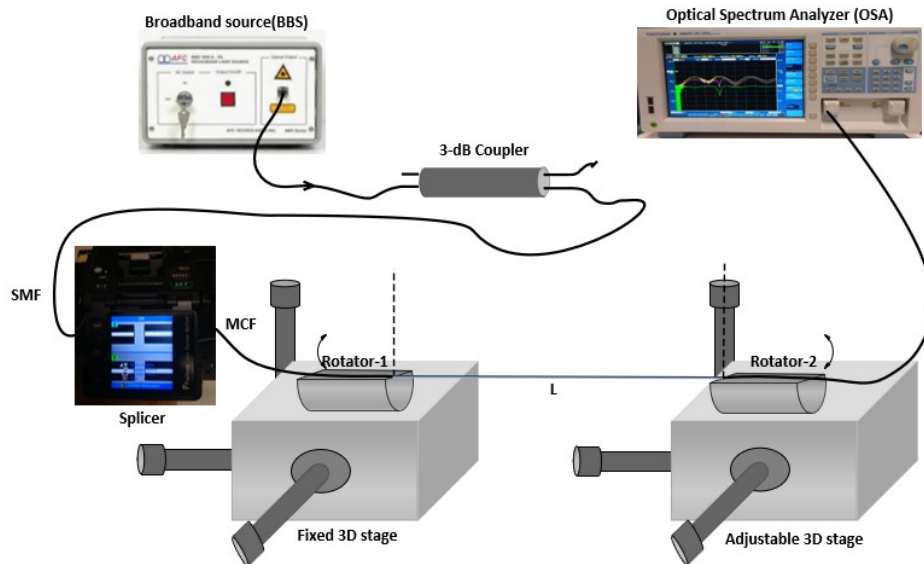
Figure 4. 7 Schematic diagram of the measurement setup for MCF – FBG for spectral characterisation and vector bending sensing.

4.3.1 FBGs in 4CF with core to core spacing of 50 μm

As seen in the optical microscope images in Fig. 4.1 (a, b) there are 4CFs with two different core spacings of 50 μm and 36 μm respectively. The perpendicular view for four core positions was identified using the microscope setup shown in Fig. 4.1 (d) and labelled as (a, b, c) in Fig. 4.8 (a), where there is one core for each top and bottom plane and two cores in the same plane at the centre. However, by adjusting the fibre height the diffraction of focused laser beam for the top core is seen in Fig. 4.8 (b). Though there is a possibility of getting other weak resonances due to cross exposure by the laser irradiation caused into adjacent cores, a precise adjustment with a microscope setup (with 100x objective) provides a more perfect alignment accuracy.
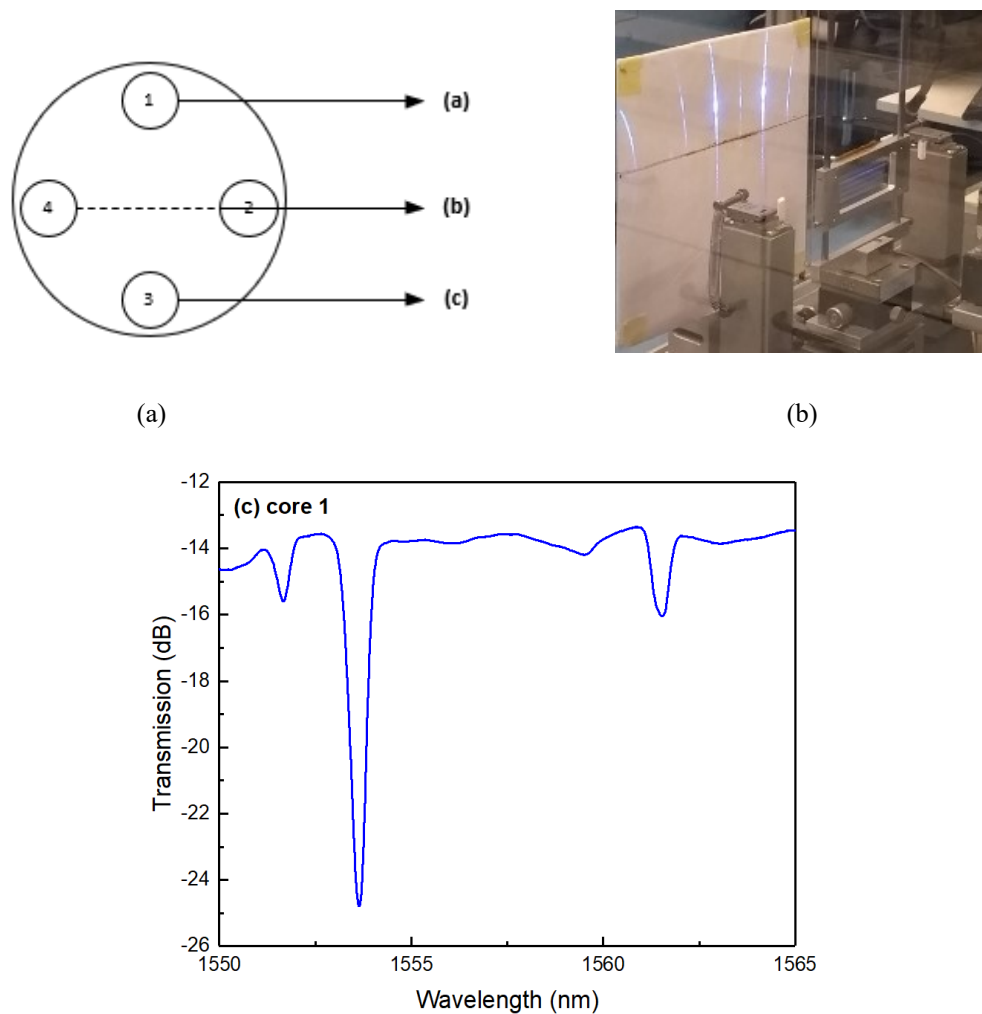
Figure 4. 8 Core marking for different core positions into 4CF: (a) cores are aligned into three planes (a, b, c); (b) diffraction of focused laser beam at top core; (c) Transmission spectrum for FBG inscription into the top core.

The transmission spectrum for UV-inscribed FBG into the top core (core 1) was measured with a BBS and an OSA following the illustrated setup as depicted in Fig. 4.5. As shown in Fig. 4.8 (c), a Bragg resonance peak of maximum transmitting loss of 11 dB is obtained for the core at position (a) with FBG period of 1071.92 nm. The two side resonances of approximately 2 dB and 3 dB are obtained due to the possibility of weak exposure through UV radiation while adjusting the vertical alignment of core for selective inscription. Another reason may occur during measurement process through cross-talk where light couples from one core to another.

To further explore the sensor fabrication capability into different cores of 4CF, the fibre cores were marked into another configuration where each core positioned in four different individual plane in a, b, c, and d as presented in Fig. 4.9 (a). In this second experiment, the laser beam was aligned at a defocusing distance for FBG inscription into the top two cores 1&4, where these are situated diagonally in the planes a & b respectively. The transmission response was characterised for the FBG

written at centre wavelength of 1551.7 nm. It is clearly evident in the diffraction pattern in Fig. 4.9 (b), that both the cores were well aligned for UV inscription.
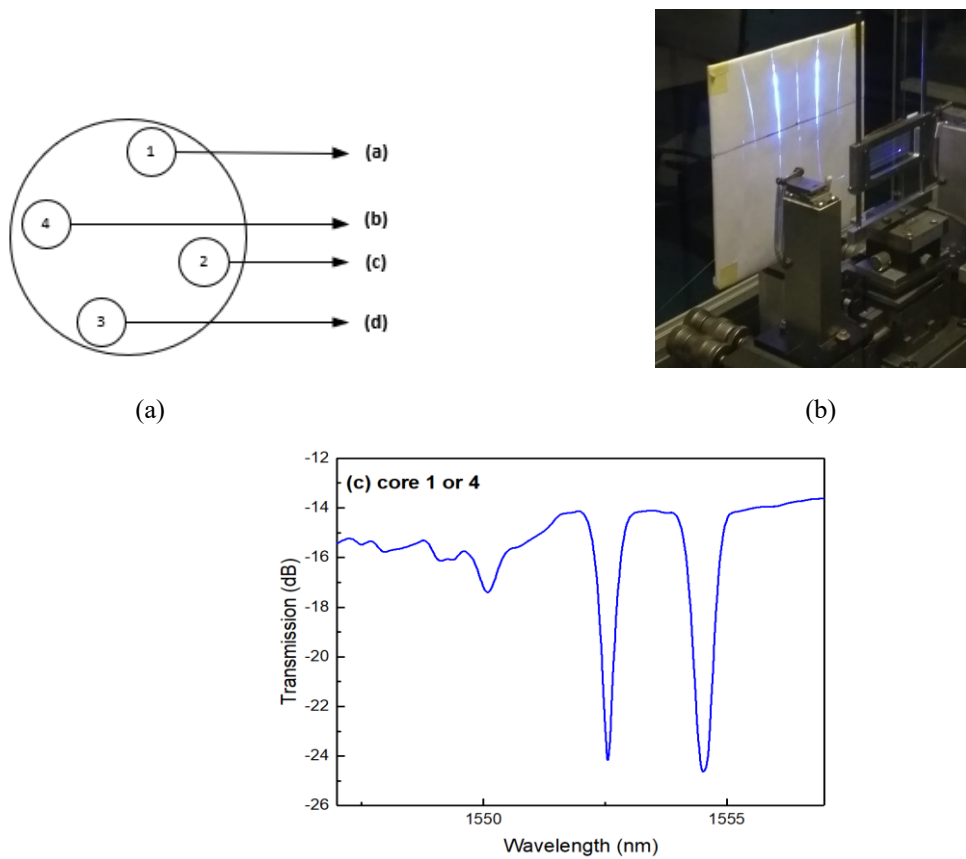
Figure 4. 9 Core marking for two different positions into 4CF: (a) cores are aligned at four planes (a, b, c, d); (b) diffraction of focused laser beam at top two cores; (c) Transmission spectrum for FBG inscription into either core 1 or 4 situated in the planes a & b.

Figure 4.9 (c) represents the transmission spectrum with three individual peaks. The highest amplitude of 11 dB was measured for the resonances at ~1552.5 nm and ~1554.0 nm respectively. It is clearly visible that both the cores were well aligned for UV inscription and refractive index perturbation occurs for writing FBG period of 1071.92 nm. Here, during the vertical position alignment of core 1 and 4, an equal power of UV exposure occurs for both. Hence, similar attenuation is achieved for transmission spectra while performing measurement for either core 1 or 4. It is also possible to observe a cross-talk effect during measurement process due to butt coupling through XYZ adjustment of the splicer and approximately equal light is coupled through the cores. Another small resonance around 2 dB is also obtained, that may occur due to the possibilities for occurring both weak exposure in slight core misalignment position and light coupling through core 2 during measurement.

Further adjustment of defocusing distance between cylindrical lens and the phase mask facilitated the 4CF to be exposed of UV-radiation for all the cores. Here the refractive index modulation occurs into all the cores. The core positions are presented in Fig. 4.10 (a), where there are two cores in each plane (a) and (b).

(a)

(b)
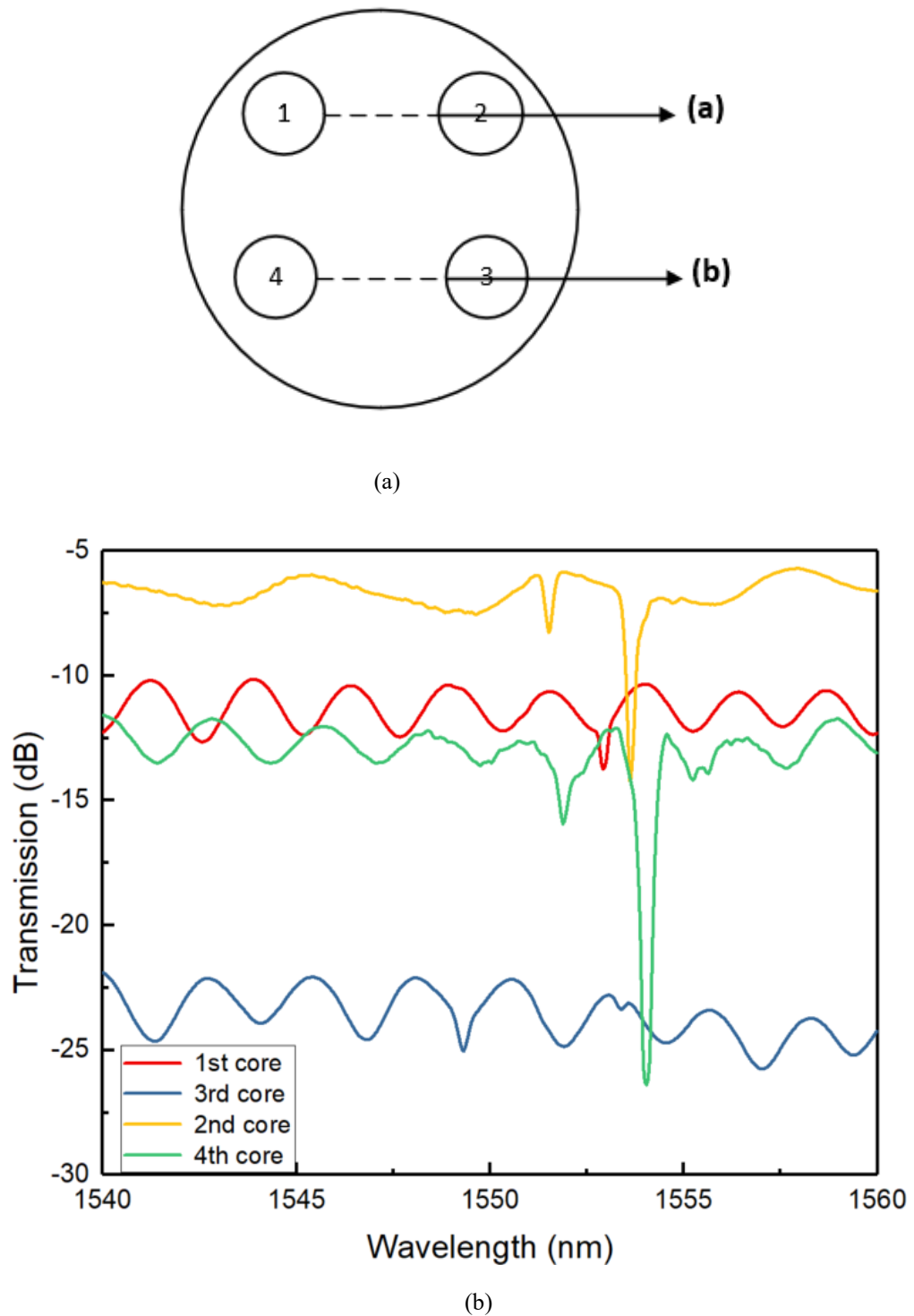
Figure 4. 10 (a) Core marking for different core positions into 4CF; (b) Transmission spectra when all the cores of 4CF were aligned for FBG inscription at period of 1071.92 nm.

Figure 4.10 (b) shows the transmission spectra with a maximum of 15 dB and 6 dB resonances for UV-inscribed FBGs into core 4 and core 2 respectively. As seen a small resonance of approximately 2 dB along with higher attenuation peak was achieved for FBGs into both the cores. This may be due to the misalignment during core marking and laser focus adjustment process. As all four cores were exposed to the UV radiation, we can see two very weak resonances for core 3 and 4, with the attenuation around 2 dB and 0.5 dB at the wavelength of ~ 1552.5 nm and 1553 nm respectively. It is clearly visible that the refractive index perturbation is weak in these two cores. It is considered that the effective refractive index of each core is non-identical, as may be caused by the laser power variation with different cores during FBG inscription. There is also crosstalk effect when the light is coupled through the splicer.

4.3.2 FBGs in 4CF with core to core spacing of 36 μm

The FBG fabrication in 4CF with core-to-core distance of 36 μm was also investigated. Figures 4.11 (a) & 4.12 (a) show the positional arrangement of the cores. The corresponding reflection and transmission spectra for FBG written into these cores were measured by utilising the experimental setup as explained in previous sections in Fig. 4.6.

(a)
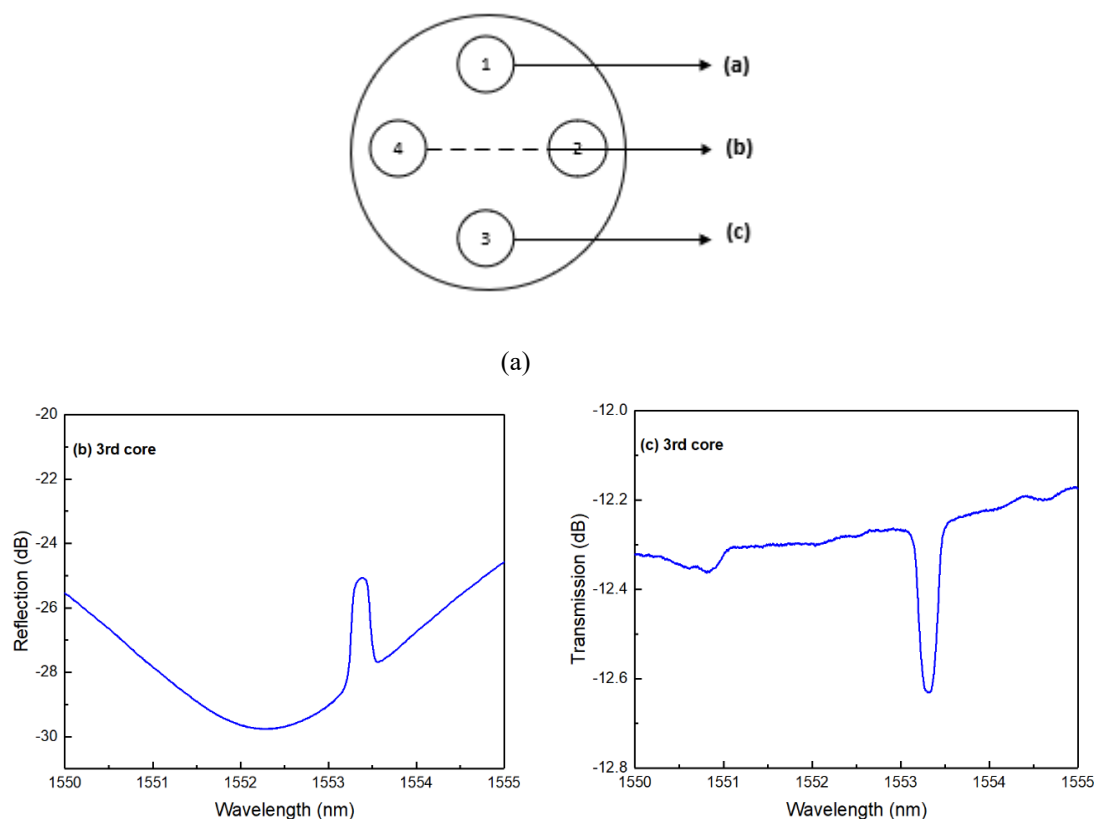
Figure 4. 11 (a) Core marking into three different planes with one core in each top and bottom planes; the centre plane contains two cores simultaneously; (b) and (c) Reflection and transmission spectra were measured when the bottom core was aligned for UV radiation.

Figure 4.11 (a) represents the core marking with three positions similar to Fig. 4.8 (a). The FBG inscription for the bottom core (c) provides the reflection and transmission resonance of 3 dB and 0.4 dB respectively while the similar writing parameters were chosen as discussed for 4CF with 50 µm core spacing. Therefore the achieved Bragg reflection of this 4CF is only 0.4 dB. This observation is associated with the variation of material property for the MCF after the hydrogen loading efficiency and annealing at a certain temperature condition after the inscription completed.

Another selective inscription was performed with the core positions as shown in Fig. 4.12 (a). In this case the 4CF was aligned for writing FBG into top cores. The reflection resonance of 5 dB was measured for core 2 placed in position (a) as depicted in Fig. 4.12 (b). However, there are significant resonance response for other cores which is due to light partially coupled through these cores while continuing measurements. It is clearly noticed that the maximum transmission of 30 dB is achieved with the top core aligned and focused for UV inscription as seen in Fig. 4.12 (c). A significant refractive index modulation takes place for the other cores of 4CF such as cores 3 and 4 with the resonances achieved as 15 dB and 8 dB respectively. Whereas, for the UV-inscribed FBG into core 1 situated at plane (a) results very weak resonance response and is not presented into the plot. This is due to positional error introduced from the core shifting during core marking step and may not be at the same plane with core 2, hence off focused. It can be noticed that the reference level in the reflection spectra varies with the core alignment through the splicer setup and also the resolution & sensitivity adjustments in the OSA. The normalised spectra are achieved by allowing the input-output light coupling in a stable position through 4CF.

(a)

(b)

(c)
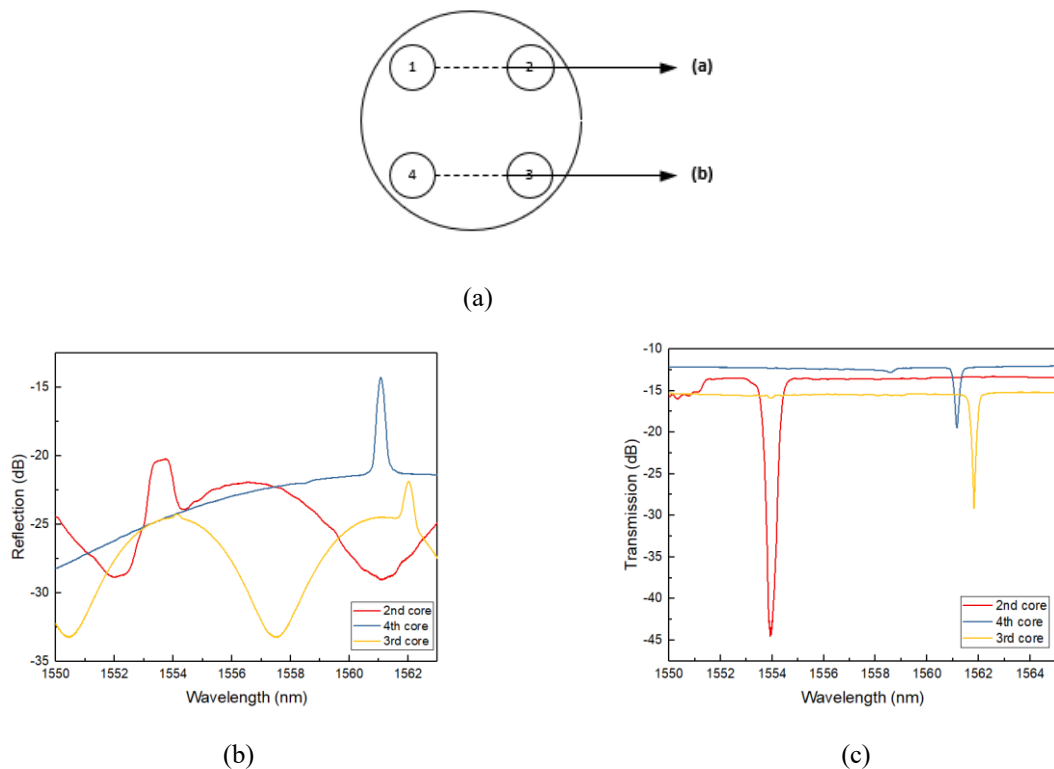
Figure 4. 12 (a) Core marking into two different planes with two cores in each top and bottom plane; (b)&(c) Reflection and transmission resonance were measured when the top cores were aligned for UV radiation.

4.3.3 FBGs in 7CF with core to core spacing of 35 μm

The 7CF is one of the new multicore fibre with huge potential in optical fibre communications. FBGs in 7CF will present some sensing capability for monitoring health condition or structure changes for more complex engineering configuration. Therefore, this PhD project has also investigated the fabrication of FBGs in 7CF. Figure 4.13 (a) shows the 5 core positions identified and labelled as (a, b, c, d, e), where (a), (c) and (e) are the top, central and bottom cores respectively, and the two sets of cores (2 & 6 and 3 & 5) in a same plane are marked as (b) and (d). It is intended to inscribe FBGs into all the cores of the 7CF with the centre wavelength around 1550 nm. After the inscription, the FBG spectra of all cores were measured using the butt-coupling method.

(a)	(b)
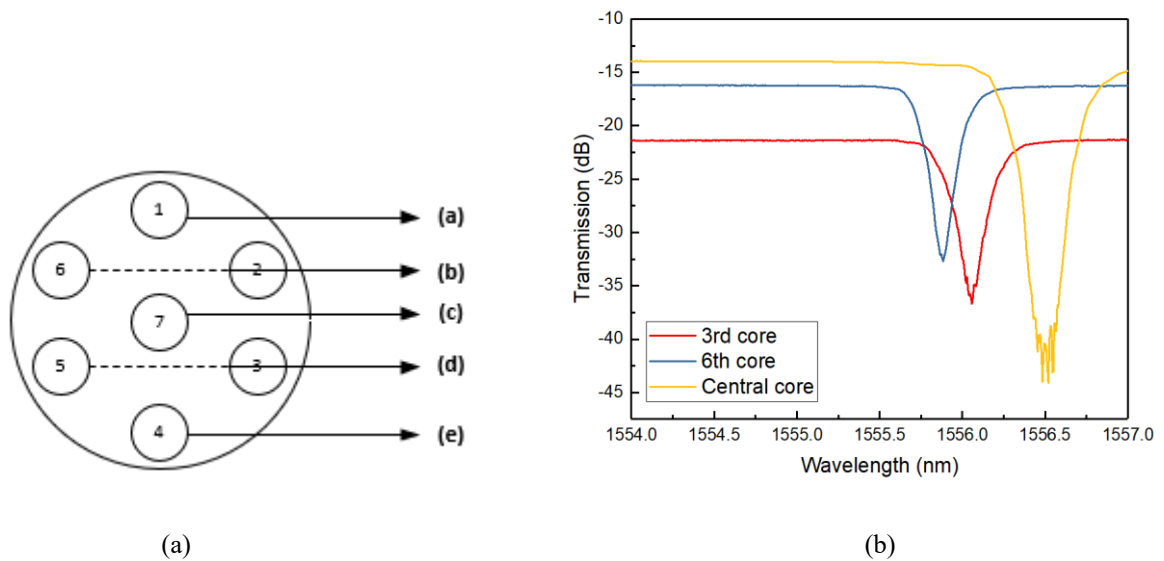
Figure 4. 13 (a) The 5 positions (a, b, c, d, e) marked for the 7CF; (b) Transmission spectra for FBGs inscribed into 3rd, 6th and the central core of the 7CF.

Figure 4.13 (b) shows the transmission spectra of FBGs inscribed into the central core and 3rd and 6th cores, respectively. It is seen that the FBG resonances of these three cores are shifted to longer wavelengths ranging from 1555.7 nm to 1556.5 nm. The maximum resonance (Bragg reflection) achieved for the central core is the strongest reaching 27 dB, whereas for other two cores (3rd & 6th), it is approximately 15 dB. The variation in resonance wavelength and strength is due to the alignment and focusing condition and inscription efficiency. In principle, if the alignment and the UV beam focusing condition are precisely controlled, FBGs can be written into all cores with similar wavelength and strength. Although here we only show spectra of the FBGs in three cores, there are several samples with Bragg resonance shown for all seven cores.

4.4 Vector sensing measurement principle and experimental setup

Due to the FBGs are in the cores, distributed at different locations in MCF, vector sensing is possible as the FBG spectral responses of different cores will provide both direction and amplitude of the structure change, for example under bending and twisting. We can explain the vector sensing of MCF-FBG corresponding to the bending in the orthogonal directions (x and y) as depicted in Fig. 4.14 (a, b) for a 4CF and 4.15 (a, b) for a 7CF. The angle θ is formed between y-axis (for θ = 0°) and the distance d between centre and an outer core. Fig. 4.14 (b) & 4.15 (b) show the curvature at θ = 270° and the propagating light is bent along the arc of a circle. Mathematically the change in bending curvature can be expressed as $\sin\left(\frac{LC}{2}\right) = \frac{(L-\Delta L)}{2} C$. Here, C is the radius of curvature (1/R) and can be calculated for different bending positions of fibre [7, 109], L is the initial distance between two fixed ends of the fibre, ΔL is the shift in distance of the 3D stage (Fig. 4.16). The bending is applied along the two-dimensional plane of the fibre.

(a)   (b)
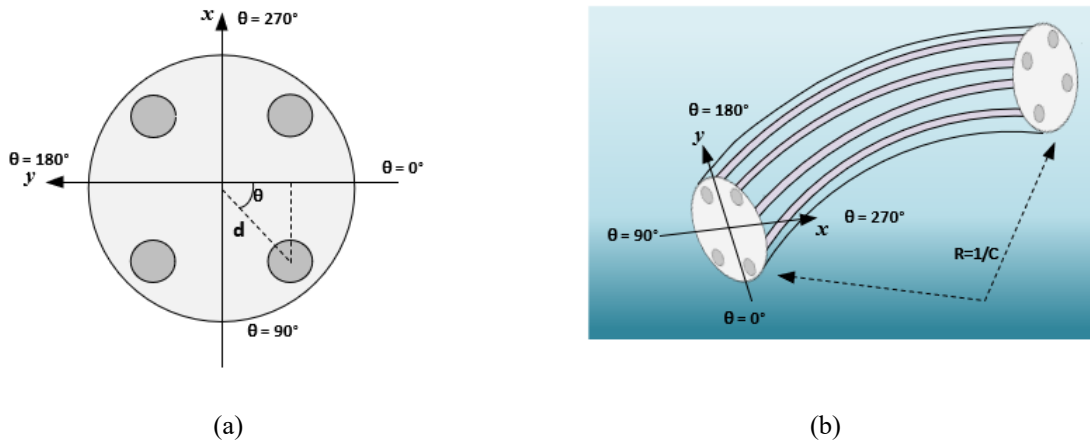
Figure 4. 14 Schematic diagram for vector sensing mechanism [7].

(a)   (b)
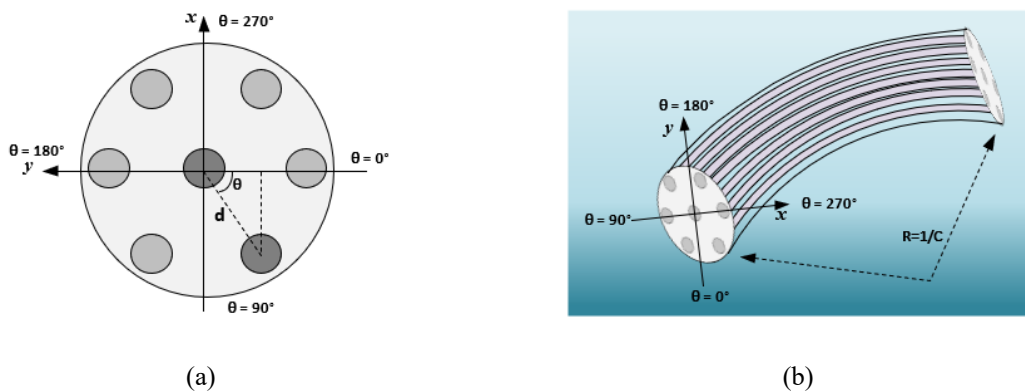
Figure 4. 15 Schematic diagram for vector sensing mechanism [109].
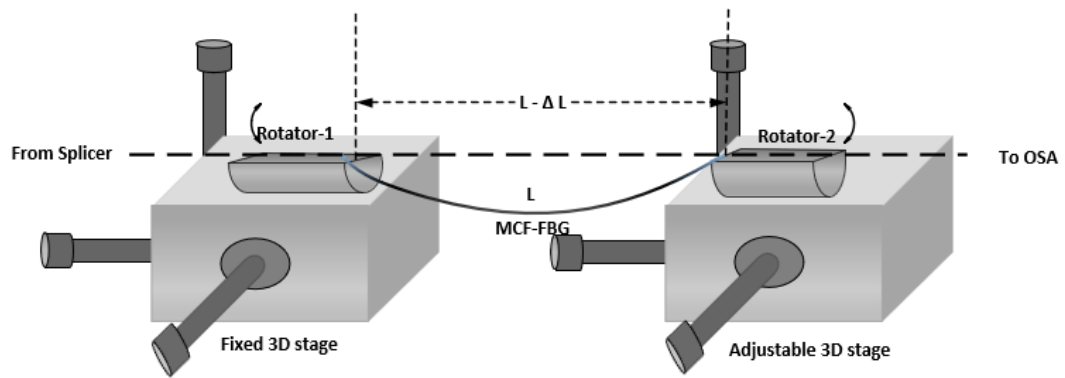
Figure 4. 16 Schematic diagram of the measurement setup for vector bending and twist sensing.

For the twist and bending sensing measurement, the MCF-FBG was placed between two 3D translation stages with a distance of L = 12.5 cm. The twist response can be studied while one end of the fibre is fixed and the other side of the fibre is rotated at different angles of 0°, 90°, 180° and 270° respectively. The experimental findings presented here on vector bending sensor utilises rotation of both ends of MCF-FBG at varying rate generating twist through rotators 1&2 as depicted in Fig. 4.16. The bending measurement was performed with the inward movement of one 3D stage to introduce curvature to the fibre (shown in Fig. 4.16), and the maximum movement was 10 mm. The spectrum for each bending was recorded on to the optical spectrum analyser.

4.5 Vector bending-twist sensing measurement results

It is clearly found that the MCF-FBG responds to the bending and twisting, showing not just the spectrum shift but also the shift direction. The sensitivity varies depending on selective inscription of FBGs into MCF. The results are analysed for 4CF-FBG with core spacing distance of 50 μm and 36 μm respectively, and also for 7CF-FBG.

4.5.1 Result analysis for 4CF-FBG with core to core spacing of 50 μm

Figure 4.17 (b-e) shows the resonance response for bending applied at four twist angles (0°, 90°, 180° and 270°) for the core 2 at position (a) (Fig. 4.17a). It is seen in Fig. 4.17 (f) that for the twist angle settings of 90°, the resonance is blue shifted giving the sensitivity value of -0.101 nm/m^{-1}. A similar magnitude of ±0.122 nm/ m^{-1} as the highest sensitivity is obtained for the twist angles at 0° and 270°. However, the resonance becomes blue shifted for twist angle setup at 0° and positive wavelength shift is achieved for the twist angle at 270°. The lowest bending sensitivity of -0.085 nm/ m^{-1} at 180° is obtained with a reflectivity response as blue shifted.
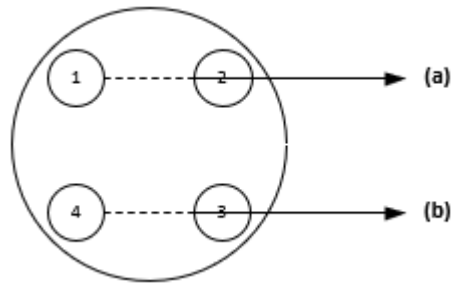
(a)
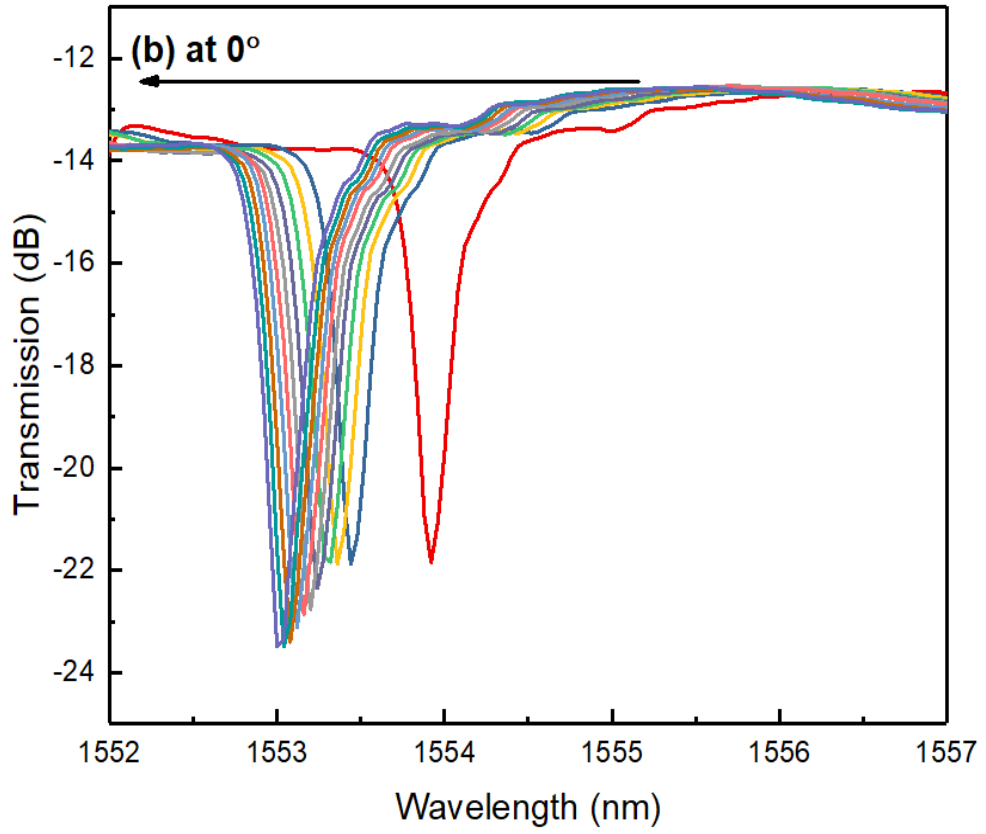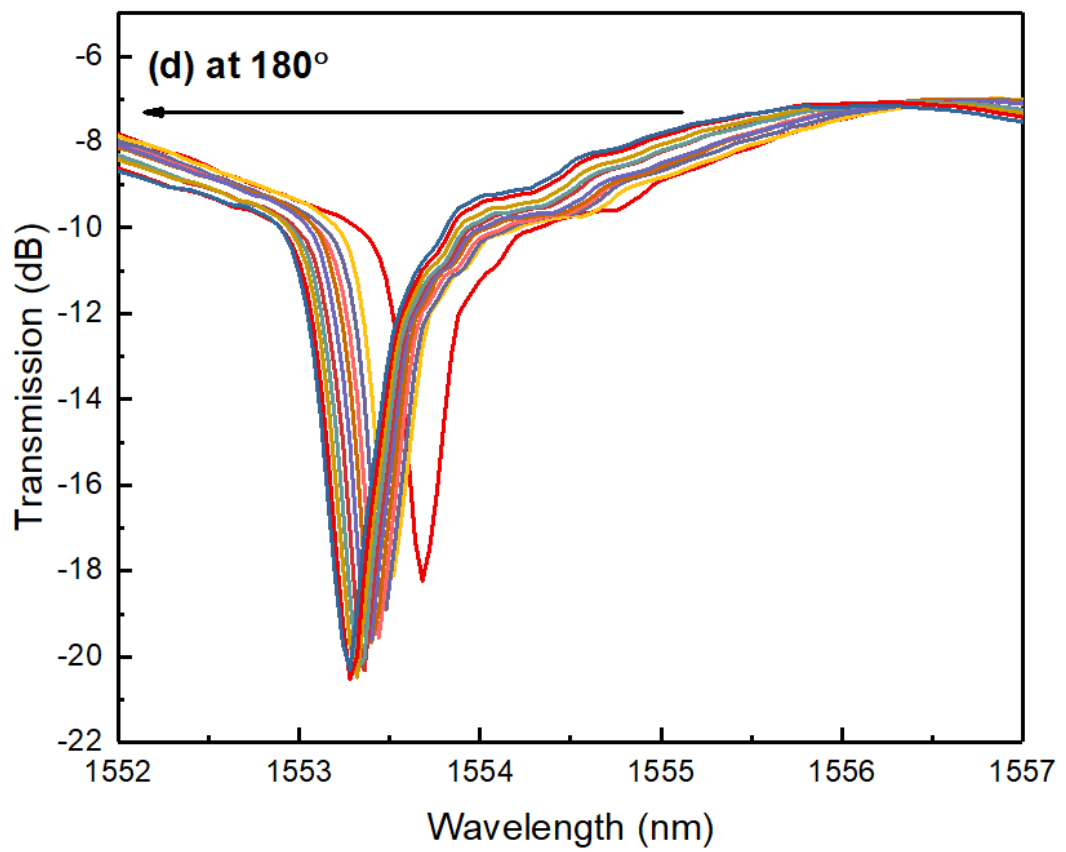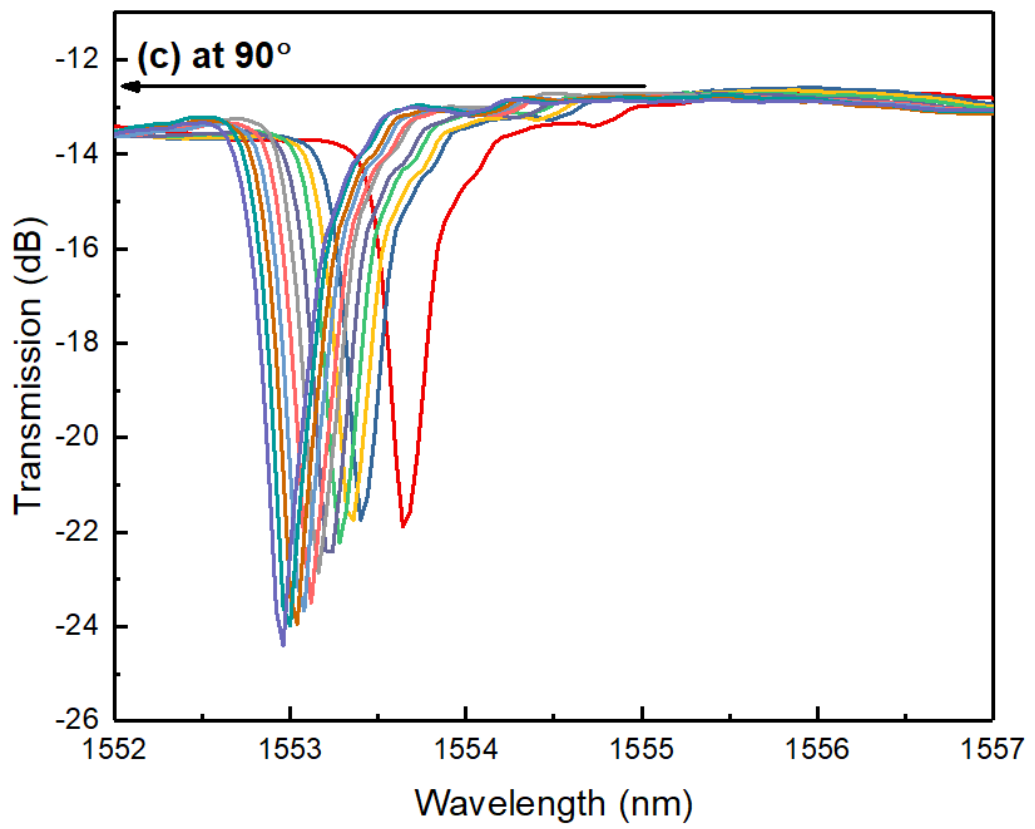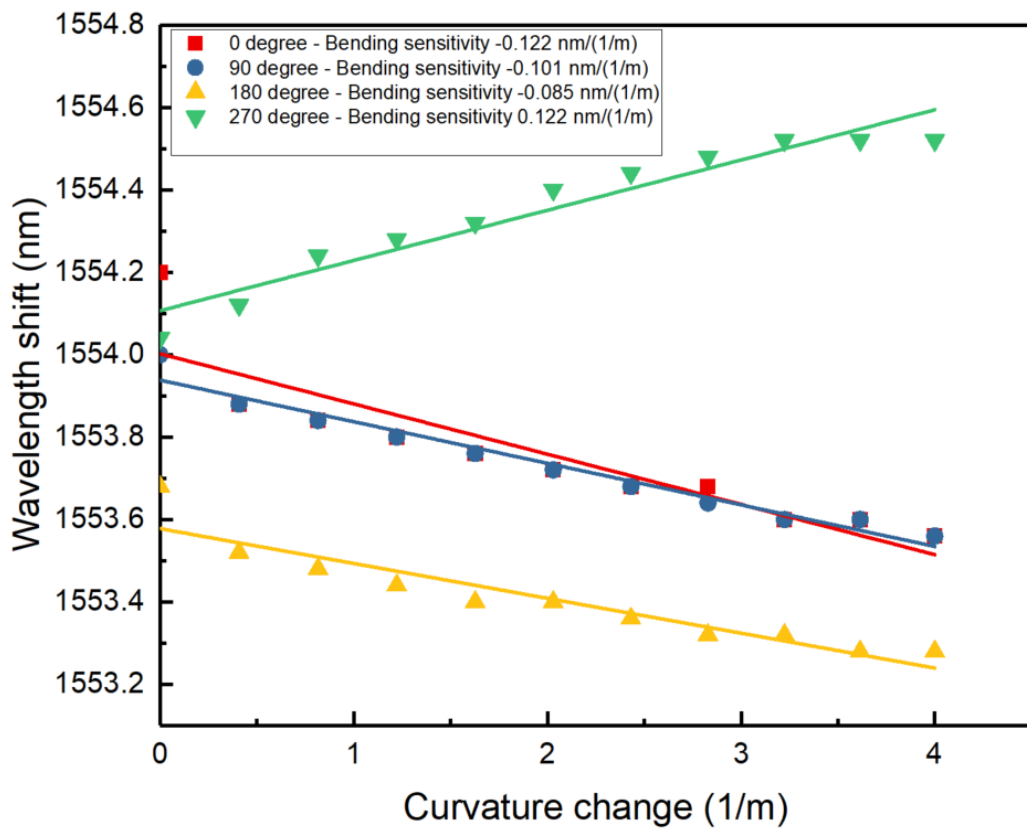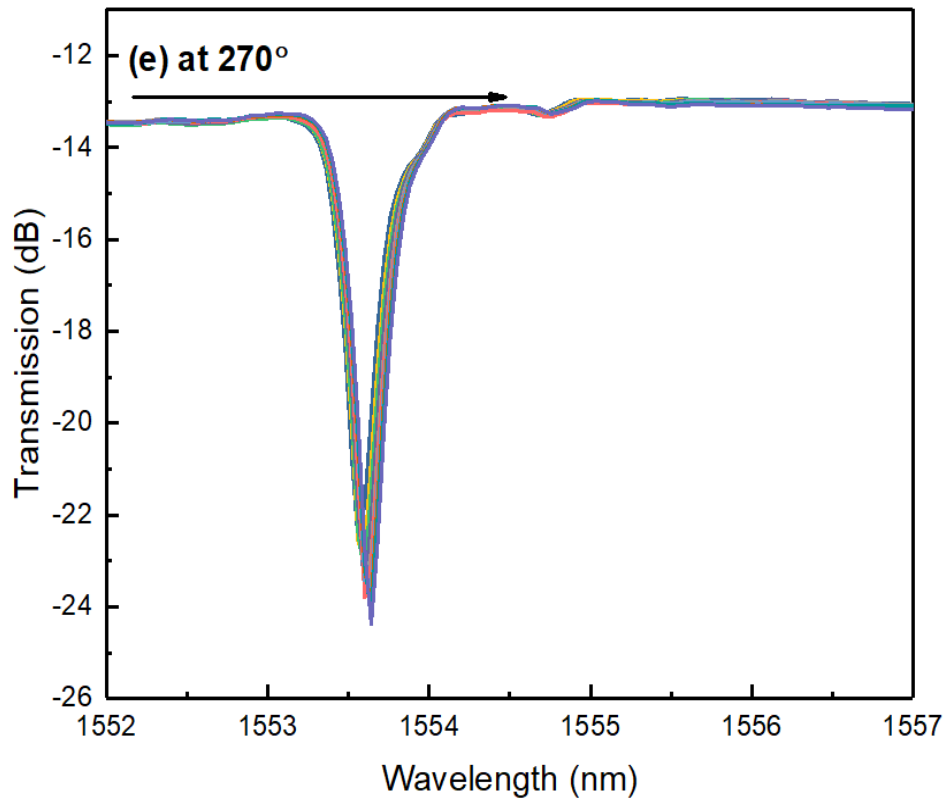
(f)

Figure 4. 17 (a) The core positioning for 4CF; (b) The core 2 with FBG spectral responses when the fibre subjected to the bending under four twist angles: (b) 0°; (c) 90°; (d) 180°; (e) 270°. (f) Plotted bending sensitivities for the core 2 with FBG, clearly showing the changes in curvature and in direction.

The bending sensitivity measurement was evaluated for FBG written into core 4. The core is situated at diagonally opposite position as in Fig. 4.17 (a). The analysed results for resonance response are presented in Fig. 4.18 (a, b, c, d). The resultant FBG sensitivity plotted in Fig. 4.18 (e). Here, at twist angles of 0° & 90° the wavelength is blue shifted with magnitudes of -0.115 nm/m^{-1} and -0.123 nm/m^{-1} respectively. Whereas, for the twist angles at 180° & 270° the resonance wavelength is red shifted and there are small sensitivity values of 0.052 nm/m^{-1} and 0.02 nm/ m^{-1} are achieved.
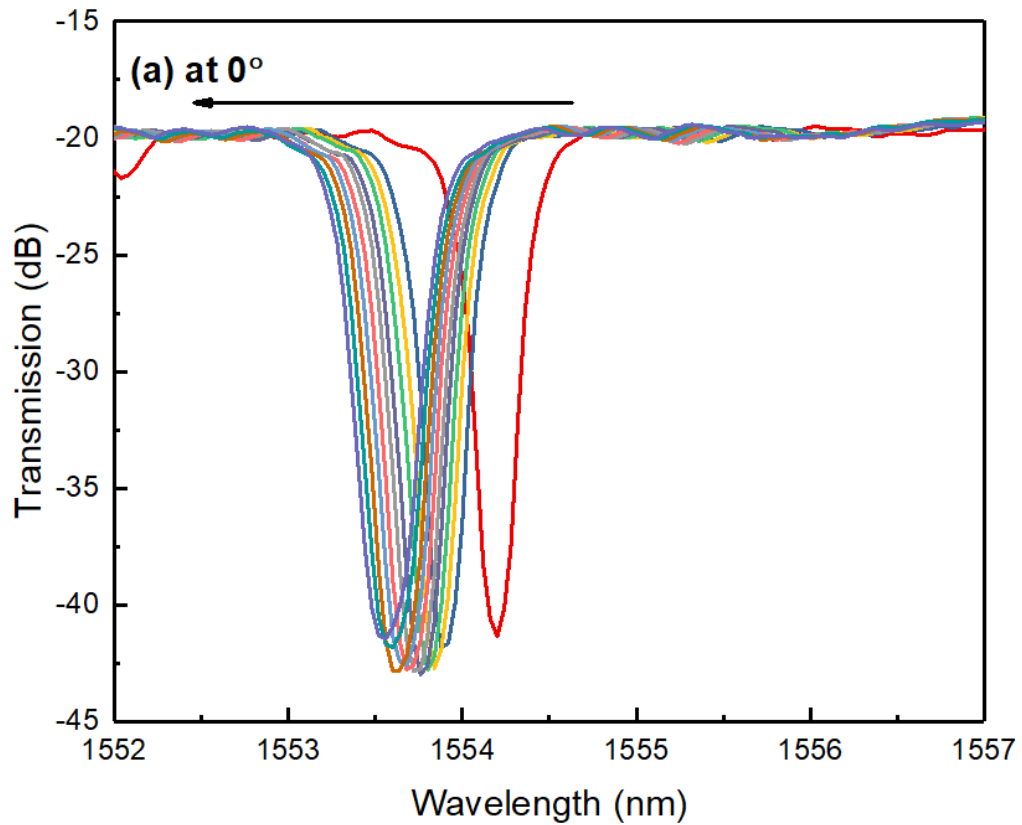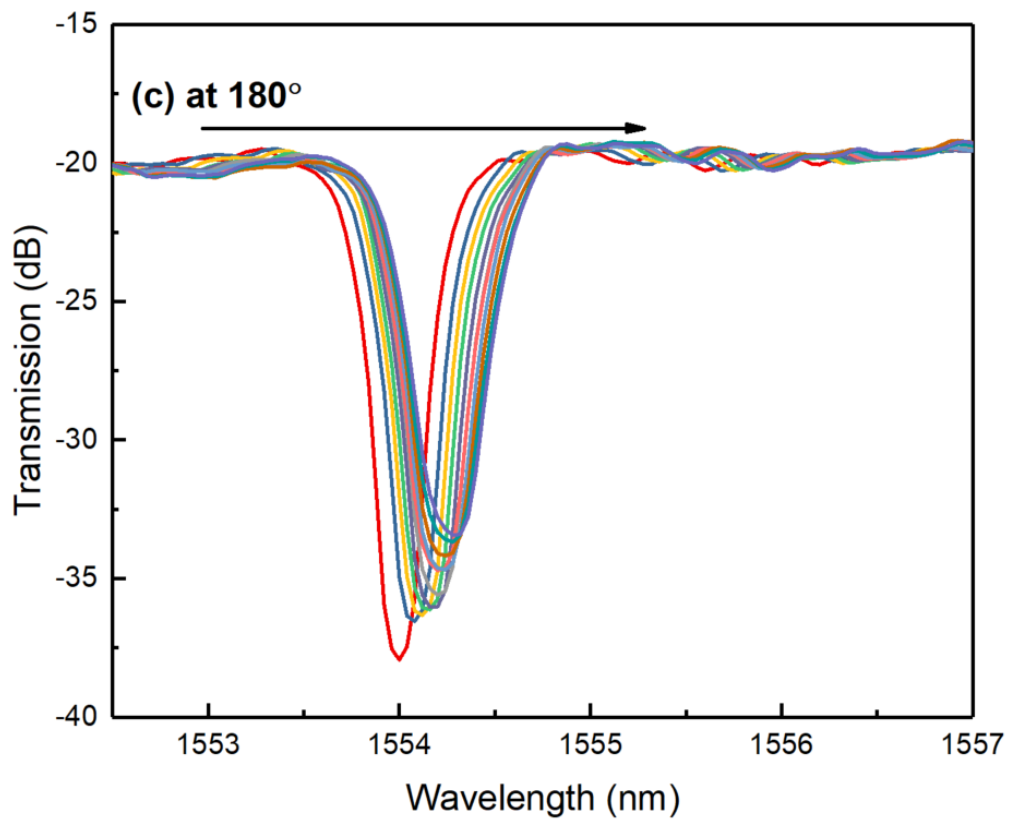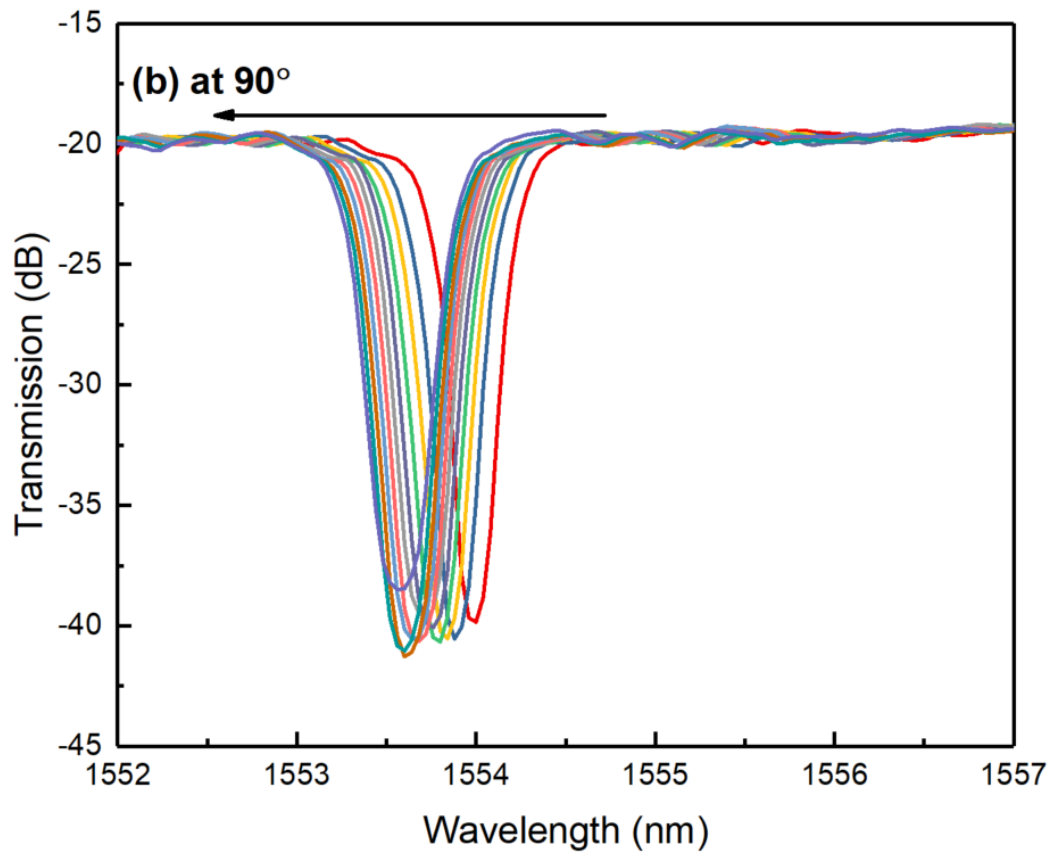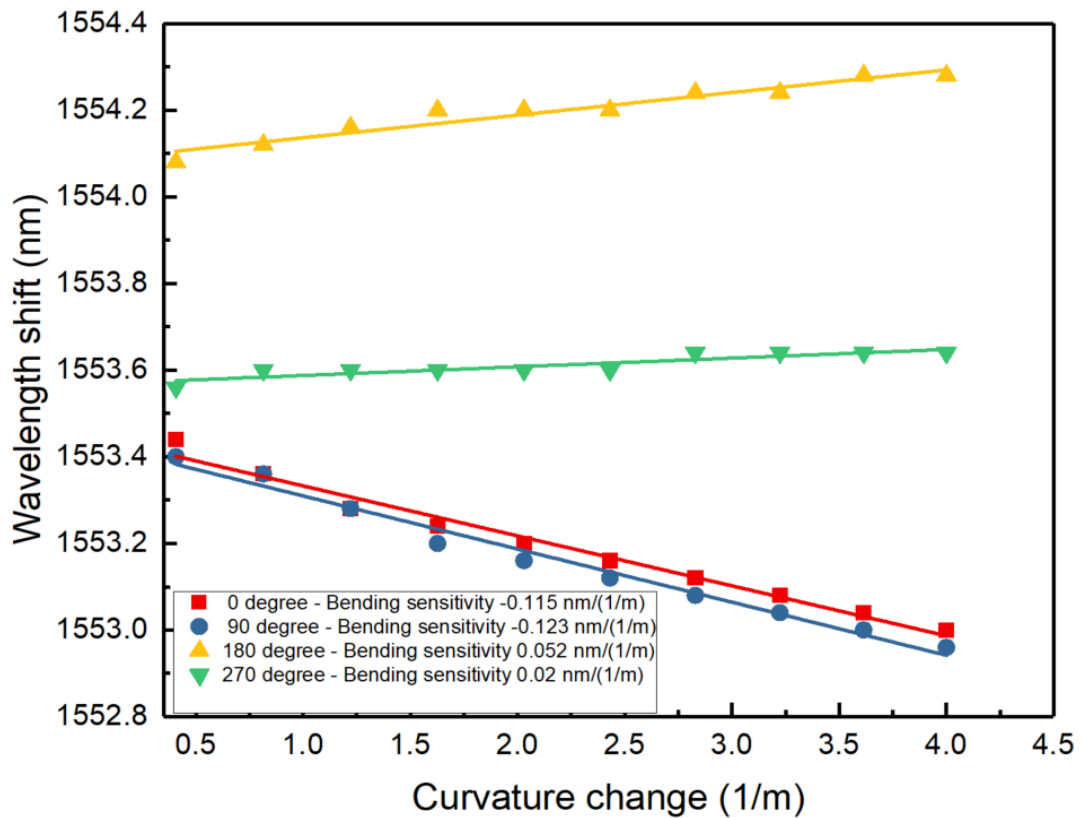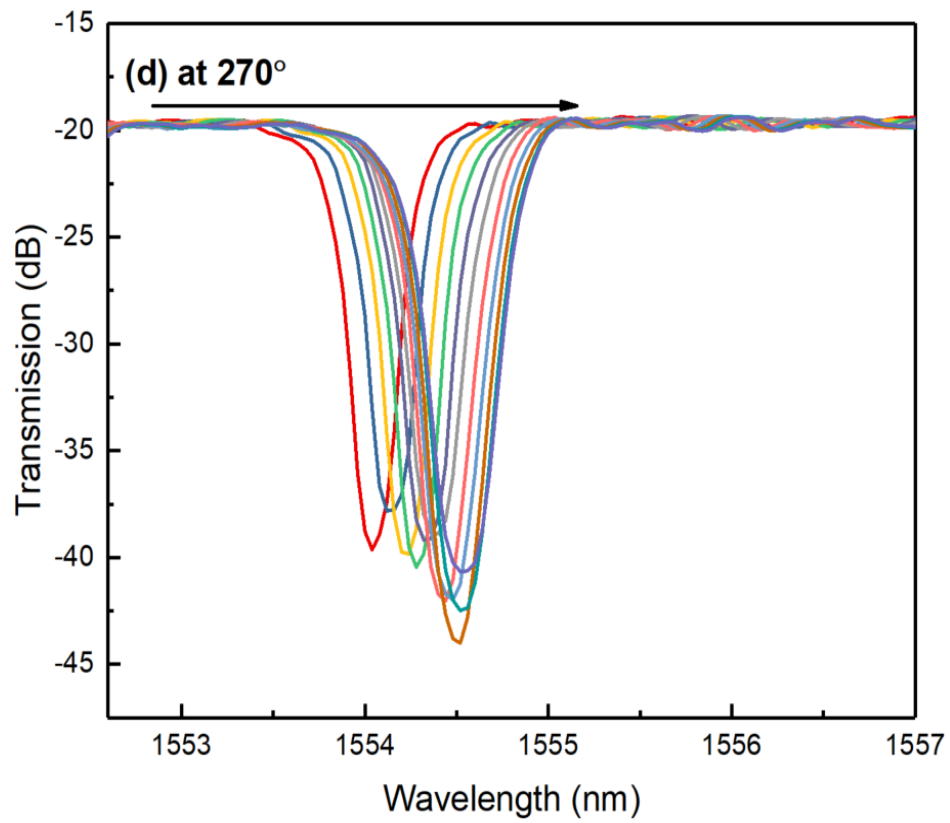
(e)

Figure 4. 18 The core 4 with FBG spectral responses when the fibre subjected to the bending under four twist angles: (a) 0°; (b) 90°; (c) 180°; (d) 270°. (e) Plotted bending sensitivities for the core 4 with FBG, clearly showing the changes in curvature and in direction.
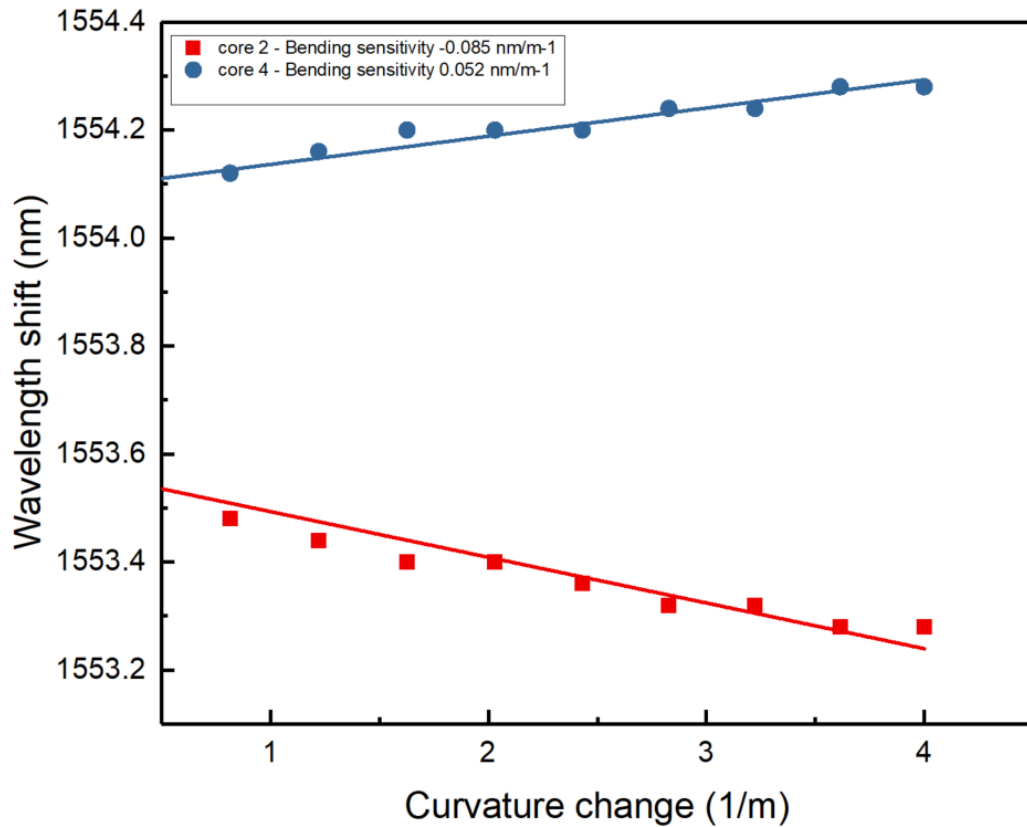
Figure 4. 19 Vector bending sensing for two opposite cores 2 & 4.

Effectively the measurement results clearly show that there is an opposite resonance shift for two cores (core 2&4) situated diagonally opposite positions and the twist angle setup of 180° is considered as represented in Fig. 4.19.

4.5.2 Result analysis for 4CF-FBG with core to core spacing of 36 μm

The vector bending/ twist sensing measurement was also performed for a 4CF-FBG with core to core spacing of 36 μm. The sensitivity response for FBG inscribed into core 2 is shown in Fig. 4.20 (b, c, d, e). The analysis for the total response for all four twist angles is presented in Fig. 4.20 (f). A significant higher sensitivity is achieved at 90° and 270° with oppositely directed resonance shift with magnitudes of 0.241 nm/m^{-1} and -0.304 nm/m^{-1} respectively. Comparatively lower sensitivity values of 0.125 nm/m^{-1} and -0.118 nm/m^{-1} are obtained while the 4CF-FBG was set at twist angles of 0° and 180° respectively.
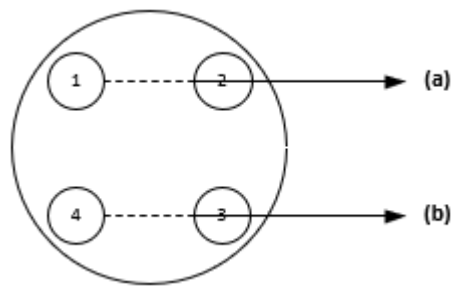
(a)
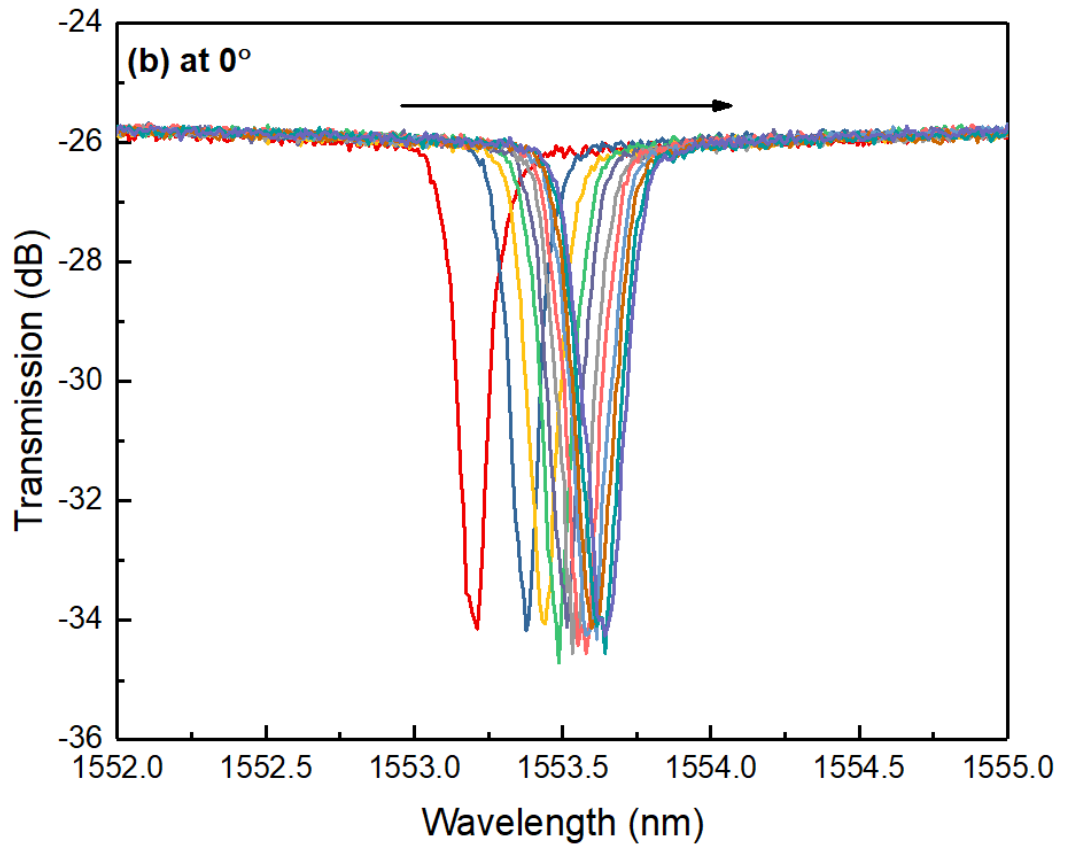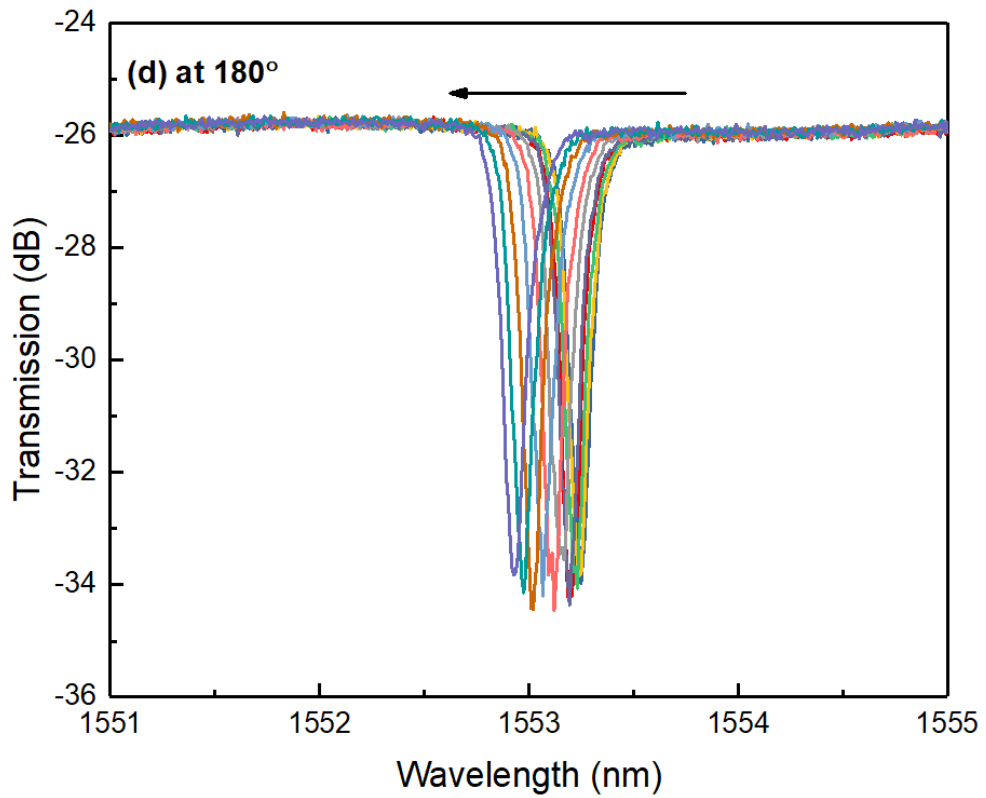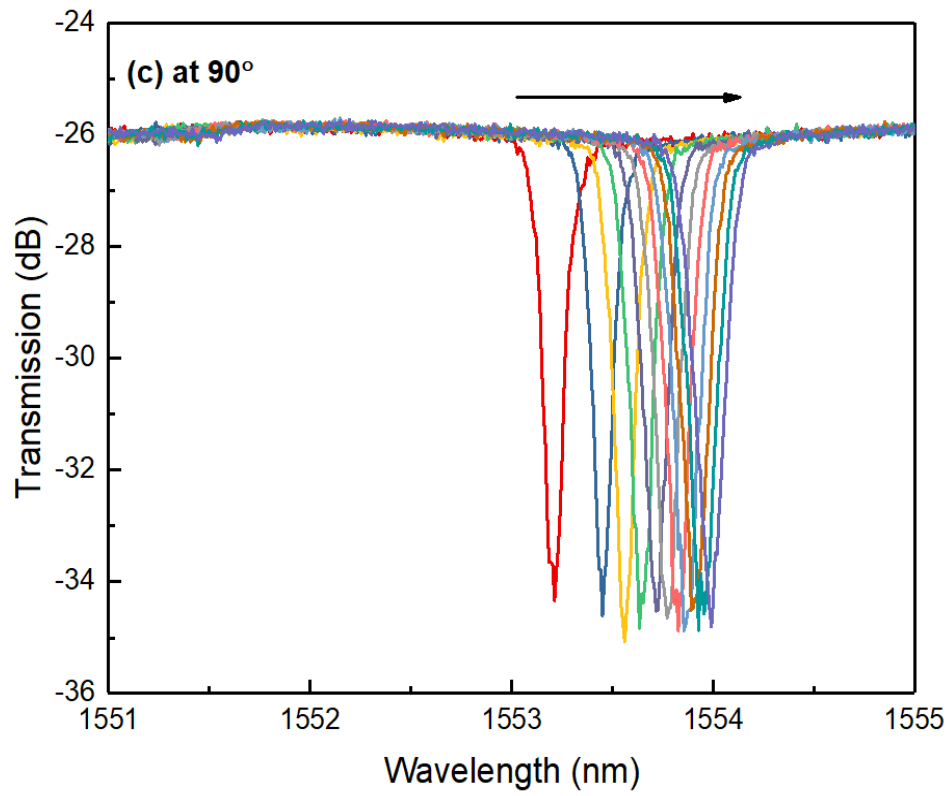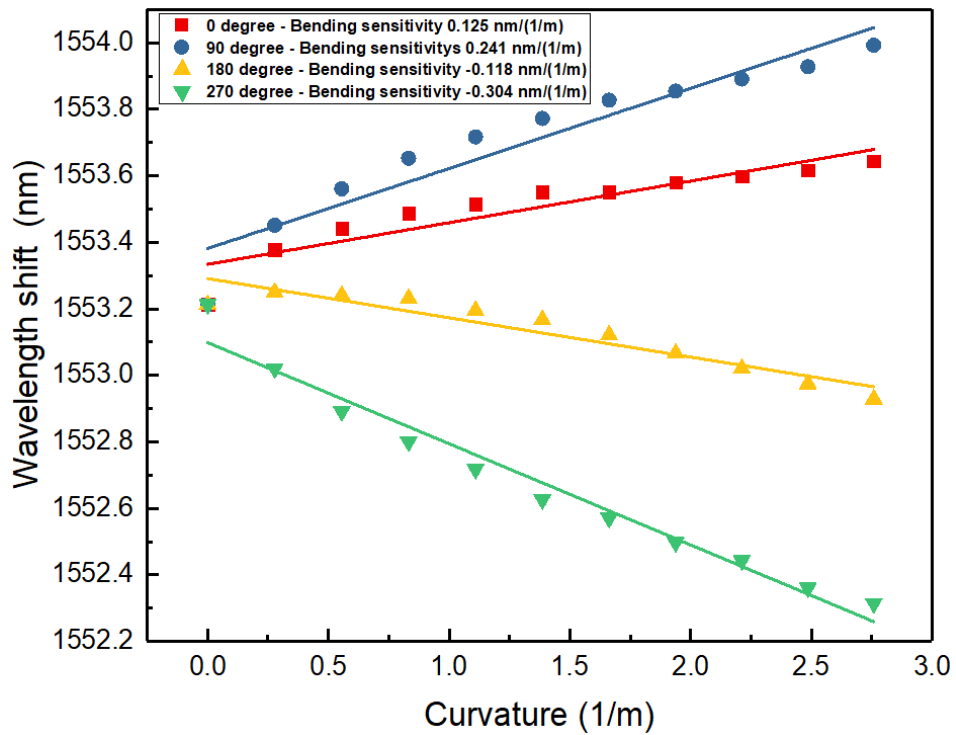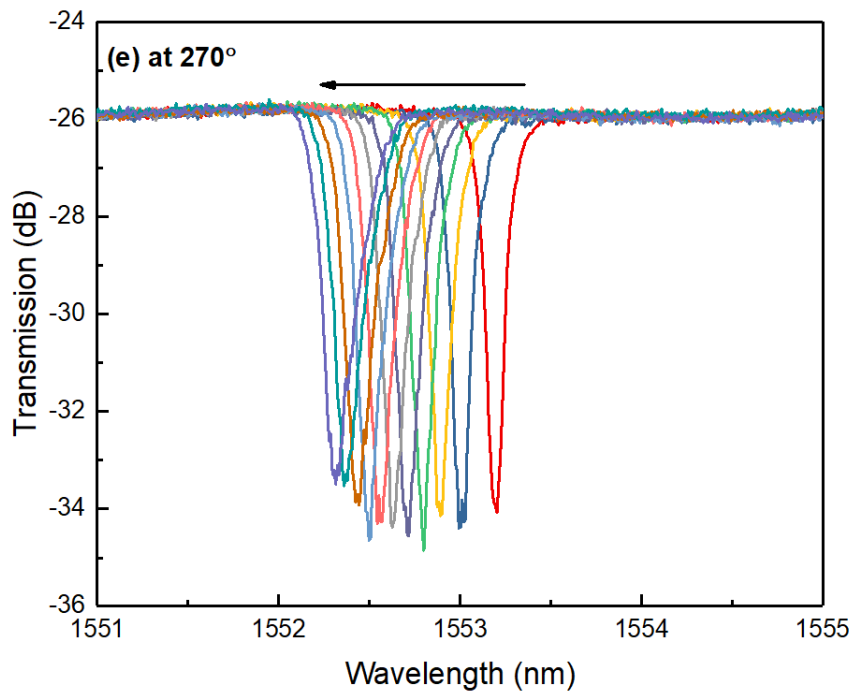
(f)

Figure 4. 20 (a) The core positioning for 4CF; The core 2 with FBG spectral responses when the fibre subjected to the bending under four twist angles: (b) 0°; (c) 90°; (d) 180°; (e) 270°. (f) Plotted bending sensitivities for the core 2 with FBG, clearly showing the changes in curvature and in direction.

The investigation for bending sensitivity of another core 3 situated at the perpendicular plane same as core 2 was carried out and the plotted results are shown in Fig. 4.21 (b, c, d, e). In this case higher sensitivity value is achievable for all the twist angles as depicted in Fig. 4.21 (f). Here the resonance

peaks are blue shifted at three twist angles of 0°, 180° and 270°. The analysed results achieved with magnitude of -0.163 nm/m^{-1}, -0.429 nm/m^{-1} and -0.202 nm/m^{-1} respectively. Whereas the sensitivity response is positive for twist angle at 90° and the magnitude becomes 0.325 nm/m^{-1}. As expected, there is opposite sensitivity response achieved for bending at twist angle of 0°. It is clearly visible in both summarised results in 4.20 (f) and 4.21 (f).
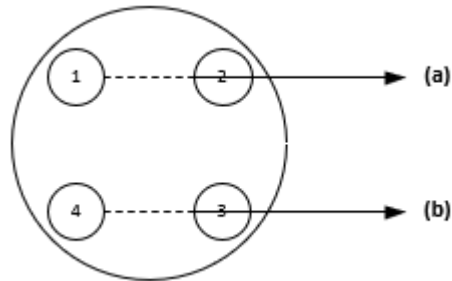
(a)
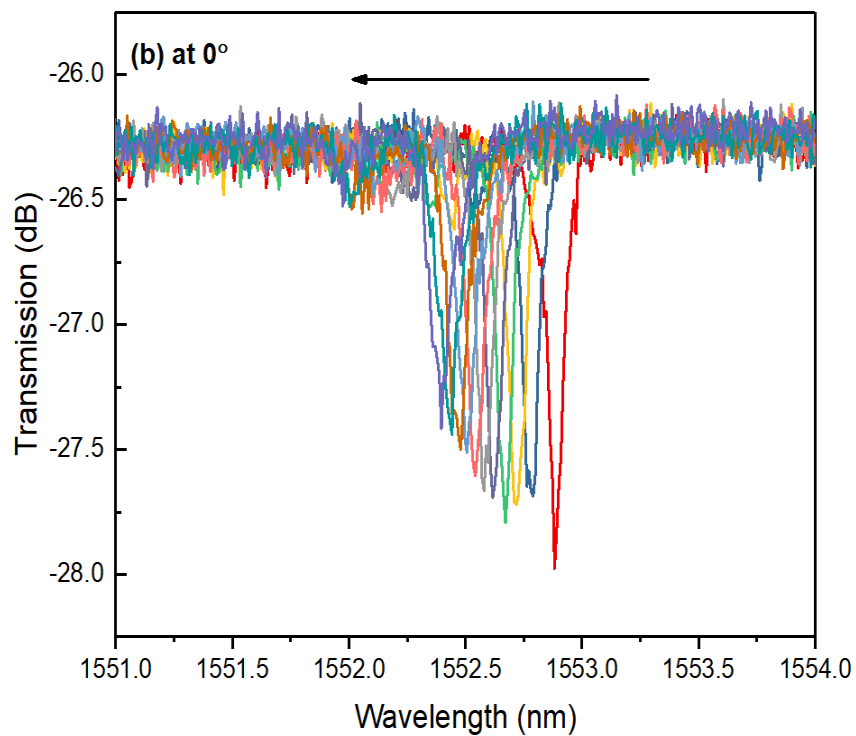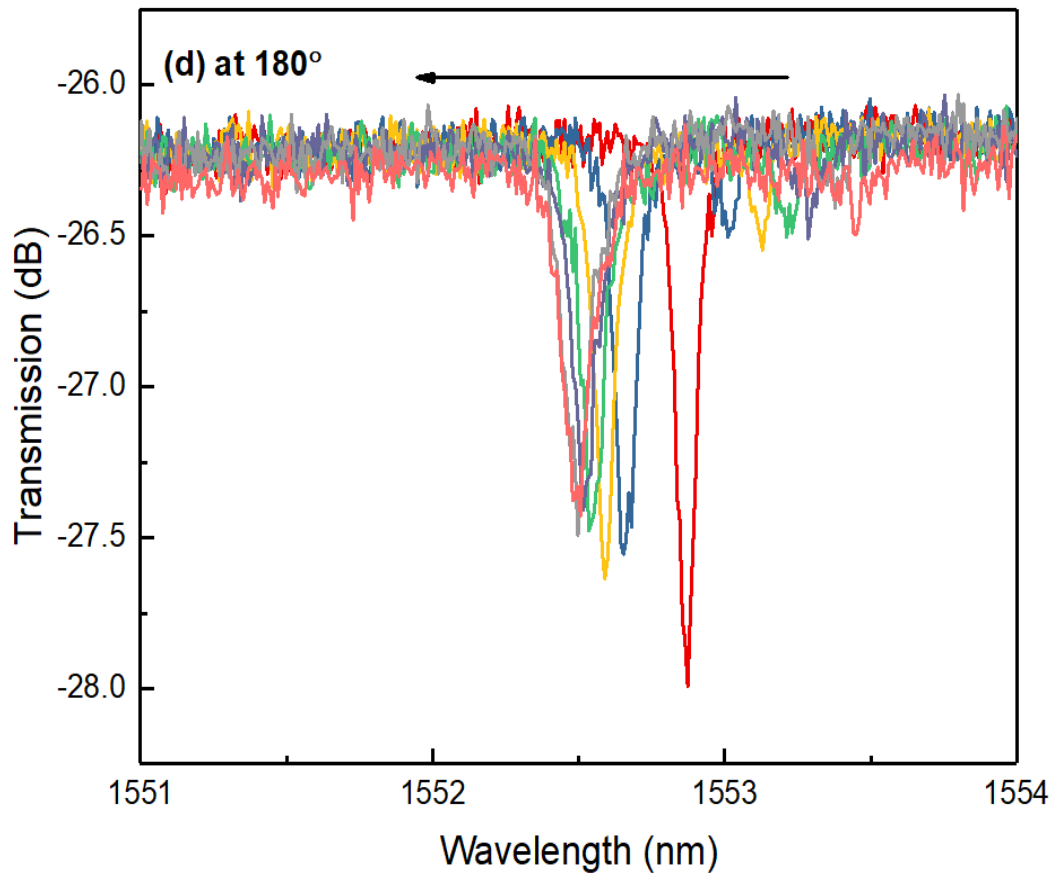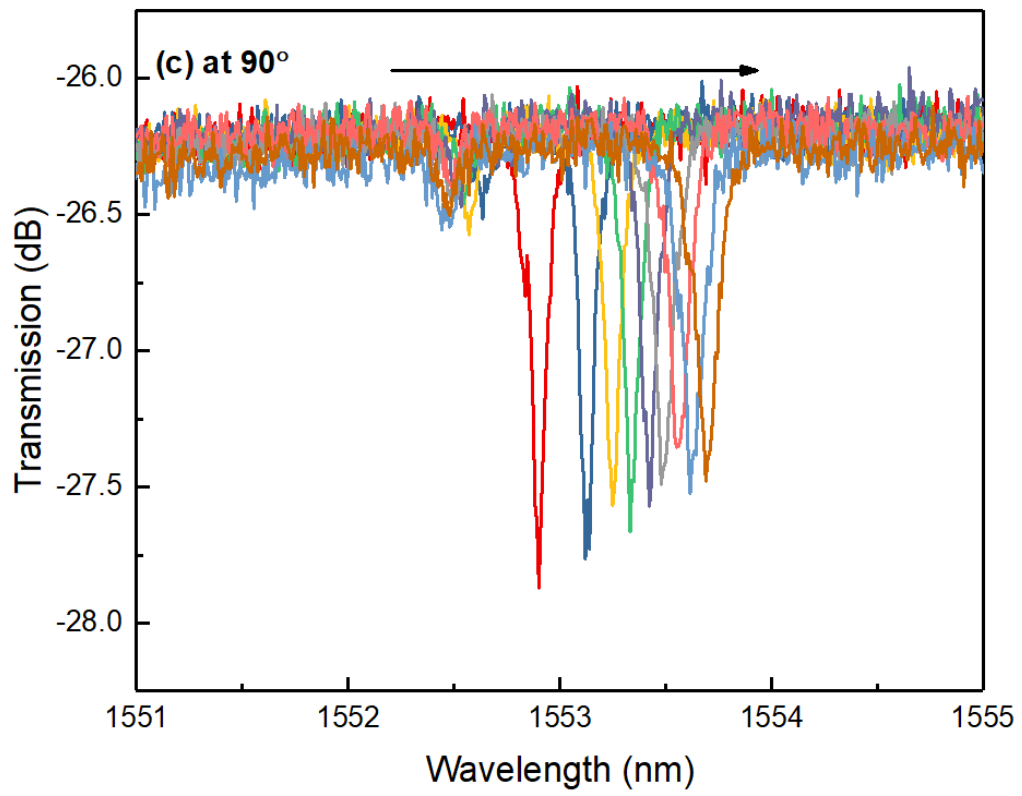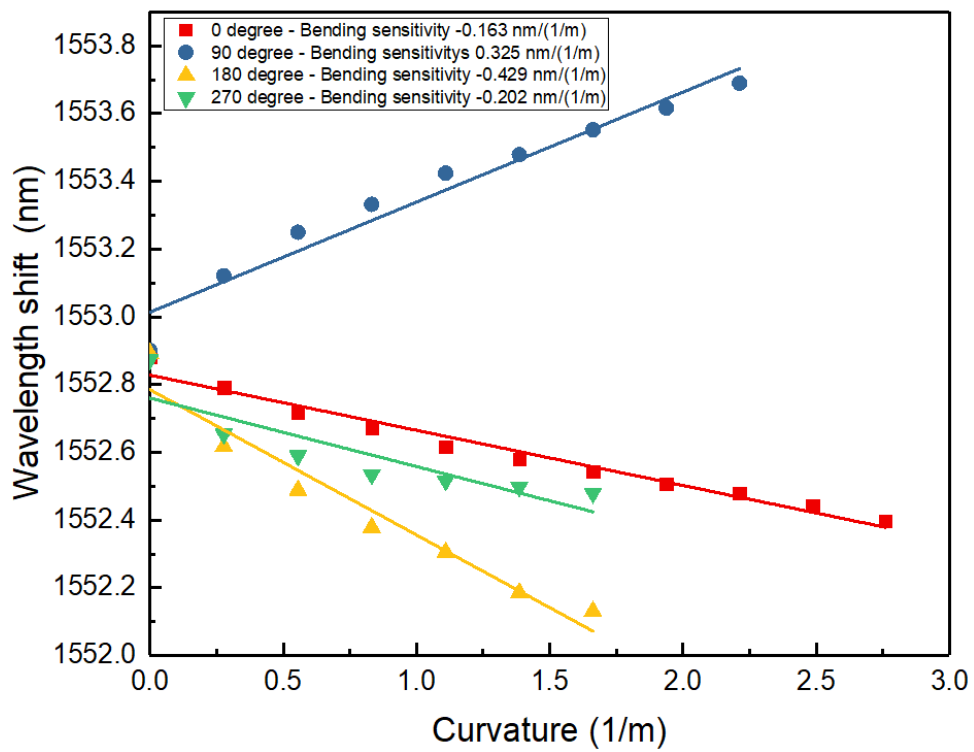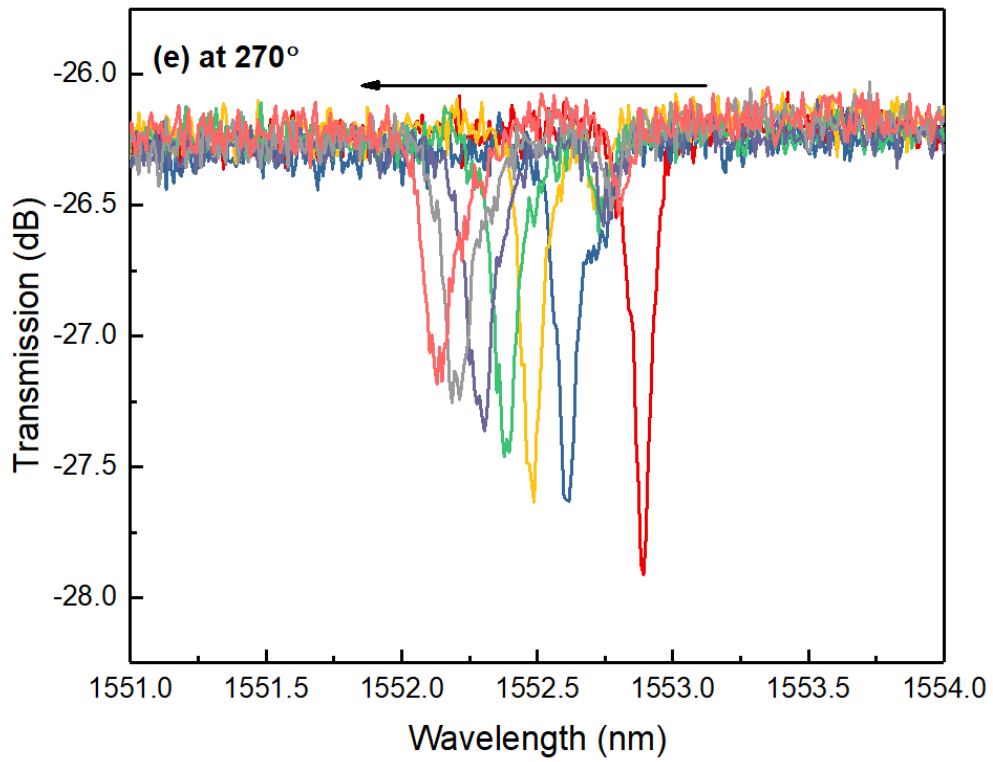
(f)

Figure 4. 21 (a) The core positioning for 4CF; The core 3 with FBG spectral responses when the fibre subjected to the bending under four twist angles: (b) 0°; (c) 90°; (d) 180°; (c) 270°. (f) Plotted bending sensitivities for the core 3 with FBG, clearly showing the changes in curvature and in direction.

In a MCF the variation of core spacing is influencing the effective index at the core-cladding interface [110]. Effectively with the same magnitude of bending applied there is a phase delay for the propagating modes with the larger core spacing. So here, the higher sensitivity response is achieved with lower core spacing of 36 μm in comparison with 50 μm core to core distance in a 4CF.

4.5.3 Result analysis for 7CF-FBG with core to core spacing of 35 μm

Figure 4.22 (b, c, d, e) display the spectral responses of the FBG inscribed in the 3rd core when the fibre was subjected to the bending and twisting at four different angles. From Fig. 4.22 (b, c) we can clearly see when the 7CF-FBG fibre was twisted at 0° and 90°, the increase in bending applied to the fibre induces the Bragg resonance shifts towards the longer wavelength (red-shift), whereas when the fibre is twisted at 180° and 270°, results in Bragg resonance shift towards to shorter wavelength (blue-shift). We plotted the bending sensitivities at these four bending/twisting condition in Fig. 4.22 (f), the two plots for 0° and 90° exhibit the upward slope with curvature responsivity of 89.57 pm/m^{-1}, 63.27 pm/m^{-1}, respectively, and the two plots for 180° and 270° show downward slope with the curvature responsivity of -68.51 pm/m^{-1} and -134.62 pm/m^{-1} respectively. From the results we can see some inconsistent trends in curvature responsivity. For example, the curvature responsivity at 270° is larger than at 180° as expected, however, the results for 0° and 90° are irregular because the two plots crossover. This could be caused by the precision of the alignment and how accurately the bending was applied to the 7CF-FBG. We will evaluate more carefully in future experiments to improve the consistence in the results.

(a)

(b) at 0°

(c) at 90°
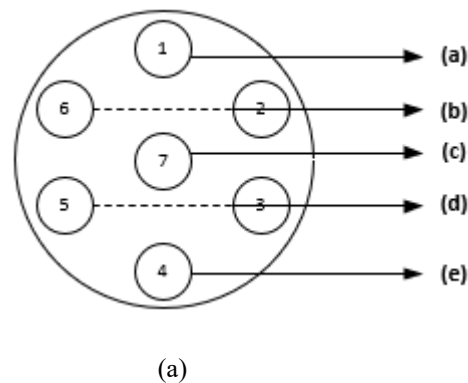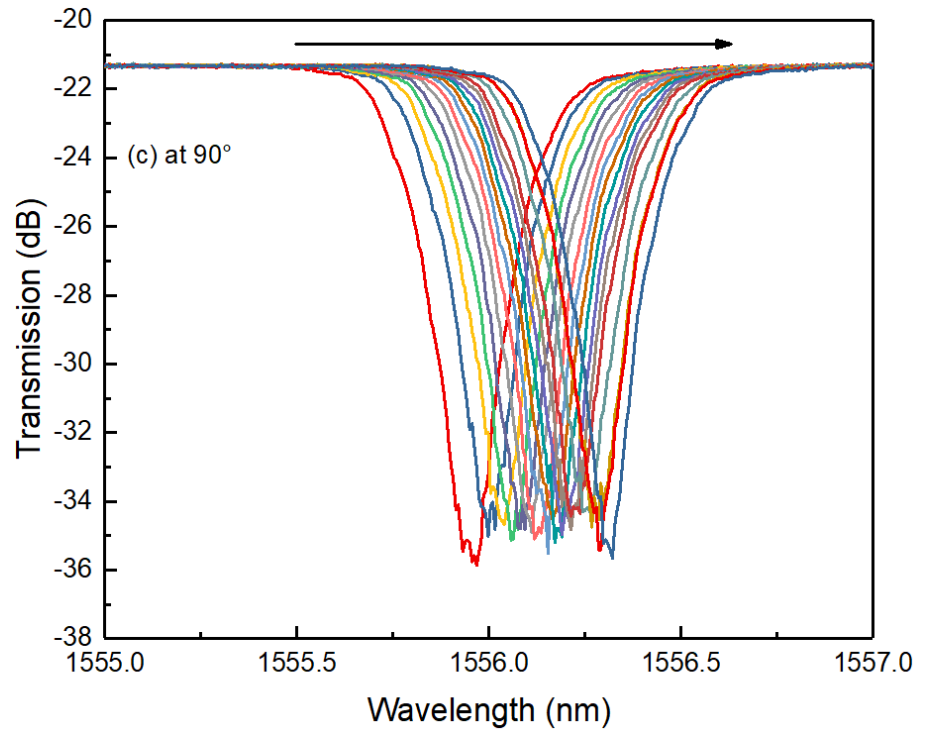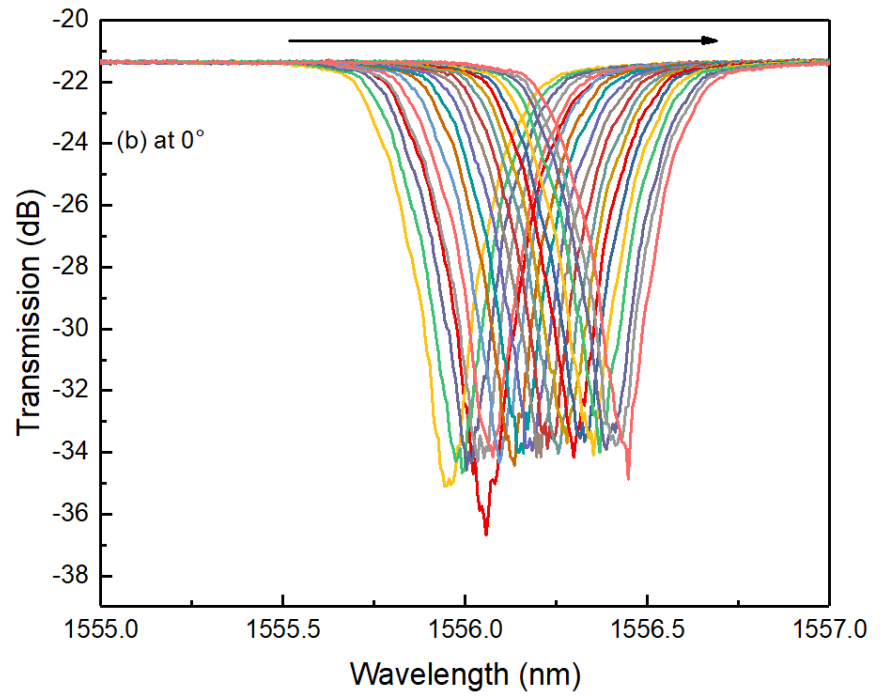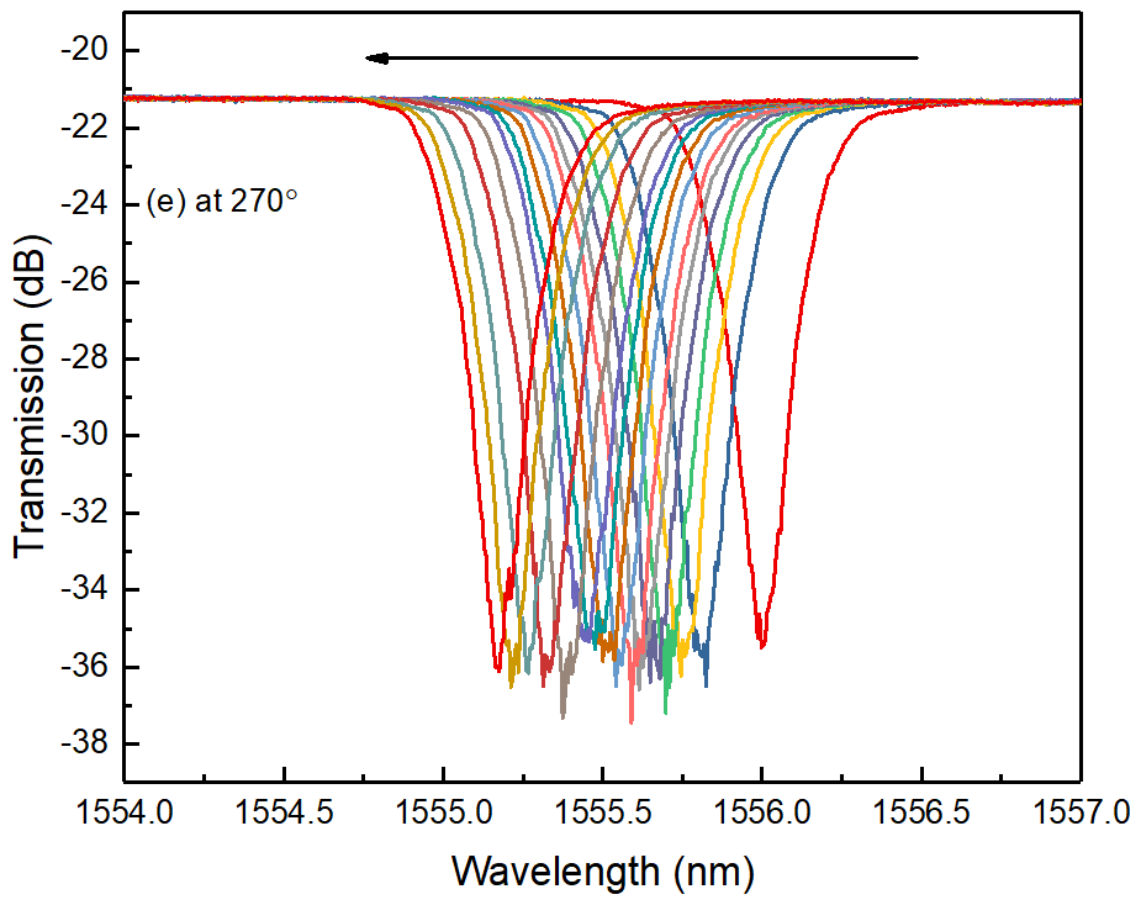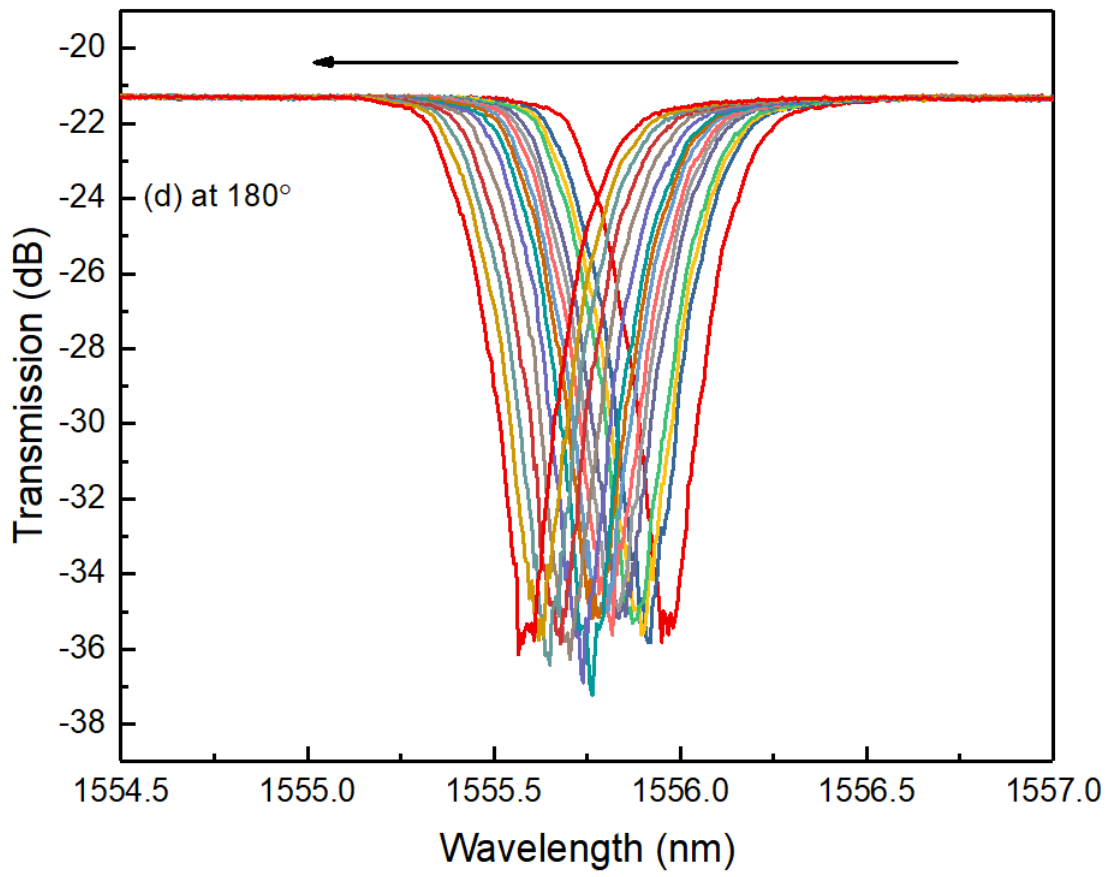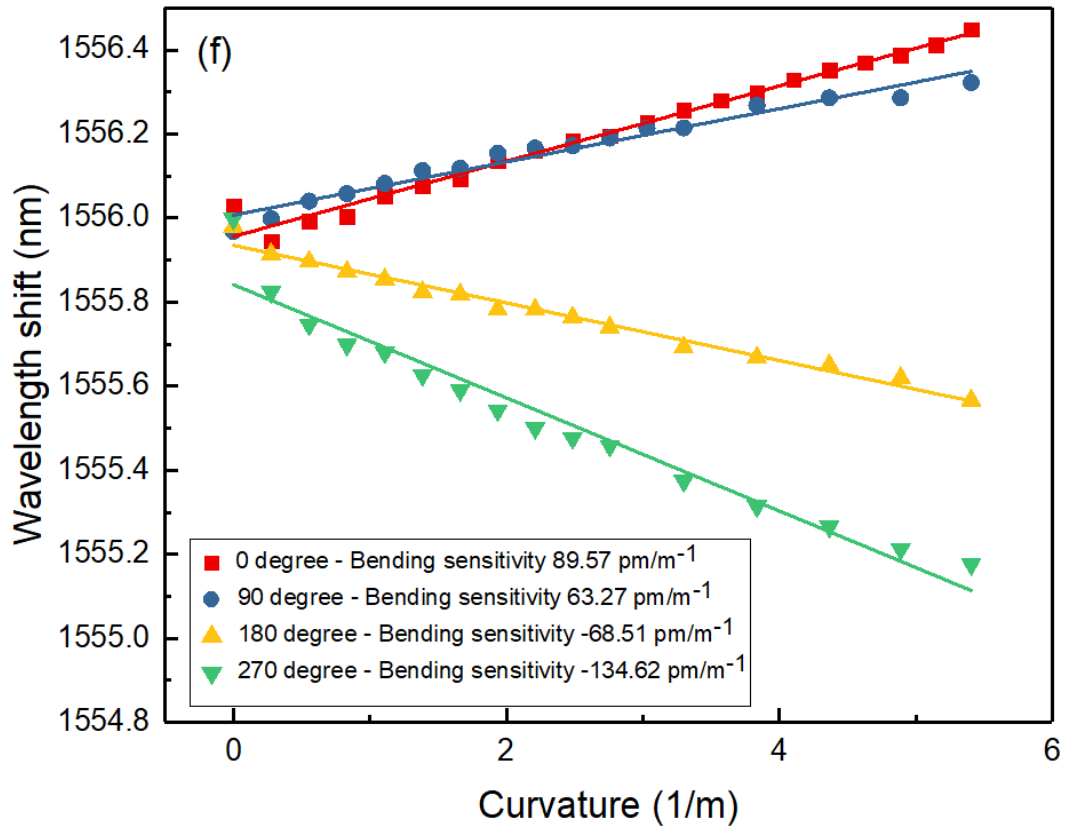
Figure 4. 22 (a) The core positioning for 7CF; The 3rd core FBG spectral responses when the fibre subjected to the bending under four twist angles: (b) 0°; (c) 90°; (d) 180°; (e) 270°. (f) Plotted bending sensitivities for the 3rd core FBG, clearly showing the changes in curvature and in direction.

To investigate the full bending/twisting capability of the 7CF-FBG, we also evaluated the FBG spectral change of the 6th core, which is in the opposite position as the 3rd core. Figure 4.23 (a, b, c, d) show the spectral evolution of the FBG inscribed in the 6th core when the fibre subjected to the bending and twisting at 0°, 90°, 180° and 270°. As the 6th core is opposite to the 3rd core, we expect the curvature induced Bragg resonance shifts will show opposite trends to the 3rd core. From Fig. 4.23 (a, b) we can clearly see when the fibre is twisted at 0° and 90°, the increase in bending applied to the fibre induces the Bragg resonance blue-shifts, whereas when the fibre is twisted at 180° and 270°, results in Bragg resonance of red-shifts. The bending sensitivity trends at the four twist angles are plotted in Fig. 4.23 (e), showing the values of -55.2 pm/m^{-1} and -71.79 pm/m^{-1} at 0° and 90°, and 47.37 pm/m^{-1} and 120.68 pm/m^{-1} at 180° and 270°, respectively. In an ideal model, as the 3rd core and 6th core are opposite and symmetrically distributed in the 7CF, their spectral response to the bending under the same twist angle should be identical in sensitivity of amplitude and opposite in movement direction. Our experimental results of the 3rd and 6th core clearly show the opposite movements but with some discrepancy in bending sensitivity amplitudes due to inaccuracies in the fibre alignment and the applied curvature to the fibre.

(c) at 180°

(d) at 270°
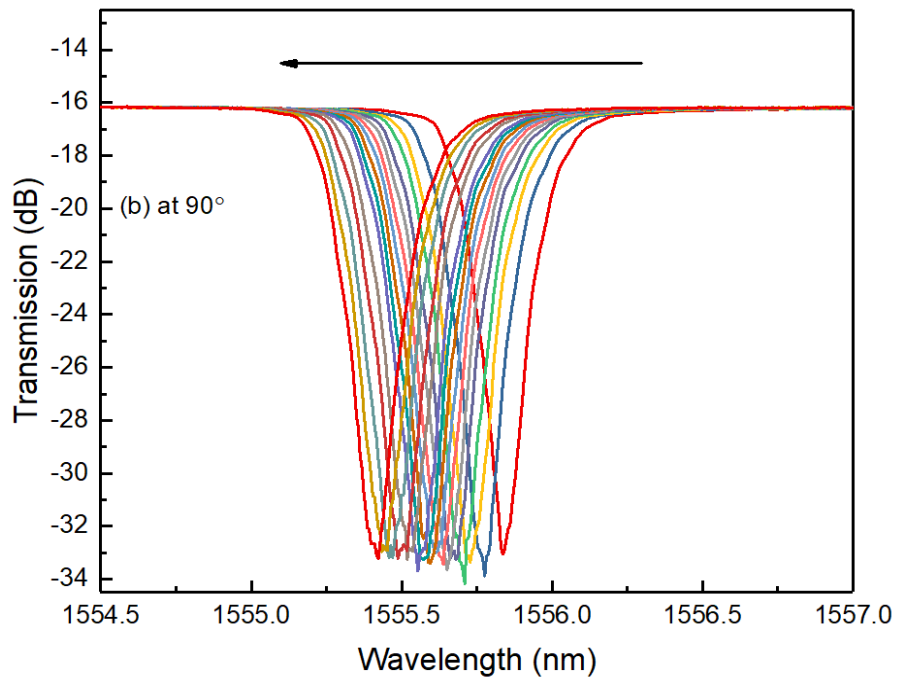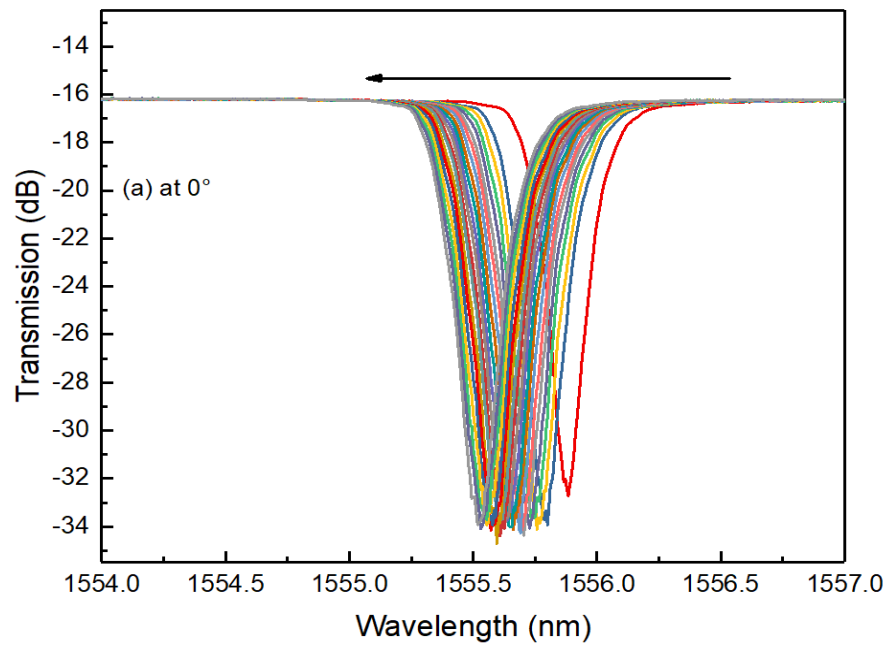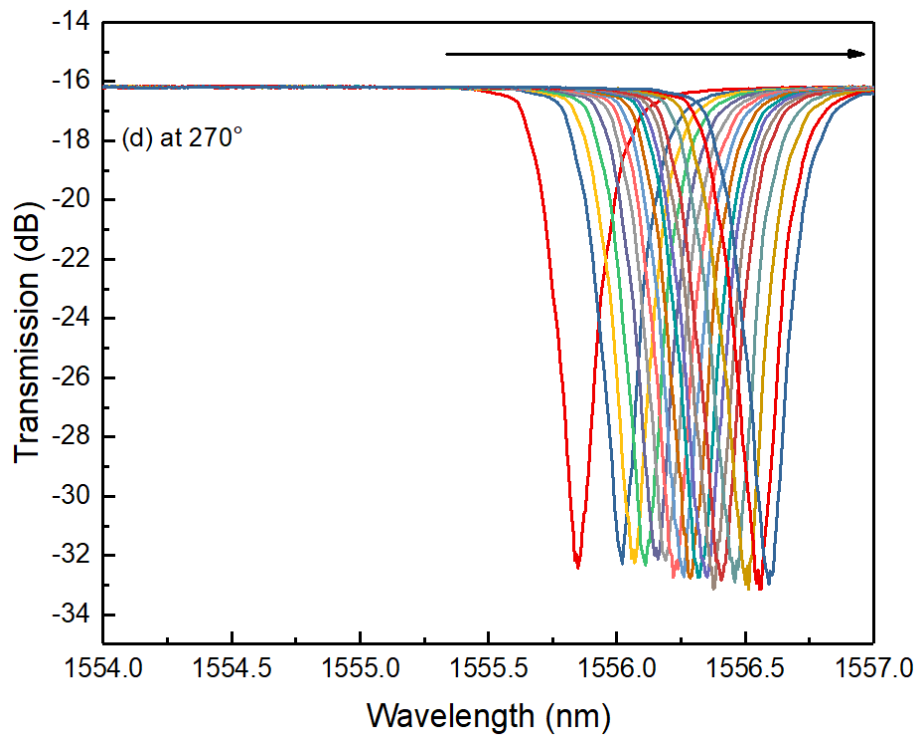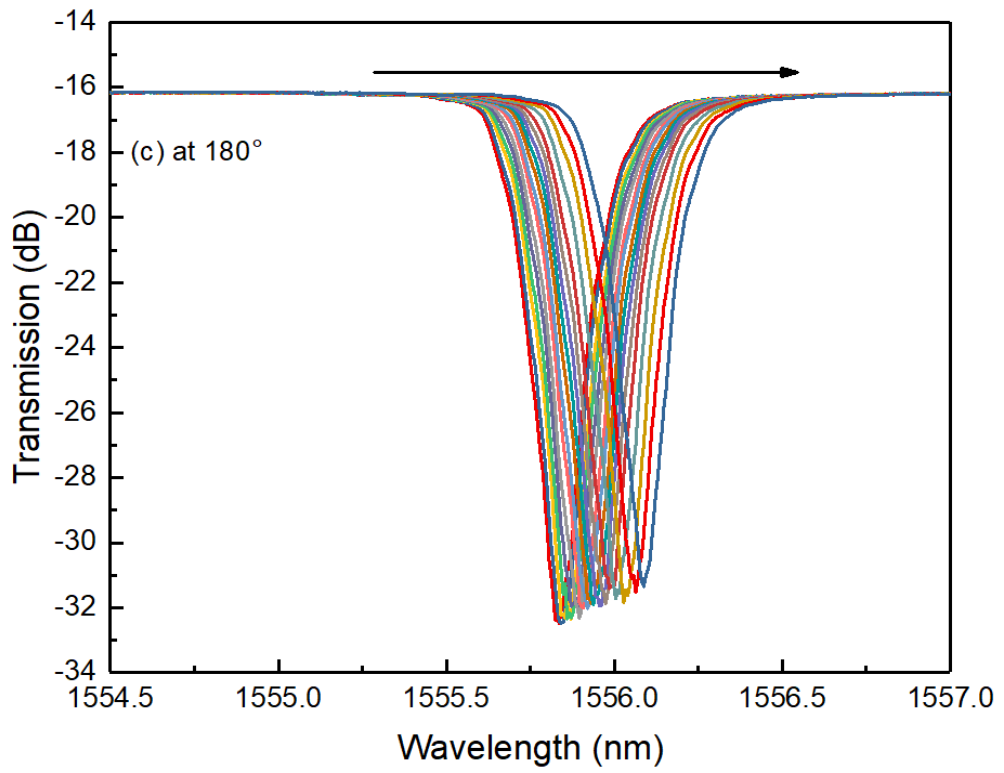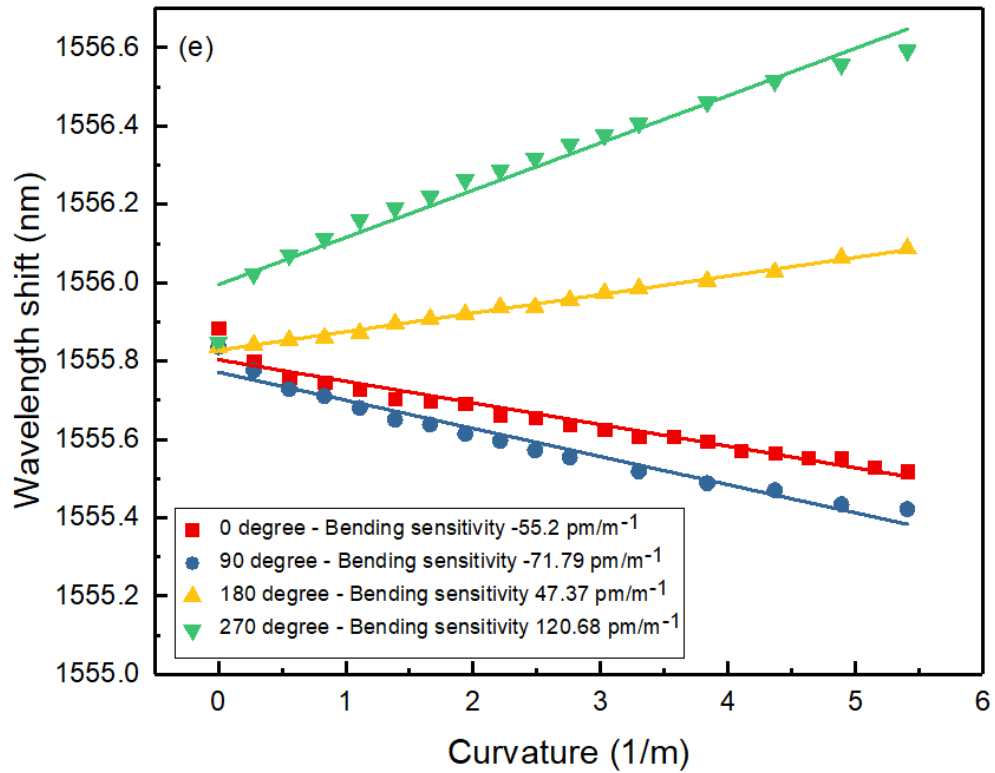
Figure 4. 23 The 6th core FBG spectral responses when the fibre subjected to the bending under four twist angles: (a) 0°; (b) 90°; (c) 180°; (d) 270°. (e) Plotted bending sensitivities for the 6th core FBG, clearly showing the changes in curvature and in direction.

As mentioned in the introduction, one of added unique advantages of vector sensing using the 7CF is that the central core will only be sensitive to the temperature and immune to the structure deformation caused by bending, loading, or twisting. To prove this merit, we have also measured the spectral evolution of the central core labelled as 7, and the results of bending response of the 7th core FBG are given in Fig. 4.24. In comparison with the 3rd and 6th core, the Bragg resonance of the central core hardly moved (Fig. 4.24a). The wavelength shift against the curvature for the central core is plotted in Fig. 4.24 (b), as shown, the shift is consequently small as the maximum curvature caused resonance shift is less than 0.1 nm, and the slope is only -8.83 pm/m^{-1}, which is about one order of magnitude lower than that of the 3rd and 6th core FBGs. This evidently indicates that the central core can be used as the reference to eliminate the temperature effect on the 7CF-FBG as structure monitoring sensor.
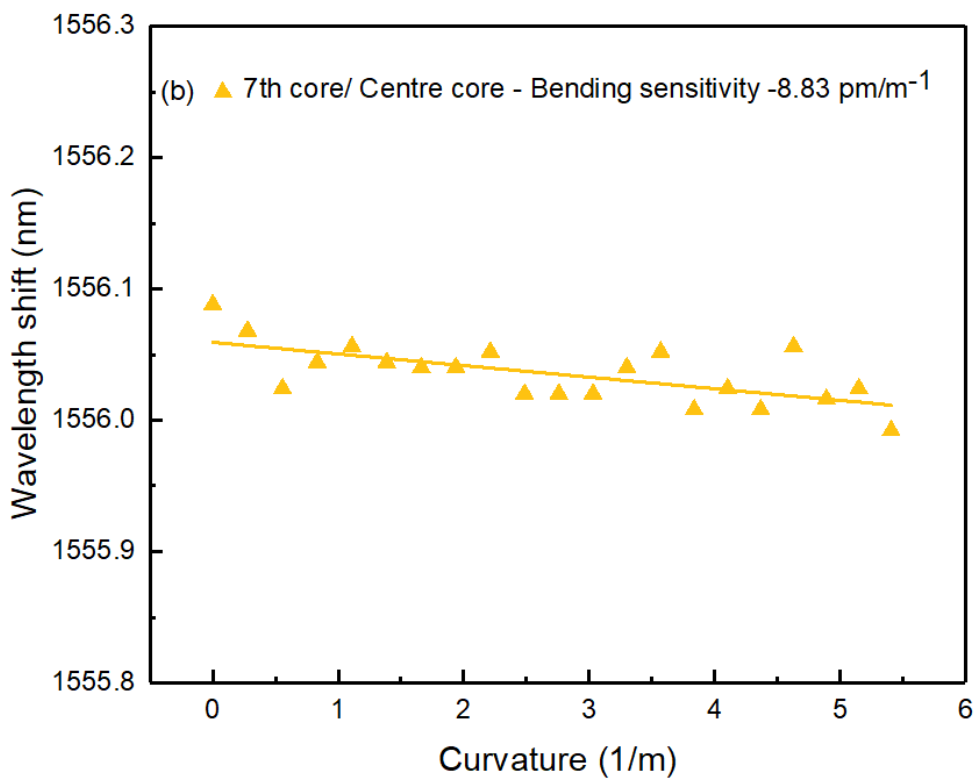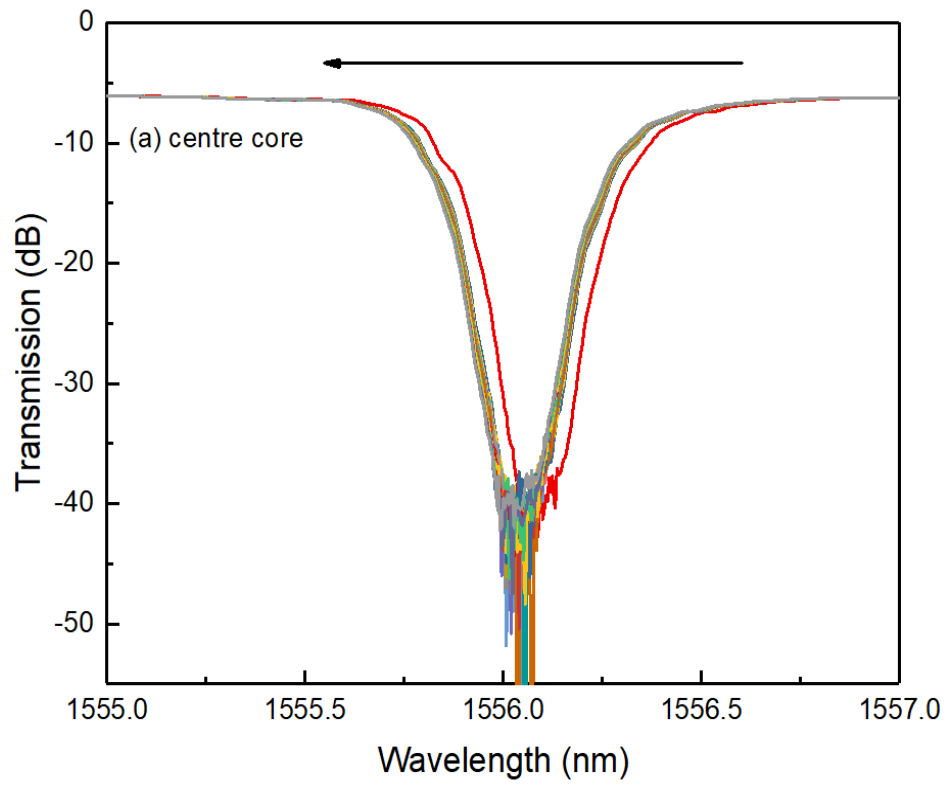
Figure 4. 24 (a) The spectra of the central core FBG under bending change; (b) Wavelength shift plot against the curvature for the central core.

4.6 Chapter conclusion

We have demonstrated an effective selective inscription method for UV inscribed FBG structures depending on the geometrical arrangement of cores, defocusing length and relative position between laser irradiation beam and fibre cores.

FBGs are fabricated for various core positions of 4CF with 50 μm core to core spacing. The three different core arrangements have been considered and these are aligned for achieving UV-inscribed FBGs at single top core only, top two cores and all the cores respectively where the cores are distributed in the rhombus and square geometry. A maximum of ~14 dB transmission is achieved when all the cores are aligned at a defocusing distance of 94 mm for UV radiation. However, the spectral measurement for FBG inscribed into other cores show variation in transmission amplitude due to light coupling and required more precise alignment. The bending/twist sensing measurement results with two diagonally opposite positioned cores show opposite wavelength shift at 180° with bending sensitivities of -0.085 nm/m^{-1} for core 2 and 0.052 nm/m^{-1} for core 4 respectively.

The 4CF with core to core spacing of 36 μm has also been investigated for characterisation and sensing measurements of UV inscribed FBG into both bottom core and all the cores respectively. The cores are aligned in the rhombus and square geometry similar to the previous structure of core spacing arrangement. Highest transmission of ~30 dB has been obtained for the fibre set at a defocusing distance to be radiated with larger UV focused beam. The bending sensing results in inversed wavelength shift for two orthogonally located core 2 and 4 with the bending sensitivity values of 0.125 nm/m^{-1} and -0.163 nm/m^{-1} respectively, which are significantly higher than that of FBGs in 4CF with 50 μm core to core spacing.

The Bragg resonance can be as strong as 27 dB in the central core of 7CF. Due to the alignment condition and the fluctuation of the UV power, the FBGs in the distributed cores show some difference in Bragg resonance wavelength and strength. More precise alignment and control will reduce the discrepancy and generate more uniform FBGs in the cores of a 7CF. We have also investigated the vector bending responses of the FBGs inscribed in the two oppositely situated cores under four twisting angles (0°, 90°, 180° and 270°) with the measured sensitivity values of 0.089 nm/m^{-1}, 0.063 nm/m^{-1}, -0.068 nm/m^{-1} and 0.135 nm/m^{-1} for 3rd core and -0.055 nm/m^{-1}, -0.072 nm/m^{-1}, 0.047 nm/m^{-1} and 0.120 nm/m^{-1} for 6th core respectively.

The results clearly demonstrated the capability of such an MCF-FBG as a vector sensor because their resonances not just respond to the curvature amplitude but also direction. In addition, we have also

evaluated the central core as temperature reference function in the 7CF and the Bragg resonance of the central core showed insignificant response to the bending and twisting.

There are challenges with both intrinsic and extrinsic parameters such as variation of material properties and core alignment within MCF during fibre manufacturing process, along with laser power fluctuations and beam size. Also, a good control of cross exposure during height adjustment of core alignment situated in a particular plane for selective inscription and light cross coupling during measurements are required. Further improvement with the introduction of a microscope/camera control into the inscription system and installation of a fan-in-fan-out device while continuing measurements would facilitate the improvement for this sensor device performance.

Chapter 5

Fibre gratings based refractive index sensors for bio and environmental sensing applications

5.1 Introduction:

The application of biosciences and photonic sciences develops technological advancement in interdisciplinary field known as biophotonics [111]. It consists of interaction between light and biological molecules. The combination of major technological fields including lasers, photonics, nanotechnology, and biotechnology are integrated into biophotonics. This enhances the opportunity of light-guided applications such as in healthcare for detection and treatment of disease, clinical analysis, drug discovery, environmental and security sectors.

The optical biosensor is a key area in Biophotonics as these sensors utilise novel optical structures, coating materials and methods for analysing capability of detecting and distinguishing various classes of biomolecules [112-115]. Typically, the biomolecules are of small size, low weighed and consists of weak charge. So, this becomes very challenging for the detection via physical properties. As both sensitivity and selectivity are fundamentally important for biosensors, it is necessary to detect the rate of change of optical signal as a function of surrounding analyte concentration. The solutes with low concentration are ideal for sensors as these require binding of the analyte for sufficient sensitivity. The development of chemsensors and biosensors for the analytes are limited to the materials ability to acquire the affinity from interfering substances [116-118].

Optical fibre gratings are advantageous in the application as optical sensors due to high sensitivity and environmental ruggedness. The sensitivity is determined with respect to the effective refractive index changes in the surroundings of the fibre surface. The variations can be modified with the light propagating condition and resulting spectral modulations in the transmission or reflection spectra [119]. Till now, fibre-optic refractive index-based sensors are largely used for the determination of material purity, monitoring surface binding event, detection of analyte layers and finding quantity of biomolecules and studying antigen-antibody features [120-122]. Generally, there are two common types of sensing principles for fibre-optic refractive index-based sensors, i.e., amplitude-based [123] and spectral-based [124]. The former detection scheme is associated with the increased or decreased value in the amplitude and is correlated with the refractive index variations, whereas the latter is related to resonance peak shift due to the modulation of refractive index of an analyte in the surrounding of certain grating structures, such as Bragg gratings [125], interferometers [126], and whispering-gallery-mode resonator [127]. These would modify the resonant property of sensor structure and result in wavelength shifts of the spectra.

In Aston photonics research lab, we have developed label-free detection methods where the target molecules could be detected with their natural forms without any label or modification so that the in-

situ detection is enabled. This method is easy to implement and allows quantitative and direct measurement of molecular interaction. The SRI-sensitive device based on label free technique has been developed by UV-inscribing normal Bragg, tilted and long period grating structures in various type of fibres. Appropriate choice of fibre type can provide intrinsic or enhanced SRI sensitivity to grating structures. The fibre grating based sensor device can be coated with bioactive materials to interact with certain types of biological agents, thus the application of accurate biosensors with high sensitivity and selectivity.

The optical fibre biosensors are applicable in food safety where it is required for identification and detection of any contaminants for the prevention of any disease [128], medical diagnosis such as monitoring the sugar and haemoglobin in blood stream [129, 130] and environmental monitoring with relative humidity (RH) sensing for industrial application and in the detection of heavy metals in drinking water [131-133].

In this chapter firstly, the RI sensitivity is studied with different glucose concentrations using different types of fibre sensors. Then a novel glucose sensor with enzyme immobilised dual-peak long period grating device is analysed. Secondly, by applying two-dimensional nanomaterial such as graphene coated novel fibre sensors are demonstrated and characterised for haemoglobin (Hb) sensing. Also, the graphene oxide coated sensors are demonstrated for environmental sensing application for relative humidity (RH) sensing. Finally, the carbon nanotube coated fibre sensing device is evaluated for surrounding refractive index sensing.

5.2 Refractive index sensing principle of core-cladding coupled in-fibre gratings

In an FBG the light coupling occurs as core-to-core mode and the light is well confined in the core by the cladding, effectively protecting strong interaction with the surrounding medium, thus it is intrinsically insensitive to SRI. However, LPGs are intrinsically sensitive to SRI as the light is coupled from core to cladding modes. The light guiding properties of LPGs are dependent on the variation of core-cladding mode and hence it will affect the LPGs transmission spectra. The output optical signal modified with the information of external parameters. The LPGs are used for monitoring various physical parameters such as strain, temperature, load, curvature and different structures for SRI sensing [72, 134].

A complete theoretical analysis of SRI sensitivity of normal and dual peak LPG structures is presented by Shu. et al. An optimised design tool was expressed for SRI LPG based sensor device. Recalling the analytical equations, as expressed in Chapter 3 for the SRI sensitivity at resonant wavelength of $d\lambda_{res}/dn_{sur}$ [72, 134, 135],

$$\frac{d\lambda_{res}}{dn_{sur}} = \lambda_{res}.\gamma.\Gamma_{sur} \tag{5.1}$$

where γ is the waveguide dispersion and is given by,

$$\gamma = \frac{d\lambda_{res} / d\Lambda}{n_{co}^{eff} - n_{cl,m}^{eff}} \tag{5.2}$$

The term Γ_{sur} is the surrounding refractive index dependent factor and is defined as,

$$\Gamma_{sur} = -\frac{u_m^2 \lambda_{res}^3 n_{sur}}{8\pi r_{cl}^3 n_{cl}(n_{co}^{eff} - n_{cl,m}^{eff})(n_{cl}^2 - n_{sur}^2)^{3/2}} \tag{5.3}$$

Here, u_m is the m-th root of the zeroth order Bessel function of the first kind, r_{cl} is the radius of fibre cladding, n_{cl} and n_{sur} are the refractive indices for the fibre cladding and surrounding medium respectively. Therefore, the SRI sensitivity of LPG based sensor devices are determined from the γ and Γ factors. These are dependent on the grating design parameters and fibre materials. Further explanation by Shu et al., also demonstrates ultrasensitive SRI sensing features for dual peak LPG at the dispersion turning points [72]. The experimental results in chapter 3 demonstrates a proper agreement with theoretical analysis.

5.3 Enzyme-functionalised biosensor based on fibre gratings for glucose detection

Fundamentally the chemical sensing principle of the in-fibre gratings is dependent on the resonance response to the SRI change. Here, various types of grating sensors are evaluated for their SRI sensitivity with respect to the measurements of different concentrations of sugar solutions. The calibration of refractive index for different sugar concentrations is presented here.

Glucose is important for human health by providing essential nutrient for maintaining healthy brain performance and protecting muscles from malfunctions. In principle, long period fibre gratings (LPGs) and large angled tilted gratings (Ex-TFGs) are associated with the coupling of light between fundamental core mode to the forward propagating lower & higher order cladding modes respectively. This enables the interaction between the surrounding medium and the radiation modes. The grating inscription method and sensitivity analysis are detailed previously in Chapter 3. The following section discusses the LPGs and Ex-TFGs which are surface treated and followed by SRI sensing achieved for different concentrations of sugar solutions.

5.3.1 Calibration of RI and sugar concentration

Raw brown sugar has been known to contain various useful nutrients with vitamins and especially minerals such as calcium, phosphorous, magnesium, iron, potassium, zinc, and sodium, with less calories than white sugar. Different concentrations (0% - 50%) of sugar solutions were prepared with the sugar purchased from supermarket and deionised water. The RI increases linearly with the increase in concentration of sugar solutions. Figure 5.1 shows the prepared solutions for various concentrations. The refractive index of each solution was measured with Abbe refractometer. Table 5.1 represents in detail the conversion relationship between the percentage sugar concentration and the refractive index. Figure 5.2 plots graphically the presented data in the mentioned table.

(a)　　　　　　　　　　　　　　　　　　　　　(b)

Figure 5. 1 Photographs of raw sugar (a) and different concentration of sugar solutions prepared with DI water (b).

Table 5. 1 Measured RI for different concentrations of sugar solution.

Concentration of solution (%)	Sugar (gm)	DI water (ml)	RI measured
0	0	10	1.3330
10	1	10	1.3475
20	2	10	1.3590
30	3	10	1.3695
40	4	10	1.3795
50	5	10	1.3885
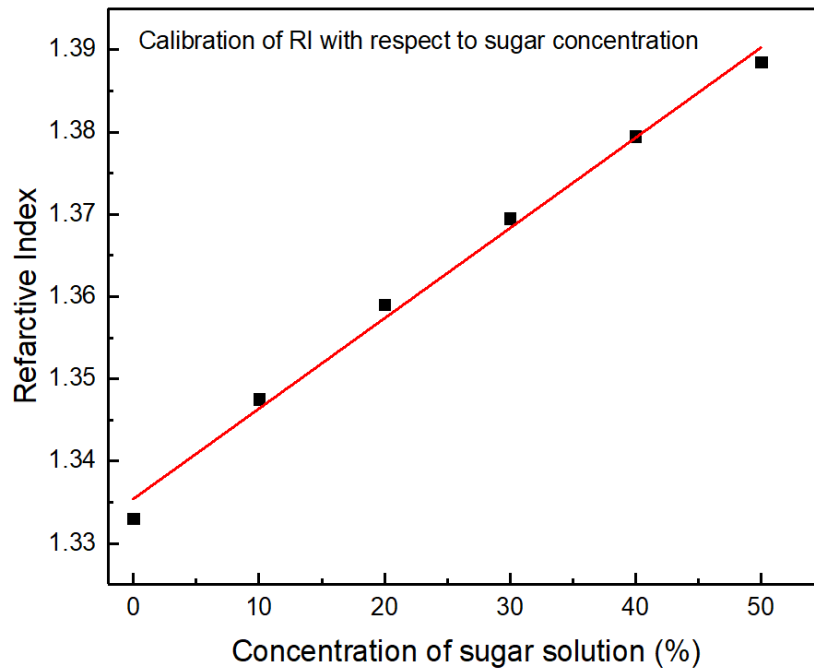
Figure 5. 2 Calibration plot for refractive index for different concentration of sugar solutions.

5.3.2 Fibre grating devices for sugar level sensing measurement at room temperature

The sugar level sensing was performed for fibre gratings using the setup shown in Fig. 3.16 in Chapter 3. Three different types of grating, such as UV inscribed LPG and dLPG with 415 μm and 150 μm period, an Ex-TFG with 81° tilt angle was considered for this purpose. During SRI sensing measurement process each grating device was set firmly between two 3D translation stages and input light launched through a broadband source (BBS Agilent 83437A) at one end. As mentioned in Table 5.1, a set of sugar solutions with refractive index ranging from 1.3330 to 1.3795 were prepared and applied onto the sensor to characterise the SRI sensitivity. The spectra were evaluated with an OSA connected at the other end of the device. The grating surface was thoroughly cleaned after applying each sugar solution to maintain the same reference level.

The sensitivity analysis with different sugar solutions for normal LPG provides a blue wavelength shift of 16 nm for the higher order resonance peak 2 and the sensitivity is achieved at -103.2 pm/ % conc. as shown in Fig. 5.3 (a & b). Figure 5.3 (c & d) shows a real time shifting of dual peak LPG in two opposite directions with peak 1 shifted towards shorter wavelength while peak 2 moved towards longer wavelength as the concentration of sugar solution increases. Both peak 1 and peak 2 has the sensitivities of -0.548 nm/ % conc. and 1.048 nm/ % conc. in the range of 0% - 40% concentration of sugar solution. From Fig. 5.3 (c), peak 1 is blue shifted with 23 nm and peak 2 is red shifted with

42 nm for varying concentration of sugar solutions. As expected, the evaluated SRI sensitivity for dLPG results higher value compared to normal LPG.

(a)

(b)

(c)

(d)
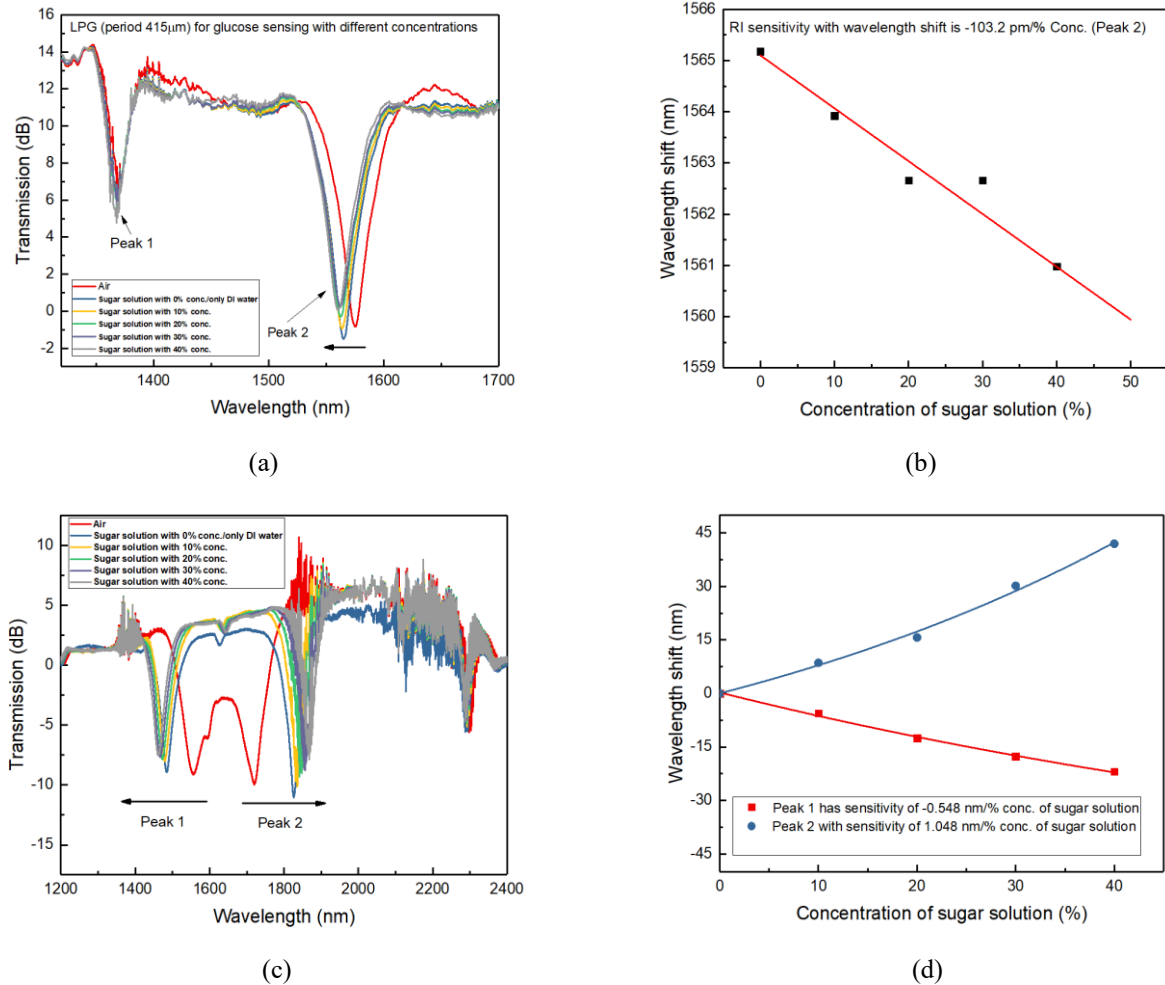
Figure 5. 3 Transmission spectral evaluation and resonant wavelength shift of normal LPG with blue wavelength shift in (a) & sensitivity plot for higher order resonance of peak 2 in (b); dual-peak LPG with opposite wavelength shift for peak 1 and peak 2 in (c) and sensitivity plots for the peaks 1 & 2 in (d).

A further investigation with Ex-TFG was also conducted. The coupled cladding modes are created into two sets of orthogonal polarisation states as shown in Fig. 5.4 (a). The corresponding zoomed spectra for peak resonance at ~1420 nm for both transverse magnetic (TM) and transverse electric (TE) modes are shown in Fig. 5.4 (b) providing an amplitude of 4 dB with both TM and TE polarised modes respectively. As for a normal Ex-TFG the TM mode is more sensitive to the SRI change, so the evaluation of SRI sensitivity for the TM mode is performed and there is a red shifted wavelength with the change in concentration of sugar solution. The corresponding sensitivity becomes 0.21 nm/ % conc. as depicted in Fig. 5.4 (c, d, e).

(a)

(b)

(c)

(d)

(e)
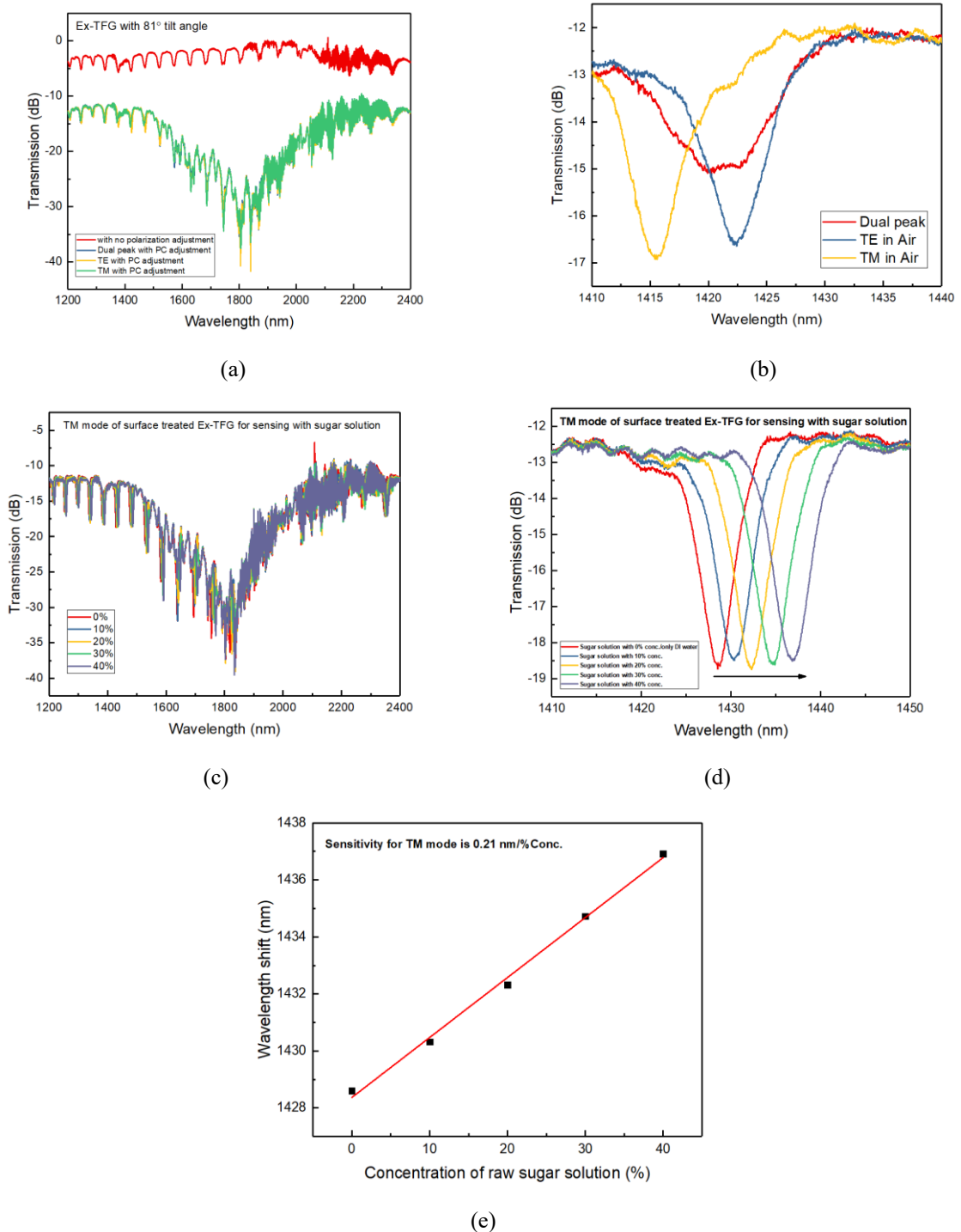
Figure 5. 4 Transmission spectral evaluation and resonant wavelength shift of Ex-TFG with full spectrum with and without polarisation controller (PC) in (a) and zoomed spectra for a dual peak resonance, and resonance peaks for TM & TE mode in (b), Sensitivity plots for TM mode for the entire spectrum (c) and at ~1420 nm in (d & e) for varying concentration of sugar solutions.

5.4 Glucose sensor based on enzyme-immobilised dLPG

Functionalisation of LPG surface with molecular reactive elements such as enzymes, nucleic acids (DNA), antibodies and antigens has enabled several bio-receptor immobilisation methods including covalent bonding [136], ionic bonding [137, 138] and absorption [139]. The most effective method

for covalent bonding is associated with active sites to chemically reactive and uninterrupted. Currently, the electrochemical method is implemented most frequently for the glucose detection. Here, we have investigated a more suitable sensor device that can be applied with high sensitivity achieved. A selective method can be followed with the conversion of glucose to gluconic acid by applying an enzyme. As a result, it is capable of detecting very low glucose concentration in the range of 0.10-3.0 mg/mL. Here, enzymes have been utilised as molecular recognition elements.

As discussed in previous chapters, the maximum sensitivity of cladding modes is associated with the wavelength shifts at the dispersion turning points for dual-peak LPG (dLPG). The high sensitivity is achieved by this dLPG structure inscribed into thin cladding fibre with core and cladding diameters of 4.2 μm and 80 μm respectively. This sensor device is functionalised with enzyme for immunosensing with glucose solutions. Enzyme functionalised sensors with normal LPG and Ex-TFG has been already reported [9, 140]. Here, a novel glucose sensor is fabricated with dLPG, and the results are analysed.

5.4.1 Grating surface modification by immobilising it with an enzyme known as glucose oxidase (GOD)

The glucose oxidase (GOD) is an enzyme which is enabling the oxidisation of D-glucose to its corresponding lactone when sufficient oxygen is present. All the chemicals including GOD, D-glucose, and a buffer solution of sodium acetate (SA) for pH 5.2 were purchased from Sigma Aldrich. The grating surface modification with GOD involves several steps. Firstly, the fibre sensors were immersed into HNO_3 solution (5% v/v) for 2 hours by placing these onto a hotplate at an ambient temperature condition of 40 °C. It would effectively remove any contamination onto the sensor and then washed with de-ionised water and ethanol multiple times. Afterwards, the cleaned fibres were immersed into H_2SO_4 solution (95% v/v in H_2O_2) for 1h at room temperature condition to activate the hydroxyl-groups (i.e., '-OH') on the sensor surface and drying at an incubated temperature of 40 °C for 18 hours. Then the device was silanised with (3-Aminopropyl) triethoxysilane (APTES) (10% v/v into ethanol) solution. The sensor device was immersed into the solution at room temperature for a duration of 40 mins. In this process the NH^{3+} groups of the APTES molecules would covalently link with the '-OH' groups of the sensing surface. Thereafter, the fibre was cleaned with de-ionised water and ethanol for several times to remove the non-covalently bonded silane compounds. Then a 10 mg/mL sodium acetate (SA) buffer solution was prepared with GOD. Finally, the dLPG device was immersed into the buffered solution of GOD for 2h incubation, where the GOD's '-COOH' group would bind with NH^{3+} groups on the surface of the silanised fibre. Figure 5.5 shows the whole chemical reactions onto the fibre surface.
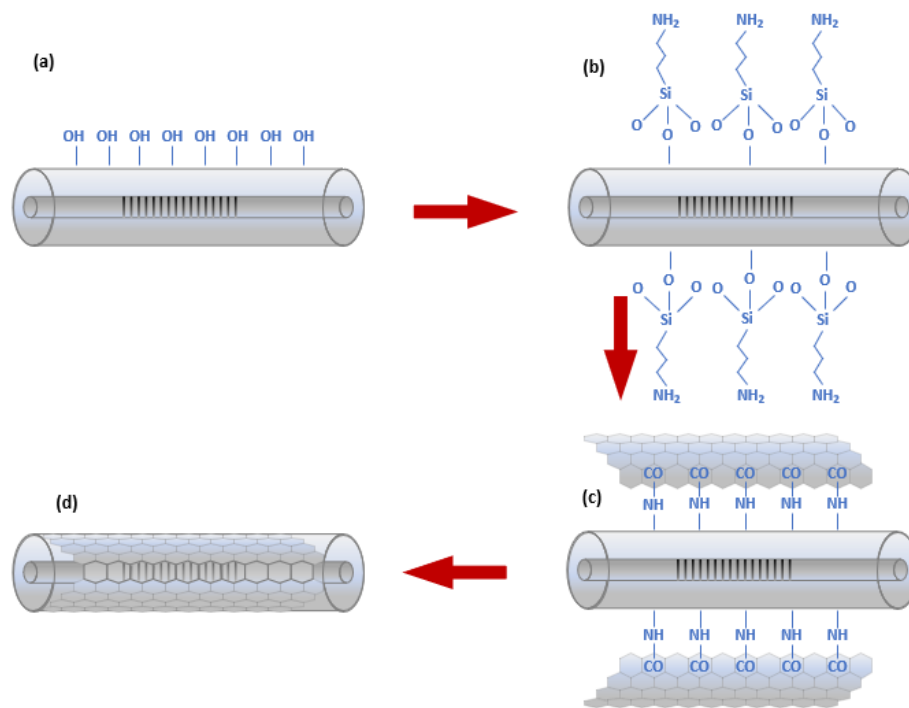
Figure 5. 5 The functionalisation process for the dLPG fibre sensor surface with (a) cleaning of the fibre, (b) APTES silanisation and (c&d) during and after GOD immobilisation.

The spectral property was examined in-situ during the enzyme immobilisation process. Figure 5.6 (a, b) shows the resonance responses for all the attenuation peaks after each step of surface treatment process. It is seen from the figures that after the sensing device is surface treated and silanised with APTES there is no wavelength shift of attenuation bands has been observed. However, after enzyme functionalisation with GOD significant wavelength shifts are obtained for all the attenuation peaks. There is opposite wavelength shift for two conjugated peaks 2 and 3 with the magnitudes of -45 nm and 86 nm respectively. A comparatively very small resonance shifts are observed for peaks 1 and 4 with both as blue shifted. The evaluated values are analysed as ~3 and ~5 nm for both peaks 1 and 4 respectively. These results clearly show that the dual peaks are ultra-sensitive to SRI in respect to the other order resonances 1.
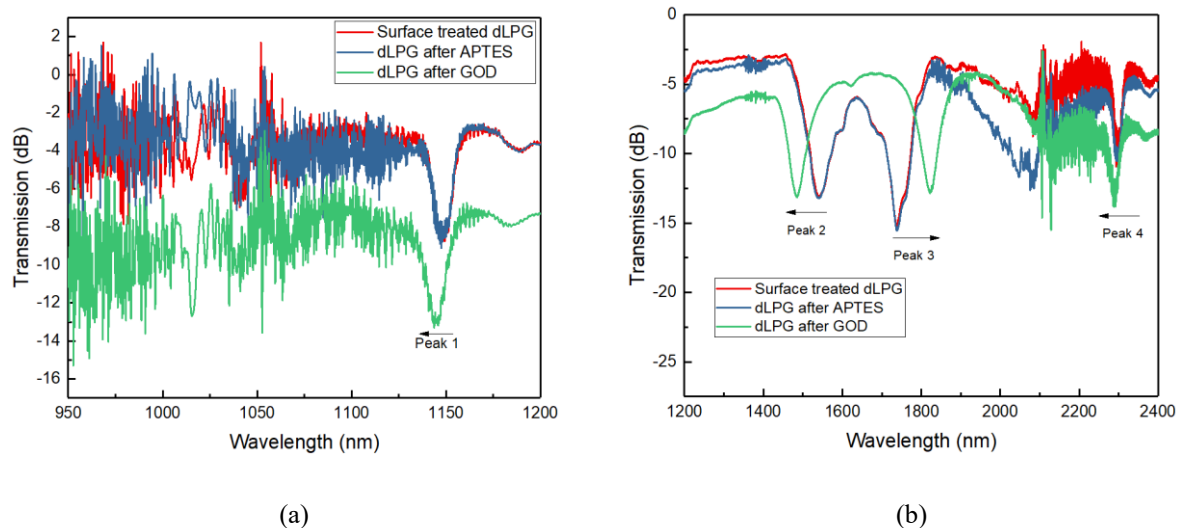
Figure 5. 6 Spectral evaluation for dLPG after each process of surface treatment, silanisation with APTES and enzyme functionalisation with GOD in both lower wavelength peak 1 (a) and higher wavelength peaks 2,3 & 4 (b).

5.4.2 Glucose detection by GOD-immobilised dLPG

The prepared GOD-immobilised dLPG sensor device was used for glucose detection. The experimentation followed the selective method where the enzyme immobilised on the fibre surface of dLPG will convert the glucose into gluconic acid as shown in Fig. 5.7 causing a large refractive index change in the glucose concentration range of 0.1-3 mg/mL. This in turn introduces a resonance wavelength shift of the grating sensor.
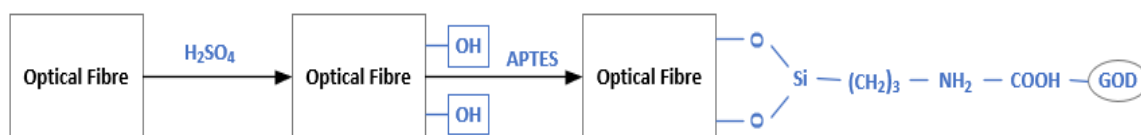
Figure 5. 7 The modified process onto the fibre surface converting the glucose into gluconic acid.

GOD used for the experiment was procured from Sigma-Aldrich with 50,000 units/g solid (without added oxygen) and after oxidisation the β-D-Glucose is converted into D-gluconic acid and H_2O_2 with a buffered solution of pH 5.2. Preparation of glucose solutions was performed with D-glucose (0.1-3 mg/ mL) in the sodium acetate (SA) buffer. This provides a suitable chemical environment for this chemical reaction. The experimental setup for investigating the glucose sensing for enzyme immobilised dLPG sensing device is shown in Fig. 5.8. Light from supercontinuum source (Fianium superK, 950-2400 nm) was launched into the one end of the grating and the spectra were recorded through two optical spectrum analysers (OSA HP- 950-1200 nm & OSA YOKOGAWA - 1200-2400

nm) to cover all four resonance peaks from 1150 nm to 2300 nm (peak 1 in the lower wavelength range and peaks - 2, 3, 4 in the higher wavelength range). The resolution of the OSA was set as 0.20 nm for both, and each sweep scan was considered between 30-60 seconds.

The SA buffered solutions with various concentrations of D-glucose were prepared following the vol/vol measurement. In the process, firstly a maximum concentration of 3 mg/mL of D-glucose solution was prepared. Then consecutively 2.5, 2.0, 1.5, 1.0, 0.5 and 0.1 mg/mL solutions were prepared by adding required solvent to it. The measured refractive index value for the highest concentration was achieved as 1.3715 and reached to 1.3704 for 0.1 mg/mL of glucose solution. Then the SRI sensing for the GOD immobilised dLPG was achieved with different glucose solutions. The change in average refractive index occurs within the evanescent field area in the vicinity of grating surface and hence there is wavelength shifts for all the peaks. The combined effect of a large number of D-glucose molecules and enough active GOD molecules existing in the evanescent field area makes the greater change of n_{cl}^m , thus resulting in the wavelength shift of the dLPG resonance.
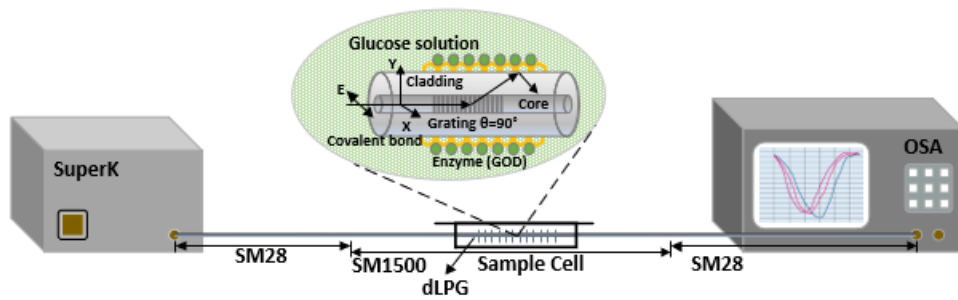
Figure 5. 8 Schematic of the experimental setup for glucose sensing of enzyme immobilised dLPG.

The plots in Fig. 5.9 (a&b) and (c&d) show the dLPG resonance shift for different concentrations of glucose solutions and the sensitivity analysis results respectively. It is seen in Fig. 5.9 (a&b) that a small red shift is achieved for the resonance peaks 1&4 of this normal dLPG sensing device. Whereas there are opposite wavelength shifts achieved for the conjugated attenuation peaks with the decrease in surrounding refractive index value as depicted in Fig. 5.9 (b). The analysed results in Fig. 5.9 (c) show the sensitivity for peak 1 and peak 4 are as 2.13 nm/ (mg/mL) & 2.97 nm/ (mg/mL) respectively. A maximum sensitivity of 19.92 nm/ (mg/mL) and -36.25 nm/ (mg/mL) are obtained for peaks 2 & 3 at 1470.72 nm and 1863.28 nm respectively. The evaluated results clearly demonstrate that enzyme functionalised dual peak resonances are more sensitive to SRI in comparison with the normal peaks 1 and 4.
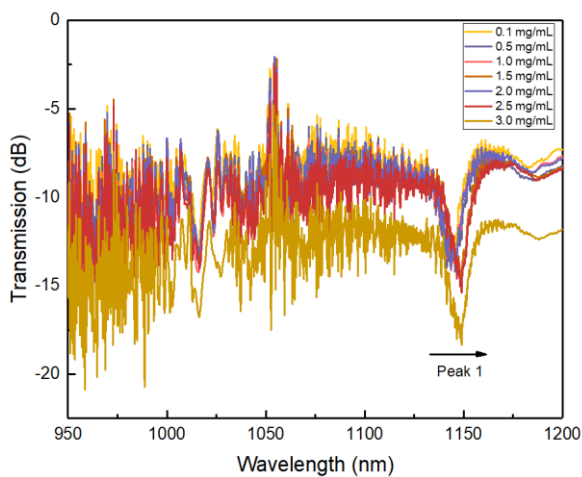
(a)
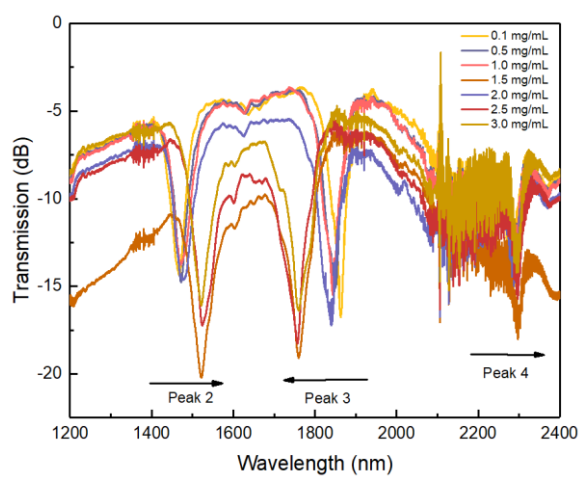
(b)
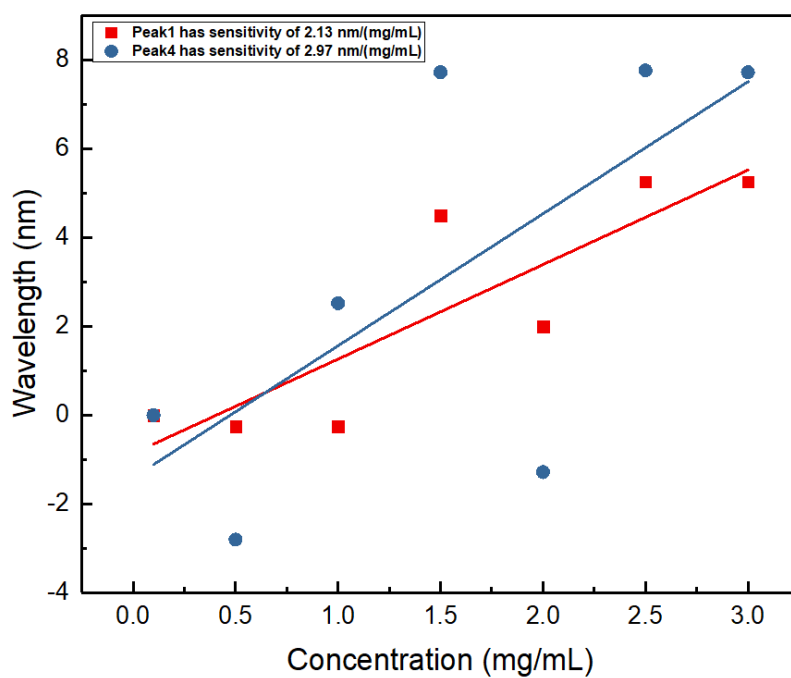
(c)
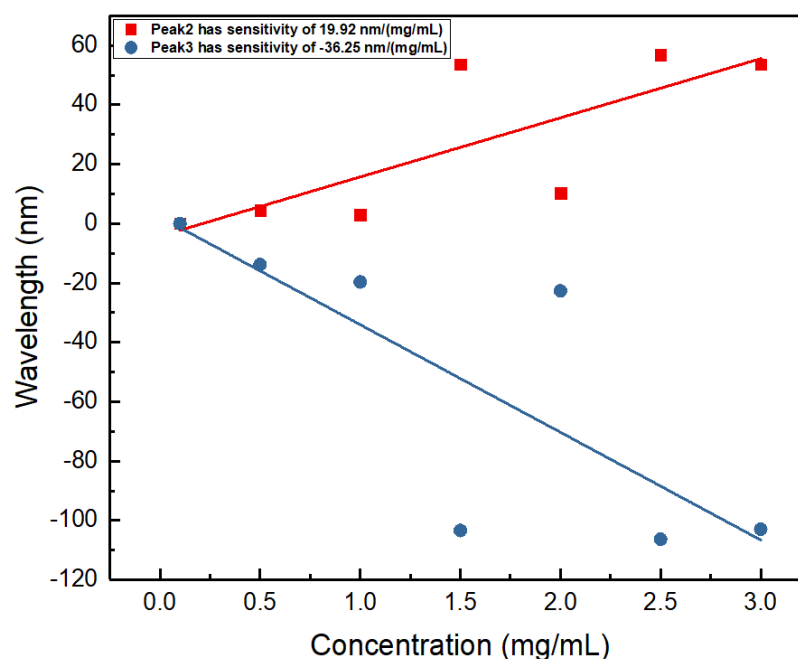
(d)

Figure 5. 9 Spectral evaluation for enzyme functionalised dLPG with various glucose concentrations for resonance peak 1 (a) and resonance peaks 2,3&4 (b); Sensitivity analysis for normal dual peaks 1 & 4 in (c) and for conjugated attenuation peaks 2 & 3 in (d).

5.5 Graphene oxide (GO)-based biosensor

Graphene oxide is a two-dimensional nanomaterial and an important precursor of graphene. It contains various oxygen-containing functional groups with hydroxyl and epoxies located in the basal plane. Besides these, it also contains some amounts of carboxyl, carbonyl and sometimes phenol, lactone and quinone at the edge of GO sheets [141-143]. These oxygenated functional groups introduce structural defects to the GO sheets and hence it affects the electronic and mechanical properties. The advantage of GO is the oxygen functional groups, which are generally hydrophilic and dispersible in many solvents, especially in water [144-146]. GO is an excellent photosensitive material showing good absorption. Hence, this is applied for the label free biosensing application with the effective refractive index (n_{eff}) is modified after GO coating. It is expressed with both real and imaginary parts of the refractive index equation. The imaginary part is responsible for optical absorption, whereas the real part is for wavelength shift [147]. As it will influence the cladding mode resonance through evanescent field, hence, the optical absorption is more effective with the intensity modulation occurring after an increase in GO concentration and number of layers deposited onto sensor surface.

Utilising the GO unique optical property, GO-coated sensing devices based on LPG and dLPG were fabricated for haemoglobin detection. This is an important application in health science where many

diseases need to be diagnosed by measuring the level of haemoglobin, such as anaemia. It affects the quality of life, and a timely clinical attention becomes necessary.

5.5.1 Graphene oxide deposition on grating surface

The GO nano colloidal solution with concentration of 2 mg/ mL was purchased from Sigma-Aldrich. The complete GO deposition process is shown in Fig. 5.10 (i & ii). A schematic of the method where the sensor was fixed onto a v-groove bath for GO dispersion using dip coating technique is presented in Fig. 5.10 (i). In this process, firstly, the LPG surface was cleaned with methanol and then with deionised (DI) water for multiple times. Then the fibre surface was alkaline treated by immersion into 1.0 M (1.0 mol/L) sodium hydroxide (NaOH) solution that enriches a number of hydroxyl ('-OH') group onto it to bind the GO film more effectively. Then the fibre surface was washed thoroughly with DI water and dried (Fig. 5.10 (ii - a)). The grating device was then immersed into a 5% of (3-Aminopropyl) triethoxysilane (APTES) solution (v/v in ethanol) to form Si- O- Si bonding onto the grating surface for 1h at room temperature. Then it was followed by washing with ethanol to remove unbound monomers and baked at 70 °C for half an hour to improve the stability of APTES monolayer (Fig. 5.10 (ii - b)). Finally, two separate GO solutions were prepared with DI water for two different concentrations of 0.5 and 1.2 mg/mL respectively and these solutions were used for multilayer deposition on the LPGs. In the GO deposition process the APTES-silanised LPG sensor device was placed onto the Teflon mini-bath and was immersed with the ~500 μL of GO-solution. After each deposition, the GO-LPG was placed onto a hotplate with set temperature at 55 °C for approximately 40 minutes. During this time the aqueous solution was evaporated slowly, leaving GO-nanosheets gradually absorbed onto the grating surface. Once the sensing device dried completely, then the second coating was applied following the same procedure. After GO coating the fibre surface appeared as brownish. A schematic during and after GO-deposition is shown in Fig. 5.10 (ii - c & d).

(i)

(ii)
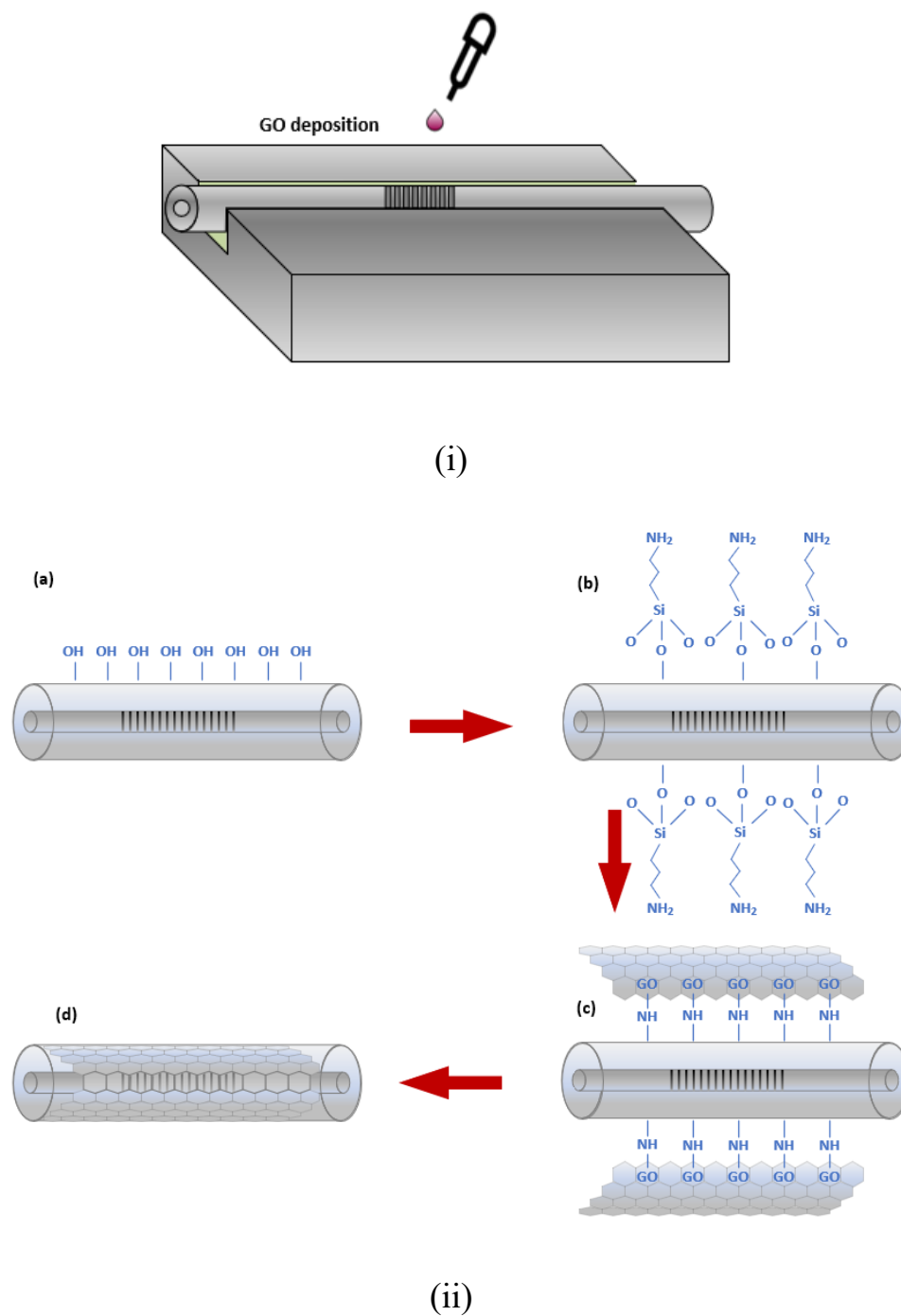
Figure 5. 10 (i) Schematic representation of GO-deposition process into a v-groove bath; (ii) Schematic of GO deposition process onto the fibre surface with (a) surface cleaning, (b) APTES silanisation and (c & d) during and after the GO deposition.

During the GO deposition process the grating surface was examined under the microscope for each step. Figure 5.11 shows the images of a grating device for each step involved in the GO-deposition process using an optical microscope (Carl Zeiss) by an objective of 20x. The comparison of Fig. 5.11 (a) and (b) shows that the grating surface has been silanised with a smooth layer of APTES. Whereas a brownish colored GO coating is seen in Fig. 5.11 (c&d) for GO concentrations of 0.5 mg/ mL &

1.2 mg/ mL. Overall, the images clearly show the GO coated layers are relatively uniform across the LPG surface.

(a)

(b)

(c)
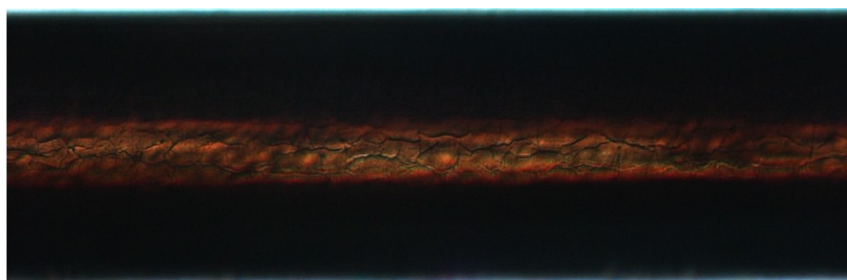
(d)

Figure 5. 11 Optical microscope images of the LPG & dLPG based on (a) NaOH treated, (b) silane fibre, (c) GO-coated fibre with GO concentration of 0.5 mg/ mL and (d) GO-coated fibre with GO concentration of 1.2 mg/ mL.

5.5.2 Optical properties with GO deposition

The optical properties of the GO-coated grating devices were investigated to find the capabilities of light-matter interaction in the vicinity of sensing structures. A uniform thickness can enhance the sensitivity of the fibre gratings to surrounding refractive index change. The difference in coating thickness over the sensing region shows different optical effect for the grating device. Two LPGs with 430 μm and 428 μm periods were coated with multilayers of different GO concentrations. The sensitivity measurements were performed for both LPGs for SRI and temperature change respectively.

5.5.2.1 Two-layers GO coated LPG for SRI sensing

To evaluate the SRI sensitivity an LPG with 430 μm period was considered for the experiment. The APTES silanised LPG was immersed into GO solution of concentration of 0.5 mg/mL and 2-layers of GO deposition were applied. Then the GO-coated LPG was utilised for SRI measurement by applying immersion oil in the range of higher refractive indices. Figure 5.12 (a) shows the spectral change for the large SRI values ranging between 1.412-1.460. It is seen that the higher order resonance band is more sensitive to SRI with respect to other lower order peaks in LPG. A zoomed spectra for 4th resonance peak at 1671.64 nm in Fig. 5.12 (b) shows both wavelength and intensity of peak 4 respond to the SRI change significantly. Fig. 5.12(c) plots the intensity change against the SRI showing a maximum sensitivity of -22.45 dB/RIU for peak 4. Fig. 5.12 (d) plots the red wavelength shift against SRI, presenting a sensitivity of 313.09 nm/ RIU with the increase in SRI. Here we clearly see the optical absorption through GO-layers is enhanced with the increase in SRI. The coupled forward propagating cladding modes are influenced by the effect of evanescent field and hence the increased attenuation as well as wavelength shift. As the effective index of the cladding mode is influenced by the both thickness of GO-coating and the number of layers depositing, hence the resonance shift varies accordingly. Therefore, a positive wavelength shift is observed in the surrounding refractive index range of 1.412 – 1.460 which agrees with the reported simulation results [148].
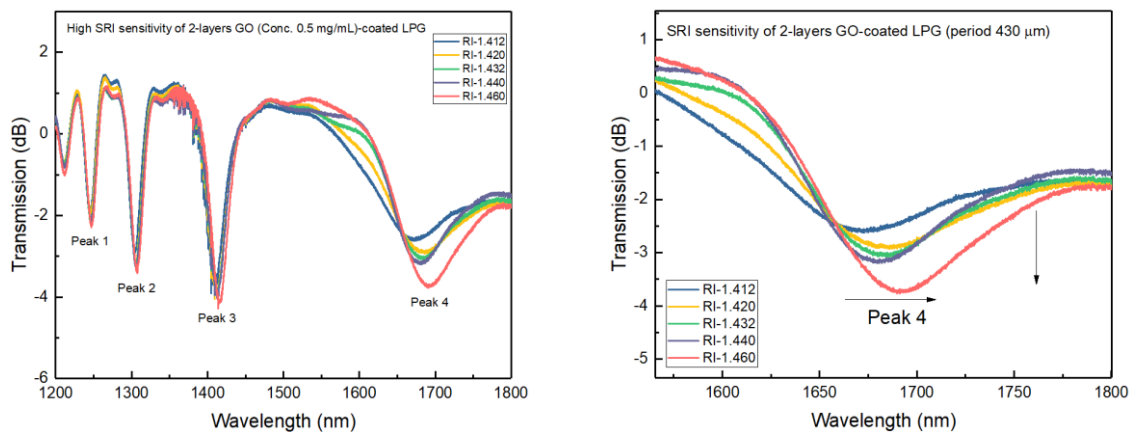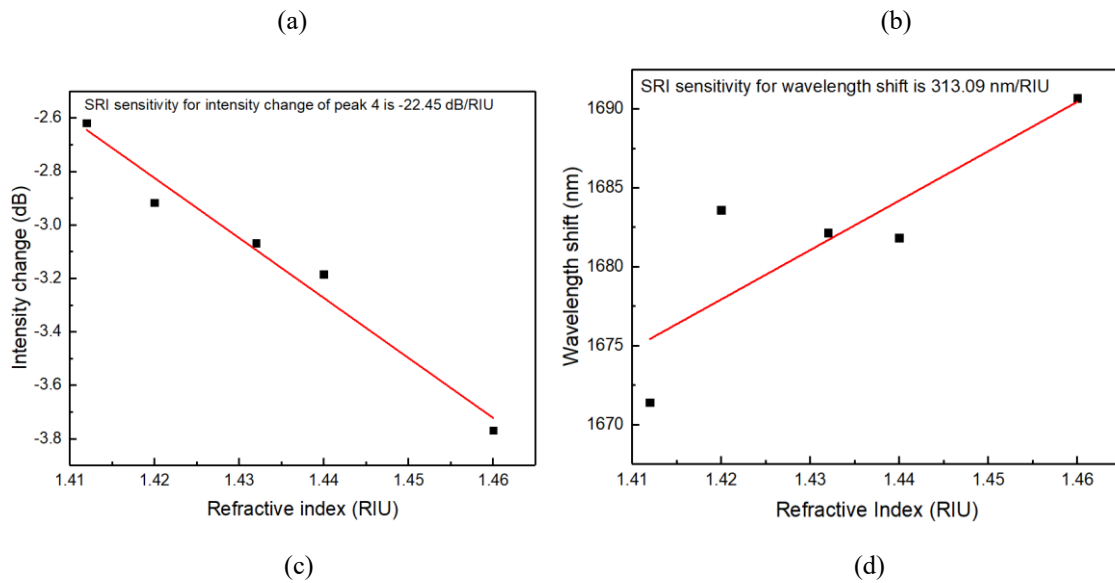
Figure 5. 12 SRI sensing measurement results for 2-layers GO-coated LPG; (a) spectral evaluation, (b) zoomed spectra for Peak 4, (c) sensitivity plot for intensity change, (d) sensitivity plot for wavelength shift.

5.5.2.2 Four-layers GO coated LPG for temperature sensing

A further investigation for optical properties with GO-coated LPG was performed for thermal sensing. In this case the temperature sensitivity of LPG is compared before and after GO-coating. Firstly, the LPG with 428 μm period was placed onto the Peltier setup for the spectral evaluation at different set temperature values. The process was continued for an entire range of 10-70 °C with an incremental step of 10 °C. Then, following the GO-deposition method the silanised LPG was immersed into GO solution of concentration of 1.2 mg/ mL. Consecutively, 4-layers of GO-coating were applied. Then the GO-coated LPG is set for thermal sensing measurement. The thermal sensitivity results are shown in Fig. 5.13 (a & b) for uncoated LPG. It is seen that the higher order resonance bands at 1410.96 nm and 1660.92 nm are more sensitive to thermal change with blue shifted wavelength. The higher sensitivity results for the resonance peaks 2 and 3 are investigated as -431.43 and -774.43 pm/°C respectively. Furthermore, the thermal sensitivity is analysed for 4-layers GO-coated LPG with same period of 428 μm. The plotted results are shown in Fig. 5.13 (c & d). The analysis for higher order resonances shows blue wavelength shift with sensitivity results as -275.57 and -586.43 pm/°C for peaks 2 and 3 respectively. The thermal sensitivity for resonance peak 3 of the GO-LPG is decreased by approximately ~200 pm/°C. A comparison of achieved sensitivity for wavelength shift is detailed in table 5.2. The resonance shift is influenced by a number of factors such as, the thermal expansion coefficient of the sensing device and the coating material, coating thickness and effective refractive index into the core and cladding modes. It is clearly seen that there is enhanced light- matter interaction after GO-layer deposition and hence the decreased thermal sensitivity for both the resonances as shown in Fig. 5.13 (b&d).

(a)

(b)

(c)

(d)
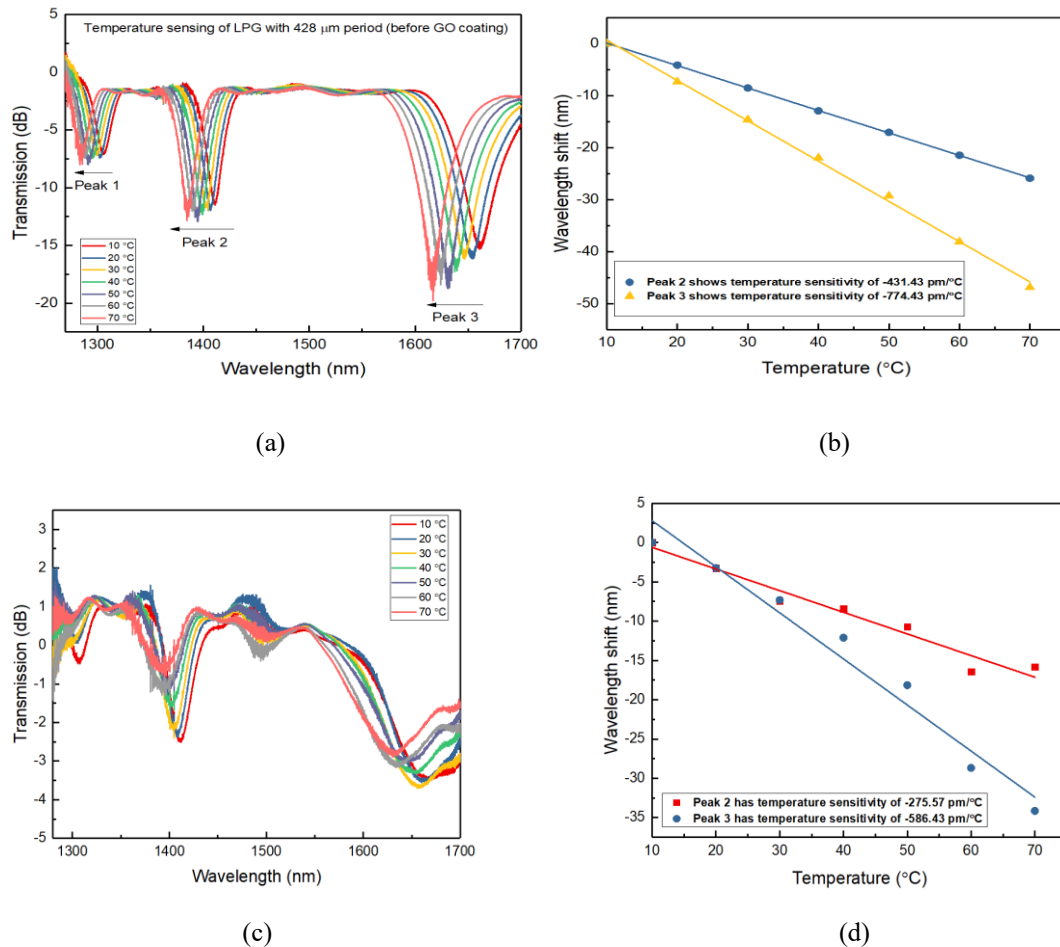
Figure 5. 13 Thermal sensing measurement results for LPG before and after 4-layers of GO-coating; (a & b) spectral evaluation and sensitivity results for peaks 2 & 3 before coating; (c & d) spectral evaluation and sensitivity results for peaks 2 & 3 after coating.

Table 5. 2 Temperature sensing of LPG before and after GO-coating.

Resonance wavelength	Sensitivity	
	Before coating with GO	After coating with GO
Peak 2 – 1410.96 nm	-431.43 pm/ °C	-275.57 pm/ °C
Peak 3 – 1660.92 nm	-774.43 pm/ °C	-586.43 pm/ °C

5.5.3 GO-LPG based biosensor for haemoglobin detection

The LPG based biosensing devices were functionalised with NaOH, APTES, and GO aqueous dispersion, and then were investigated for the detection of human haemoglobin. All the chemicals were acquired from Sigma-Aldrich. The other chemicals, such as methanol, ethanol and DI water were used as solvent to prepare the solutions and for surface cleaning purposes.

A 17 mm long LPG with a period of 400 μm was UV-inscribed into B-Ge photosensitive fibre with point-by-point inscription technique. Then the LPG was cleaned, undergone through NaOH treatment and silanised with APTES as mentioned the whole method for fabricating sensing device in section 5.5.1. Following similar steps as described in the same section 5.5.1 a GO solution with concentration of 0.5 mg/mL was prepared and deposited onto the LPG sensor by dip coating method. In this process the fibre sensor was immersed into the solution for a certain time of ~40 mins for each layer and it was dried by placing it onto a hotplate with set temperature of 55 °C.

The GO-LPG was then subjected to haemoglobin detection experiment. Figure 5.14 shows the measurement technique where the GO-LPG was placed into an SRI sensing setup and the light was launched through a supercontinuum source. The spectrum was captured through an optical spectrum analyser (OSA YOKOGAWA). The bend cross-talk effects was avoided by straightening and keeping the fibre grating fixed between two 3D stages.
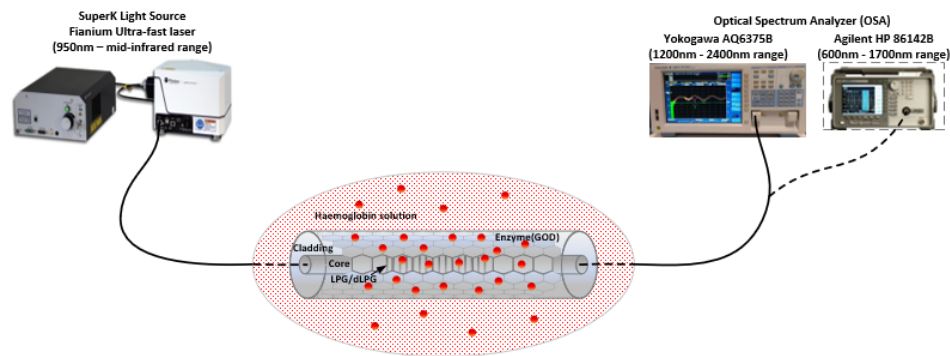
Figure 5. 14 Schematic of the measurement setup with GO-coated LPG sensor for haemoglobin sensing.

Figure 5.15 (a) shows the spectral evaluation after each step during the pre-treatment, GO coating process and the haemoglobin detection. It is seen from the figure that after 2-layers of GO-deposition the attenuation is decreased for all the resonance peaks. The amplitude is decreased by maximum around 8 dB for the higher order resonance at 1520 nm, whereas it is reduced approximately by 3 dB for other two lower order peaks 1 and 2.

Then the GO-LPG was investigated as a biosensor for haemoglobin detection. A set of haemoglobin concentrations of 0.14 mg/mL, 0.22 mg/mL, 0.27 mg/mL, 0.31 mg/mL, and 0.33 mg/mL were prepared with sucrose solution (RI = 1.39) acting as a buffer solution. The spectral evaluation was recorded for each solution, after it was applied onto the sensor. Following each haemoglobin solution applied, the fibre sensor was cleaned with DI water to maintain the same reference level. It is observed from the plotted spectra in Fig. 5.15 (b) that an increased attenuation is achieved as the

concentration of haemoglobin solution is increased. The plots for sensitivity are shown in Fig. 5.15 (c) where a maximum intensity change of -4.34 dB/(mg/mL) is achieved for the higher order resonance, peak 3. However, a lower sensitivity is obtained for peaks 1 &2 as -1.65 dB/(mg/mL) and -2.83 dB/(mg/mL) respectively. This demonstrates that an enhanced sensitivity is achievable with the linkage of biocompatible GO-molecules onto the sensor surface to significantly increase the optical absorption through the evanescent field.

(a)

(b)

(c)
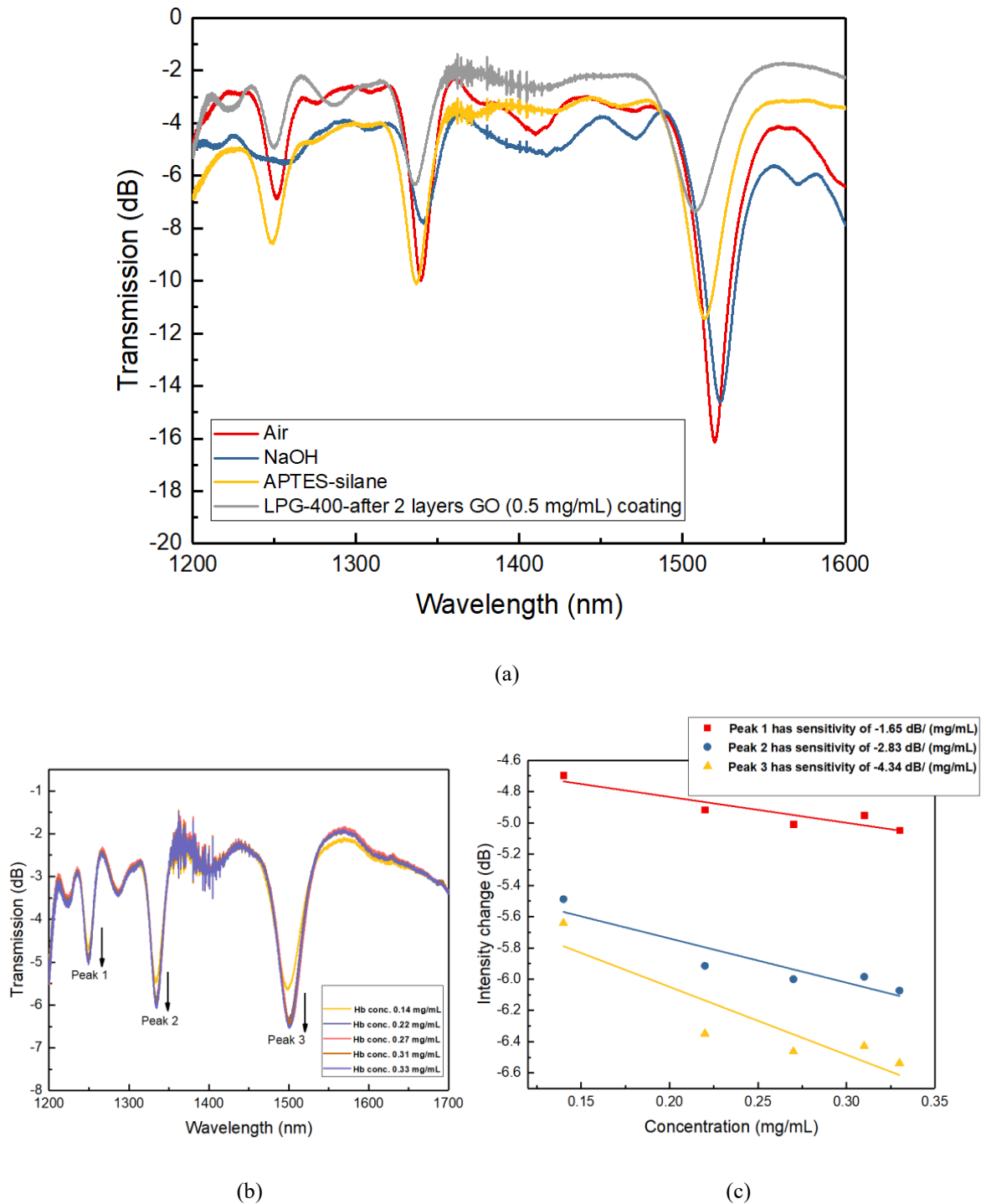
Figure 5. 15 Spectral evaluation during deposition process (a), after each Hb solutions with different concentrations applied (b) and sensitivity analysis (c) for GO-coated LPG with various haemoglobin concentrations for all the attenuation peaks (1, 2& 3).

To further demonstrate, an ultra-high sensitive biosensor was fabricated with dual-peak LPG. Similarly, two layers of GO deposition with the concentration of 0.5 mg/mL was applied onto the dLPG. The sensor device was placed in the measurement setup as depicted in Fig. 5.14. The spectral modification after GO-coating is shown in Fig. 5.16 (a&b) for all the resonance peaks 1,2,3&4, measured with two OSAs (HP & YOKOGAWA) at a set resolution of 0.20 nm. It is seen from the figure (b) that, after GO coating, the attenuation increases by 3 dB and 5 dB approximately for the dual peaks (peak 2 and 3) at 1570 nm and 1708 nm respectively. Whereas the normal resonance peaks 1 and 4 has the amplitude modulation of ~4 dB and ~1 dB respectively. Then the prepared haemoglobin solutions with the same concentrations as described for GO-LPG, were applied to the GO-dLPG. The spectral evaluation in Fig. 5.16 (c&d) shows the gradual rise in intensity with the increase in concentration of haemoglobin solution. The sensitivity analysis for all the resonances is shown in Fig. 5.16 (e&f). A comparatively small attenuation change is observed for the resonance peaks 1&4. These are evaluated as -4.49 dB/ (mg/mL) and -3.07 dB/ (mg/mL) respectively as depicted in Fig. 5.16 (e). The maximum amplitude change is achieved at the dispersion turning points with the values of -10.65 dB/(mg/mL) and -13.60 dB/(mg/mL) for peaks 2 and 3 respectively as represented in Fig. 5.16 (f). This sensor device shows much higher sensitivity compared to GO-LPG while the same conditions were maintained during the GO-coating process, keeping the similar concentrations and number of layers deposited.

(a)　　　　　　　　　　　　　　　　　　　　　(b)
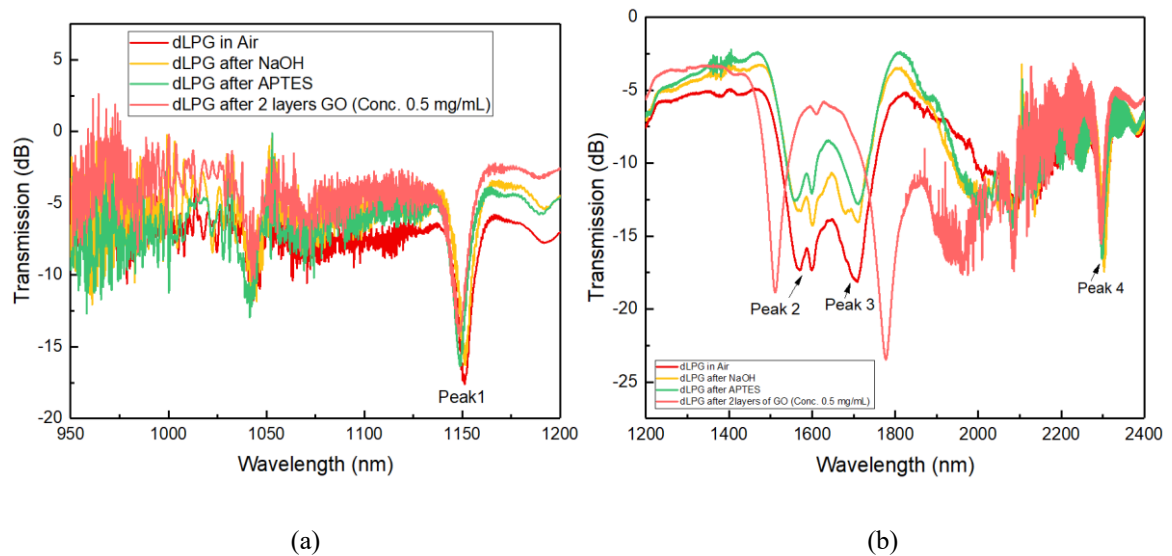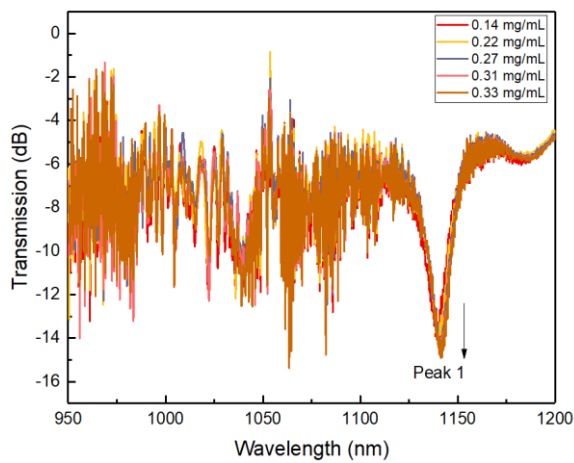
(c)
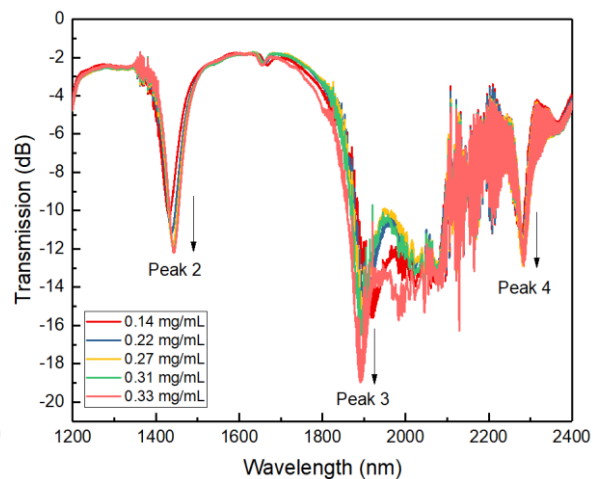
(d)
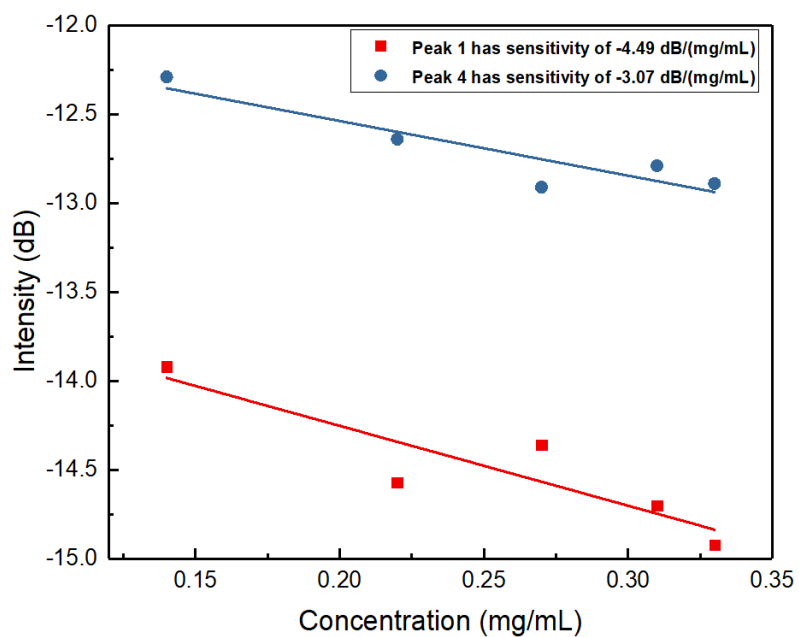
(e)
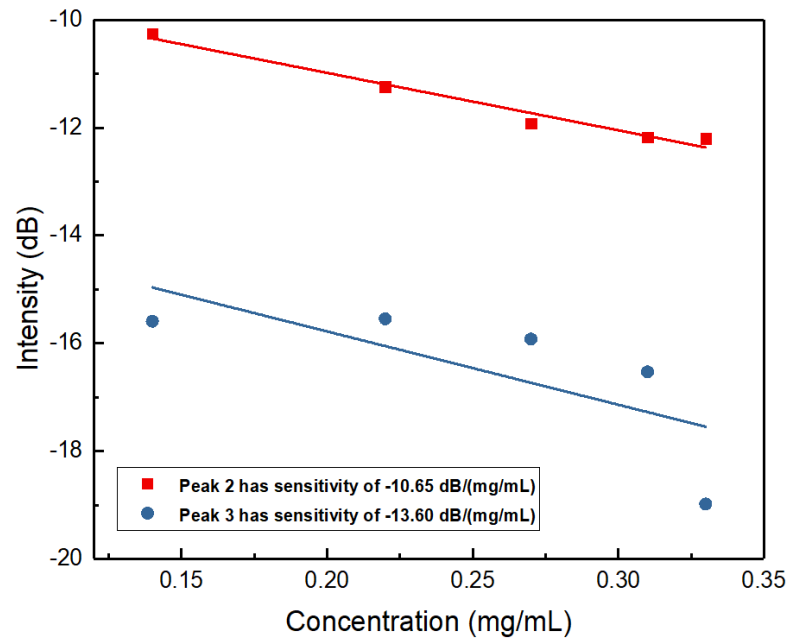
(f)

Figure 5. 16 Spectral evaluation during deposition process for normal dLPG peak 1 (a); for conjugated dual resonance peaks 2&3, and normal dLPG peak 4 (b)., Investigation for spectral response after each Hb solution with different concentrations applied for normal dLPG peak 1 (c); for conjugated dual resonance peaks 2&3, and normal dLPG peak 4 (d). Sensitivity analysis for GO-coated dLPG with various haemoglobin concentrations for both the attenuation peaks (1&4) (e) and conjugated dual peaks (2&3) (f).

5.6 Graphene- oxide functionalised LPG sensor for environmental sensing

Relative humidity (RH) sensing plays a major role in food processing industry, structural health monitoring and many other environmental sensing applications [2, 10]. Besides, comparing with resistor and capacitive type of sensors, the optical fibre sensors are more advantageous as they are highly sensitive, structurally very simple, immune to electromagnetic interference, resistant to corrosive environment etc. In recent works, many fibre sensors, such as fibre Bragg gratings (FBGs) made with polymer fibre [10] and long period gratings (LPGs) with different refractive index coatings [149], have been explored for different RH sensing applications.

Long period gratings have typical periods ranging from tens to few hundred microns. The relatively large period structure enables the light coupling from the core mode to the low order cladding modes under phase matching condition, generating a set of attenuation bands centred at different wavelengths in the transmission spectrum. The spectral distribution of each cladding mode depends on the fibre structure and surrounding medium. Thus, the wavelength shift of the LPG attenuation bands can be obtained with the change in refractive index of surrounding medium as the effective

refractive index of the core and cladding modes varies [88]. This is the mechanism of an LPG acting as a refractive index sensor.

Graphene is a planar sheet of carbon material which consists of sp^2 bonding structure. It has excellent electronic and optical property that has been explored in fibre sensors for various applications such as RH sensing for environmental monitoring and bioscience applications. Graphene has advantages of large surface area, mechanical stability and good thermal and electrical conductivities [150]. Particularly, the tuneable optical properties of graphene make it more suitable for fibre grating sensors. It has been reported that the graphene oxide (GO) adsorbs water molecules that enhances the conducting carrier density, thus decreases the effective refractive index of GO film with increase in RH.

As for bio and environmental sensing applications, a multilayer GO-coated LPG as an RH sensor device is investigated. A dip coating technique was used to deposit GO on to the LPG surface. As GO absorbs water molecules, the effective refractive index of cladding modes changes, enabling the humidity change to be monitored. The refractive index of GO film has real and imaginary parts and in RH sensing, the imaginary part of the GO index is significantly affected by the water absorption. This proposed sensor can be extended to more advanced work with fabricating biosensors by varying the GO-coating thickness.

5.6.1 GO-LPG fabrication and spectrum measurement

The LPGs were designed with 428 μm period for a length of 20 mm. Following the cleaning, NaOH treatment and APTES silanisation as mentioned in section 5.5.1 the whole sensing device was well treated. A GO solution with concentration of 1.2 mg/mL was prepared with DI water, for multilayer deposition with 2-layers and 4-layers onto LPG. In each deposition the fibre sensor was immersed into the solution, and it was dried by placing it onto a hotplate with set temperature of 55 °C for a certain time of ~40 mins for each layer.

The spectrum of the LPG was measured after the GO coating and plotted alongside the original spectrum as shown in Fig. 5.17. It is clear from the figure that the attenuation bands of the three coupled cladding modes have significantly reduced after the GO coating, especially for the peak at 1650 nm, the strength reduced from 15 dB to only 4 dB. This is due to the change in cladding mode coupling coefficient induced by the extra layer of GO film on the LPG surface.
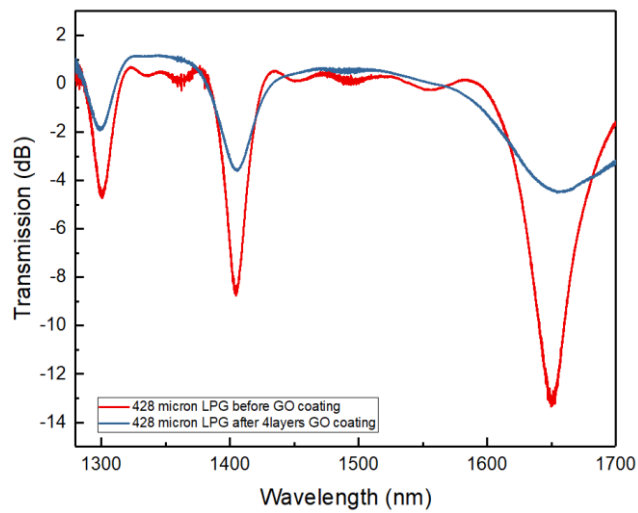
Figure 5. 17 LPG spectra before and after GO coating.

5.6.2 GO-LPG experimental setup for RH sensing

Figure 5.18 shows the experimental setup for RH sensing measurement. We used a humidity chamber (Binder KBF 115) and the GO-coated LPG was placed inside the chamber. The two fibre ends were taken out from the chamber and one end was connected with the broadband light source and the other end was connected to the optical spectrum analyser. Initially, the chamber was set at a constant temperature at 25 °C and with an RH of 20% for aprroximately 30 minutes to get a stabilised RH environment inside the chamber. For the actual measurement, the RH was varied from 50% to 80% with a step of 10%. When changing the RH, a 10 mins setting time was maintained to reach the constant value of RH and then the LPG spectrum was recorded.
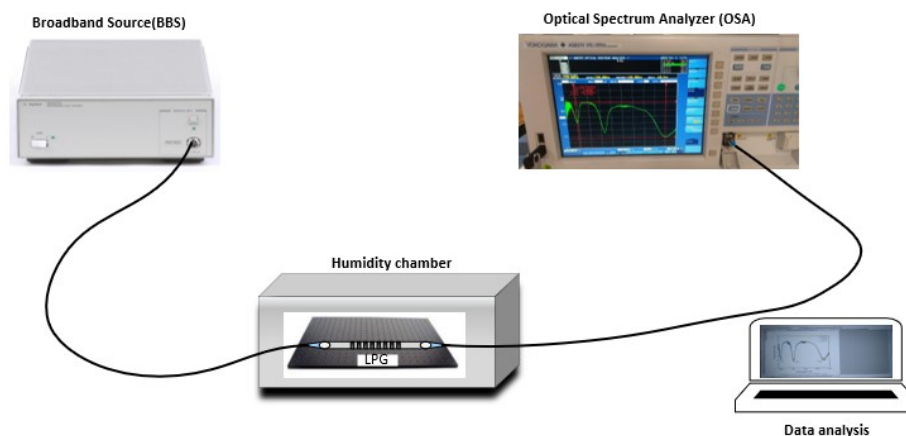
Figure 5. 18 Experimental Setup for humidity sensing measurement.

As to examine the effect of GO film thickness on LPG for the RH response, initially the LPG with 2-layer of GO coating was measured. After the first set of measurement, the LPG was further coated

with two more GO layers following the same procedure. When the grating was totally dried, the 4-layer GO coated LPG was subjected to the RH measurement and the results were recorded and compared with that of 2-layer GO-coated grating.

5.6.3 RH sensing measurements and results

Figure 5.19 and 5.20 show the spectral responses to different RH levels for the 2-layer and 4-layer GO-coated LPGs. From Fig. 5.19 (a), clearly it is observed that only peak 3 at ~1650 nm of the 2-layer GO-coated LPG responded to RH change. However, after the deposition of two more layers, all three peaks of the 4-layer GO-coated LPG have responded to the RH change, as shown in Fig. 5.20 (a). In some previously reported work, the GO-coated gratings (LPG and TFG) have shown both amplitude variation and wavelength shift under RH change [150, 151]. In these GO-coated LPGs, the resonance amplitude change is more pronounced whereas the shift of resonance peak is hardly visible. This can be explained by the fact that the GO coating on the LPGs may have limited thickness, thus only the absorption, which is associated with the imaginary part of the GO refractive index, is dominant.

(a)   (b)
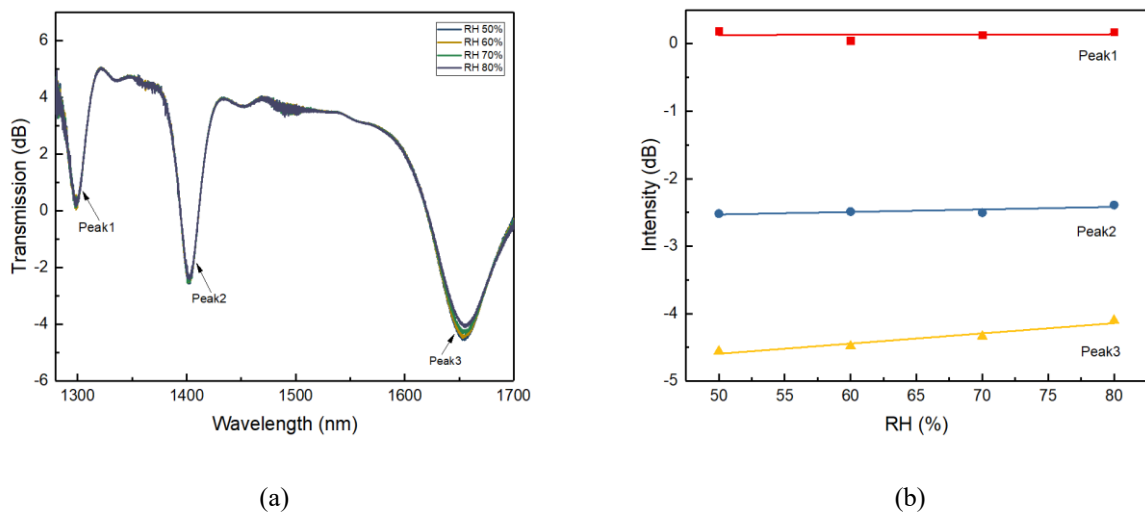
Figure 5. 19 (a) Transmission spectra of 2-layer GO-coated LPG for different RH changes; (b) Peak value vs RH (%) plot for three resonance peaks.

(a)   (b)
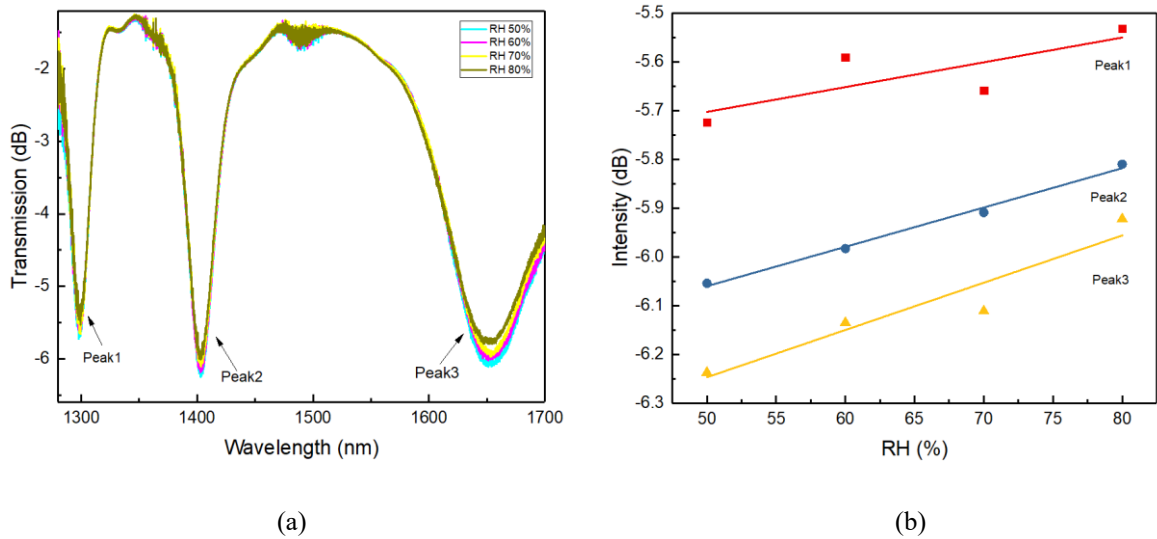
Figure 5. 20 (a) Transmission spectra of 4-layer GO-coated LPG for different RH changes; (b) Peak value vs RH (%) plot for three resonance peaks.

The plotted attenuation peak amplitude against RH change for the 2-layer and 4-layer GO-coated LPGs is shown in Figure 5.19 (b) and 5.20 (b), from which the RH sensitivities for the two gratings can be estimated. It is noted from the figures that the RH sensitivity of the longest wavelength peak (peak 3 at ~1650 nm) is the highest at ~0.01 dB/%RH, but it did not change considerably after two more layers of coating. However, for peak 1 at ~1300 nm, the RH sensitivity increased from 0.00037 dB/ %RH for the 2-layer coating to 0.0051 dB/ %RH for the 4-layer coating, i.e., enhanced by 14 times. While for peak 2 at ~1400 nm, the RH sensitivity increased from 0.0037 dB/ %RH for the former to 0.0081 dB/ %RH for the latter, i.e., enhanced by ~2 times. Due to limited facility, the actual thickness of the GO-coating couldn't be measured with accuracy. With more controllable and measurable GO-coating, the RH response of the LPGs can be improved.

Finally, in order to evaluate how RH level was maintained in the environment chamber, the stability of RH measurement was investigated by using the 4-layer GO-coated LPG. In the experiment, the RH level was varied from 30% to 80% with an interval of 10%. Two minutes were set for the environment chamber to reach each of the new level and five measurements were undertaken by recording the spectrum of the grating with an interval of 2 minutes. Figure 5.21 plots the humidity response with time, and it clearly shows that the GO-coated LPG responds to RH change rapidly and maintains constant transmission while the RH level is unchanged.
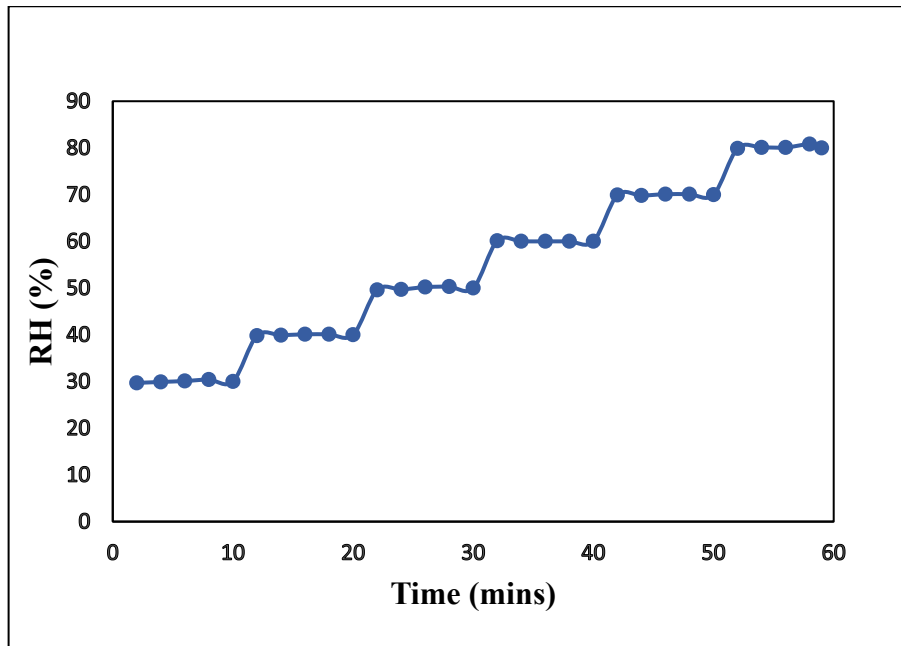
Figure 5. 21 Multiple measurements of RH response of the 4-layer GO-coated LPG.

5.7 Surrounding refractive index (SRI) sensors based on LPG with carbon nanotube (CNT) deposition

Carbon nanotubes (CNTs) are recognised as hollow cylindrical tubes of rolled-up graphene sheets with carbon atoms arranged in a hexagonal structure. Depending on number of layered graphene sheets these can be of two types. A single layered structure is known as the single-walled CNT (SWCNT) with diameters range from 0.4 nm to 3 nm, whereas a multi-rolled graphene sheet of diameters varying between 1.4 nm to 100 nm and consisting of an interlayer spacing of 0.34 nm is called as multi-walled CNT (MWCNT) [152-154]. Figure 5.22 shows the schematic of graphene sheet and a carbon nanotube.
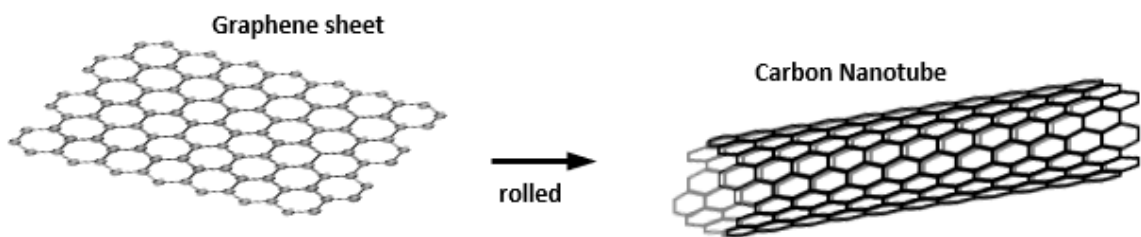
Figure 5. 22 Schematic representation of graphene sheet and CNT adapted from [154].

CNTs are advantageous as it has good stability, broader operation wavelength and easy to fabricate. In principle by incorporating CNTs on optical fibres it is affecting the evanescent field and the light leaked through CNT coating layer greatly influence the interaction with surrounding medium. These light absorption and complex refractive index between core-cladding and surroundings, has been utilised with CNTs coated with microfibre, photonic crystal fibre, LPG, tilted gratings (TFG) and etched FBG for increased SRI sensitivity and applications for biosensing [155-158].

5.7.1 SWCNT deposition and experimental setup

A sample solution of 5 mL was prepared by dispersing SWCNT powder (CG100; average diameter of 0.82 nm) into N-methyl-2-pyrrolidone (NMP) solution and sonicated for enough time to achieve a uniform dispersion. The NMP is an excellent organic solvent and is efficient in the direct dispersion of hydrophobic materials (CNT) at lower concentrations of (< 0.02 mg/mL) [159]. This well-prepared sample solution was deposited on fibre sensing device. An UV-inscribed LPG of ~16 mm length fabricated into normal B-Ge photosensitive fibre with period of 428 μm was considered for this purpose. It was fixed onto a v-grooved mini-bath before starting the nanomaterial deposition with prepared CNT dispersion. The schematic representation of this experimental setup is shown in Fig. 5.23 (i). Firstly, the sensing region was cleaned with methanol and DI water for several times.

Thereafter, a ~200 µL of sample solution was directly applied onto the LPG device for easy repeatability, and it was remained for ~5 mins. Then the one-layer nano-deposited LPG was lifted up to dry by placing it onto a customised glass slide setup above the hotplate at set temperature of 55 °C for ~30 mins. Thereafter the fibre sensor brought into room temperature and set for SRI sensing measurement setup as represented in Fig. 5.23 (ii). A set of refractive index gels with index values ranging from 1.335 to 1.380 were applied onto the SWCNT-coated LPG. An input light was launched through a broadband source (Agilent, 83437A) and the resonance wavelength shift was recorded in an OSA after the sensing length was completely immersed into each index gel.

(i)

(ii)
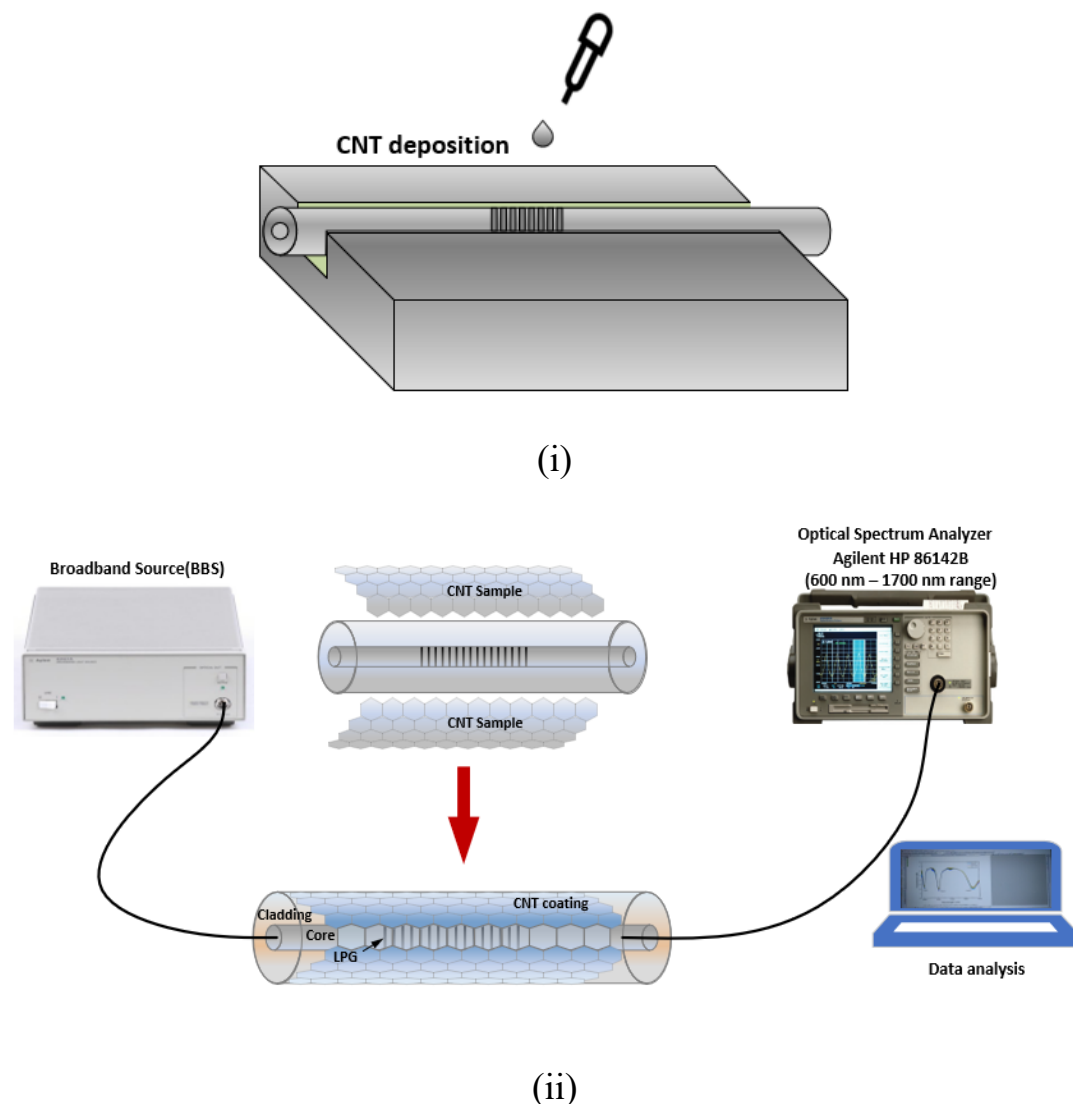
Figure 5. 23 (i) Schematic representation of CNT-deposition process into a v-groove bath; (ii) Experimental setup for surrounding refractive index (SRI) sensing measurement of one-layer SWCNT coated LPG sensing device.

The spectral evaluation of LPG device was performed to record both of the original spectrum and after one layer of coating applied, considering the surrounding medium as air. It is clearly evidenced

from Fig. 5.24 that there is significant effect on resonance response after SWCNT coating applied. The decreased attenuations are achieved as ~4 dB, ~5.50 dB and ~6 dB for peaks 1,2 & 3 respectively. However, a blue shifted wavelength of ~47 nm is observed for higher order resonance at ~1660 nm.
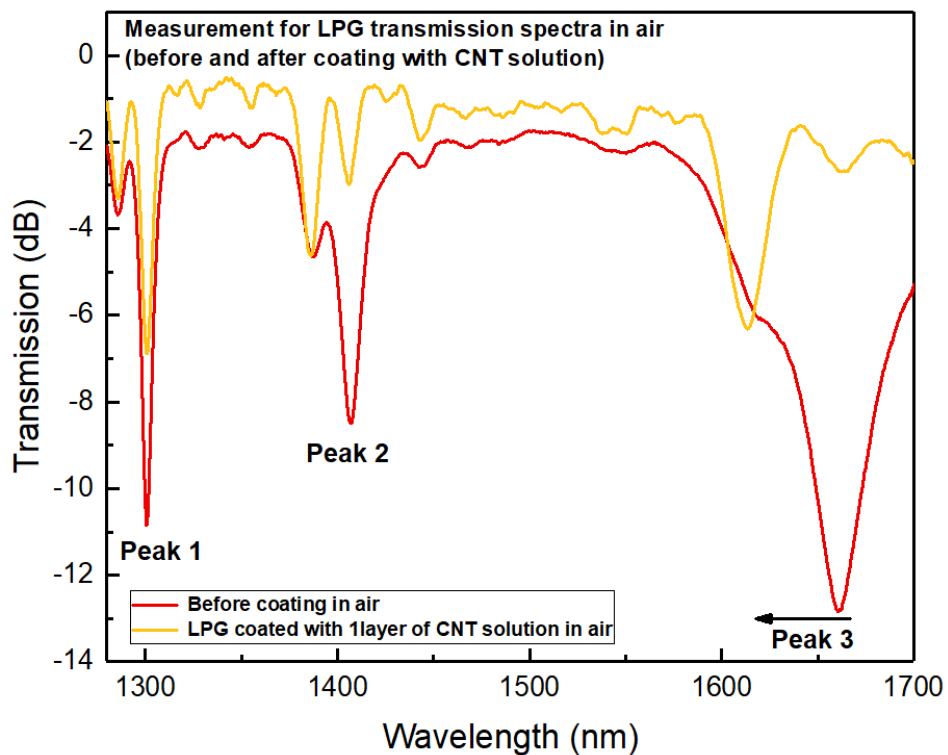
Figure 5. 24 Transmission spectra of LPG into air before and after 1layer of coating with SWCNT solution.

5.7.2 Sensing measurements and results

As seen the higher order resonance is more sensitive compared to other lower order resonances, the plotted results in Fig. 5.25 are presented for spectral evaluation of peak 3, when the SWCNT-coated LPG device was subjected to SRI sensing. It is clearly observed from Fig. 5.25 (a), with increase in SRI there is gradual decrease in transmission amplitude with the resonance blue shifting. The sensitivity analysis for this device results in SRI sensitivities of 6.34 dB/RIU for intensity change and -96 nm/RIU for wavelength shift respectively as shown in Fig. 5.25 (b&c). In comparison with uncoated LPG with period of 400 μm the measured resonant shift was recorded in chapter 3 as ~ -46.7 nm/RIU in the SRI range of ~ (1.335-1.38) for higher order cladding mode at ~1500 nm. Hence, it is clearly seen that an enhanced SRI sensitivity was achieved for one layer CNT- deposited LPG device with slightly higher period of 428 μm and for the higher order resonance peak 3 in the similar range of surrounding refractive index variation. The achieved performance of this sensing device makes CNT-LPG as a good potential sensor for the applications in biosensing and environmental sensing, where bio/chemical detection is possible with high RI sensitivity, inexpensive power-based demodulation and with large mechanical strength. Since, the real-time implementation of medical

equipment is in progress, we can find its potential application in cancer cell detection and medicines [160, 161].
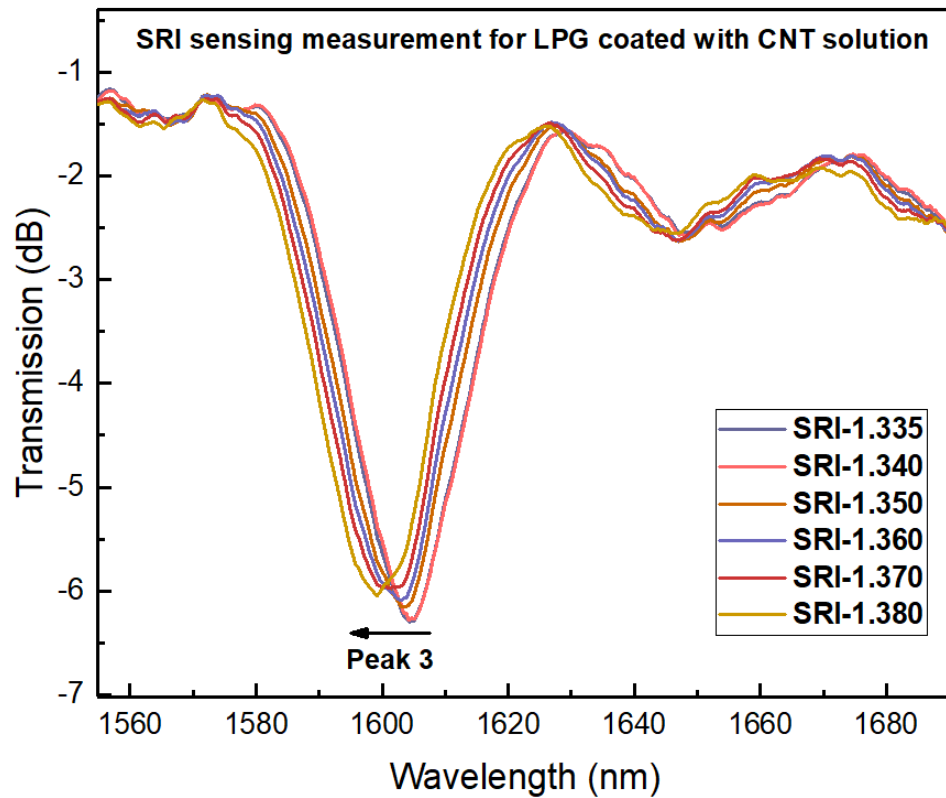
(a)
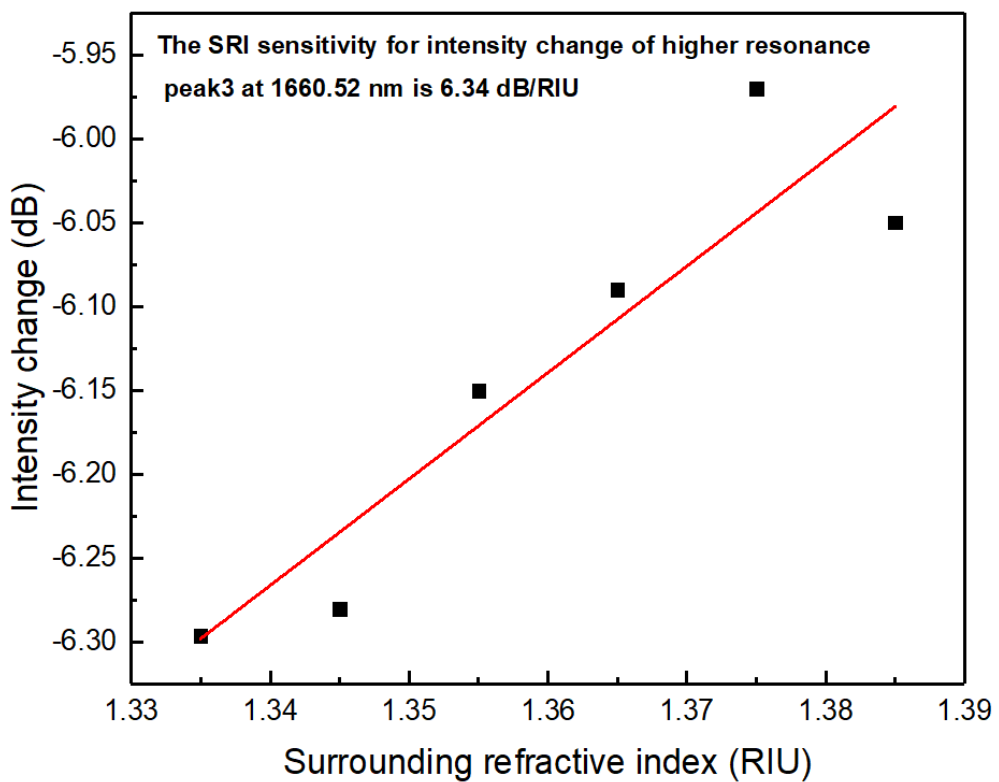
(b)
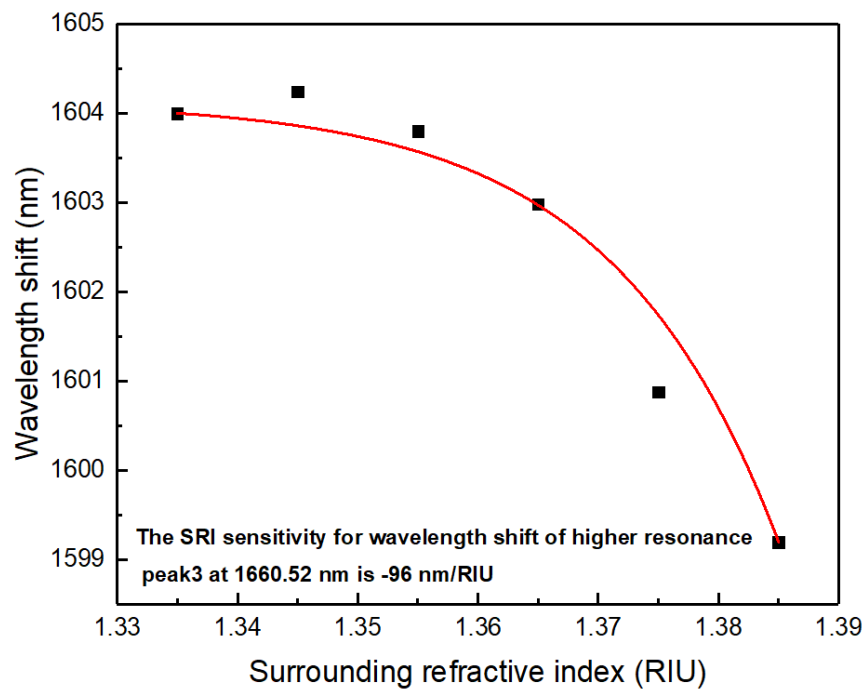
(c)

Figure 5. 25 (a) Transmission spectra of 1layer SWCNT-coated LPG for different SRI changes; (b) Evaluation of SRI sensitivity for intensity change; (c) Investigation of SRI sensitivity for wavelength shift for the highest order resonance peak 3 at ~1660 nm.

5.8 Chapter conclusion

In this chapter the RI based biosensors are demonstrated by applying bioactive coating for potential applications in chemical, biomedical and biological detection. Several inexpensive, easy to prepare biosensors based on LPG, dLPG and Ex-TFG are fabricated and evaluated for SRI sensing. An enzyme immobilised sensing device enables this for glucose sensing application in the range of 0.1 – 3.0 mg/mL which is in the physiological range in human beings. Compared with the previously reported sensitivity here we are able to obtain a maximum sensitivity of -36.25 nm/ (mg/ mL) using the most sensitive dual-peak LPGs.

The second type of biosensors is GO-LPG and GO-dLPG based highly sensitive sensors for the applications in haemoglobin sensing. Following the two layers of GO deposition method for both gratings, the SRI sensing measurements using the GO functionalised LPG and dLPG have been performed with haemoglobin solutions of different concentrations in the range of 0.14 – 0.33 mg/mL. A highest SRI sensitivity for intensity change of -4.34 dB/ (mg/mL) for GO-LPG with higher order resonance peak 3 and -13.60 dB/ (mg/ mL) for GO-dLPG considering the conjugated peak at ~1708 nm is obtained. These devices may be useful for the detection of anaemia in human health.

Then, the demonstration of RH sensor based on LPG with GO coating has been implemented for environmental sensing applications. We have evaluated the RH response of the GO-LPGs with 2-layers and 4-layers of GO-coating and the results have clearly showed that thicker GO coating may increase the RH sensitivity. The GO-coated LPG has also showed good constant response to certain RH values. These convincing results may open the opportunity for high RH sensitivity sensors by fabricating LPGs in mid IR range with thicker GO layer deposition, and these sensors may be deployable for gas and environment sensing applications.

Finally, the nano-characterisation with SWCNT coating for optical fibre grating device has been investigated. An LPG with one layer coating shows significant sensitivity results with respect to intensity modulation of 6.34 dB/RIU and resonance shift of -96 nm/RIU respectively. A further multilayer deposition will enhance the sensitivity performance of this grating device to make them suitable in the application for harsh environment.

Chapter 6

Conclusions and Future research

6.1 Conclusions

This thesis represents a thorough investigation on the inscription, characterisation, and applications of different types of optical fibre gratings (FBGs, LPGs and TFGs) with transmission from near-IR to mid-IR range. The grating based sensors are fabricated into standard telecom fibre (SMF-28) and in special fibres, such as B/Ge doped single mode, multi-core, and thin cladding fibres. The vector sensors with potential for various applications in structural health monitoring are investigated by making vector bending sensor device into variety of multicore fibres such as four core fibre (4CF) and seven core fibre (7CF) respectively. For biosensing applications, the ultra-high sensitive grating sensors with enzyme immobilisation and 2D nanomaterial coating are employed as glucose and haemoglobin sensor for monitoring human health to enable them with available precautions from severe disease, such as mainly diabetes and anaemia. In addition, GO-coating integrated grating based sensors are also explored for relative humidity detection, presenting possibility for environmental monitoring.

The beginning of the thesis explains a brief literature review of fibre grating history and photosensitivity mechanism of optical fibres. To enhance the optical fibre photosensitivity three different techniques have been discussed briefly. A theoretical analysis for mode coupling and phase matching condition are elaborated in detail for all types of gratings. Two UV-fabrication techniques are available in AiPT research facility, such as phase or amplitude mask scanning and point-by-point writing are presented with very detailed experimental results.

For the projects presented in this thesis, phase mask scanning and point-by-point writing methods have been employed for fabricating FBGs and LPGs in the near-and mid-IR range. The inscription for TFGs is mainly using amplitude mask method, depending on exposure of UV radiation periodically for a certain time along the fibre length. All these methods show an efficient inscription for writing good, stable and high quality grating structures for various successful experiments. However, mask methods require expensive variety of masks depending on inscription wavelength, whereas the point-by-point writing is the low cost and flexible method although only suitable for LPGs inscription. We have fabricated FBGs into photosensitive SMF at different centre wavelengths. The mask method is also utilised for UV-inscribed small and large angled tilted gratings with the resonances ranging from the near to mid infrared wavelength. Furthermore, the normal, dual peak and 1st & 2nd order LPGs are inscribed by point-by-point writing method for enhanced sensitivity.

The highlight of the research projects presented in this thesis is the fabrication and characterisation methods achieved for FBGs inscribed into special multicore fibres of 4CF and 7CF. Selective

inscription into different cores of a MCF has been efficient by core marking technique, involving the core positioning by placing fibre between two three dimensional rotating stages and observing the alignment through optical microscope setup. FBGs written into selective core have shown effective inscription when characterised through a novel measurement system. The vector sensing applications using FBGs written into different cores have shown effective detection of the changes in both the magnitude and direction. Specially, an opposite directional sensitivity has been observed for two diagonally positioned cores in the 4CF. The bending/twist sensing measurement for 4CF with both core spacing of 50 μm and 36 μm has been performed. This resulted in the sensitivities of -0.085 nm/m^{-1} and 0.052 nm/m^{-1} at a twist angle of 180° for a selective inscription into 4CF with 50 μm core spacing. Whereas, considering two cores located in the same perpendicular plane into another 4CF with 36 μm core to core spacing provides bending sensitivities of 0.125 nm/m^{-1} and -0.163 nm/m^{-1} respectively at a twist angle of 0° with opposite wavelength shifts. Further experimentation with fabrication and vector sensing measurement were demonstrated for 7CF using a systematic writing method followed as 4CF. The vector sensing results for the central core have been shown very small sensitivity or insensitive response to bending at different twist angles, which proves the central core is very effective as a temperature reference. Consecutively, the FBGs inscribed into other selected cores of the 7CF have been investigated for bending sensing at different twist angles of 0°, 90°, 180° and 270°. This has been shown the sensitivity results for two diagonally placed cores as amplitudes of 89.57 pm/m^{-1}, 63.27 pm/m^{-1}, -68.51 pm/m^{-1} and -134.62 pm/m^{-1} for one core and for diagonally opposite core the amplitudes have been obtained as 55.2 pm/m^{-1}, -71.79 pm/m^{-1}, 47.37 pm/m^{-1} and 120.68 pm/m^{-1} at twist angles of 0°, 90°, 180° and 270° respectively.

Another highlight of the research work is the biosensor implementation based on LPG, dLPG and Ex-TFG. An ultrasensitive dLPG biosensor was investigated utilising the feature of the forward propagating core mode coupled with co-propagating cladding mode at dispersion turning points. An UV-inscribed dLPG has been obtained into thin cladding fibre by point-by-point writing technique. This sensing device have been employed for biosensing applications for the detection of glucose concentration. The dLPG surface was treated by APTES silanisation and GOD immobilised. Then it has been subjected to the glucose detection in the range of (0-3.0 mg/mL). Compared to GOD-immobilised LPG, the dLPG based sensor is designed with higher sensitivity of -36.25 nm/ (mg/mL) at dispersion turning point.

Further biomedical application with 2D nanomaterials deposited fibre grating sensors has been demonstrated for haemoglobin detection. The sensing device has been gone through the whole surface modification method through cleaning, NaOH treatment and silanisation with APTES. Thereafter, the multilayer deposition with Graphene oxide (GO) has been employed for LPG and

dLPG sensing devices. The measurements have been performed with haemoglobin solution into sucrose buffer for the concentration in the range of 0.14 – 0.33 mg/mL. Based on intensity change of the attenuation resonance of the LPG and dLPG sensing devices, typical sensitivities of -4.34 dB/ (mg/mL) and -13.60 dB/ (mg/mL) were realised for them respectively.

Another, GO-coated LPG has been demonstrated for monitoring relative humidity (RH) applied in environmental sensing. As mentioned for GO-LPG/dLPG biosensing applications, similar steps have been followed for the surface treatment of sensing device for enhancing the covalent bonding and 2-layer and 4-layer of GO-deposition were implemented. An increased absorption of water molecules with the change in RH has been achieved. By enhancing the light matter interaction at the core-cladding interface, it has been possible to influence the effective refractive index and hence resonance response with relative humidity change in the range of 50% - 80%. The sensitivity for higher order resonance peak 2 has been increased with ~2 times from 0.0037 dB/ %RH to 0.0081 dB/ %RH.

Finally, an optical fibre based sensor with another advanced nanomaterial of SWCNT has been explored for performing SRI sensing measurements. Here, an UV-inscribed LPG with 428 μm period is nano-deposited with one layer of SWCNT solution into NMP. The measurement analysis results show an amplitude modulation of 6.34 dB/RIU and a blue wavelength shift of -96 nm/RIU for higher order resonance response. The device fabrication can be modified with multilayer deposition for variable coating thickness and enabling them suitable for bio and environmental sensing applications.

6.2 Future research

6.2.1 Optical fibre gratings fabrications in extended wavelength range from visible into mid-IR 2 μm

Recently, optical fibre sensing devices operating at visible to 2 μm region have shown potential applications in defence, health and enviroment. The future work would be focused on fabrication of fibre gratings (FBGs, LPGs and TFGs) into different types of single mode - single core (SM-SC) to single mode - multicore (SM-MC) fibres. FBGs in visible spectral range (450 – 650 nm) are useful for detection of biological samples such as DNA [162]. These are also advantageous to use in fibre lasers as the new technology requires its extensive use from infrared region to visible range. FBGs in this range is also useful for fibre resonators or for stabilisation of centre wavelength of fibre lasers. Previously reported study shows, the FBGs into 2 μm range has been fabricated utilising two-beam holographic method for the application in fibre lasers [84]. Another area of application for 2 μm fibre gratings is in gas sensing, as because some of gas (CO_2) has strong absorption in mid-IR range. So, a fibre laser with FBG in 2 μm can be designed in this range. Whereas the LPG based refractive index sensors have potential applications in bio and environmental sensing. In these sensors, the interaction of evanescent field for the cladding modes occurs with surrounding medium and results in the resonance wavelength shift with the change in surrounding refractive index (SRI) [163]. Furthermore, an enhanced SRI sensitivity is achieved for the dual peak LPG (dLPG) operating near the turnaround points [72]. An ultra sensitive device with UV-inscribed Ex-TFGs are designed with high SRI sensitivity and low thermal sensitivity [9]. In these asymmetric structures the coupled cladding modes are very closely spaced. An input polarised light is sent through this sensing device and dual peak resonance response is obtained with two orthogonal polarisation modes in the transmission spectrum. All these refractive index based sensing devices are applicable for real time applications such as in food industry and agriculture.

6.2.2 Fibre sensor devices using multicore fibre for applications in astronomy

In astrophotonics it is very important to remove any atmospheric variations for imaging spectroscopy. An astronomical telescope is capable of covering a large wavelength range from near to middle infrared capturing image through a wide background. All these backgrounds are coming from the bright and narrow emission lines of hydroxyl (OH) ions into the atmosphere. The captured data is continuously getting distorted due to continuous fluctuation of brightness. So, a OH suppression fibres with fibre Bragg gratings (FBG) and photonic lanterns can be designed with the combination of telescope and spectrograph. Firstly, an aperiodic FBGs can be fabricated into a single sensing device using MCF enables with filtering more than 100 irregularly spaced wavelengths over

a bandwidth of 200 nm as reported in [164]. Secondly, a photonic lantern with MCF can be utilised to receive the light coupled information into the telescope [165, 166].

The ability to create a spectrograph by constructing a photonic lantern is possible using SM-MCF. The photonic lantern is a device where the light is guided through multimode fibre (MMF) to single mode fibre (SMF). Due to inefficient light coupling from a multimode fibre (MMF) into multiple SMF it is required to design a compact system for mode coupling. The photonic lantern can be constructed from MMF to SM-MCF for this purpose. It is important to avoid atmospheric turbulence effect while light coming from the telecsope to SMF. This can be presented by utilising a diffraction limited system for operation in seeing limit [104]. The schematic shown in Fig. 6.1 represents the whole imaging system where the lights coming from far distant object in the galaxy are focused through telescope and after passing through the combination of MC-FBG and photonic lantern a spectrograph is formed. My future work would be concentrated to design a photonic lantern using SM-MCF with UV-inscribed FBG to analyse the chemical composition, velocity and distance to an astronomical object. The whole designing structure is presented in Fig. 6.2.
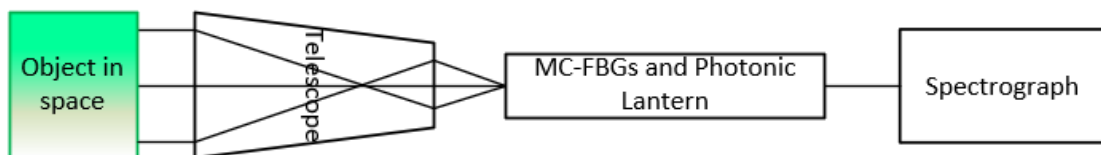
Figure 6. 1 Schematic diagram for designing the space imaging system.
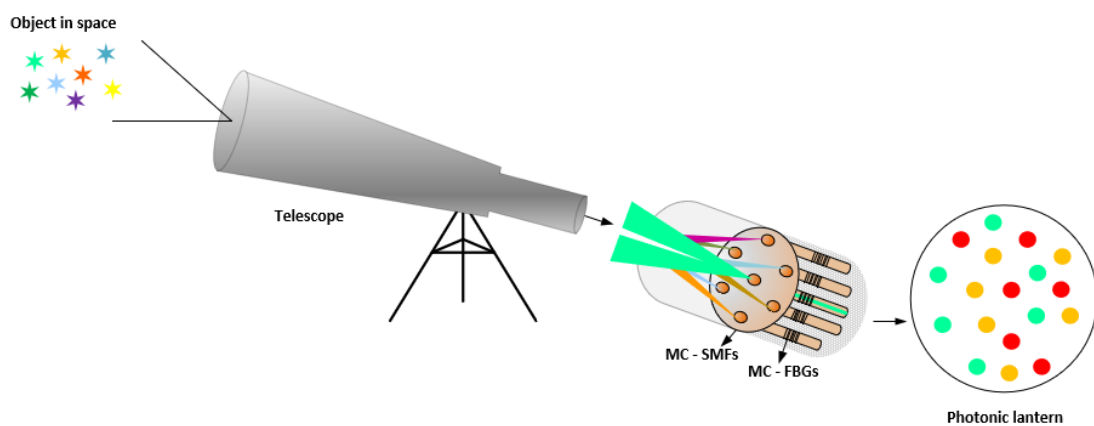
Figure 6. 2 The principle for light imaging through telescope and MC-FBG creating a photonic lantern [167].

6.2.3 Fibre gratings into multicore fibre as a shape sensor in biomedical applications

As discussed in Chapter 4, the flexibility of curvature sensing for fibre sensor devices fabricated into multicore fibre enables these for shape sensing into medical devices and applications in robotics. The FBG sensors for curvature, twist and pose measurements could be utilised in a minimally invasive instruments to provide good resolution data in space and time. Charles G. Askins et al., reported an extensive multiplexing technique employed into four core fibre (4CF) [168] for designing this. Combining a soft material robotics will enable medical devices more flexible by motion detection into different complex circumstances within the human body. In this case an actuator can provide high-resolution shape information and supporting the fibre sensor for the targetted location within human body. One of our future work will be associated with the designing of this type of fibre sensor for medical instruments. Figure 6.3 represents a schematic setup for pose measurement where an SM-MCF is embedded with S-curve catheter. Applying a soft material robotic system [169] the shape information would be collected and the high resolution image is formed by recording the spectrum reflected back through test sample.
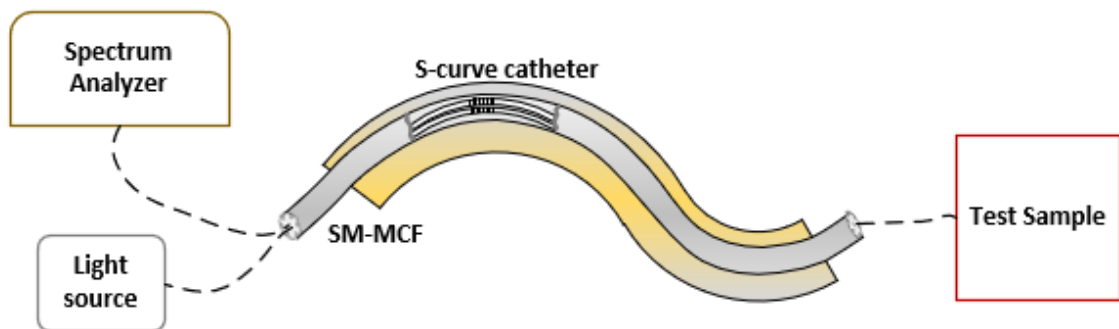
Figure 6. 3 An SM-MCF is passing through S-curve and image analysis performed by collecting high resolution shape information [168, 169].

6.2.4 Nanomaterials coated fibre sensor for biosensing applications

S. Deng, et al., have reported graphene oxide-film-coated splitting ratio-adjustable Mach-Zehnder interferometer for relative humidity sensing [170] and Chen Liu et al. showed that graphene oxide (GO) coated dLPG enhances surrounding refractive index sensitivity [150]. As discussed in Chapter 5 the dual-peak LPG (dLPG) has greater sensitivity around the dispersion turning point. Our future work will be focused on developing fibre sensors coated with high absorption material such as carbon nanotube (CNT). It is known as a dark material and fibre sensors coated with CNT enables the interaction between the light leaked through evanescent field with the external environment [171].

By utilising the absorption characteristics and complex refractive index both the position of resonance wavelengths and the amplitudes of the resonance peaks are affected with the variation of coating thickness. The greater sensitivity is achievable as the higher order cladding mode resonances are more sensitive with different coating thickness. There is an effect of coupling coefficients between the core and the high order cladding modes. Figure 6.4 shows the schematic of proposed design setup for CNT-coated fibre sensor would be implemented for environmental sensing for monitoring global warming, air quality monitoring, process control in food industry and biomedical fields.
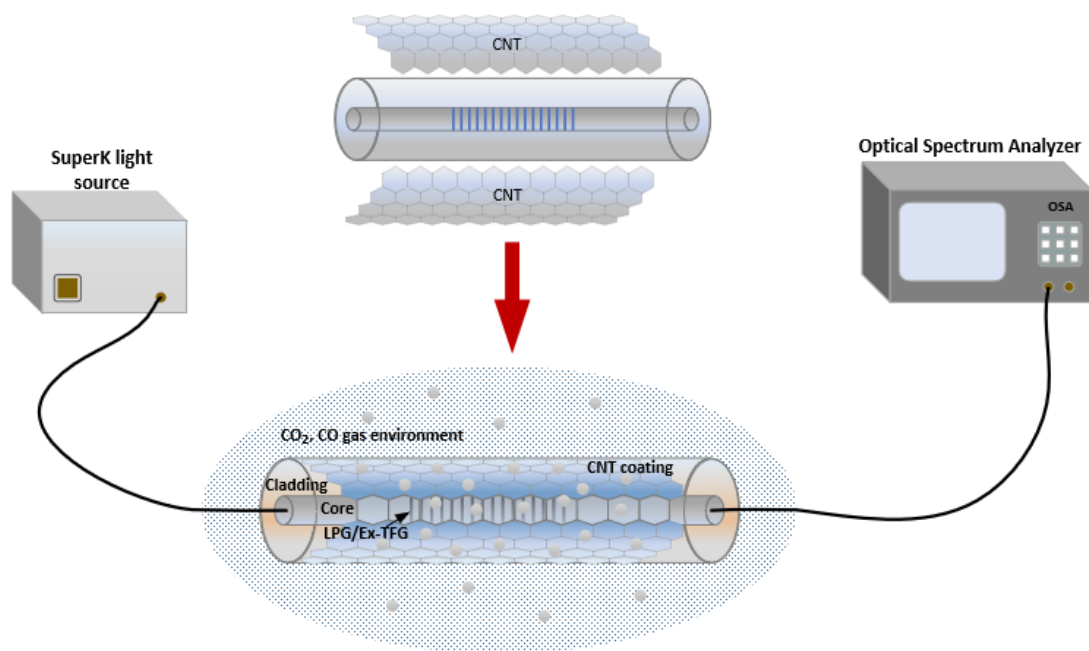
Figure 6. 4 Schematic of the proposed design setup with CNT-coated fibre sensor for gas (CO₂, CO, NH₃) sensing.

Publications

1. R. da Silva, E. Manuylovich, **N. Sahoo**, M. Becker, H. Bartelt, and D. Webb, *"Highly Efficient Side-Coupled Acousto-Optic Modulation of a Suspended Core Fiber Bragg Grating,"* IEEE Photonics Technology Letters, vol. PP, pp. 1-1, 10/26 2021.

2. **N. Sahoo**, W. Bao, S. Liu, Y. Tan, K. Zhou, and L. Zhang, *Fibre Bragg grating inscription into a seven core fibre and its application as a vector bending sensor*. Proc. SPIE 11772, Optical Sensors 2021, 117720O (18 April 2021).

3. R. da Silva, E. Manuylovich, **N. Sahoo**, M. Becker, H. Bartelt, and D. Webb, *Ultra-compact acousto-optic modulator of a fibre Bragg grating in a highly birefringent suspended core fibre*. Proc. SPIE 11773, Micro-structured and Specialty Optical Fibres VII, 117730U (18 April 2021).

4. W. Bao, **N. Sahoo**, Z. Sun, C. Wang, S. Liu, Y. Wang, and L. Zhang, *"Selective fiber Bragg grating inscription in four-core fiber for two-dimension vector bending sensing,"* Optics Express, vol. 28, 08/10 2020.

5. **N. Sahoo**, Z. Sun, K. Zhou, X. Chen, Y. Tan, and L. Zhang, *Graphene-oxide coated LPGs for humidity sensing applications*. Proc. SPIE 11355, Micro-Structured and Specialty Optical Fibres VI, 1135505 (1 April 2020).

6. Y. Chen, S. Liu, Z. Sun, L. Zhang, **N. Sahoo**, J. Luo, Y. Zhao, C. Liao, B. Du, C. Li, and Y. Wang, *"Undamaged Measurement of the Sub-Micron Diaphragm and Gap by Tri-Beam Interference,"* Journal of Lightwave Technology, vol. PP, pp. 1-1, 09/10 2019.

7. W. Bao, C. Wang, Y. Wang, **N. Sahoo**, and L. Zhang, *"2D bending (curvature) recognition based on combination of a TFBG and an orthogonal TFBG pair,"* Applied Physics Express, vol. 12, 06/12 2019.

References

1.   Hill, K.O. and G. Meltz, *Fiber Bragg grating technology fundamentals and overview.* Journal of Lightwave Technology, 1997. **15**(8): p. 1263-1276.

2.   Hill, K.O., et al., *Photosensitivity in optical fiber waveguides - application to reflection filter fabrication.* Applied Physics Letters, 1978. **32**(10): p. 647-649.

3.   Fiori, C. and R.A.B. Devine, *Evidence for a wide continuum of polymorphs in alpha-SiO$_2$.* Physical Review B, 1986. **33**(4): p. 2972-2974.

4.   Lemaire, P.J., et al., *High-pressure H$_2$ loading as a technique for achieving ultrahigh UV photosensitivity and thermal sensitivity in GeO$_2$ doped optical fibers.* Electronics Letters, 1993. **29**(13): p. 1191-1193.

5.   Meltz, G., W.W. Morey, and W.H. Glenn. *In-fiber Bragg grating tap*. in *Optical Fiber Communication*. 1990. San Francisco, California: Optical Society of America.

6.   Erdogan, T. and J.E. Sipe, *Tilted fiber phase gratings.* Journal of the Optical Society of America a-Optics Image Science and Vision, 1996. **13**(2): p. 296-313.

7.   Khan, F., et al., *Curvature, twist and pose measurements using fiber Bragg gratings in multi-core fiber: A comparative study between helical and straight core fibers.* Sensors and Actuators A: Physical, 2021. **317**: p. 112442.

8.   Silva-López, M., et al., *Transverse load and orientation measurement with multicore fiber Bragg gratings.* Applied Optics, 2005. **44**(32): p. 6890-6897.

9.   Luo, B., et al., *Novel glucose sensor based on enzyme-immobilized 81° tilted fiber grating.* Optics Express, 2014. **22**(25): p. 30571-30578.

10.   Webb, D.J., *Fibre Bragg grating sensors in polymer optical fibres.* MEASUREMENT SCIENCE and TECHNOLOGY, 2015. **26**(9).

11.   Lam, D.K.W. and B.K. Garside, *Characterization of single-mode optical fiber filters.* Applied Optics, 1981. **20**(3): p. 440-445.

12. Broer, M.M., R.L. Cone, and J.R. Simpson, *Ultraviolet-induced distributed-feedback gratings in Ce^{3+}-doped silica optical fibers.* Optics Letters, 1991. **16**(18): p. 1391-1393.

13. Bilodeau, F., et al., *Ultraviolet-light photosensitivity in Er^{3+}–Ge-doped optical fiber.* Optics Letters, 1990. **15**(20): p. 1138-1140.

14. Sasaki, Y. and Y. Ohmori, *Phase-matched sum-frequency light generation in optical fibers.* Applied Physics Letters, 1981. **39**(6): p. 466-468.

15. Osterberg, U.L.F. and W. Margulis. *Efficient second harmonic generation in an optical fiber.* in *International Quantum Electronics Conference.* 1986. San Francisco, California: Optical Society of America.

16. Meltz, G., W.W. Morey, and W.H. Glenn, *Formation of Bragg gratings in optical fibers by a transverse holographic method.* Optics Letters, 1989. **14**(15): p. 823-825.

17. Kashyap, R., et al. *All-fibre narrowband reflection gratings at 1500 nm.* Electronics Letters, 1990. **26**, 730-732.

18. Hill, K.O., et al., *Chirped in-fiber Bragg gratings for compensation of optical-fiber dispersion.* Optics Letters, 1994. **19**(17): p. 1314-1316.

19. Eggleton, B.J., et al. *Long periodic superstructure Bragg gratings in optical fibres.* Electronics Letters, 1994. **30**, 1620-1622.

20. Malo, B., et al. *Apodised in-fibre Bragg grating reflectors photoimprinted using a phase mask.* Electronics Letters, 1995. **31**, 223-225.

21. Reid, D.C.J., et al. *Phase-shifted moiré grating fibre resonators.* Electronics Letters, 1990. **26**, 10-12.

22. Kashyap, R., P.F. Mckee, and D. Armes, *UV written reflection grating structures in photosensitive optical fibres using phase-shifted phase masks.* Electronics Letters, 1994. **30**(23): p. 1977-1978.

23. Vengsarkar, A.M., et al. *Long-period fiber gratings as band-rejection filters.* in *Optical Fiber Communications Conference.* 1995. San Diego, California: Optical Society of America.

24.   Bhatia, V., *Applications of long-period gratings to single and multi-parameter sensing.* Optics Express, 1999. **4**(11): p. 457-466.

25.   Monro, T.M., et al., *Sensing with microstructured optical fibres.* Measurement Science and Technology, 2001. **12**(7): p. 854-858.

26.   Westbrook, P.S., T.A. Strasser, and T. Erdogan, *In-line polarimeter using blazed fiber gratings.* Ieee Photonics Technology Letters, 2000. **12**(10): p. 1352-1354.

27.   Zhou, K.M., et al., *High extinction ratio in-fiber polarizers based on 45 degrees tilted fiber Bragg gratings.* Optics Letters, 2005. **30**(11): p. 1285-1287.

28.   Zhou, K.M., et al., *Optic sensors of high refractive-index responsivity and low thermal cross sensitivity that use fiber Bragg gratings of > 80 degrees tilted structures.* Optics Letters, 2006. **31**(9): p. 1193-1195.

29.   Martinez, A., I.Y. Khrushchev, and I. Bennion, *Thermal properties of fibre Bragg gratings inscribed point-by-point by infrared femtosecond laser.* Electronics Letters, 2005. **41**(4): p. 176-178.

30.   Bennion, I., et al., *UV-written in-fibre Bragg gratings.* Optical and Quantum Electronics, 1996. **28**(2): p. 93-135.

31.   Huang, F., et al., *Fiber laser based on a fiber Bragg grating and its application in high-temperature sensing.* Optics Communications, 2019. **452**: p. 233.

32.   Painchaud, Y., et al. *Ultra-narrowband notch filtering with highly resonant fiber Bragg gratings*. in *Advanced Photonics & Renewable Energy*. 2010. Karlsruhe: Optical Society of America.

33.   Kaiser, P., *Drawing-induced coloration in vitreous silica fibers.* Journal of the Optical Society of America, 1974. **64**(4): p. 475-481.

34.   Hibino, Y. and H. Hanafusa, *Defect structure and formation mechanism of drawing -induced absorption at 630 nm in silica optical fibers.* Journal of Applied Physics, 1986. **60**(5): p. 1797-1801.

35. Jackson, J.M., et al., *Preparation effects on the UV optical properties of GeO₂ glasses.* Journal of Applied Physics, 1985. **58**(6): p. 2308-2311.

36. Nishii, J., et al., *Photochemical reactions in GeO₂-SiO₂ glasses induced by ultraviolet irradiation: Comparison between Hg lamp and excimer laser.* Phys Rev B Condens Matter, 1995. **52**(3): p. 1661-1665.

37. Russell, P.S.J., et al. *Optically induced creation, transformation, and organization of defects and color centers in optical fibers.* Proc. Soc. Photo-Opt. Instrum. Eng.

38. Limberger, H.G., et al., *Compaction- and photoelastic-induced index changes in fiber Bragg gratings.* Applied Physics Letters, 1996. **68**(22): p. 3069-3071.

39. Wong, D., S.B. Poole, and M.G. Sceats, *Stress-birefringence reduction in elliptical-core fibers under ultraviolet irradiation.* Optics Letters, 1992. **17**(24): p. 1773-1775.

40. Attard, A.E., *Fermi level shift in Bi₁₂SiO₂₀ via photon-induced trap level occupation.* Journal of Applied Physics, 1992. **71**(2): p. 933-937.

41. Patrick, H. and S.L. Gilbert, *Growth of Bragg gratings produced by continuous-wave ultraviolet light in optical fiber.* Optics Letters, 1993. **18**(18): p. 1484-1486.

42. Atkins, R.M., V. Mizrahi, and T. Erdogan *248 nm induced vacuum UV spectral changes in optical fibre preform cores: support for a colour centre model of photosensitivity.* Electronics Letters, 1993. **29**, 385-387.

43. Williams, D.L., et al. *Direct observation of UV induced bleaching of 240 nm absorption band in photosensitive germanosilicate glass fibres.* Electronics Letters, 1992. **28**, 369-371.

44. Dong, L., et al., *Photoinduced absorption change in germanosilicate preforms: evidence for the color-center model of photosensitivity.* Applied Optics, 1995. **34**(18): p. 3436-3440.

45. Leconte, B., et al., *Analysis of color-center-related contribution to Bragg grating formation in Ge:SiO₂ fiber based on a local Kramers–Kronig transformation of excess loss spectra.* Applied Optics, 1997. **36**(24): p. 5923-5930.

46. Poumellec, B., et al., *UV induced densification during Bragg grating inscription in Ge:SiO₂ preforms.* Optical Materials, 1995. **4**(4): p. 441-449.

47. Williams, D.L., et al. *Enhanced UV photosensitivity in boron codoped germanosilicate fibres.* Electronics Letters, 1993. **29**, 45-47.

48. Borrelli, N.F., C.M. Smith, and D.C. Allan, *Excimer-laser-induced densification in binary silica glasses.* Optics Letters, 1999. **24**(20): p. 1401-1403.

49. Cordier, P., et al., *Evidence by transmission electron microscopy of densification associated to Bragg grating photoimprinting in germanosilicate optical fibers.* Applied Physics Letters, 1997. **70**(10): p. 1204-1206.

50. Dianov, E.M., et al., *UV-irradiation-induced structural transformation of germanoscilicate glass fiber.* Opt Lett, 1997. **22**(23): p. 1754-6.

51. Fonjallaz, P.Y., et al., *Tension increase correlated to refractive-index change in fibers containing UV-written Bragg gratings.* Optics Letters, 1995. **20**(11): p. 1346-1348.

52. Tanaka, S., et al., *Hydroxyl group formation caused by hydrogen diffusion into optical-glass fiber.* Electronics Letters, 1984. **20**(7): p. 283-284.

53. Malinin, A., et al., *Formation of Hydroxyl Due to Reaction of Hydrogen with Quartz during Optical Fiber Preform Making by Furnace Chemical Vapour Deposition (FCVD) Method.* 2006.

54. Awazu, K., H. Kawazoe, and M. Yamane, *Simultaneous generation of optical absorption bands at 5.14 and 0.452 eV in 9 SiO$_2$:GeO$_2$ glasses heated under an H$_2$ atmosphere.* Journal of Applied Physics, 1990. **68**(6): p. 2713-2718.

55. Stone, J., *Interactions of hydrogen and deuterium with silica optical fibers: A review.* Journal of Lightwave Technology, 1987. **5**(5): p. 712-733.

56. Hand, D.P. and P.S. Russell, *Photoinduced refractive-index changes in germanosilicate fibers.* Optics Letters, 1990. **15**(2): p. 102-104.

57. Dianov, E.M., et al., *Highly photosensitive nitrogen-doped germanosilicate fibre for index grating writing.* Electronics Letters, 1997. **33**(15): p. 1334-1336.

58. Yariv, A., *Coupled-mode theory for guided-wave optics.* Ieee Journal of Quantum Electronics, 1973. **QE 9**(9): p. 919-933.

59.   Kogelnik, H. and C.V. Shank, *Coupled-Wave Theory of Distributed Feedback Lasers.* Journal of Applied Physics, 1972. **43**(5): p. 2327-2335.

60.   Erdogan, T., *Fiber grating spectra.* Journal of Lightwave Technology, 1997. **15**(8): p. 1277-1294.

61.   Erdogan, T., *Cladding-mode resonances in short- and long-period fiber grating filters.* Journal of the Optical Society of America A, 1997. **14**(8): p. 1760-1773.

62.   Kashyap, R., *Fiber bragg gratings*. 2009: Academic press.

63.   James, S.W. and R.P. Tatam, *Optical fibre long-period grating sensors: Characteristics and application.* Measurement Science and Technology, 2003. **14**(5): p. R49-R61.

64.   Zhou, K.M., et al., *Low thermal sensitivity grating devices based on Ex-45 degrees tilting structure capable of forward-propagating cladding modes coupling.* Journal of Lightwave Technology, 2006. **24**(12): p. 5087-5094.

65.   Lee, K.S. and T. Erdogan, *Fiber mode coupling in transmissive and reflective tilted fiber gratings.* Applied Optics, 2000. **39**(9): p. 1394-1404.

66.   Malo, B., et al. *Point-by-point fabrication of micro-Bragg gratings in photosensitive fibre using single excimer pulse refractive index modification techniques*. Electronics Letters, 1993. **29**, 1668-1669.

67.   Anderson, D.Z., et al., *Production of in-fiber gratings using a diffractive optical-element.* Electronics Letters, 1993. **29**(6): p. 566-568.

68.   Hill, K.O., et al., *Bragg gratings fabricated in monomode photosensitive optical fiber by UV exposure through a phase mask.* Applied Physics Letters, 1993. **62**(10): p. 1035-1037.

69.   Othonos, A. and K. Kalli, *Fiber Bragg gratings : fundamentals and applications in telecommunications and sensing.* Artech House optoelectronics library. 1999: Artech House.

70.   Meltz, G. and W. Morey, *Bragg grating formation and germanosilicate fiber photosensitivity*. International Workshop on Photoinduced Self-Organization Effects in Optics. Vol. 1516. 1991: SPIE.

71.   Guan, B.-O., et al., *Simultaneous strain and temperature measurement using a single fibre Bragg grating.* Electronics Letters, 2000. **36**(12): p. 1018-1019.

72.   Shu, X., L. Zhang, and I. Bennion, *Sensitivity Characteristics of Long-Period Fiber Gratings.* Journal of Lightwave Technology, 2002. **20**(2): p. 255.

73.   Wang, Q., et al., *Characterization of temperature and strain using a tilted fiber Bragg grating.* Instrumentation Science & Technology, 2015. **43**(2): p. 244-254.

74.   Dong, X., et al., *Tilted fiber Bragg gratings: Principle and sensing applications.* Photonic Sensors, 2011. **1**(1): p. 6-30.

75.   Chen, X., et al., *Study on a Plasmonic Tilted Fiber Grating-Based Biosensor for Calmodulin Detection.* Biosensors, 2021. **11**(6): p. 195.

76.   Mihailov, S., et al., *Fabrication of tilted fibre-grating polarisation-dependent loss equaliser.* Electronics Letters, 2001. **37**: p. 284-286.

77.   Zhou, K., et al. *Low-cost in-fiber WDM devices using tilted FBGs*. in *Conference on Lasers and Electro-Optics/Quantum Electronics and Laser Science Conference*. 2003. Baltimore, Maryland: Optica Publishing Group.

78.   Simpson, A.G., et al., *Optical sensor interrogation with a blazed fiber Bragg grating and a charge-coupled device linear array.* Applied Optics, 2004. **43**(1): p. 33-40.

79.   Kashyap, R., R. Wyatt, and R.J. Campbell *Wideband gain flattened erbium fibre amplifier using a photosensitive fibre blazed grating*. Electronics Letters, 1993. **29**, 154-156.

80.   Henderson, S.W., et al., *Eye-safe coherent laser radar system at 2.1 μm using Tm,Ho:YAG lasers.* Optics Letters, 1991. **16**(10): p. 773-775.

81.   Johnson, D.E., *Use of the holmium-yag (Ho-YAG) laser for treatment of superficial bladder-carcinoma.* Lasers in Surgery and Medicine, 1994. **14**(3): p. 213-218.

82.   Futao, S., et al., *Application of endoscopic Ho:YAG laser incision technique treating urethral strictures and urethral atresias in pediatric patients.* Pediatr Surg Int, 2006. **22**(6): p. 514-8.

83. Sugimoto, N., et al., *Eye-safe 2.1-μm Ho lidar for measuring atmospheric density profiles.* Optics Letters, 1990. **15**(6): p. 302-304.

84. Sun, Z., et al., *UV-Inscribed optical fiber gratings in Mid-IR range and their laser applications.* 2015. **13**: p. 328-342.

85. Shu, X., L. Zhang, and I. Bennion, *Sensitivity characteristics near the dispersion turning points of long-period fiber gratings in B/Ge codoped fiber.* Optics Letters, 2001. **26**(22): p. 1755-1757.

86. Shu, X., L. Zhang, and I. Bennion, *Fabrication and characterisation of ultra-long-period fibre gratings.* Optics Communications - OPT COMMUN, 2002. **203**: p. 277-281.

87. Nemova, G. and R. Kashyap, *Theoretical model of a planar integrated refractive index sensor based on surface plasmon-polariton excitation with a long period grating.* Journal of the Optical Society of America B, 2007. **24**(10): p. 2696-2701.

88. Patrick, H.J., A.D. Kersey, and F. Bucholtz, *Analysis of the response of long period fiber gratings to external index of refraction.* Journal of Lightwave Technology, 1998. **16**(9): p. 1606-1612.

89. Pilla, P., et al., *Giant sensitivity of long period gratings in transition mode near the dispersion turning point: an integrated design approach.* Optics Letters, 2012. **37**(19): p. 4152-4154.

90. Shu, X., et al. *High sensitivity of dual resonant peaks of long-period fibre grating to surrounding refractive index changes.* Electronics Letters, 1999. **35**, 1580-1581.

91. Chen, X.F., et al., *Dual-peak long-period fiber gratings with enhanced refractive index sensitivity by finely tailored mode dispersion that uses the light cladding etching technique.* Applied Optics, 2007. **46**(4): p. 451-455.

92. Yan, Z., et al., *Numerical and Experimental Analysis of Sensitivity-Enhanced RI Sensor Based on Ex-TFG in Thin Cladding Fiber.* Journal of Lightwave Technology, 2015. **33**(14): p. 3023-3027.

93. Kinet, D., et al., *Fiber Bragg Grating Sensors toward Structural Health Monitoring in Composite Materials: Challenges and Solutions.* Sensors, 2014. **14**(4): p. 7394-7419.

94.   Westbrook, P.S., et al., *Continuous Multicore Optical Fiber Grating Arrays for Distributed Sensing Applications.* Journal of Lightwave Technology, 2017. **35**(6): p. 1248-1252.

95.   Jantzen, S.L., et al., *Individual inscription of spectrally multiplexed Bragg gratings in optical multicore fibers using small spot direct UV writing.* Optics Express, 2020. **28**(14): p. 21300-21309.

96.   Ye, X.W., Y.H. Su, and J.P. Han, *Structural Health Monitoring of Civil Infrastructure Using Optical Fiber Sensing Technology: A Comprehensive Review.* Scientific World Journal, 2014.

97.   Mizuno, T., et al., *Long-Haul Dense Space-Division Multiplexed Transmission Over Low-Crosstalk Heterogeneous 32-Core Transmission Line Using a Partial Recirculating Loop System.* Journal of Lightwave Technology, 2017. **35**(3): p. 488-498.

98.   Richardson, D.J., J.M. Fini, and L.E. Nelson, *Space-division multiplexing in optical fibres.* Nature Photonics, 2013. **7**(5): p. 354-362.

99.   Saitoh, K. and S. Matsuo, *Multicore Fiber Technology.* Journal of Lightwave Technology, 2016. **34**(1): p. 55-66.

100.   Essiambre, R.J., et al., *Breakthroughs in Photonics 2012: Space-Division Multiplexing in Multimode and Multicore Fibers for High-Capacity Optical Communication.* Photonics Journal, IEEE, 2013. **5**: p. 0701307-0701307.

101.   Imamura, K. and R. Sugizaki. *Recent advances in multi-core transmission fibers*. in *2012 17th Opto-Electronics and Communications Conference*. 2012.

102.   Anderson, J., et al. *Multi-Core Fiber Lasers*. in *Frontiers in Optics 2015*. 2015. San Jose, California: Optical Society of America.

103.   Kochanowicz, M., et al., *Beam Quality of Multicore Fibre Lasers.* Acta Physica Polonica A, 2010. **118**(6): p. 1177-1182.

104.   Jovanovic, N., R.J. Harris, and N. Cvetojevic, *Astronomical Applications of Multi-Core Fiber Technology.* IEEE Journal of Selected Topics in Quantum Electronics, 2020. **26**: p. 2975636.

105. Silva-Lopez, M., et al. *Transverse loading of multicore fibre gratings. Second European Workshop on Optical Fibre Sensors*. Vol. 5502. SPIE, 2004.

106. Flockhart, G.M.H., et al., *Two-axis bend measurement with Bragg gratings in multicore optical fiber.* Optics Letters, 2003. **28**(6): p. 387-389.

107. Wolf, A., et al. *Femtosecond pulse inscription of 3D arrays of Bragg gratings in Selected cores of a mutlicore optical fiber*. in *Conference on Lasers and Electro-Optics Europe / European Quantum Electronics Conference (CLEO/Europe-EQEC)*. 2019. Munich, GERMANY.

108. Scholl, S.L., et al., *Thermal approach to classifying sequentially written fiber Bragg gratings.* Optics Letters, 2019. **44**(3): p. 703-706.

109. Zhang, H., et al., *Fiber Bragg gratings in heterogeneous multicore fiber for directional bending sensing.* Journal of Optics, 2016. **18**(8): p. 085705.

110. Hayashi, T. and T. Nakanishi, *Multi-core optical fibers for the next-generation communications.* SEI Technical Review, 2018: p. 23-28.

111. Prasad, P.N., G. Keiser, and J.P. Fitch, *Introduction to Biophotonics.* Assessment, 2003.

112. Wolfbeis, O.S., *Fiber-optic chemical sensors and biosensors.* Anal Chem, 2006. **78**(12): p. 3859-74.

113. Turner, A., I. Karube, and G.S. Wilson, eds. *Biosensors : Fundamentals and Applications*. 1 ed. 1987, Oxford University Press: Oxford, New York. 770.

114. Ligler, F.S. and C.R. Taitt, *Optical biosensors: present & future*. 2002: Gulf Professional Publishing.

115. Mehrvar, M., et al., *Fiber-optic biosensors-trends and advances.* Analytical sciences, 2000. **16**(7): p. 677-692.

116. Wong, D., *Chemical and Biochemical Sensing with Optical Fibers and Waveguides*. 1997, IOP Publishing.

117. Lieberman, R.A., *Recent progress in intrinsic fiber-optic chemical sensing II.* Sensors and Actuators B: Chemical, 1993. **11**(1-3): p. 43-55.

118. Schwotzer, G., et al., *Optical sensing of hydrocarbons in air or in water using UV absorption in the evanescent field of fibers.* Sensors and Actuators B-Chemical, 1997. **38**(1-3): p. 150-153.

119. Li, J., *A review: Development of novel fiber-optic platforms for bulk and surface refractive index sensing applications.* Sensors and Actuators Reports, 2020. **2**(1): p. 100018.

120. Kunz, R.E. and K. Cottier, *Optimizing integrated optical chips for label-free (bio-)chemical sensing.* Anal Bioanal Chem, 2006. **384**(1): p. 180-90.

121. Kawase, K., et al., *Non-destructive terahertz imaging of illicit drugs using spectral fingerprints.* Optics Express, 2003. **11**(20): p. 2549-2554.

122. Federici, J.F., et al., *THz imaging and sensing for security applications—explosives, weapons and drugs.* Semiconductor Science and Technology, 2005. **20**(7): p. S266-S280.

123. Li, J., *On the sensitivity of liquid-core photonic Bragg fibers.* Optical Engineering, 2019. **58**: p. 1.

124. Skorobogatiy, M., *Nanostructured and Subwavelength Waveguides: fundamentals and applications*. 2012: John Wiley & Sons.

125. Chryssis, A.N., et al., *Detecting hybridization of DNA by highly sensitive evanescent field etched core fiber bragg grating sensors.* Ieee Journal of Selected Topics in Quantum Electronics, 2005. **11**(4): p. 864-872.

126. Liu, Y., et al., *Nanopatterned evanescent-field fiber-optic interferometer as a versatile platform for gas sensing.* Sensors and Actuators B: Chemical, 2019. **301**: p. 127136.

127. Ye, M.-Y., M.-X. Shen, and X.-M. Lin, *Ringing phenomenon based whispering-gallery-mode sensing.* Scientific Reports, 2016. **6**(1): p. 19597.

128. Sotomayor, M., et al., *Bi-enzymatic optode detection system for oxalate determination based on a natural source of enzyme.* Analytica Chimica Acta, 2001. **447**: p. 33-40.

129.   DiCesare, C., I. Biran, and D.R. Walt, *Individual cell migration analysis using fiber-optic bundles.* Anal Bioanal Chem, 2005. **382**(1): p. 37-43.

130.   Atias, D., et al., *Chemiluminescent optical fiber immunosensor for the detection of IgM antibody to dengue virus in humans.* Sensors and Actuators B: Chemical, 2009. **140**: p. 206-215.

131.   Andreou, V.G. and Y.D. Clonis, *A portable fiber-optic pesticide biosensor based on immobilized cholinesterase and sol-gel entrapped bromcresol purple for in-field use.* Biosensors & Bioelectronics, 2002. **17**(1-2): p. 61-69.

132.   Brogan, K.L. and D.R. Walt, *Optical fiber-based sensors: application to chemical biology.* Curr Opin Chem Biol, 2005. **9**(5): p. 494-500.

133.   Bosch, M.E., et al., *Recent Development in Optical Fiber Biosensors.* Sensors, 2007. **7**(6).

134.   Shu, X., et al. *Room-temperature operation of widely tunable loss filter*. Electronics Letters, 2001. **37**, 216-218.

135.   MacDougall, T.W., et al., *Generalized expression for the growth of long period gratings.* IEEE Photonics Technology Letters, 1998. **10**(10): p. 1449-1451.

136.   Disley, D.M., et al., *Covalent coupling of immunoglobulin G to a poly(vinyl)alcohol-poly(acrylic acid) graft polymer as a method for fabricating the interfacial-recognition layer of a surface plasmon resonance immunosensor.* Biosens Bioelectron, 1998. **13**(3-4): p. 383-96.

137.   Cesar, E., et al., *Volatile alcoholic compunds fibre optic nano sensor.* Sensors and Actuators B: Chemical, 2006. **115**: p. 444-449.

138.   Wang, Z., et al., *Biosensors employing ionic self-assembled multilayers adsorbed on long-period fiber gratings.* Sensors and Actuators B: Chemical, 2009. **139**: p. 618-623.

139.   Liu, X., et al., *Molecular Beacons for DNA Biosensors with Micrometer to Submicrometer Dimensions.* Analytical Biochemistry, 2000. **283**(1): p. 56-63.

140.   Deep, A., et al., *Immobilization of enzyme on long period grating fibers for sensitive glucose detection.* Biosens Bioelectron, 2012. **33**(1): p. 190-5.

141. Eda, G. and M. Chhowalla, *Chemically derived graphene oxide: towards large-area thin-film electronics and optoelectronics.* Adv Mater, 2010. **22**(22): p. 2392-415.

142. Li, X., et al., *Highly conducting graphene sheets and Langmuir-Blodgett films.* Nat Nanotechnol, 2008. **3**(9): p. 538-42.

143. Kim, F., L.J. Cote, and J. Huang, *Graphene Oxide: Surface Activity and Two-Dimensional Assembly.* Advanced Materials, 2010. **22**(17): p. 1954-1958.

144. Stankovich, S., et al., *Graphene-based composite materials.* Nature, 2006. **442**(7100): p. 282-6.

145. Paredes, J.I., et al., *Graphene Oxide Dispersions in Organic Solvents.* Langmuir, 2008. **24**(19): p. 10560-10564.

146. Compton, O.C. and S.T. Nguyen, *Graphene oxide, highly reduced graphene oxide, and graphene: versatile building blocks for carbon-based materials.* Small (Weinheim an der Bergstrasse, Germany), 2010. **6**(6): p. 711-723.

147. Wang, Y., et al., *Fiber optic relative humidity sensor based on the tilted fiber Bragg grating coated with graphene oxide.* Applied Physics Letters, 2016. **109**(3): p. 031107.

148. Bandyopadhyay, S., et al., *Long Period Fiber Grating for Biosensing: An Improved Design Methodology to Enhance Add-Layer Sensitivity.* Journal of Lightwave Technology, 2018. **36**(4): p. 1178-1184.

149. Esposito, F., et al., *Ultrasensitive biosensor based on long period grating coated with polycarbonate-graphene oxide multilayer.* Sensors and Actuators B-Chemical, 2018. **274**: p. 517-526.

150. Liu, C., et al., *Graphene oxide functionalized long period grating for ultrasensitive label-free immunosensing.* Biosensors & Bioelectronics, 2017. **94**: p. 200-206.

151. Jiang, B., et al., *Graphene-induced unique polarization tuning properties of excessively tilted fiber grating.* Optics Letters, 2016. **41**(23): p. 5450-5453.

152. Iijima, S., *Carbon nanotubes: Past, present, and future.* Physica B: Condensed Matter, 2002. **323**: p. 1-5.

153. Ajayan, P.M. and T.W. Ebbesen, *Nanometre-size tubes of carbon.* Reports on Progress in Physics, 1997. **60**(10): p. 1025-1062.

154. Baughman, R.H., A.A. Zakhidov, and W.A.d. Heer, *Carbon Nanotubes--the Route Toward Applications.* Science, 2002. **297**(5582): p. 787-792.

155. Tan, Y.C., et al., *Carbon-nanotube-deposited long period fiber grating for continuous refractive index sensor applications.* Sensors and Actuators B: Chemical, 2014. **196**: p. 260-264.

156. Jia, L., et al. *A Sensitivity Enhanced Gas Sensor Based On Carbon Nanotubes Around Microfiber*. in *3rd Asia Pacific Optical Sensors Conference (APOS)*. 2012. Sydney, AUSTRALIA.

157. S, S., et al., *Optical bio-sensing devices based on etched fiber Bragg gratings coated with carbon nanotubes and graphene oxide along with a specific dendrimer.* Sensors and Actuators B: Chemical, 2014. **195**: p. 150–155.

158. Jiang, B., et al., *Carbon Nanotube-Deposited Tilted Fiber Bragg Grating for Refractive Index and Temperature Sensing.* IEEE Photonics Technology Letters, 2016. **28**(9): p. 994-997.

159. Giordani, S., et al., *Debundling of Single-Walled Nanotubes by Dilution: Observation of Large Populations of Individual Nanotubes in Amide Solvent Dispersions.* The Journal of Physical Chemistry B, 2006. **110**(32): p. 15708-15718.

160. Sireesha, M., et al., *A review on carbon nanotubes in biosensor devices and their applications in medicine.* Nanocomposites, 2018. **4**(2): p. 36-57.

161. Reilly, R.M., *Carbon Nanotubes: Potential Benefits and Risks of Nanotechnology in Nuclear Medicine.* Journal of Nuclear Medicine, 2007. **48**(7): p. 1039.

162. Lindner, E., et al., *Generation and characterization of first order fiber Bragg gratings with Bragg wavelengths in the visible spectral range.* Optics Communications, 2008. **281**(18): p. 4612-4615.

163. Bhatia, V. and A.M. Vengsarkar, *Optical fiber long-period grating sensors.* Optics Letters, 1996. **21**(9): p. 692-694.

164. Trinh, C.Q., et al., *GNOSIS: the first instrument to use fiber bragg gratings for oh suppression.* The Astronomical Journal, 2013. **145**(2): p. 51.

165. Seong-sik, M., et al. *Multicore fibre Bragg grating developments for OH suppression*. in *Proc.SPIE*. 2012.

166. Ellis, S.C. and J. Bland-Hawthorn. *Speciality optical fibres for astronomy*. in *Proc.SPIE*. 2015.

167. Jovanovic, N., R.J. Harris, and N. Cvetojevic, *Astronomical Applications of Multi-Core Fiber Technology.* IEEE Journal of Selected Topics in Quantum Electronics, 2020. **26**(4): p. 1-9.

168. Askins, C.G., G.A. Miller, and E.J. Friebele. *Bend and twist sensing in a multi-core optical fiber*. in *LEOS 2008 - 21st Annual Meeting of the IEEE Lasers and Electro-Optics Society*. 2008.

169. Galloway, K.C., et al., *Fiber Optic Shape Sensing for Soft Robotics.* Soft robotics, 2019. **6**(5): p. 671-684.

170. Deng, S., et al., *Graphene oxide-film-coated splitting ratio-adjustable Mach-Zehnder interferometer for relative humidity sensing.* Optics Express, 2019. **27**(6): p. 9232-9240.

171. Shivananju, B.N., et al., *CO_2 sensing at room temperature using carbon nanotubes coated core fiber Bragg grating.* Rev Sci Instrum, 2013. **84**(6): p. 065002.